Study of dielectric liquids as alternative encapsulant for high temperature electronics power modules applications

Joko Muslim

▶ To cite this version:

Joko Muslim. Study of dielectric liquids as alternative encapsulant for high temperature electronics power modules applications. Electric power. Université Grenoble Alpes, 2019. English. NNT : 2019GREAT109 . tel-02905480

Communauté UNIVERSITÉ Grenoble Alpes

THÈSE

Pour obtenir le grade de

DOCTEUR DE LA COMMUNAUTE UNIVERSITE GRENOBLE ALPES

Spécialité : **Génie Électrique**

Arrêté ministériel : 25 mai 2016

Présentée par

Joko MUSLIM

Thèse dirigée par **M. Olivier LESAINT**
et codirigée par **Mme. Rachelle HANNA**
et **M. Ngapuli Irmea SINISUKA**

préparée au sein du **G2Elab**
dans **l'École Doctorale EEATS**

Study of Dielectric Liquids as Alternative Encapsulant for High Temperature Electronics Power Module Applications

Thèse soutenue publiquement le **20/12/2019**,
devant le jury composé de :

M. Hervé MOREL
Directeur de Recherche au CNRS-INSA Lyon, Lyon, Président du Jury et Examinateur
Mme. WANG Zhongdong
Professeur à The Manchester University, Manchester, UK, Rapporteur
M. Thierry PAILLAT
Professeur à l'Université de Poitiers, FUTUROSCOPE CHASSENUIL, Rapporteur
M. Olivier LESAINT
Directeur de Recherche au CNRS-G2Elab, Directeur de thèse
Mme. Rachelle HANNA
Maître de Conférences à Grenoble INP-G2Elab, co-Encadrant de thèse
M. Ngapuli Irmea SINISUKA
Professeur à Institut Teknologi Bandung, Bandung, Indonésie, co-Encadrant de thèse

وَأَوْفُوا الْكَيْلَ إِذَا كِلْتُم وَزِنوا بِالْقِسْطَاسِ الْمُسْتَقِيمِ ۚ ذَٰلِكَ خَيْرٌ وَأَحْسَنُ تَأْوِيلًا

وَلَا تَقْفُ مَا لَيْسَ لَكَ بِهِ عِلْمٌ ۚ إِنَّ السَّمْعَ وَالْبَصَرَ وَالْفُؤَادَ كُلُّ أُولَٰئِكَ كَانَ عَنْهُ مَسْئُولًا

(QS 17:35-36)

Remerciements

بِسمِ اللَّهِ الرَّحمْنِ الرَّحِيمِ الْحَمدُ لِلَّهِ رَبِّ العالَمِينَ

Table of Content

Figure List

Table List

Abbreviation

AC	:	Alternating current
ALN	:	Aluminium Nitride
Alumina	:	Aluminium oxide (Al2O3)
AMB	:	Active metal brazing
BD(s)	:	Breakdown(s)
BDEF	:	Breakdown Electric Field
BDV	:	Breakdown voltage
BJT	:	Bipolar Junction Transistor
BNC	:	Bayonet Neill-Concelman (connector)
CTE	:	Coefficient of thermal expansion
DBC	:	Direct bonded copper
DBT	:	Dibenzyltoluene, refers to Jarytherm® DBT
DC	:	Direct current
EBD	:	Breakdown field
EHD	:	Electrohydrodynamic
GaAs	:	Gallium Arsenide
GaN	:	Gallium Nitride
Ge	:	Germanium
HT	:	High temperature
HV	:	High voltage
IGBT	:	Insulated Gate Bipolar Transistor
MOSFET	:	Metal-Oxide-Semiconductor Field-Effect Transistor
ΔT	:	Temperature difference

pC	:	Pico coulomb
PD(s)	:	Partial discharge(s)
PDIV	:	Partial discharge inception voltage
PFPE	:	Perfluoropolyether
PI	:	Polyimide
PRPD	:	Phase resolved partial discharge
PTFE	:	Polytetrafluoroethylene/Teflon
P_{Vap}	:	Vapour pressure
r_C	:	Critical point tip radius
r_P	:	Point tip radius
RT	:	Room temperature
SC	:	Semiconductor
SE	:	Synthetic Ester, refers to MIDEL®7131
SF6	:	Sulphur hexafluoride
Si	:	Silicone
SiC	:	Silicone Carbide
SIV	:	Streamer inception voltage
T_{boil}	:	Boiling temperature
t_D	:	Time delay
t_{HV}	:	HV impulse applied time duration
TOF	:	Time of flight, transit time of charge carriers
V_{app}	:	Applied voltage
V_i	:	Streamer inception voltage
WBG	:	Wide band-gap

Introduction

Todays, power electronics cover wide range of applications in our daily life, starting from household appliances, communications, transportation systems up to harsh and extreme environment as in oil and gas exploration and the deep space missions. The main advantages of power electronics are energy efficiency, compact size, reliability, long durability. Improving power electronics will surely mean to deal with materials, packaging system, switching technologies, heat dissipation, dielectric properties, thermal stability etc. Power electronics started with the first arc-mercury rectifying in traction system, and was deeply reshaped by the discovery of classical semiconductor (Si based), and ultimately by the development of wide bandgap semiconductor materials, such as SiC, GaN, and carbon based (diamond). They have superior thermal and dielectric properties compared to previous classical semiconductor technologies (Ge, Si and GaAs), and allow devices to operate at higher voltage, temperature and switching frequency in power modules. Unfortunately, these developments are not equally followed by other parts within modules, such as dielectric encapsulant materials.

Despite their key roles to provide mechanical and electrical protection inside a power module, silicone gels used as major encapsulants are limited to 200°C, which is far below the temperature that may occur in switching devices (e.g. SiC is still operative at 500°C). Encapsulation comes from polymerization and curing process of silicone liquids mixture that transforms into gel. They worked very well when used with classical Si devices, but not with new wide band gap (WBG) semiconductors at high temperature. Thus, it is necessary to solve this thermal related issue by either improving silicone gel, or starting looking for alternative types of encapsulants, with better thermal performance. Elastomers (harder than gels) and pressurized electronegative gases (such as SF6) are currently considered. The objective of this work is to evaluate dielectric liquids as potential alternatives.

Dielectric liquids have been used as insulating medium for high voltage (HV) applications for decades. Their excellent self-healing and arc quenching properties were used in the HV circuit breaker applications, even though nowadays replaced by gas. Their low viscosity allow the fluid flow to exchange heat from internal source yielding effective cooling system in power transformers. Other industries use dielectric liquids for heat transfer at much higher temperatures compared to those present in HV applications. Of course as heat transfer liquids, their dielectric properties are out of consideration, and mostly unknown. Nevertheless, several high temperature liquids of hydrocarbon nature, non-polar and thus probably rather insulating, seem interesting as potential alternative encapsulant. Questions then arise about their electrical properties at high temperature (HT), their stability, and their possible contribution to cooling of devices inside power module.

This work presents an initial study of dielectric liquids for HT power electronics module applications. We will carry out electrical characterization of several dielectric liquids under influence of temperature, with several complementary methods such as dielectric spectroscopy, partial discharge measurements, streamers and breakdown characterization. This will done either with the liquid alone, and with simple structures involving substrates, representative of real modules. In terms of application, conditions will be adapted to replicate those present in power modules, with ceramic substrates under quasi-uniform to highly divergent electric field, under AC, DC, impulse voltage, and high temperature.

While not covering all aspects of encapsulant requirements, this work aims at establishing essential basis for a better knowledge about electrical properties of dielectric liquids at high temperature that received very few previous attentions.

Introduction

L'électronique de puissance couvre aujourd'hui un large éventail d'applications dans notre vie quotidienne, allant des appareils électroménagers aux systèmes de communication, en passant par les systèmes de transport jusqu'à des environnements extrêmes comme la prospection pétrolière et gazière et les missions dans l'espace. Les principales caractéristiques de l'électronique de puissance sont l'efficacité énergétique, la taille compacte, la fiabilité et la longévité. Améliorer l'électronique de puissance impliquera sûrement de traiter des matériaux, du système d'emballage, des technologies de commutation, de la dissipation de chaleur, des propriétés diélectriques, de la stabilité thermique, etc. Ceci concerne les semiconducteurs conventionnels à base de Silicium, et plus récemment les matériaux semi-conducteurs à large bande interdite, tels que le SiC, le GaN et le carbone (diamant). Ils possèdent des propriétés thermiques et diélectriques supérieures à celles des technologies classiques précédentes (Ge, Si et GaAs) et permettent aux dispositifs de fonctionner à des tensions, des températures et une fréquence de commutation plus élevées. Malheureusement, ces développements récents ne sont pas suivis de la même manière par d'autres éléments, tels que les diélectriques utilisés comme encapsulants.

En dépit de son rôle clé en matière de protection mécanique et électrique à l'intérieur d'un module, le gel de silicone en tant que principal moyen d'encapsulation est limité à 200 ° C, ce qui est bien inférieur aux températures qui peuvent exister dans les nouveaux dispositifs (par exemple avec du SiC qui reste fonctionnel à 500 ° C). L'encapsulation provient du processus de polymérisation et de durcissement d'un mélange de liquides de silicone qui se transforme en gel. Ils ont jusqu'à présent très bien fonctionné lors de l'assemblage avec des semiconducteurs classiques, mais pas avec matériaux à large bande interdite. Par conséquent, il est nécessaire de résoudre ce problème lié à la température, que ce soit en améliorant le gel de silicone afin d'avoir de meilleures propriétés thermiques, ou en cherchant d'autres types de produit d'encapsulation offrant de meilleures performances thermiques. Jusqu'à présent des élastomères plus durs que les gels ont été considérés, ou encore des gaz sous pression. L'objectif de ce travail est d'évaluer le potentiel de liquides pour l'isolation haute température.

Les liquides diélectriques sont utilisés depuis des décennies comme milieu isolant pour des applications haute tension (HT) comme les transformateurs de puissance. Leurs excellentes propriétés d'auto-cicatrisation et d'extinction d'arc ont été utilisées dans les applications de disjoncteurs HT, bien qu'ils soient aujourd'hui remplacées par des gaz. Leur faible viscosité permet au flux de fluide d'échanger la chaleur de la source interne, offrant ainsi un système de refroidissement efficace dans les transformateurs de puissance. D'autres industries utilisent des liquides pour le transfert de chaleur dans une plage de température beaucoup plus élevée que celle utilisée dans les applications haute tension. Bien sûr, en tant que liquides caloporteurs, leurs propriétés diélectriques ne sont pas prises en considération. Certains liquides caloporteurs haute température, d'origine hydrocarbure, non polaires et donc probablement isolants électriques, pourraient également être considérés. Certaines questions se posent alors, telles que: quelles sont leurs propriétés diélectriques à haute température (HT), sont-elles stables, et peuvent-ils contribuer au refroidissement des dispositifs à l'intérieur d'un module de puissance ?

Ce travail présente une étude préliminaire des liquides diélectriques pour des applications de modules d'électronique de puissance HT. Nous réaliserons la caractérisation électrique de plusieurs liquides diélectriques sous l'influence de la température, avec diverses méthodes telles que la spectroscopie

diélectrique, les décharges partielles, le claquage. Ceci sera fait soit sur le liquide seul, soit sur des structures élémentaires représentatives de modules de puissance. En termes d'application, les conditions seront adaptées et simplifiées pour représenter un module de puissance, en présence de substrats céramiques réels, sous un champ électrique quasi uniforme à fortement divergent, avec une tension alternative, alternative et continue, et sous haute température.

Bien que tous les aspects nécessaires à la validation complète d'un encapsulant ne soient pas couverts, ces travaux permettent d'établir une base pour une meilleure connaissance des propriétés électriques des liquides diélectriques sous haute température. Ce sujet a été très peu étudié jusqu'à présent.

1 | State of the art on dielectrics for packaging of high temperature power electronics modules

Contents

Power electronics is involved in a very large number of applications, ranging for low power systems, up to very high power devices far exceeding the MW range. An example is found with HVDC power grids, which are presently developed to take advantage of a better energy efficiency, and increased control possibilities (Smart grids). High voltage power electronics is required for such application. Several other applications, such as down-hole oil and gas industry for well logging, aircrafts, automotive, and space exploration, also frequently require operation at high temperatures. High voltage and high temperature power electronics can both benefit from the recent development of wide bandgap (WBG) semiconductor materials (SC), such as SiC, GaN, and even Diamond. In order to take full advantages of these materials, packaging components operating under high voltage and/or high temperature are required. Since the most temperature-limited component is the encapsulating material, identifying new types of insulating materials is mandatory. Among different alternative solutions, liquid dielectrics has received very few attentions up to now. Its use in high power modules would lead to an increased technical complexity (packaging should be tight), but one may also expect several advantages: increased cooling, self-healing, and possibly good properties at high temperature and high voltage. This thesis constitutes a prospective study in order to investigate the dielectric properties of liquids as encapsulants in high voltage / high temperature semiconductor modules.

This state of art chapter details all these aspects. It starts with a description of the conventional structure of a power module, followed by a discussion on the limitations of classical semi-conductor devices and their alternatives (WBG devices). The electrical and thermal limitations of packaging materials are also discussed with a special focus on the problem of partial discharges. Some limitations of the silicone gel (the most used encapsulating material), under high electric field and high temperature are detailed. A comparison of the properties of different alternative materials is also discussed. Then, a state of art on the properties of dielectric liquids is presented, with a special focus on pre-breakdown and breakdown phenomena, which are of major importance for the performance and reliability of insulation. Finally, the main objectives and the outline of the thesis are presented.

1.1 Overview on conventional structure of power module

A power module is an assembly containing several components, mostly power semiconductor devices (so-called dies), interconnected to perform a power conversion function. Different structures of power

module are available [1-6], in order to increase the heat dissipation and the efficiency of the power system. The most used structure is the classical wire-bonding module (Fig 1.1)
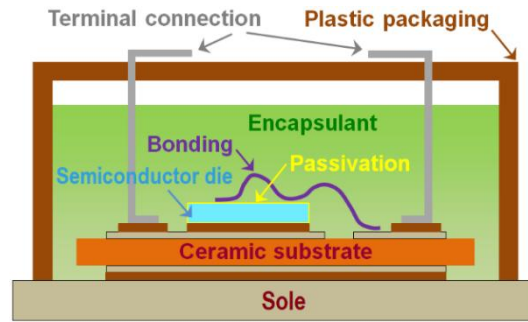
Fig 1.1 - Structure of classical wire-bonding power electronics module

It consists of the assembly of semiconductor devices on an insulating ceramic substrate metallized on both sides. The electrical interconnections are provided by the conductive tracks on the substrate and by wire bonding. On the top of the semiconductor die (or chip), a small thin layer of insulating material (usually polyimide/PI), called "passivation", is deposited. This layer reduces the electrical stress in the surrounding encapsulating material, with the objective to suppress partial discharges (PDs) and improve the breakdown strength of the system. The structure stands on a metal baseplate (sole) to allow heat evacuation to a cold source.
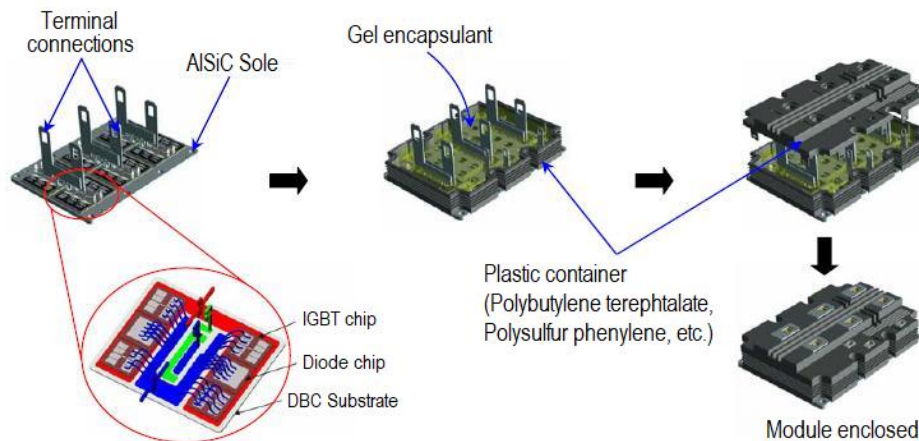
Fig 1.2 - Expanded view of complete structure of an IGBT power module (DBC: Direct Bonded Copper)

The heat transfer system is optimized to control the maximum operating temperatures, and avoid thermal semiconductor failures. The entire structure is embedded in an encapsulant dielectric material, usually silicone gel, to enhance the dielectric strength of the module, and to preserve the semiconductor components from external aggressions (moisture, contamination, corrosion etc.). Finally, the module is packaged in a plastic container with external terminal connections. Fig 1.2 shows an expanded view of a complete structure of an Insulated-Gate Bipolar Transistor (IGBT) power module.

1.2   Power semiconductor devices: limitations and alternatives

1.2.1   Limitations of classical power electronics devices

Technology of power electronics started with the development of mercury arc rectifier in 1901 to convert alternating current (AC) into direct current (DC) [7-8] for railway and high voltage DC link applications. During the mercury-arc rectifier implementation, several drawbacks were identified such as arc-back, radio interference, inflexibility in voltage rating, maintenance and especially the occupation of large spaces. Innovation of monocrystalline semiconductor in 1940 substituted the mercury-arc to devices

based on Silicone (Si) and Germanium (Ge) which in turn reduced the enormous size of these first power electronics components in much smaller shape with higher power density.
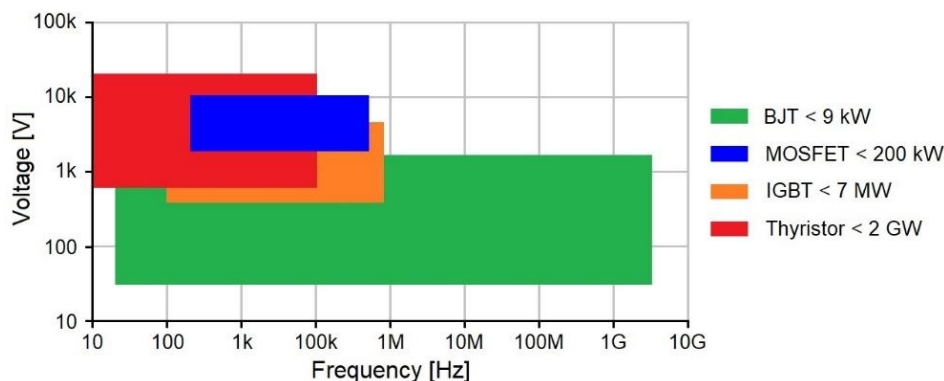
Fig 1.3 - Operating voltage and frequency range of power devices based on classical SC materials [9-20]

The main power semiconductor devices are Bipolar Junction Transistor (BJT), Metal-Oxide-Semiconductor Field-Effect Transistor (MOSFET), Insulated-Gate Bipolar Transistor (IGBT) and thyristor. They are used in different applications according to their intrinsic characteristics. Fig 1.3 shows the operating voltage and frequency range of these power semiconductor devices. BJT has basic function as current amplifier and used in less than 9 kW application at operating voltage from 32 V to 1200 V under wide range of frequency up to 5.8 GHz (i.e. power supplies, radar applications, electrical vehicles, wireless telecommunication [9-11]). MOSFET is featured with higher voltage application up to 10 kV, however with narrower frequency range up to 800 kHz for applications of AC-DC inverter, uninterruptible power system, space applications, solid-state transformer applications, etc. [12-14]. IGBT is primarily used as electronic switch at higher power rating than MOSFET and used up to 7 MW for applications such as traction, power storage system, electric vehicles, high voltage DC converters, renewable energy applications etc. [15-17]. Thyristor is mainly used as high power control up to 13 kV such as circuit breakers, high voltage DC converters, etc. [18-20].

Despite the excellent performance of these power devices, they exhibit high switching and conduction losses, which reduces the system efficiency. This is the main reason why they cannot operate simultaneously at high frequency and at high voltage. Furthermore, their maximum operating temperature is limited i.e. maximum junction temperature of Si Schottky diode is below 175°C.

The lookout for a more efficient, robust, fast and cheap switching power devices has led to introduce new category of semiconductor materials, wide bandgap (WBG) semiconductor materials. Thus a new era of power electronics was born.

1.2.2   Alternatives: wide bandgap semiconductor devices

WBG are semiconductor materials, which have relatively large bandgaps (2eV-5eV) compared to conventional semiconductors (<2eV). Silicone Carbide (SiC), Gallium Nitride (GaN) and Diamond (C) are WBG materials. Their characteristics are presented in TABLE 1.1.

According to their band structure, WBG devices can operate under high temperature (HT). This is attractive not only for applications requiring HT power electronics, but also for the reduction of the bulky cooling units. These units are often required in Si-based power converters.

The run-away temperature of WBG is represented in Fig 1.4 as a function of breakdown voltage. It should be noted that WBG devices themselves can operate even at 500°C or higher, but performance factors such as their on-resistance generally degrade at such high temperatures [21].

TABLE 1.1 - Comparison between electrical and thermal properties of classical and WBG semiconductor materials

		Classical SC			Wide bandgap SC				
		Ge	Si	GaAs	3C-SiC	6H-SiC	4H-SiC	GaN	Diamond
Gap energy	[eV]	0.66	1.12	1.42	2.3	2.9	3.2	3.39	5.6
Electron mobility	[cm^2·V^{-1}·s^{-1}]	3900	1450	8500	1000	415	950	2000	4000
Hole mobility	[cm^2·V^{-1}·s^{-1}]	1900	450	400	45	90	115	350	3800
Thermal conductivity	[W·cm^{-1}·K^{-1}]	1.5	1.3	0.54	5	5	5	1.3	20
Breakdown field	[V·cm^{-1}]	10^5	3×10^5	4×10^5	2×10^6	2.5×10^6	3×10^6	5×10^6	10^7
Saturation velocity	[cm·s^{-1}]	3.1×10^7	10^7	2×10^7	2.5×10^7	2×10^7	2×10^7	2×10^7	3×10^7
Relative permittivity		16	11.7	12.9	9.6	9.7	10	8.9	5.7

Furthermore, WBG semiconductor materials exhibit both electron and hole mobilities higher to those of classical SC materials. Their saturation velocity are thus higher (except of Gallium Arsenide GaAs, widely used for high frequency application), which explains their possible operation at higher frequency. As can be seen from TABLE 1.1, the breakdown field (E_{BD}) of WBG is one or two order of magnitude higher than that of classical semiconductor materials and thus for same depletion region width, WBG materials can operate under higher voltage.
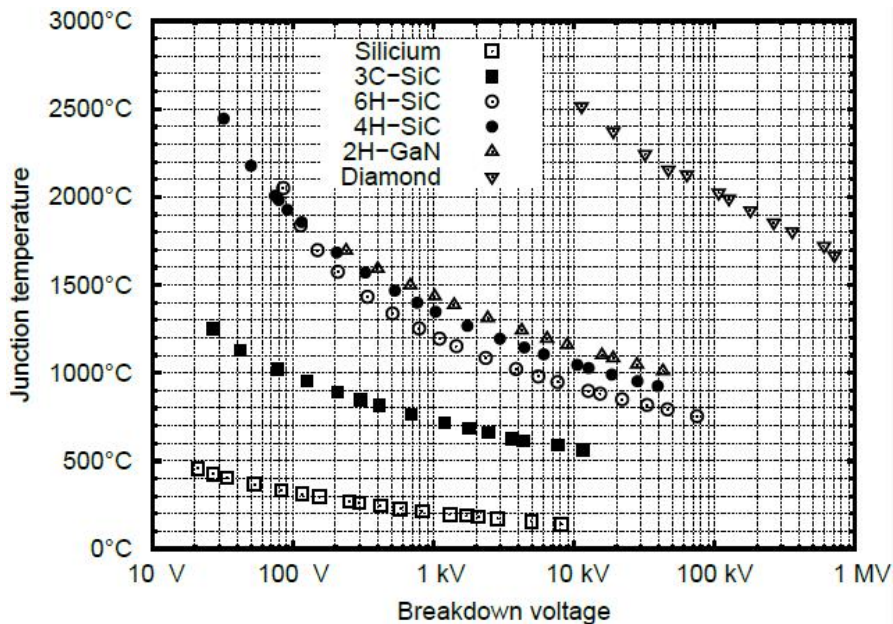
Fig 1.4 - Runaway temperature as a function of breakdown voltage for Si and WBG semiconductor materials [22]

Fig 1.5 shows the impact of the intrinsic properties of WBG semiconductor on power system. It can be concluded that WBG power devices can operate at **higher temperatures**, **voltages**, and **switching speeds** than those based on classical semiconductor devices, which results in a reduction of system size, weight and cost.

Fig 1.5 - Impact of intrinsic properties of WBG semiconductors on power system [23]

WBG power devices were built in research laboratories since 1980's. The first schottky diode based on SiC was introduced to the market in 2001 [24]. Within the last decade, SiC Schottky diodes have become available commercially in 300 V to 1700V with operating junction temperatures over 200°C. Through recent progress in the crystal growth and process technology, the production of power MOSFET has started with an operating temperature range up to 450°C allowing operation up to several kilovolt.

GaN power electronic devices are even more recent innovation than SiC devices. The development of GaN components is focusing on GaN transistors growing on silicone substrates. The first commercial 200 V GaN power devices were released in 2010 and followed by 600 V devices in 2014. Today, the focus is on the technology development for high level of integration and for 1200V applications.

Diamond technology is currently at a very early stage, with a poor wafer quality and many technological steps still to develop.

1.3 Packaging materials of a power module and their limitations

Power modules are subject to degradation and ageing mechanism related to the operating conditions and the environment. Mechanisms of degradation and failure modes of power module have been widely studied. Nowadays, with the introduction to the market of WBG power module, studies are focusing essentially on failures related to thermal and electrical stresses. In this part, the impact of electrical and thermal stresses on power modules is presented.

1.3.1 Partial discharge phenomena and its effects on the power module

1.3.1.1 Overview on partial discharge

Partial discharges (PDs) are localized electrical discharges that concern only a small portion of an insulator (i.e. solid, fluid or gas) placed between conductors, which does not bridge the space between these conductors. The impacts of PDs vary depending on their intensity and the environment in where they emerge. PDs are usually followed by a gas generation (formation of cavities, ozone and acids such as nitric acid, oxalic acid, etc.) thus deteriorate the insulation materials. PDs also inflict mechanical

erosions and carbonization of surfaces by ion bombardment and heat generation in the discharge channel. These effects result in degradation of the dielectric material and thus shorten the lifetime of the whole system.

Several classifications of PDs have been proposed depending on the criterion used. For example, Kreuger et al. [25] classifies discharges according to their location and defines into four categories:

- Internal discharges occur in places where the dielectric strength is low, for example a cavity in a solid or gel-like, a bubble in a liquid (Fig 1.6 a);
- Surface discharges occur when a large tangential field exists on the surface of a dielectric (Fig 1.6 b);
- Corona discharges occur inside material where the local electric field is very strong e.g. by a peak effect (see ANNEX A - Corona discharges). Discharges are normally restricted to a small area around the sharp edge or tip (Fig 1.6 c);
- Electrical treeing occurs on a fault in the solid/gel-like insulation. The branches grow inside insulation material forming different branches starting from the discharge point (Fig 1.6 d).

(a)   (b)   (c)   (d)
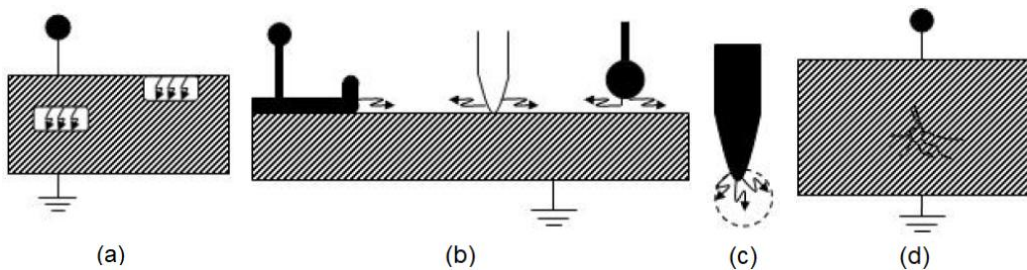
Fig 1.6 - PDs type: (a) internal discharge, (b) surface discharge, (c) corona discharge and (d) treeing

In the next section, discharges inside cavities, which are frequent PDs type encountered in power module (e.g. due to bubbles in encapsulant gel), is detailed.

1.3.1.2   Discharges inside cavities and capacitance model

Consider an insulation containing a cavity as described in Fig 1.6 a. The behavior of AC-powered PDs can be simply represented by an equivalent circuit of three capacitances. The cavity is modeled by the capacitance *a* and by a spark gap in parallel. The capacitance of the dielectric in series with the cavity is represented by *b*. The healthy part of the dielectric material is represented by the capacitance *c*.

(a)   (b)
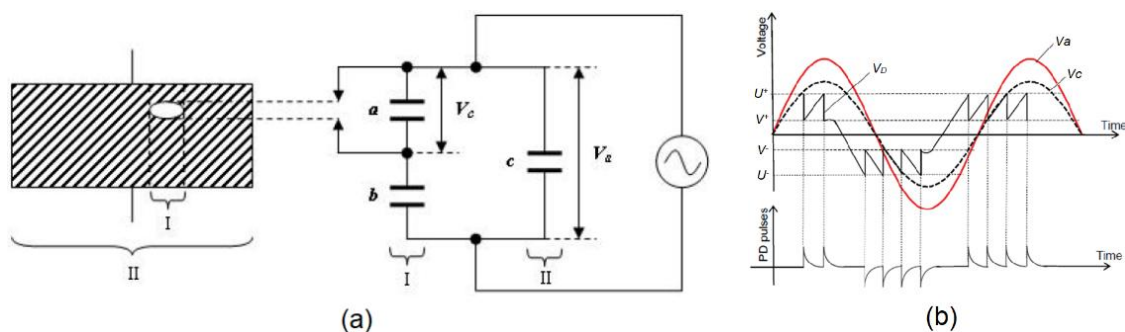
Fig 1.7 - Cavity discharge model and equivalent circuit, (b) cavity discharge recurrence voltage waveform

The high voltage V_a is applied to the dielectric material and the voltage across the cavity is V_c (Fig 1.7a). When the voltage in the cavity (V_c) equals to a certain critical value U^+ (discharge voltage), a discharge occurs, then V_D drops to a base value V^+ and the discharge stops. This voltage drop occurs over a very short time (some ns) compared to that of the sinusoidal voltage wave at 50 Hz. Subsequently, the voltage across the cavity increases again; when it reaches again U^+, a new discharge occurs. This is

repetitive until the high voltage *Va* no longer increases (phase φ = 90°). The same mechanism occurs during the negative half-cycle (270° discharge stop). The discharges in the cavities produce fast current pulses (ns) in the sample and the external circuit (Fig 1.7 b).

1.3.1.3 Partial discharges in power module

Improvement of blocking voltage well above 6.5 kV for WBG devices such as IGBT will cause higher local electric field, and thus occurrences of more PDs. Reducing PDs activity is of primary importance to extend the lifetime of power modules.

(a)   (b)
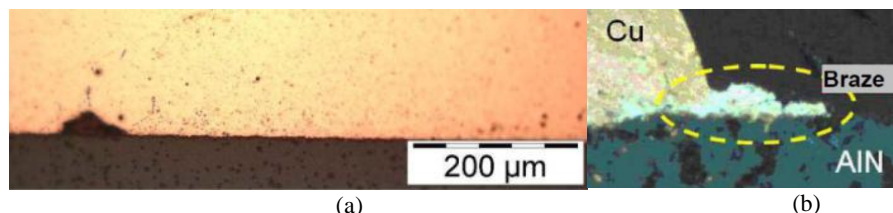
Fig 1.8 - (a) Cross section of copper metallization/ceramic substrate junction with a bond void [22] and (b) protrusions with extremely sharp edges of some braze below the metallization in Active Metal Brazing (AMB)[23]

In power modules, different regions and materials can be concerned by PDs:

- porous ceramic substrates [26]. Simulations and measurements on various thicknesses (0.38 mm, 0.63 mm and 1 mm) of ceramic substrates (Aluminium Nitride/AlN and Alumina/Al_2O_3) demonstrated that Partial Discharge Inception Voltage (PDIV) is a function of substrate thickness [27].
- voids at metallization and substrates junction (see Fig 1.8 a)
- protrusions with metallic sharp edges (see Fig 1.8 b)
- cracks of bonding with sharp edges.
- encapsulant close to the so-called "triple-point": point of contact among substrate, metallization and encapsulant. This material in conjunction with particular region nearby are of major interest for this study, and will be detailed hereafter.

1.3.1.3.1 Partial discharges in silicone gel

Surface discharge traces at the substrate/gel interface evidence the propagation of cavities and discharge treeing processes. Typical discharge initiated by a sharp metallic point in silicone gel consists in bubble-like cavities recorded by Do et al. in Fig 1.9.
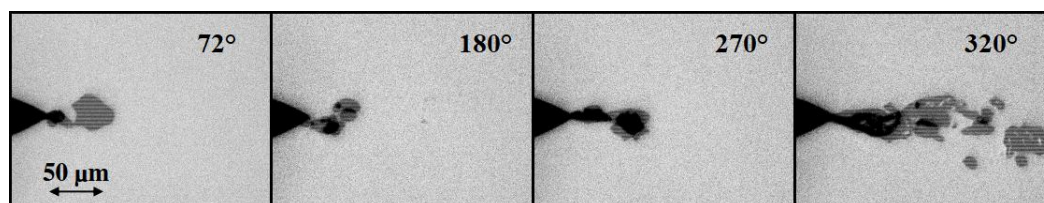
Fig 1.9 - Shadow photograph of bubbles in silicone gel during a discharge burst under AC at 7 kV and 50 Hz. Photographs were taken at various phase delay (72°, 180°, 270° and 320°) [28]

Discharges burst start to create cavities near the point, which then move violently away from the point. For new samples, these cavities may disappear after few bursts exposure when the PD burst ceases. However, when bursts are repeated, permanent defects occur in silicone gel close to the point. This illustrates the rather limited self-healing properties of silicon gels.

Further investigations of initial formation and development of cavities due to discharges in silicone gel were carried out by applying single HV impulse in a point-plane configuration. Roughly spherical cavities (Fig 1.10a) appeared and developed with slow velocity after a positive impulse threshold applied to point electrode. When the applied voltage is increased further above another threshold, fast

propagation of gaseous filament cavities (called "filamentary streamers") emerged, with a tree-like shape involving many ramifications as in Fig 1.10b.
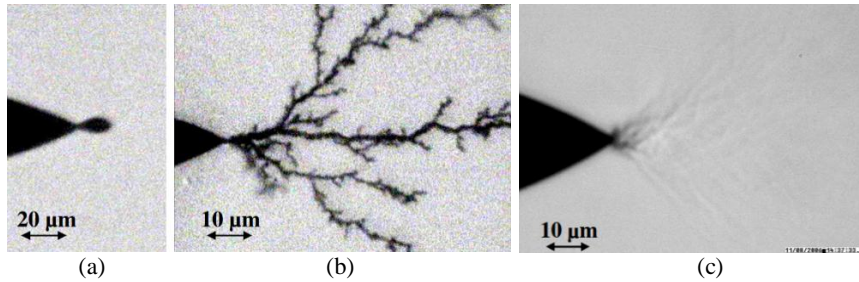
Fig 1.10 - Shadow photographs of (a) slow streamer (V = 13 kV), (b) filamentary streamer (V = 17 kV) and (c) permanent degradations of gel induced by positive filamentary streamers.
Measurements done in a point-plane configuration (curvature radius of 1.3 μm and distance of 3 mm in silicone gel [28]

Experiments with negative impulse applied to point electrode also demonstrated similar spherical cavities as well as in the positive impulse. The main difference is that no filamentary streamer in negative polarity occurred, even after the voltage was raised up to 1.5 of the positive threshold for filamentary streamer. The first cavity or channel formed during a single voltage impulse disappeared totally thereafter, and no evidence of streamers remained after the impulse. However, after several impulses, progressive irreversible degradations appears (Fig 1.10c). These degradations ultimately induced permanent cavities at the point tip, and blurred area where the refractive index is modified, also observed [28].

Ebke et al. demonstrated that PDs in cavities could induce breakdown in silicone gel. They placed a spherical void of 1 mm diameter in the middle between two spherical electrodes of 5 mm diameter with 3 mm gap distance. The gel endured PD-induced breakdown at 11 kV, i.e. only 1.5 kV above the PDIV of 9.5 kV, far below the breakdown strength of the gel itself (15 kV/mm according to the manufacturer's datasheet) [29].

1.3.1.3.2   Partial discharges at the triple point (metallization/substrate/encapsulant)
Imperfect adhesion of encapsulant, and sharp metallic points induced by the etching process of metallization are the major causes of the increase of partial discharge probability in power modules. Etching process to obtain the desired geometrical shape, configuration, and thickness of metallized tracks on ceramic substrates involve numbers of repetitive etching steps. Etching a 300 μm copper in a short time (10 passes of standardized printed circuit process) result in a thin copper layer remaining on surface of substrates along the edges of metallization. Further repetitive passes will remove this thin copper layer.
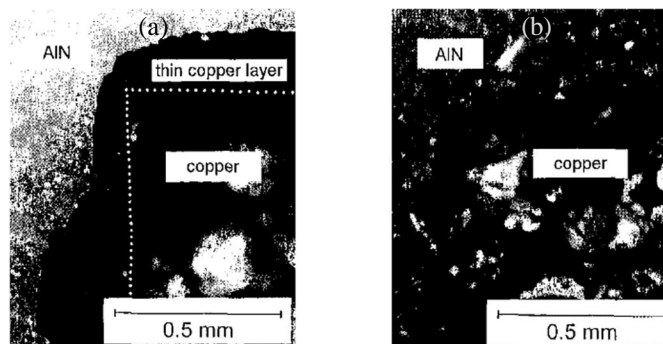
Fig 1.11 - Photomicrographs of the corner of a sample etched for: (a) 10 times and (b) 16 times [30]

Fig 1.11 shows photomicrographs of the corner of AlN substrate where copper metallization (Cu) was etched 10 times and 16 times. The dash line in figure (a) indicates the designated edge of metallization

while the area above and on the left are the remaining thin copper layer. This region is critical because some extremely sharp metallization edges are formed [30]. These edges increase the electric field strength tangential to the substrate and could lead to partial discharges.

In another ways, size and shapes of metallization statistically influence the PDs behaviour. Larger electrode size tends to induce more PDs than smaller ones. Fig 1.12 shows different shapes of copper metallization on AlN substrate and the corresponding PDs comparison [30]. It is obvious that sharper corners of metallization induce more PDs, which is related to slightly higher maximum electric field.
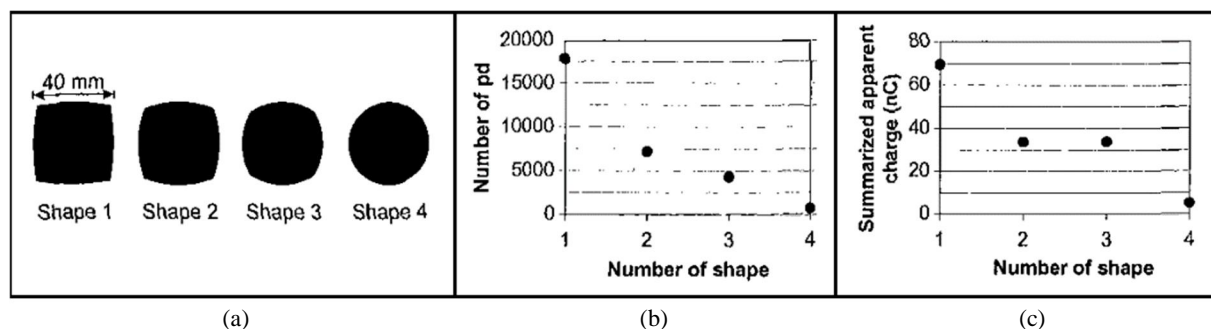
Fig 1.12 - Metallization on substrate: (a) shapes, (b) PDs numbers and (c) apparent charges [30]

Numerical simulations were performed by changing the curvature radius of the edge of metallization close to the triple point. It was observed that the maximum electric field (F_{max}) is reduced by a factor of 2 when the radius is increased from 5 to 150 µm, from 243 kV/mm to 112 kV/mm [31].
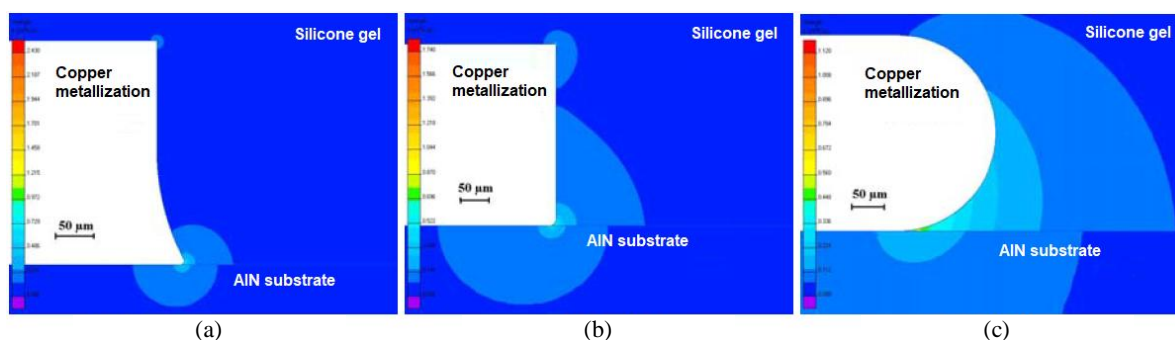
Fig 1.13 - Electric field distribution for various curvature radius of the metallization edge: (a) 5µm (F_{max} 243 kV/mm), (b) 10µm (F_{max} 174 kV/mm) and (c) 150µm (F_{max} 112 kV/mm) [31]

However, the edge geometry shown in Fig 1.13a unfortunately turned to be more realistic, when compared to the actual metallization shape induced by etching, as it can be seen from Fig 1.14 and Fig 1.15.
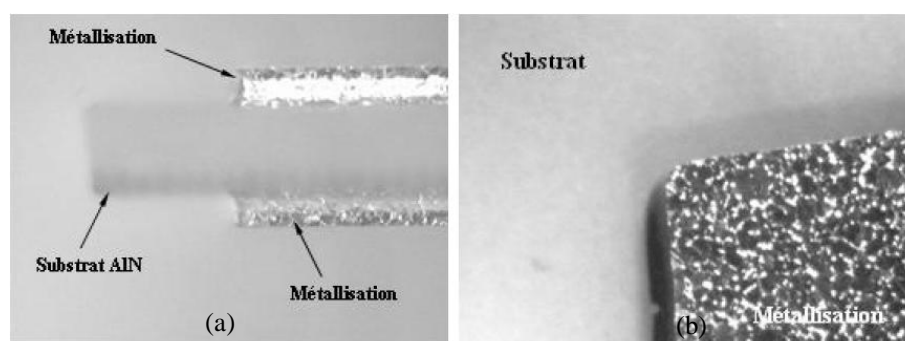
Fig 1.14 - Actual geometry of metallization edge on AlN substrate: (a) Cross section view and (b) top view [31]

The same electric field reinforcement with the decrease of the metallization curvature radius was observed in the numerical simulation performed by Reynes et al [32] (see Fig 1.15).
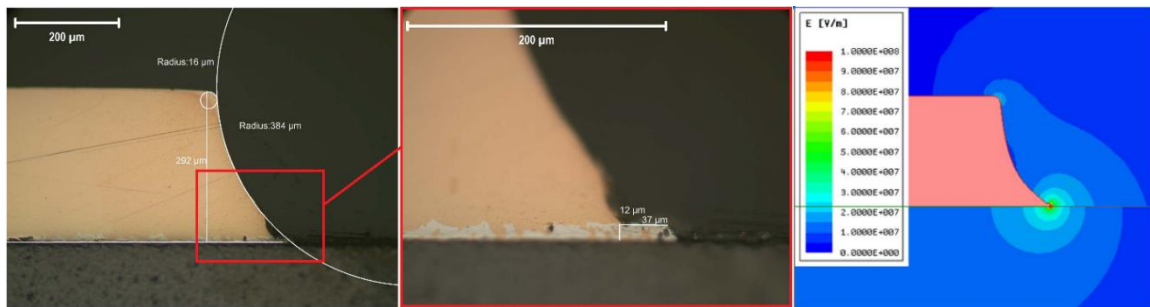
Fig 1.15 - Actual geometry of metallization edge on AlN substrate and simulation geometry with edge radius of 6 µm [32]

Electric field can be reduced to avoid electrical breakdown and suppress PDs by increasing the thickness of the ceramic substrate. Applying this technique for low power applications is feasible. However, this is not practical for high power applications, since heat dissipation from semiconductor devices is mainly evacuated through the ceramic substrate. Increasing the thickness of substrate will degrade its thermal performances.

Simulations done by Do [31] on AlN substrates with a curvature radius of metallization edge of 1 µm (Fig 1.16a) showed that the maximum electric field decreases by nearly 50% (from 430 to 230 kV/mm) for thickness increasing from 630 µm to 2 mm (Fig 1.16b).
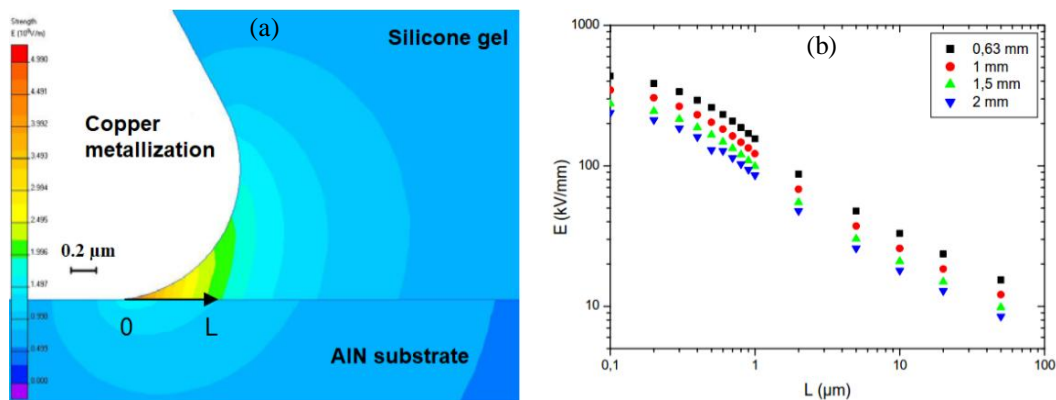
Fig 1.16 - Simulation results at triple-point of copper metallization/AlN substrate/silicone gel: (a) electric field distribution and (b) variation of electric field intensity over axes L of interface between substrate and encapsulant [31]

Very sensitive measurements of light emission coupled to PD measurements (see Fig 1.17) carried out by Vu et al. for AlN substrates embedded in either silicone gel or silicone oil demonstrated that below PDIV, a weak light emission is still recordable. This light emission was attributed to the electro-luminescence of the AlN material under high electric field. When the applied voltage is raised above PDIV, PDs with higher light intensity burst randomly [26].
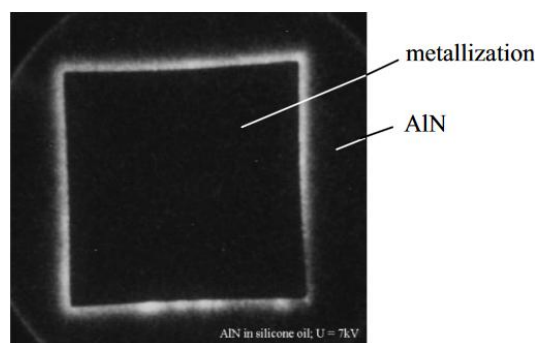
Fig 1.17 - Light emission of low amplitude discharges of AlN substrate in silicone oil at 7 kV [26]

Such "parasitic" light emission due to electro-luminescence did not occurred in alumina and epoxy substrates. In such materials, the average discharge current (I_{PD}) and light intensity current (I_{PM}) versus

voltage show good agreement. Measurement of light emission then constituted a good alternative to classical electrical measurements in order to detect PDs. This is especially interesting when impulse voltage is used, since classical electrical measurements become impossible, while light detection can still be done.
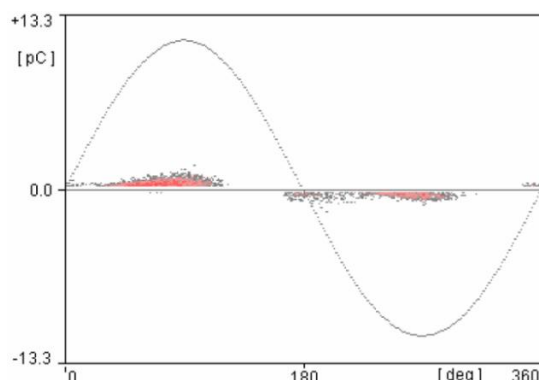
Fig 1.18 - Typical phase resolved PD pattern of a point-plane sample (r_0 = 1.3 μm, d = 3 mm) embedded in silicone gel under 7 kV ac 50 Hz [34]

PDs with ceramic substrates embedded in silicone gels or liquids are characterized by very stable and roughly symmetric discharge pattern in both polarities. Discharges of small amplitudes (a few pC) occur over wide phase and start slightly before the zero crossing of voltage as it can be seen from Fig 1.18. These investigations led to the conclusion that small PDs occurring at PDIV do not occur in the encapsulant, but in the porous ceramic material itself. Several arguments were used to obtain this unusual conclusion, which contradicts most of previous hypotheses. First, PDs induced by non-porous substrates (epoxy) embedded in liquid dielectric occur at voltage peaks (90° and 270°), show a large instability typical of discharges occurring in the liquid, and are highly non-symmetrical in positive and negative polarities. Second, PDs in silicon gels produce irreversible degradation (i.e. permanent cavities) whereas a very stable regime is obtained with ceramic substrates. Third, changing the encapsulant nature (gels and various liquids) had nearly no influence on PDs with ceramic substrates.

1.3.1.3.3   Partial discharges on embedded substrates at high temperatures (below 200°C)

Partial discharge inception voltage (PDIV) is likely to be dependent on temperature [33]. Fig 1.19 shows the typical phase resolved PD (PRPD) pattern of AlN substrates embedded in silicone gel at 20°C and 100°C. It is obvious that at higher temperature the number of discharges increases. However, the charge amplitude did not rise, as well as the PDIV.

(a)   (b)
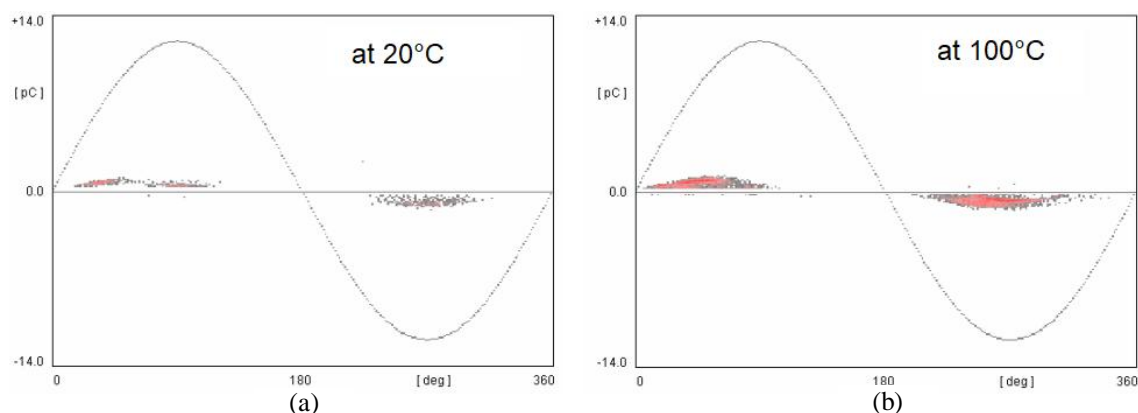
Fig 1.19 - Phase resolved PD pattern of AlN substrates embedded in silicone gel under 5 kV ac 50 Hz at: (a) 20°C and (b) 100°C [33]

Measurements of PDs in a high electric field (using point-plane electrode system) within silicone gel revealed that not only the number of discharge but also their amplitude increased with temperature [33].

PRPD presented in Fig 1.20 shows that at room temperature the number of discharges for positive polarity is much lower than that of negatives. At 100°C, the number of discharges between positive and negative polarity becomes nearly equal. In this point-plane geometry, PDs occurred within small cavities due to the gel degradation close to the point.
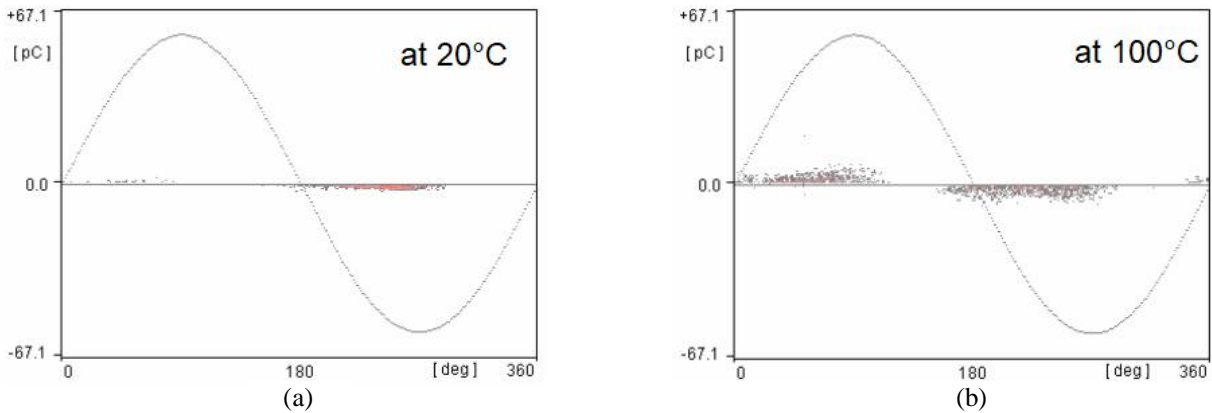
Fig 1.20 - Phase resolved PD pattern of point-plane (point radius of 1.5 μm and gap of 3 mm) electrodes embedded in silicone gel under 5.3 kV AC at 50 Hz at: (a) 20°C and (b) 100°C [33]

PDIV in both measurements show different behaviour (Fig 1.21) with temperature, further evidencing that PDs do not occur in the gel with substrates. Considering the large scatter of PD measurements with the substrates, no clear tendency about the influence of temperature was obtained from these recordings up to 140°C.
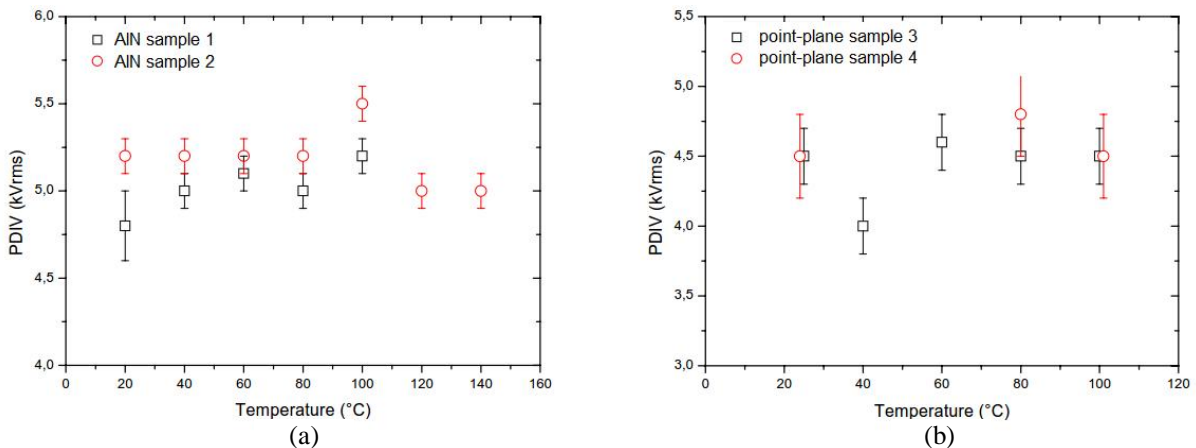
Fig 1.21 - PDIV versus temperature for: (a) AlN substrates and (b) point-plane electrodes. All samples embedded in silicone gel under ac 50 Hz. Error bars represents the standard deviation from 5 measurements for each temperature [33]

1.3.2   Thermal limitations of power module components

For power modules based on WBG semiconductor materials, the increase of the maximum operating temperature may reduce the system reliability for long-term operations, leading eventually to failure. It should be noted that failures in metallized substrates, wire bonding and solder are essentially due to differences of Thermal Expansion Coefficients (CTE) between materials. For example, in a copper metallized substrate, the CTE mismatch between Cu and ceramic may result in the fracture of the ceramic, and peel-off of the Cu foil. It has been found that a minimum of 20 to 30 thermal cycles with a temperature variation of about 300°C are typically needed to crack an alumina or AlN substrate. The same behaviour was also observed between bond wires and their bonding components (die or metallized substrate), and between solder layers and the metallized substrate (see Fig 1.22).

(a)   (b)
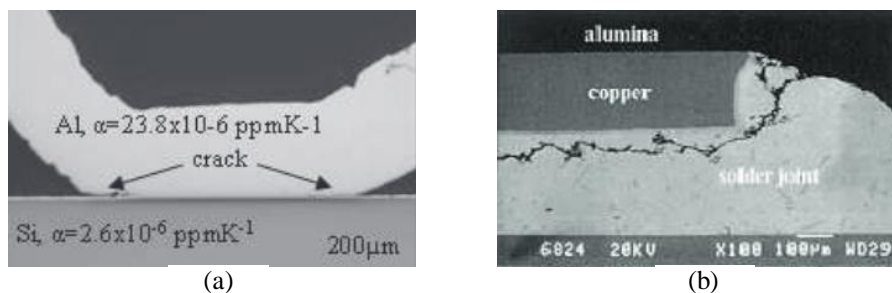
Fig 1.22 - Failure in: (a) bond wire and (b) solder layer [35]

Nevertheless, the technology today enables packaging elements such as ceramic substrate, solder and wire bonding, passivation, operating up to 600°C, 300°C and 250°C respectively as shown in Fig 1.23. It seems clear that the encapsulant remains the weakest element for high temperature operation. Thus, the main objective of the thesis will be to find a suitable encapsulating material for high temperature power modules. The next session will discuss the main properties and limitations of conventional encapsulating materials such as silicone gel.
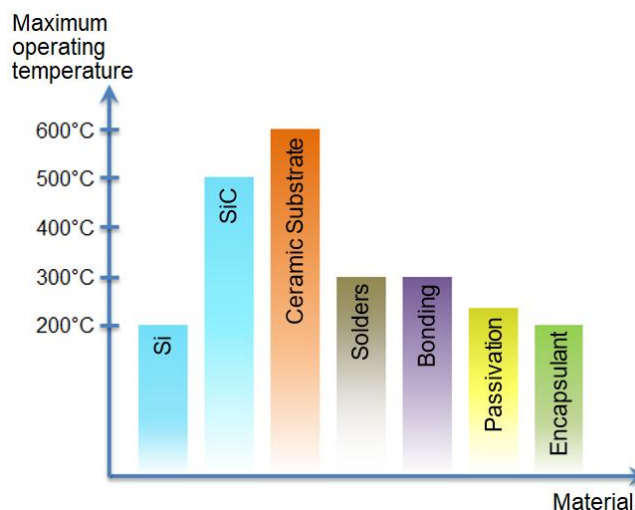
Fig 1.23 - Maximum operating temperature of different materials composing the power module

1.4 Encapsulation properties and related issues

1.4.1 Role and properties

Encapsulating materials are mainly used to improve the dielectric strength of the power module. By replacing air, encapsulants reinforce the electrical insulation between the different conductors brought to various potentials, in particular on the dies surface and around electrical connections, in order to supress partial discharges. This electrical feature is mandatory for power modules operating at high voltage, typically beyond 600 V. A second role of encapsulating materials is to protect power devices from moisture diffusion, chemical contamination and mechanical damages (vibration, shocks, etc.).

Silicone gel is the most used encapsulating material for classical semiconductor power modules due to the following properties:
- low viscosity < 200 cP
- high electrical resistivity (10^{14} - 10^{15} $\Omega \cdot$cm at room temperature)
- high dielectric strength ($15 - 20$ kV/mm at room temperature)
- high coefficient of thermal expansion CTE (200 ppm/°C)

The latter property is an asset, especially for power module where electrical connections are done by wire bonding, and when components with various CTE are used. The very high flexibility of the gel (hardness shore A) allows the encapsulation of power modules with low mechanical stresses applied to the components.

The majority of commercial silicone gel encapsulants are dedicated to operate at temperatures lower than 200°C [36], which is acceptable for classical silicon semiconductor devices, but not for WBG semiconductors. Therefore, identifying new encapsulating materials for higher temperature is mandatory.

1.4.2   Alternative materials for high temperature encapsulation

High temperature encapsulating materials must have excellent physical, electrical and thermal characteristics. They should also be thermally stable over time, over a wider temperature range than silicone gels.

The essential desired properties are:
- minimum operating temperature for continuous service higher than 250°C
- high electrical resistivity (> 10^{13} Ω·cm at 250°C)
- high dielectric strength up to maximum temperature (typical reference value for silicone gel is about 20 kV/mm in standard tests)
- CTE close to that of the packaging components, or very high flexibility (hardness shore A at 250°C)

Three types of materials are mostly considered for high temperature packaging [37]:
- **Hydroset ceramics:** they can be used at temperatures higher than 1000°C and get good chemical stability and good dielectric properties. However, they suffer from a high Young modulus (>100 GPa) and a CTE between 3 to 6 ppm/°C. These properties induce high mechanical stresses due to the CTE mismatch with other packaging materials, and may cause failures.
- **Polymers:** They can be divided into two categories: soft and hard encapsulation. These types of polymers have respectively a glass transition temperature (T_g) lower than the lowest operating temperature, and higher than the highest operating temperature. Soft silicone gels have low Young modulus and high CTE but cannot be used (maximum operating temperature for continuous service <250°C). A slight extension of the temperature range (possibly up to 275°C) might be obtained with harder silicone elastomers. The second category, hard encapsulation such as polyimide (like BBDA-PDA and PA-HT) shows satisfactory dielectric properties up to 300°C. However, they suffer from a high Young modulus (several GPa), and from the deposition technique which limits their thickness to bout 50 µm. They can be used as a primary passivation layer, but not for bulky encapsulation.
- **Hermetic encapsulation:** it is obvious that gases and liquids may be considered, since the problem of CTE and hardness can be neglected. Their also show interesting self-healing properties (i.e. good resistance to occasional PDs). However, electrical properties of fluids under high temperature (above 200°C) are almost not yet studied.

  A lot of information are available regarding the electrical properties of gases used in power engineering applications, but the temperature range does not exceed 80°C. Recently, various gas (such as N_2, SF_6, CF_3I, C_3F_8, c-C_4F_8 and their mixture with N_2) have been studied in order to evaluate their suitability for high temperature power module packaging. SF_6 and CF_3I present relatively low decomposition temperature (catalytic decomposition in the presence of conductors used in the power module structure). For other gases, it seems that their insulating properties are too low, especially the decrease of the PDIV above 300°C [38].

Up to now, the suitability of liquids as encapsulating materials for high temperature applications received very little attention. Insulating liquids are frequently used in applications such as power transformers, capacitor or cables at temperatures lower than 100°C. Few specific applications (such as railway on-board transformers filled with silicone oil) are operated at higher temperatures about 150°C. Both the liquid nature that may be used and the evolution of liquid properties at very high temperatures remain unknown. This will constitute the main objective of this work. A state of art on liquids properties is discussed in the next section.

1.5 Properties of dielectric liquids in a high temperature and high voltage environment

1.5.1 General properties

Dielectric liquids have generally good electrical, thermal, mechanical and chemical properties. For decades, they have been widely used in high voltage applications i.e.: arc quenching, insulating, cooling, in power transformers, circuit breakers, capacitors, bushings, cables, etc. Dielectric liquids are classified according to their chemical structures or fire points. Todays, at least 14 categories of dielectric liquids are known commercially starting from mineral oils (paraffinic, naphthenic and mixed crude oils), halogenated hydrocarbons liquids, aromatic hydrocarbons (such as capacitor liquids: M/DBT, PXE, MIPB, etc.), liquefied gasses or cryogenic liquids, high-fire-point liquids (HMWHs liquids, esters, silicone oils, vegetable oils), up to polychlorinated biphenyls (PCB) which has been banned due to health issues [39].

Table 1.2 shows a comparison of the different properties of dielectric liquid used in medium voltage (MV) and high voltage (HV) applications.

TABLE 1.2 - Properties of dielectric liquids used in MV and HV applications

Category	Type of liquid	Application	Operational Properties	Temperature Properties
Mineral oils	Naphthenic, paraffinic	HV power equipment (transformers, circuit breakers, load tap changers, etc.)	- Oxidation resistance - Low viscosity - Low fire point - Low moisture tolerance	- Boiling point: >400°C - Flash point: >145°C
Silicone oils	Poly-dimethyl siloxanes (PDMS)	Traction and distribution transformers	- Low viscosity - High flash point - Gas absorbing under PDs - High oxidation stability - Low biodegradability	- Boiling point: >140°C - Flash point: >250°C
Synthetic hydrocarbons	Alkyldiarylalcanes (M/DBT)	Capacitors Heat transfer fluids	- Gas absorbing under PDs - Low viscosity - High temperature operability	- Boiling point: 390°C - Flash point: 200°C
Organic esters	Synthetic and natural esters	Capacitors, PCB substitutes, traction and distribution transformers	- High flash point - High moisture tolerance - Biodegradable	- Boiling point: 340°C - Flash point: >250°C

Electrical properties of dielectric liquids according to [40-41] are characterized by:
- high electrical resistivity (> 10^{11} Ω·cm at 25°C)
- low dielectric losses (tan δ > 0.05 at 25°C and 0.30-0.40 at 100°C)
- high breakdown voltage (BDV) in standard tests (> 20 kV under IEC 156 AC voltage, >145 kV under ASTM D3300 impulse voltage at 25°C)

-   low partial discharge. There is no commonly accepted standard to regulate the partial discharge
    requirement in dielectric liquids. The gassing tendency, which enhance discharges initiation in
    liquids, is limited up to +30 µL/min [41].

Standards of insulating liquids for high voltage apparatus are not relevant to power electronics
applications. For example, the flash point for electrical apparatus such as transformers, regulators,
reactors circuit breakers, etc., shall be minimum of 145°C. This limit should be higher for WBG power
module. Thus, it is necessary to considerably extend the liquid characterizations to more realistic
conditions according to the applications [42] i.e.:
-   ✓ DC and impulse voltage due to high frequency switching
-   ✓ Divergent electric field geometry such as sharp edge and triple-point
-   ✓ High temperature
-   ✓ Fluid flow due to thermal convection and electrohydrodynamic
-   ✓ Presence of contaminant such as carbon by-product and gaseous microscopic bubbles

1.5.2   Reliability of dielectric liquids at high temperature and for packaging

For decades, liquids have been used in power electronic systems for cooling (especially in traction
systems [43]). However, there are very few studies on the suitability of liquids as encapsulant materials,
and even fewer studies on their properties at high temperature.
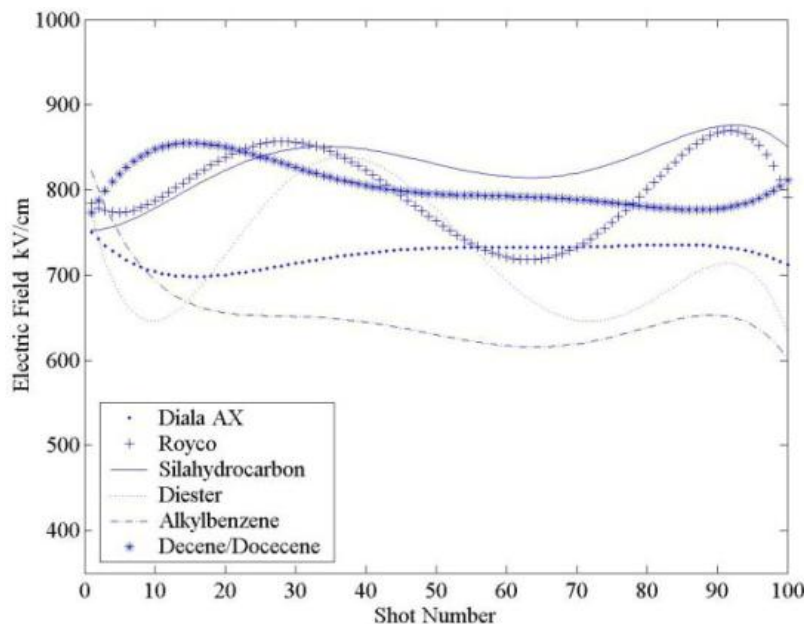
*Fig 1.24 - Breakdown trends for various type of oils under 70 kV/µs rise time impulse and 6.89 MPa. Gap distance was
adjusted to obtain average breakdown between 100 – 130 kV. Oils were filtered before each test [50]*

1) The reliability of dielectric liquids as encapsulant for electronic systems, for a maximum operating
    temperature of 80°C and for subsea pressurized applications, have been studies for several liquids.
    Results showed that high pressure improves the partial discharge inception voltage [44], and that the
    liquid is not the source of discharges [45]. Synthetic ester Midel® 7131 has high breakdown voltage
    (~80 kV in IEC 156 test) at room temperature with moisture tolerance up to 600 ppm and low thermal
    expansion. Silicone gel and liquids have similar PDs behaviour, but the self-healing capability of
    liquids is much better [34]. Moreover, dielectric liquids are prone to high-power switching producing
    excess vapour and carbon by-product [46]. However, as the number of breakdown increases, each
    type of dielectric liquid exhibit distinct behaviour (see Fig 1.24). Highly divergent field facilitates
    the generation of gaseous bubbles, which mainly depends on pressure and temperature [47]. When

ceramic substrates are embedded in liquids, the porous nature of substrates explains the origin of PDs [48]. The reduction of contaminants and water contents within the liquids can highly improve the lifetime of electronics components embedded in liquids [49].

2) Liquid hydrocarbons have been the subject of interest for high temperature characterization [51]. Mono/dibenzyl-toluene (M/DBT) is used commonly as impregnant materials for power capacitors. The presence of an aromatic ring improves the oxidation resistance, gassing properties and impulse strength. The influence of temperature on electrical conductivity of liquids hydrocarbons and esters were also studied [52-54]. Ageing experiments on transformer insulating oils at temperature up to 100°C in air resulted in the rise of more than one order of dissipation factor in less than 500 hours [55-56]. Mixture of M/DBT and mineral oils or ester enhanced the electrical properties [57-58]. Blends of DBT isomers show excellent thermal cracking and high oxidation resistance, and are mainly used as synthetic thermal fluids up to 380°C [59], but their dielectric properties are not yet known.

1.5.3   Pre-breakdown and breakdown phenomena in dielectric liquids

The "Streamer" phenomenon, constituted by the fast propagation of ionized gaseous cavities or filaments under high electric field, constitutes the basic process explaining the occurrence of partial discharges in the liquid bulk, and the breakdown process when conditions are such that streamers propagate from one electrode to the other. Most of streamers in liquids were studied using point-plane electrodes by applying a high impulse voltage on the tip. In liquids, negative streamers inception voltage are lower than positive streamer. Streamers shows a wide range of properties (shape, velocity, etc.) and are generally classified into modes according to their shape and velocity [60]:

➢ 1st mode streamers.

These streamers, known as "slow mode", "bush-like", "subsonic", "primary", etc., correspond to bush-like shape with subsonic/low propagation velocity (<1 km/s), very weak light emission. Their propagation frequently cease without inducing any breakdown. It is difficult to obtain images of these streamers by light recording, and observation was essentially carried out by shadowgraph and/or Schlieren techniques.

➢ 2nd mode streamers

They have finer filamentary shape, supersonic speed/propagation velocity 1-3 km/s, more intense light emission, higher inception voltage, relatively high transient current with DC component in the mA range, and generally lead to breakdown.

➢ 3th mode streamers

These streamers have propagation velocity >10 km/s, luminous filaments, step propagations.

➢ 4th mode streamer has velocity >100 km/s and independent on the applied voltage.

| (a) | (b) | (c) | (d) | (e) |
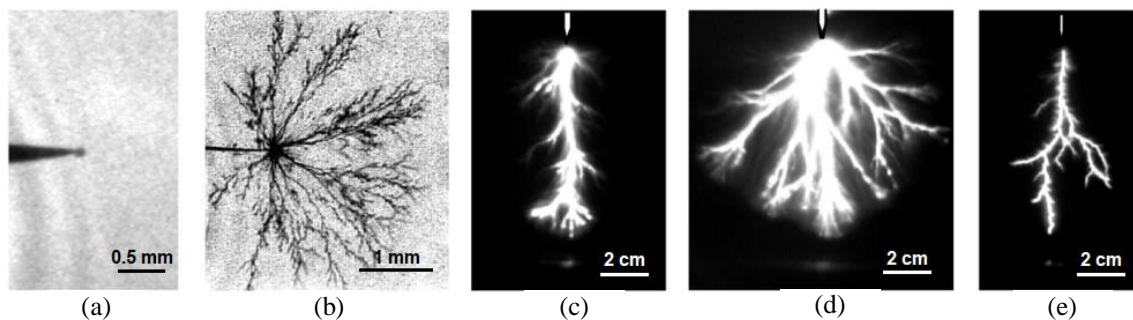
Fig 1.25 - Typical images of positive streamers in mineral transformer oils: (a) 1st mode, (b) 2nd mode, (c) 2nd mode, (d) 3rd + 2nd mode and (e) 4th mode. Figures (c)-(e) courtesy of IEEE, copyright IEEE [60]

Fig 1.25 shows typical streamer modes in a single liquid (mineral transformer oil) under wide range of applied voltages (starting from 6 to 424 kV) and inter-electrode distances d (from 6 mm to10 cm). Modes of streamers, average propagation velocity (v_{av}), applied voltage (V_{app}) and gap distance (d) between point-plane electrodes are showed in TABLE 1.3.

TABLE 1.3 - Parameter of streamers as images in Fig 1.25

Parameters/Fig 1.25	(a)	(b)	(c)	(d)	(e)
Mode of streamer	1st mode	2nd mode	2nd mode	3rd+2nd mode	4th mode
v_{av} [m/s]	100	2 000	2 000	10 000	100 000
V_{app} [kV]	6	30	160	304	424
d [mm]	6	6	10	10	10

The streamer modes relevant for the studies that will be carried out in this study are 1st and 2nd modes, which appear in typical conditions occurring in power electronics modules (i.e. short distances, divergent fields, voltages in the 10 kV range).

Comprehensive investigations of streamer initiation and transition between 1st and 2nd modes require strict control of experiment conditions [61]. To measure accurately streamer initiation voltages and calculate the field strength on the tip at the instant of initiation, the following conditions shall be comply:

- Sharp points (radius if curvature r_p **< 10** μm)
- High voltage impulse with fast rise time ($t_r \approx$ **10** ns)
- Large visual magnification (res. approx. 1 μm) and fast recording time (aperture time ~1 μs)
- Sensitive current and light emission measurement

Sharp points allow the high field (> 1 MV/cm) generation, and fast voltage rise time prevents the field modification by injection of ionic spaces charges from occurring [62]. Experiments on the influence of point tip radius on the streamer propagation mode in pentane (Fig 1.26) by Gournay and Lesaint reveal that the minimum voltage required to generate streamers (either 1st or 2nd mode) increases with tip radius (r_p). The 1st mode positive streamers evolve only in a narrow voltage range below V_2 with very sharp points (tip radius r_p smaller than a critical value r_c).
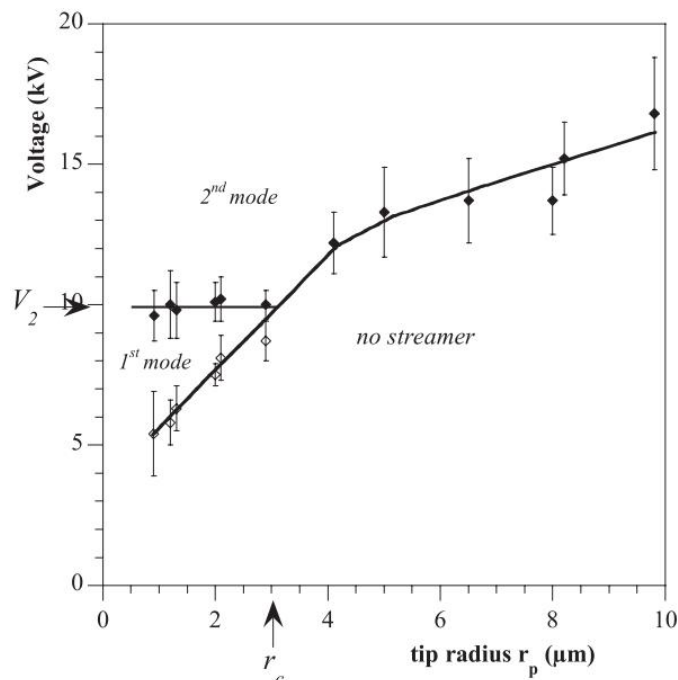
Fig 1.26 - Existence domain of 1st and 2nd mode streamers in pentane (point-plane geometry, d = 2.5 mm, t_r = 10 ns) [62]

Local high field and pulse rise time govern the streamer inception voltage. Chemical structure of liquids also strongly influence the streamer propagation. Streamer propagation in halogenated liquids (positive velocity: 10-80 km/s, negative: ~25 km/s) is much faster than in pure hydrocarbons (positive: 1-3 km/s, negative: ~0.5 km/s) [60-61]. Studies of various gap distance revealed that liquids of benzyltoluene type have high breakdown voltage for short distances [61, 63] with streamers of 1st mode or 2nd mode, and comparatively weak behaviour at large distances compared to other liquids when 3rd mode streamers appear.

Impulse voltage shape may contribute directly to the measured breakdown voltage, when short voltage duration results in shorter stopping length, and higher breakdown voltage [64]. It takes certain delay time (t_D) before discharges propagate and result in breakdowns under a fixed voltage. The voltage-time curve (as in Fig 1.27) called 'V-t curve' or 'life-curve', always decreases, no matter is the type of applied voltage (impulse, AC and DC), the field distribution within the gap (uniform field, divergent field) and the liquid type [65].

The voltage-time curve is simply divided into several regimes to describe the applicable time and breakdown voltage. The Long-term breakdown voltage (normal life operation voltage) is generally more than one order-of-magnitude lower than the short-term breakdown voltage. Short-time breakdown fields are in the order of hundreds of kV/mm for uniform field, or several MV/cm for harmonic field at the tip of point-plane geometry. Since fast impulses are present in power modules, this behaviour can be relevant.
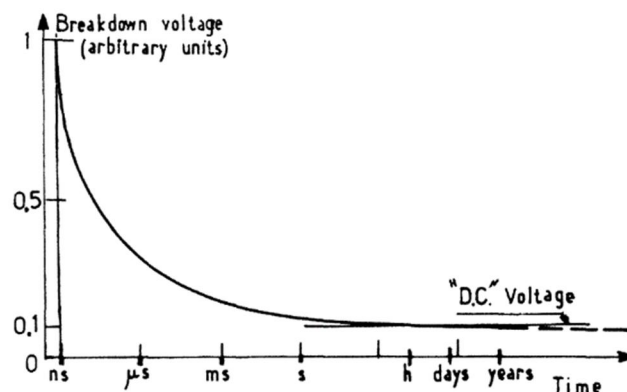
Fig 1.27 - Breakdown voltage versus breakdown lag-time under voltage step [65]

About the influence of temperature on streamers, very few results were obtained previously. Streamers composed of vapour [66] may suggest a reduction of streamer inception voltage at higher temperature, also favoured by the drop of viscosity [67-68]. Streamers measurement on cyclohexane at moderated temperature (< 70°C boiling temperature) suggested that less energy is required for propagation at elevated temperature, meanwhile no notable differences were observed for inception voltage [69]. In many researches, the investigations of streamer and partial discharges employ different types of electric field geometries, thus it is difficult to establish comparisons.

1.6 Thesis objectives and outline

The development of wide bandgap semiconductors has led to higher power density in power electronic modules, with more compact size, higher efficiency and higher temperature operation. However, packaging technology for wide bandgap power electronic devices, particularly the silicone gel frequently used as encapsulating material, is limited at temperature below 175°C. Several specific dielectric liquids, with low viscosity and high thermal stability beyond 200°C, may constitute an

alternative solution for high temperature applications. Moreover, they could also contribute to cool the modules if used in a cooling loop.

Therefore, the main objective of this thesis is to study the ability of dielectric liquids to be used as prospective encapsulating materials for power devices at temperatures approaching 300°C.

Many issues need to be addressed in the context of power electronics for high-voltage and high-temperature application:

- ➢ Which type of liquid could be compatible with such high temperature environment?
- ➢ How is the thermal stability of the liquid subjected to high temperature?
- ➢ What are the electrical properties of the liquid at high temperature, and under low and high electric field (i.e. electrical conduction, breakdown strength, PDIV, streamer propagation)?
- ➢ Can the liquid contribute to the cooling of the power electronic modules? This question will not be addressed in this thesis.

To reach the goal, this study will be divided into three main parts:

- ➢ Preliminary study on different types of liquids, in order to select the most suitable liquids for high temperature applications.
- ➢ Electrical characterisation of the selected liquids under high temperature i.e.: dielectric spectroscopy, DC electrical conductivity, breakdown measurements, partial discharge and streamer characterization.
- ➢ Electrical characterisation on substrates embedded in liquid to characterize liquids with conditions as close as possible to those present in power electronics modules.

This manuscript will be organized as follows:

- ➢ Chapter 1: State of art for high temperature power electronics applications
- ➢ Chapter 2: Dielectric liquids characterization under low electric field at high temperature
  This chapter discusses the potential liquids and their properties, experimental and set up procedure, high temperature testcell construction, low electric field characterizations i.e.: dielectric spectroscopy and conduction measurements
- ➢ Chapter 3: Dielectric liquids characterization under high electric field at high temperature, i.e.: breakdown, partial discharge and streamer measurements.
- ➢ Chapter 4: Dielectric application for high temperature power electronics
  This chapter checks the applicability of selected dielectric liquids for power module applications with alumina (Al_2O_3) substrates and aluminum nitride (AlN) substrates embedded in dielectric liquid. Particular experimental set up and testcell under high temperature up to 350°C, field calculation, substrates partial discharge and breakdown characterization embedded in liquids.
- ➢ Chapter 5: Conclusions and perspectives.

2 │ Dielectric Liquids Characterization at High Temperature

Contents

The perspective of using dielectric liquids as encapsulants for high temperature (HT) power electronics requires information and knowledge about their dielectric, physical, chemical, mechanical, properties. Particularly, the evolution of permittivity, conductivity, dielectric losses, breakdown (BD) strength, partial discharge (PD) tendency, under high temperature and high electric field shall be known in detail to comply with the working environment of power electronics modules. These dielectric properties are intrinsically associated with the nature of liquids.

This chapter presents the work carried out about dielectric characterization of several liquid candidates. In order to carry out experiments up to high temperatures about 350°C, special testcells have been constructed, allowing both low voltage and high voltage measurements. These set up were first described, and followed by the general properties of dielectric liquid candidates. The liquids studied will include two liquids already used for electrical insulation (synthetic and natural esters), and another one (dibenzyltoluene DBT) currently used for heat transfer, but with totally unknown dielectric properties. The low electric field characterizations presented in this chapter include the dielectric spectroscopy and conductivity measurements. Tentative values of ion mobility will be also derived from these data.

2.1 High temperature testcells and liquid candidates

2.1.1 Low electric field HT testcell

The HT testcell designed for spectroscopic and conduction measurements is mainly constituted by a stainless steel container, hosting two cylindrical concentric measurement electrodes with diameters of 44.7 mm and 37.2 mm, and length of 62 mm as in Fig 2.1. Gap distance between these two cylindrical electrodes is 3.75 mm and capacitance in air C_0=23.7 pF. Inner and outer cylindrical electrodes are connected to Teflon BNC coaxial feedthrough via 70 mm long metallic hollow tube extension. The hollow tube extension is intended to decrease the temperature from the testcell (max 350°C) down to a value acceptable by BNC connectors (180°C) and connection cables. The volume of liquid tested is approx. 200 mL. The constant of the testcell (κ) determined by $\kappa = \varepsilon_0 \cdot \varepsilon_r / C_0$ is 3.736×10^{-3}/cm.

The testcell is hermetically sealed with copper gaskets to prevent the exchange with the environment (i.e. moisture and air). After filling the testcell, a vacuum was applied for 10mn, and a nitrogen (N_2) blanket was then introduced above the liquid to prevent from oxidation and risk of fire. Its pressure is monitored and regulated at particular values during the experiment sequences. A 500 W metallic heating

mantle was attached around the testcell body, and controlled by automatic temperature regulation system. Prior to the experiment, the testcell was tested at 350°C under maximum 3 bar pressure.
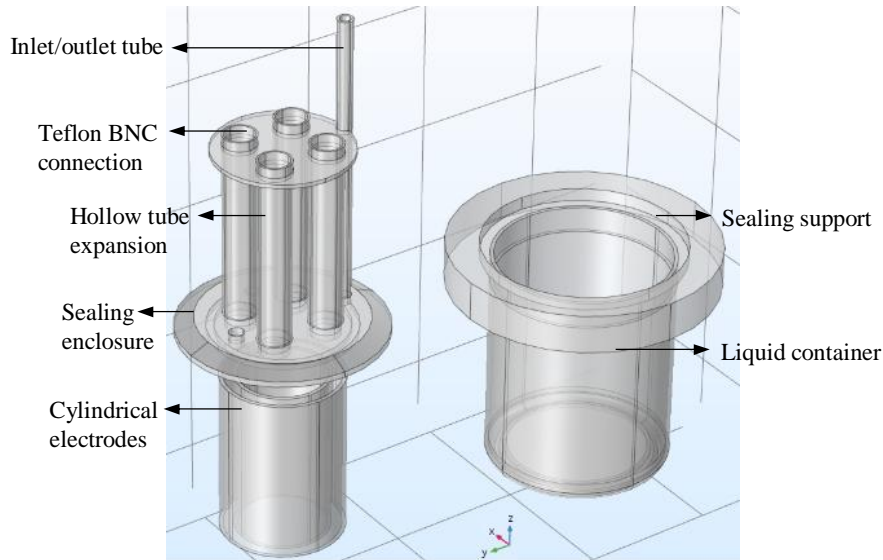
Fig 2.1 - Testcell main construction

Fig 2.2 shows the complete HT testcell installed in a thermal insulation holder. Two K-class thermocouples are installed at 30 mm and 10 mm from the cell centre to measure the liquid temperatures close to both measurement electrodes, and regarded as "outer" and "centre" temperatures. The outer thermocouple serves as input reference for temperature regulation and monitoring, while the centre thermocouple is used to monitor the temperature homogeneity inside the testcell. Even after stabilization, a temperature difference ΔT always existed between outer wall and centre of the testcell, with a maximum value about ΔT =10°C at 350°C.
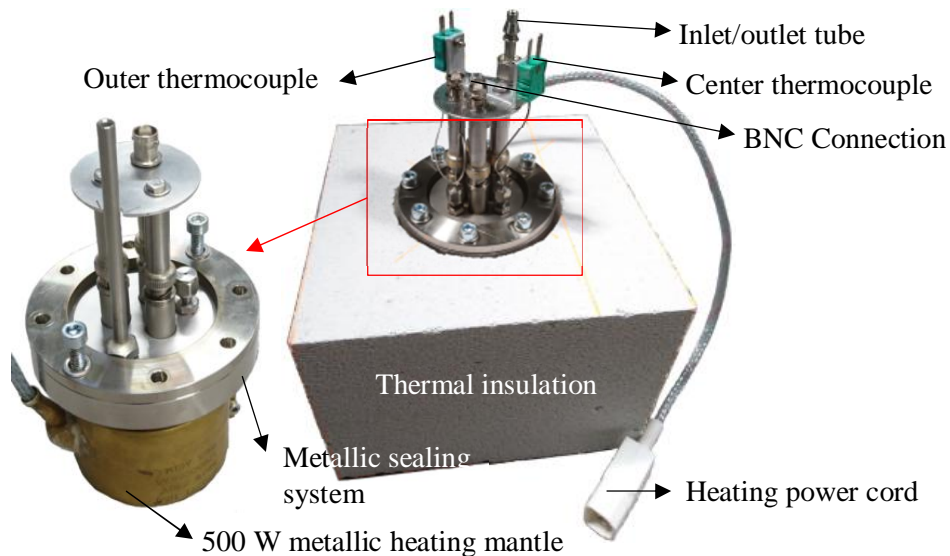
Fig 2.2 - High temperature testcell, heating system, support and connections.

Fig 2.3 shows typical recordings of temperature inside the testcell. Thermocouples set at outer and centre position show that there were always slight temperature differences. Due to the heating from the wall and heating flux direction toward the centre, the outer part of liquid is always hotter than the centre.
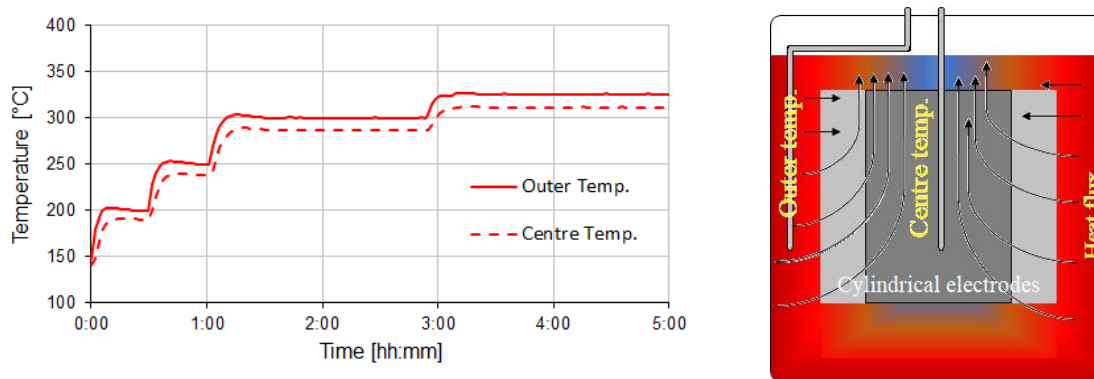
Fig 2.3 - Temperature regulation inside the testcell: (a) heating profile and (b) heat flux and thermocouples position

2.1.2 Dielectric liquids samples

Several candidates were first selected based on their high temperature properties (maximum allowed temperature >150°C). Preliminary study to observe the thermal and electrical properties under high temperature environment were done in liquids already used for electrical insulation: synthetic ester (SE), perfluoropolyether (PFPE) and colza oil. Later, it turned out that esters cannot be used above 200°C without severe degradation, and a new liquid was then investigated: a blend of dibenzyltoluene isomers (Jarytherm® DBT). TABLE 2.1 shows the general properties of liquid candidates used for these experiments.

Jarytherm® DBT is an industrial heat transfer liquid produced by ARKEMA [59]. This synthetic hydrocarbon liquid is commonly used in the chemical, petrochemical, plastic and rubber, pharmaceutical, and fine specialty chemical industries. It offers high performance and stability between -40 and 350°C under atmospheric pressure, and gets a very high boiling temperature of 390°C. However, its dielectric properties were unknown prior to this study. MIDEL® 7131 is a product of M&I Materials [71]. This synthetic ester (SE) liquid is biodegradable with high fire point and low pour point, and is mainly used in high voltage (HV) application for transformers up to 433 kV. Galden® PFPE is a heat transfer fluid produced by SOLVAY [72]. This liquid has high thermal stability up to 270°C with no flash or fire point and no auto-ignition point, compatible with metal, plastics and elastomers.

TABLE 2.1 - Properties of liquids

Properties	M/DBT	Synthetic Ester	PFPE	Colza
Commercial product	Jarytherm® DBT	MIDEL® 7131	Galden® HT 270	
Chemical name	dibenzyltoluene	Pentaerythritol	Perfluoropolyether	-
Molecular formula	$C_{21}H_{20}$	$C_{25}H_{44}O_8$	$CF_3[OCF(CF_3)CF_2]_n(OCF_2)_mOCF_3$	$C_{37}H_{110}O_6$ (simplified)
Molecular weight [g/mol]	272.384	472.61	1550	651.27
Density [g/cm³]	1.0±0.1	1.0±0.1	1.86	0.914-0.917
Kinematic viscosity at 25°C [mm2/s]	42.94	53.56	11.70	74.65
Pour point at 760 mmHg [°C]	-38.5 to -32.8	-60	-66	-22
Boiling point at 760 mmHg [°C]	390	250	270	107-232
Vapour pressure at 25°C [mmHg]	0.0±0.4	0.0±1.4	$< 10^{-2}$	< 0.1
Enthalpy of vaporization [kJ/mol]	62.8±0.8	80.3±3.0	97.34	-
Fire point [°C]	230	316	-	
Self-ignition point [°C]	500	> 260	-	424
Flash point [°C]	200	260	-	260
Specific heat 20°C [kJ/kg·°C]	1.60	1.902	0.963	
Thermal conductivity 20°C [W/m·°C]	0.128	0.147	0.065	

Volume resistivity 25°C [GΩ·m]	-	> 30[2]	6×10⁴	
Dielectric strength [kV]	-	> 75	40[3]	
Dielectric constant at 25°C	-	3.28	1.94	2.47
Water saturation at 20°C [ppm]		2700	< 20	
Index of refraction	1.594	1.461	-	1.465-1.467
Molar refractivity [cm³]	89.7±0.3	124.9±0.3	-	-
Free rotating bonds	4	24	-	-
Rule of 5 variations	1	1	-	-
Polar surface area [Å²]	0	105	-	-
Polarizability [cm³]	35.6±0.5 10⁻²⁴	49.5±0.5 10⁻²⁴	-	-
Surface tension [dyne/cm]	40.4±3.0	36.8±3.0	-	-
Molar volume [cm³]	264.5±3.0	455.2±3.0	-	-

[2] DC Volume resistivity at 90°C
[3] AC Breakdown at 2.54 mm gap

According to the manufacturer's technical datasheet, Jarytherm® DBT has the largest practical operating temperature range up to 380°C. MIDEL® 7131 SE has the lowest pour point -60°C, compared to other esters such as colza (generally known as "rapeseed oil"), but its manufacturer indicated that its maximum operable temperature should remain below 200°C.

Fig 2.4 shows the density and kinematic viscosity of liquid candidates. DBT has the lowest kinematic viscosity and the widest temperature range among these three liquids, which indicates an advantage for the cooling.

(a)   (b)
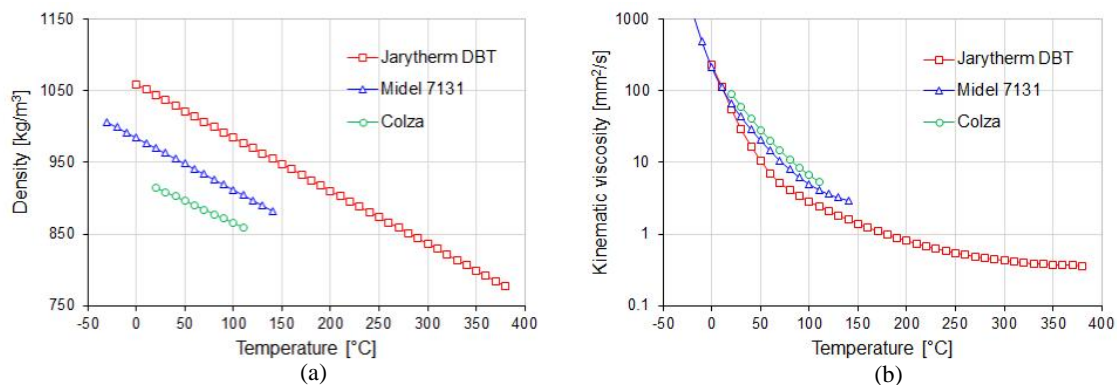
Fig 2.4 - Dielectric liquid properties comparison: (a) density and (b) kinematic viscosity

The vapour pressure profile of DBT versus temperature shown in Fig 2.5 indicates that at 380°C the vapour pressure is only 97 kPa, which is approximately equal to atmospheric pressure. The low vapour pressure properties allows simple container design that does not require high-pressure properties: at 300°C, the pressure increase is only of 15 kPa.
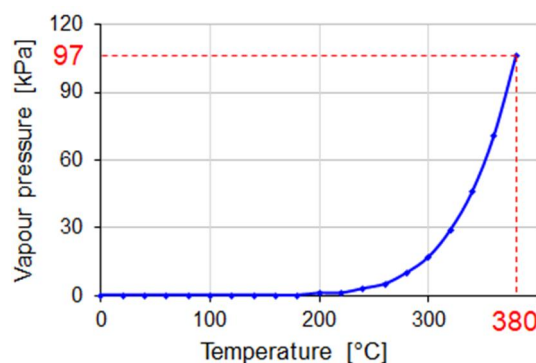
Fig 2.5 - Thermodynamic properties of DBT: vapour pressure versus temperature.

2.1.3 Sample treatment

Liquid samples were placed under vacuum at 80°C for 24 hours to degas and to remove the water from the liquid, and then vacuumed again down to room temperature for 2x24 hours. After filling into the testcell, it was placed under vacuum once again for 1 hour to de-gas the oil from air that may dissolve during the filling process. At the end of this process, N_2 was injected into the testcell above the liquid surface at 100 kPa.

The exchange with atmospheric air are avoided due to the tightness of the testcell. The pressure within the testcell was adjusted above the liquid vapour pressure to avoid boiling (by regulating the pressure of N_2 according to temperature).

2.2 Liquid resistivity measurements and dielectric spectroscopy

2.2.1 Liquid resistivity measurement method: IRLAB resistivity meter.

Fig 2.6 - IRLAB model LDTR-4 resistivity meter

Liquid resistivity measurements were performed with IRLAB resistivity-meter model LDTRP-2 (Fig 2.6). This device measures the bulk conduction due to ionic dissociation and recombination processes, by applying a 10 V quasi-rectangular wave at low frequency 0.5 Hz [73]. Ions appear and recombine according to the following thermodynamic equilibrium:

$$M(T,E,t) \leftrightarrow C^+A^-(T,E,t) \leftrightarrow C^+(T,E,t) + A^-(T,E,t) \tag{2.1}$$

where T,E,t show the dependency versus temperature, applied electric field and time; M is the neutral molecules concentration at particular temperature, applied electric field and time; C^+A^- is an associated ion pair; C^+ and A^- are the ions separation yielding cation and anion species.

The conductivity of the liquid is then provided by the contributions of positive and negative ions:

$$\sigma_0 = \mu_+ q_+ + \mu_- q_- \tag{2.2}$$

where μ, q are the ionic mobility and volume charge density. When the applied voltage is low enough, the electric field E does not significantly disturb the thermodynamic equilibrium and a quasi- ohmic law is obeyed:

$$j_0 = \sigma_0 \cdot E \tag{2.3}$$

Here j_0 denotes the current density. Hence the conductivity (σ_0) of the liquid can be derived from the measurement of current (I_0) flowing through the liquid at low field.

In order to minimize the electrode polarization, the voltage is periodically reversed with a lapse time between voltage application that is much lower than the ionic transit time ($t_0 \approx 10s$ with mobilities $\mu \approx 5 \times 10^{-10} \ m^2/V \cdot s$). The voltage rise time is lengthened up to 10 ms to reduce the charge and discharge

surge currents ($dV/dt = 10 \, kV/s$). LDTRP-2 displays the conductance ($G = I/V$) and capacitance within the range of 2×10^{-6} S to 2×10^{-14} S (error < 2%) and 10-2000 pF (error < 1%, ±0.2 pF).

2.2.2   Dielectric spectroscopy measurements: Novocontrol® system

Dielectric spectroscopy is the measurement of dielectric properties of material versus frequency, based on the interaction of external applied electric field with the electric dipole moments and charges present in the material. Dielectric spectroscopy is carried out by applying a fixed low alternating electric field starting from a low frequency to high frequency in fixed steps. Electric field and response of electric displacement in the material are recorded. The voltage and current are expressed as:

$$U(t) = U_0 \cos(\omega t) \tag{2.4}$$

$$I(t) = I_0 \cos(\omega t + \varphi) = re(I^* \exp(j\omega t)) \tag{2.5}$$
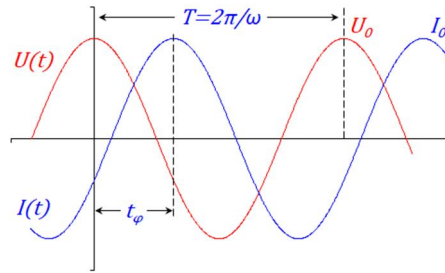
Fig 2.7 - Electric field and displacement response manifestation from voltage and current in time domain

Transformation from time domain to frequency domain by Fourier transform over n-periods of time of current measurement yields:

$$I^*(\omega) = I'(\omega) + jI''(\omega) = \frac{2}{n \cdot T} \int_0^{n \cdot T} I(t) \exp(j\omega t) \, dt \tag{2.6}$$

$$I_0 = \sqrt{I'^2 + I''^2} \tag{2.7}$$

where $I^*(\omega)$, I_0, I' and I'' are the complex current, absolute, real and imaginary value of current. Power factor is then directly derived from the current component as:

$$\tan(\varphi) = \frac{I''}{I'} \tag{2.8}$$

Impedance of the material is calculated by measuring at fix frequency $\omega/2\pi$ the applied voltage $U(\omega)$, current $I(\omega)$, and the phase angle between $\varphi(\omega)$ as:

$$Z^*(\omega) = Z' + jZ'' = \frac{U(\omega)}{I(\omega)} \left[\cos(\phi(\omega) + j \cdot \sin(\phi(\omega))) \right] \tag{2.9}$$

The ratio of $Z^*(\omega)$ components also refer to power factor $\tan(\varphi)$ as:

$$\tan(\varphi(\omega)) = \frac{Z''(\omega)}{Z'(\omega)} = \frac{\sin(\varphi(\omega))}{\cos(\varphi(\omega))} \tag{2.10}$$

Permittivity of material under test can be calculated by

$$\varepsilon^*(\omega) = \varepsilon'(\omega) - j\varepsilon''(\omega) = \frac{I^*(\omega)}{U_0} \frac{1}{j\omega C_0} = \frac{-j}{\omega \, Z^*(\omega)} \frac{1}{C_0} \tag{2.11}$$

where C_0 is the capacitance of empty testcell.

Ratio of permittivity components as well as the inverse ratio of impedance components is the loss factor $\tan(\delta)$ and can be calculated by:

$$\tan(\delta(\omega)) = \frac{\varepsilon''(\omega)}{\varepsilon'(\omega)} = \frac{Z'(\omega)}{Z''(\omega)} = \frac{1}{\tan(\varphi(\omega))} \tag{2.12}$$

The conductivity of material is calculated as:

$$\sigma^*(\omega) = \sigma'(\omega) - j\sigma''(\omega) = \frac{I^*(\omega)}{U_0} \cdot \frac{d}{A} = \frac{1}{Z^*(\omega)} \cdot \frac{d}{A} \tag{2.13}$$

d is the gap spacing between electrodes and A the area of electrodes.

The broadband dielectric spectrometer used in this study is the Novocontrol Alpha-A. The applied voltage was 1 Vrms in the frequencies range from 10 mHz to 20 MHz. The measurement accuracy depends on the capacitance of samples and the frequency, as shown by the manufacturer specification in Fig 2.8 [74]. The impedance measurements range from $|Zm^*|$ 1.5×10^{11} Ω at 10 mHz to 2.7×10^3 Ω at 1 MHz with accuracy range from 0.1% 0.6° to 0.1% 6m°. Capacitance measurements between 50-100 pF come with accuracy range from 0.1% 0.06° to 0.01% 2m° for the same frequency range. Tan (delta) accuracy is $\pm3\times10^{-5}$ between $2-2\times10^5$ Hz at 50-100 pF capacity, and fall to $\pm10^{-4}$ between $2\times10^{-3}-2\times10^6$ Hz at 10-50 pF capacity.
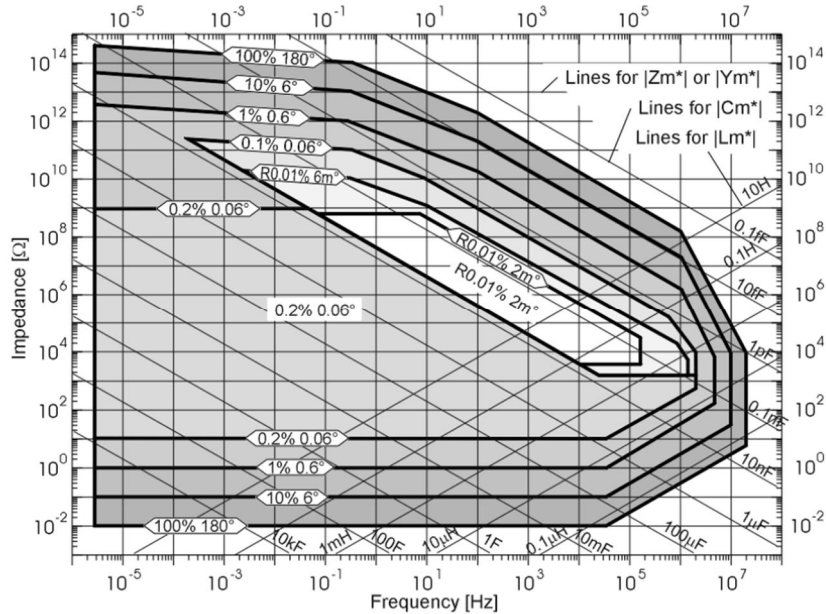
Fig 2.8 - Novocontrol Alpha Analyzer measurement accuracy specification [5]

2.2.3   Measurement protocols

Conduction measurement by IRLAB LDTR-4 and dielectric spectroscopy measurement by Novocontrol were carried out sequentially. For dielectric spectroscopy, results above 1 MHz will be not considered due to the possibility of large inaccuracy induced by the measurement system (cables and testcell).
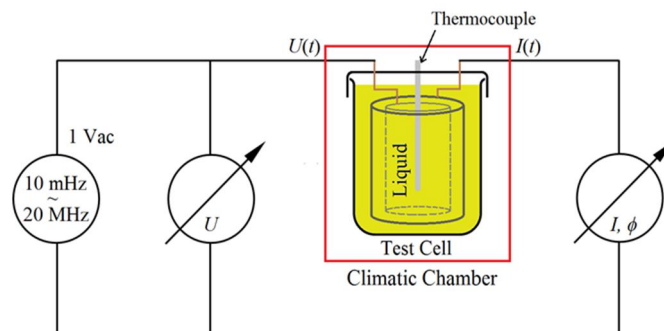
Fig 2.9 - Liquid dielectric spectroscopy experimental set up

Fig 2.9 shows the liquid spectroscopy experimental set up. Liquid conductivity was first measured during the temperature steps. After the liquid reached the thermodynamic equilibrium, indicated by the steady state of conductivity value, measurement was then switched to dielectric spectroscopy.

2.2.4   Measurement results in Synthetic Ester (SE) Midel® 7131

Based on literature [75-77], colza oils and more generally natural ester liquids exhibit electrical properties degradation for temperatures in excess of 120°C, with a rapid acceleration of thermal aging processes. According to the manufacturer's data sheet, synthetic ester has several advantages i.e.: lower pour point down to -60°C, high fire point 316°C, biodegradability, and high moisture tolerance. Esters can absorb greater amounts of water compared to mineral and silicone oils, without compromising their dielectric properties. SE provides good insulation properties and is used in medium voltage transformers.

However, despite its flash point (260°C) and fire point (316°C) are quite high, the maximum temperature in measurements was limited to 200°C, in order to avoid the rapid chemical degradation that would occur at higher temperature. The total duration of measurements with a sample was limited to a few hours, in order to minimize the influence of liquid ageing at high temperature.

Fig 2.10 shows permittivity's ε' and ε'' of SE versus frequency at various temperature. On the ε'' plot, the black solid line indicates the limit of measurement capabilities of the spectrometer. Below this limit, measurements show an erratic behaviour that should be disregarded. Real part of relative permittivity (ε') remain fairly constant within frequency range between 1 Hz – 100 Hz, and decreases when temperature is raised. Below and above this range, different behaviours are observed.
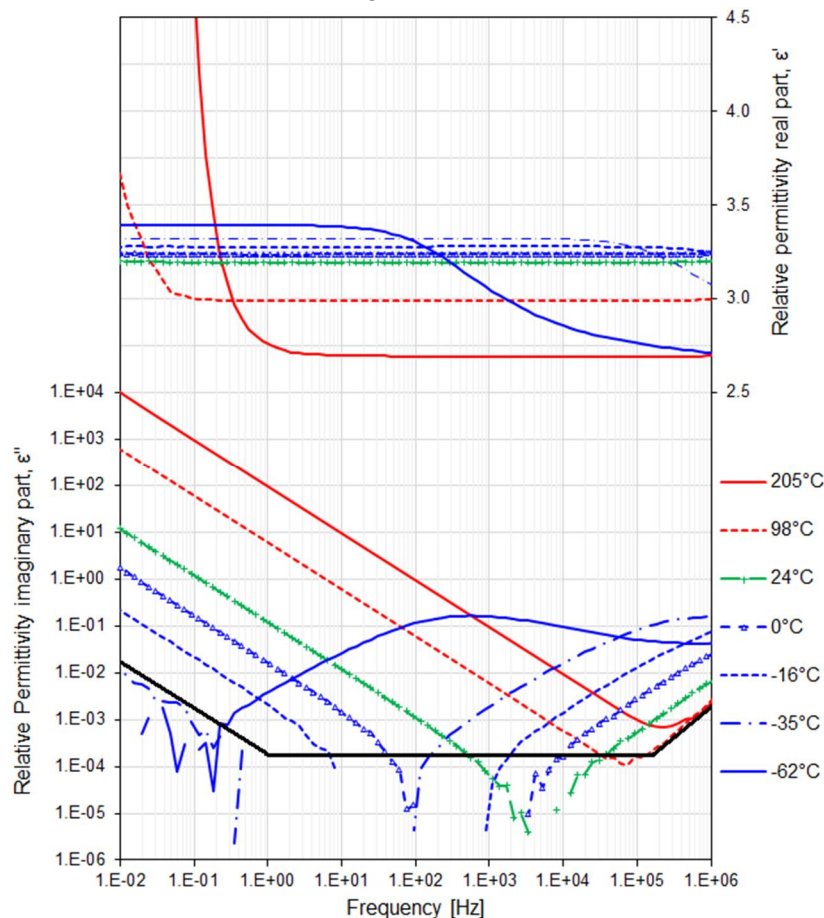
Fig 2.10 - Relative permittivity of SE at various temperature [9]

At low temperatures (< -16°C) and above 100 Hz a decrease of permittivity is observed after some critical frequency. The lower the temperature, the lower the critical frequency. This behaviour is correlated to the fact that in this temperature range, the ester is not any more a liquid, and starts to become a gel (Fig 2.11c). At the minimum temperature (-62°C), it gets the appearance of a "solid" with very high viscosity (>100 000 mm^2/s), and both ε' and ε'' show variations totally different from liquids, with relaxation processes at low frequency (e.g. around 600 Hz at -62 °C, 1 MHz at -35°C) typical of solids materials. Conversely, below 1 Hz and at high temperature (>100°C) a large increase of permittivity is recorded.

(a)　　　　　　　　(b)　　　　　　　　(c)
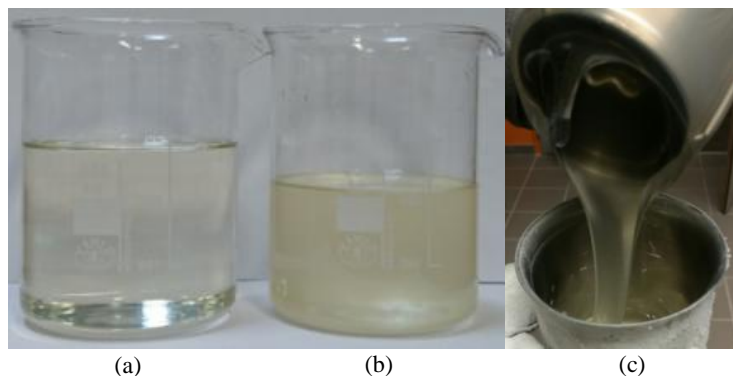
Fig 2.11 - SE appearance: (a) new condition at RT, (b) after 200°C at RT and (c) at -60°C

The decrease of permittivity versus temperature observed over a large frequency range is to be correlated to the decrease of liquid density. Fig 2.12 shows relative permittivity obtained from dielectric spectroscopy at various frequencies, compared to that calculated from capacitance measurements with the resistivity-meter (IRLAB), and plotted together with the liquid density (red solid line). The liquid density was obtained from the Midel® 7131 datasheet between -30°C to 140°C, and extrapolated to low and high temperatures considering a linear trend. Previous papers reported variations of permittivity in hydrocarbon liquids versus density, when either pressure or temperature is changed [78, 79]. Over the investigated temperature range, the relative variations of permittivity and density (about -20%) are quite similar in our measurements.
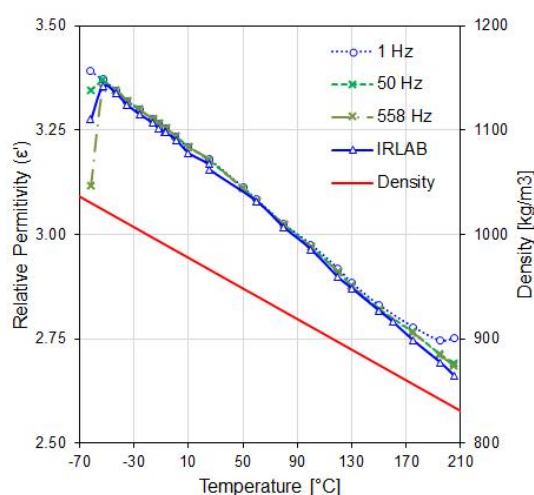
Fig 2.12 - Relative permittivity at various frequency and density of SE versus temperature [9]

Fig 2.13 shows the typical behaviour of dissipation factor tan (delta) versus frequency. In this plot, the black solid line indicates the limit of measurement capabilities of the experimental system. Over a large frequency range (1 Hz – 100 kHz), minimum tan (delta) measurements are limited to about 3.0×10^{-5}, and erratic measurements below this limit should be disregarded. Between 100 kHz and 1.0 MHz, the limit increases to about 10^{-3}. In this frequency range, all measurements carried out above 100°C become

identical to the system limit and are not valid. In a similar way, measurements carried out at temperatures lower than -35°C and frequency below 2.0×10^{-1} Hz are erratic, and out of the system capability.

When SE is in the liquid state (i.e. for temperature above -35°C), a variation proportional to $1/f$ is observed at low frequency (f). This variation is typical for losses due to conductivity, according to equation (2.14), where σ_{DC} is the dc conductivity.

$$Tan(delta) = \frac{\sigma_{DC}}{2\pi f \cdot \varepsilon_S}$$ (2.14)

When frequency is increased, Tan (delta) goes through a minimum (correctly measured only above 150°C), and increases thereafter. The higher the temperature, the higher the frequency of the minimum. At higher frequency, tan δ becomes nearly proportional to f, according to the relation:

$$Tan(delta) \cong \left(1 - \frac{\varepsilon_\infty}{\varepsilon_S}\right) 2\pi f \cdot \tau$$ (2.15)

where ε_S and ε_∞ are static and optical permittivity, and τ the dipole relaxation time (which depends on the liquid viscosity and thus on temperature). Consequently, the plot of losses versus frequency gets a "V" shape, typical for liquids. This shape is not any more observed when SE becomes a gel at low temperatures. At many temperatures, the minimum values of losses are below the measurement limit of the dielectric spectrometer (about 3.0×10^{-5}). When temperature is increased, the losses increase at low frequency and decrease at high frequency.
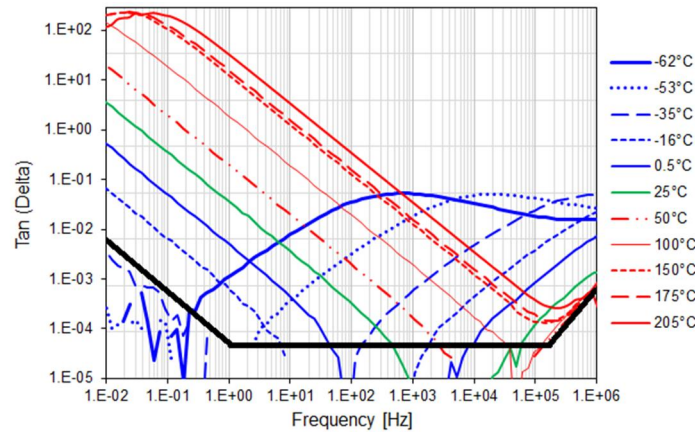
Fig 2.13 - Tan (delta) of SE at various temperature

The evolution of AC conductivity versus frequency deduced from spectroscopy measurements is depicted in Fig 2.14.
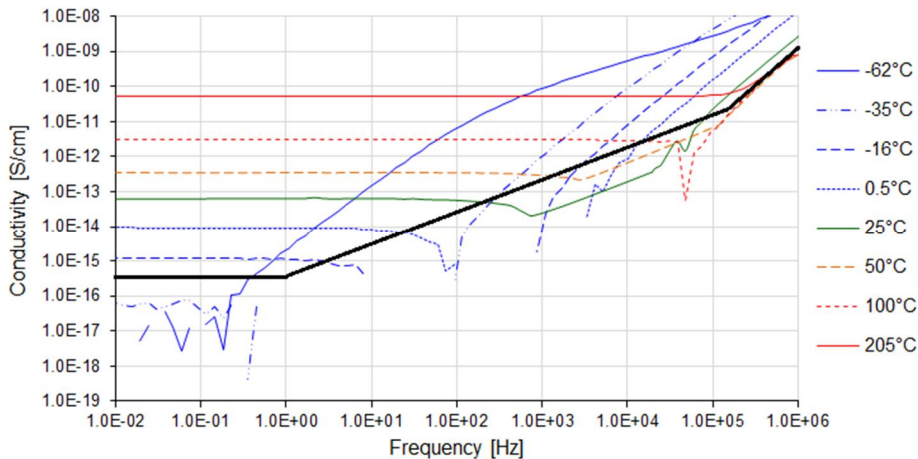
Fig 2.14 - Conductivity of SE at various temperature

It is obvious that when the SE is liquid (above -16°C), the conductivity is frequency independent over a large frequency range, from the lowest frequency investigated (10 mHz) up to a maximum frequency that increases when temperature is raised. Stable value of AC conductivity (σ_{AC}) corresponds to the DC conductivity (σ_{DC}), that strongly increases with temperature. The relation between AC and DC conduction is expressed by:

$$\sigma'_{AC} = \sigma_{DC} + k \cdot 2\pi f^a \tag{2.16}$$

where σ' is the real part of AC conductivity (σ_{AC}), k is a temperature-dependent parameter, and a is the exponent of the power law.

For high frequency and temperature above -35°C, a nearly linear variation of AC conductivity versus frequency with a slope close to 1 is observed.

Fig 2.15 shows that the dc conductivity deduced from Fig 2.14, and measured by the IRLAB resistivity-meter present a good agreement. DC conductivity increases by more than 3 orders of magnitude between RT and 200°C.
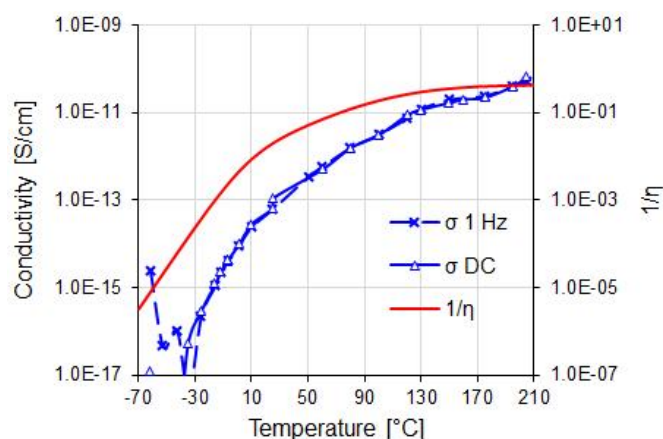
Fig 2.15 - DC conductivity (deduced from plateau of σ$_{AC}$ at 1 Hz and measured by IRLAB) and inverse of viscosity versus temperature [80]

Temperature has a large influence on the liquid density and viscosity, and thus on its electrical properties. It is known that in non-polar liquids such as esters, conduction properties are related to the density of ions, and to their mobility. According to the Walden's law, temperature has a direct influence on ion mobility µ, since the latter is inversely proportional to the viscosity η. Fig 2.15 shows that both dc conductivity and the inverse of viscosity η show a large increase with temperature (T). However, the variation of σ (T) is larger than that of 1/η (T). Within the range from -30°C to 200 °C, conductivity increases by nearly 6 orders of magnitude, while 1/η is increased by only 3 orders. This indicates that the increase in ion mobility cannot explain alone the recorded increase in conductivity. Since that conductivity is proportional to the product µn (with n is density of ions), and the mobility µ is inversely proportional to the viscosity, then the ion density n should be proportional to the product σ x η.

Fig 2.16 shows the Arrhenius plot for the product σ x η, versus temperature from -26°C to 205°C. This plot shows that the influence of temperature on conductivity is also due to a large increase of the ion density when temperature is raised.

In non-polar liquids at very low fields, ions mainly result from dissociation – recombination equilibrium of impurities, characterized by a dissociation rate that increases with temperature. Fig 2.16 shows that the ion density fairly well follows an Arrhenius-type variation, with a 0.217 eV activation energy [80].
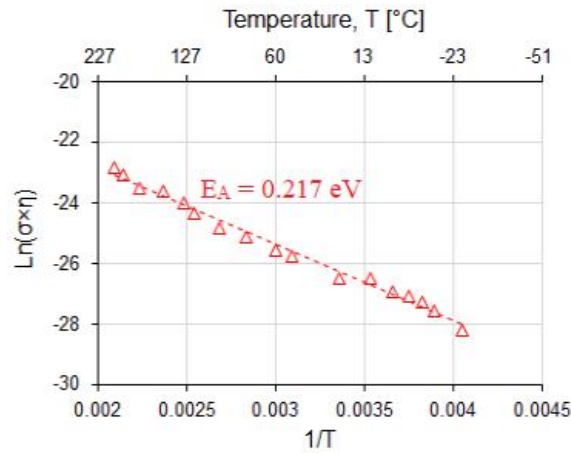
Fig 2.16 - Arrhenius plot for product of conductivity and viscosity of SE versus temperature

As concerns losses at high frequency, they can be attributed to a dipolar relaxation mechanism. With such mechanism and according to relation (eq. 2.15), tan (delta) is proportional to the product of τ and $2\pi f$. Since the dipole relaxation time τ depends on temperature and is proportional to η/T [81], the increase of tan δ versus temperature should compare with that of η/T at fixed frequency. Fig 2.17 shows a fairly good agreement at high frequencies (0.5 MHz and 1.1 MHz). The turning point of tan (delta) at around -30°C may due to the transition from liquid state into solid state, where this model is not any more valid.
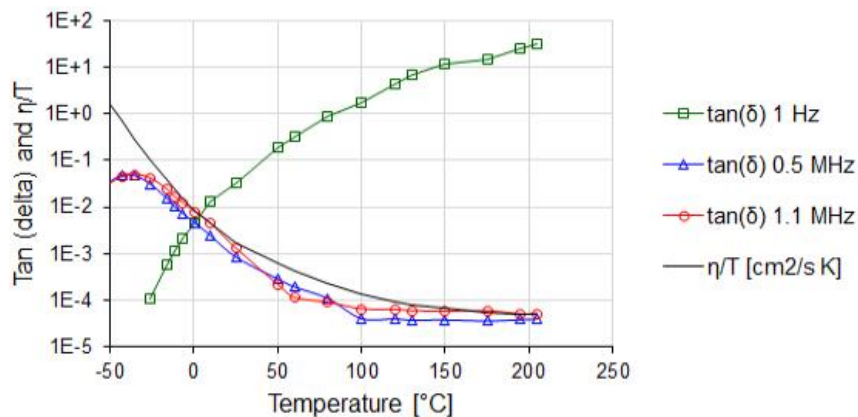
Fig 2.17 - Tan (Delta) at various frequencies and η/T of SE versus temperature

Within the low frequency range in the liquid state, i.e. when losses are due to conduction, tan (delta) increases as the temperature raises (Fig 2.17, tan (delta) at 1 Hz). At high temperature (> 150 °C) and very low frequency (< 0.1 Hz), a relaxation phenomenon is also observed, probably attributable to an electrode polarization process producing a large increase of ε' (Fig 2.10).

2.2.5 Dielectric spectroscopy of Jarytherm® DBT

Fig 2.18 shows the DC conductivity of DBT measured with the IRLAB system during the temperature rise from 50°C to 200°C. Conductivity of DBT increases almost exponentially with temperature from 1.05×10^{-13} S/cm at 50°C to 1.84×10^{-11} S/cm at 200°C. The temperature difference at 200°C between outer thermocouple (red solid line), and centre thermocouple (red dash line) was 10°C.
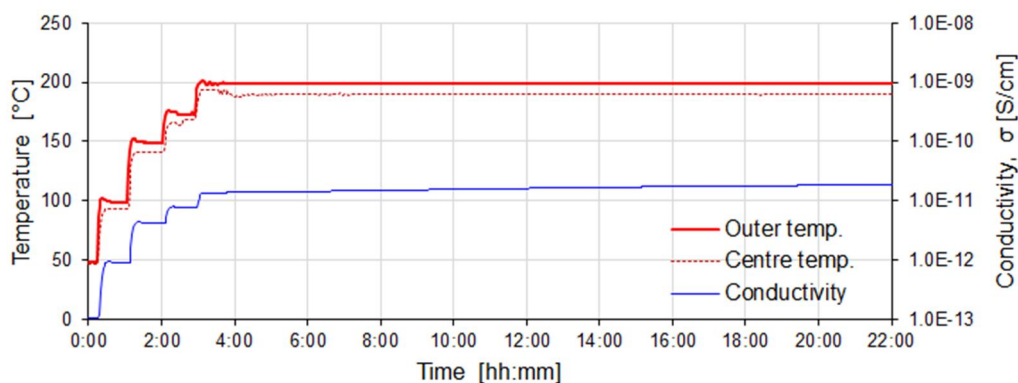
Fig 2.18 - IRLAB LDTR-4 measurement: conduction and heating process of DBT up to 200°C

The permittivity of DBT and capacitance of the testcell measured during the same sequence decrease with temperature as shown in Fig 2.19.
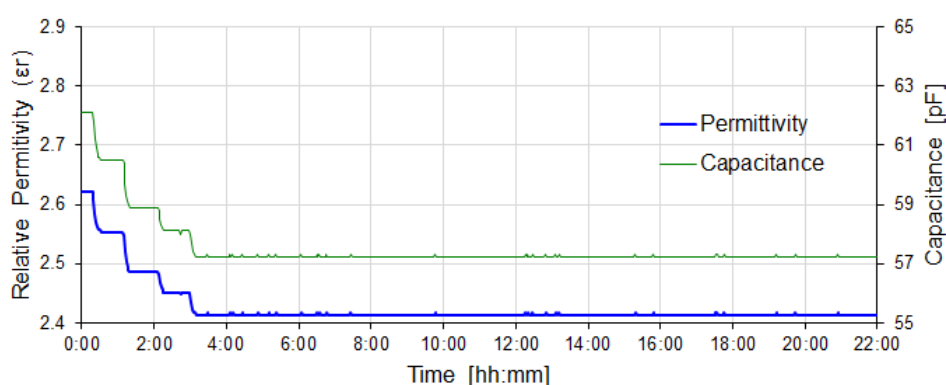
Fig 2.19 - IRLAB LDTR-4 measurement: permittivity and capacitance of DBT from 50°C to 200°C

Fig 2.20 shows the real part of relative permittivity (ε') measured by dielectric spectroscopy at different temperatures up to 325°C. At high frequency, ε' is stable up to 1.0 MHz. When frequency is decreased, a large increase of ε' occurs (such as in SE above 100°C). The critical frequency where ε' becomes stationary increases with temperature.
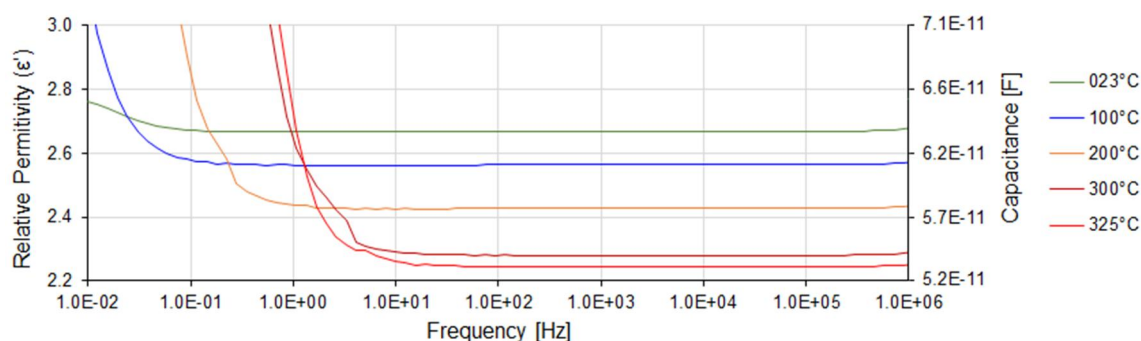
Fig 2.20 - Real part of relative permittivity (ε') and capacitance of DBT versus frequency at various temperatures

As in SE, the increase of ε′ at low frequency may be attributed to interface polarization process. The strength and frequency of electric field will contribute to the rate and type of charge carrier involved in the dissociation / recombination equilibrium. Over time, ions will migrate to the corresponding polarity of electrode, and accumulate in a thin layer of space charge region known as "double layer", depending on how long the applied electric field is applied. Since ion mobility increases with temperature (due to a decrease of liquid viscosity), the space charge accumulation will be faster (i.e. corresponding to higher frequencies).

At very low frequency (<100 mHz at RT, and < 20 Hz at 325°C in Fig 2.20), this manifests as a large increase of apparent capacitance, which may reach up to several µF/cm² [13]. Insulating liquids in this frequency region mainly behave as a capacitance through electrochemical processes in the polarization layer, in series with the bulk resistance of the liquid. The real part of the complex capacitance increases when the frequency decreases.

Within the stationary region, dielectric constant (or capacitance) of DBT get a liner correlation to the temperature (Fig 2.21), which can be expressed as:

$$\varepsilon'(T) = -0.0015 \cdot T + 2.6956 \tag{2.17}$$

$$C(T) = -3.49 \times 10^{-14} \cdot T + 6.39 \times 10^{-11} \, F \tag{2.18}$$

where T is the temperature in Celsius. The decrease of permittivity (about -20% from 25 to 350°C in Fig 2.20) versus temperature in liquids is mainly associated with the decrease of density (-24% in the same temperature range), although there does not usually exists a perfect linear relation between density and permittivity, due to variations of the dipole moment of molecules with temperature.
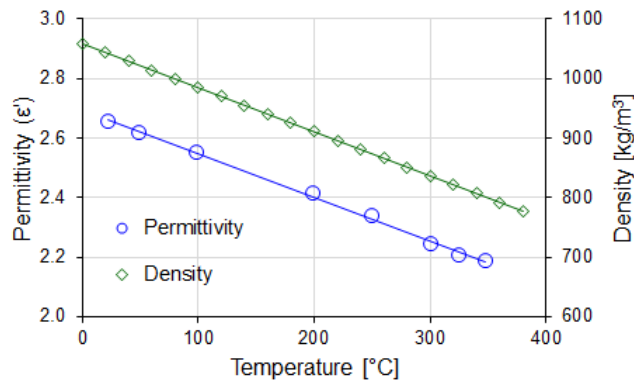
Fig 2.21 - Permittivity and capacitance of DBT at stationary region as function of temperature at 50 Hz

Fig 2.22 shows the imaginary part of relative permittivity (ε'') generally referred as "dielectric losses" of DBT at different temperature. There are no peaks, no dielectric relaxation identified, and the plots are typical of losses due to conduction.
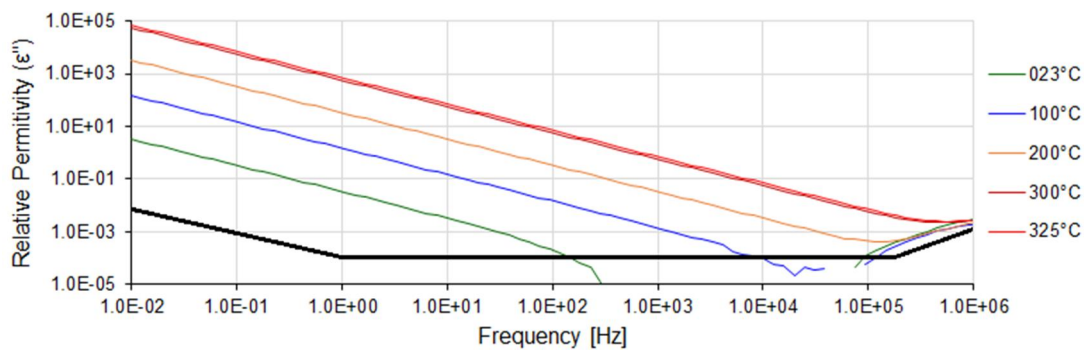
Fig 2.22 - Imaginary part of relative permittivity (ε") of DBT at various temperature

Fig *2.23* shows the plot of tan (delta) versus frequency. These plots compare well with those obtained in SE above RT. On a large frequency range, tan (delta) varies as 1/f, indicating losses due to conduction. At high frequency (above 100 kHz) measurements are limited by the experimental system. At very low frequency and high temperature (> 200°C), tan delta goes through a maximum at a frequency that increases with temperature. This behaviour can be attributed to electrode polarization processes.
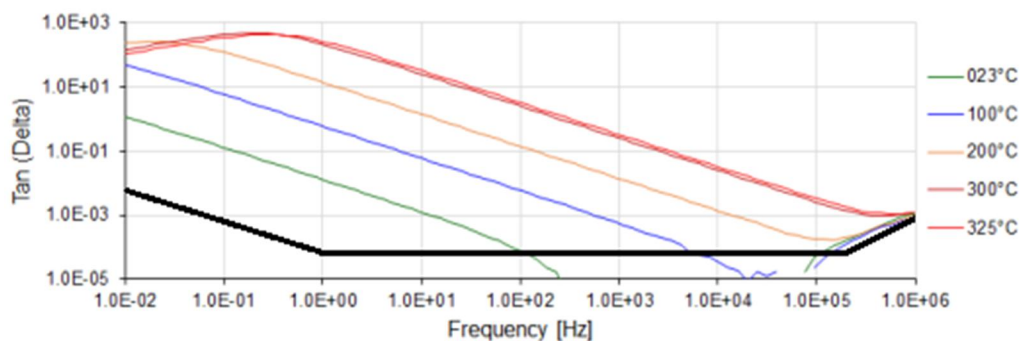
Fig 2.23 - Tan (delta) of DBT at various temperature

Fig 2.24 shows conductivity of DBT at various temperatures. On this plot, only the stable DC conductivity is observed from RT to 325 °C. Conductivity varies from 1.89×10^{-14} S/cm at 25°C to 3.18×10^{-10} S/cm at 300°C. At RT, the conductivity is slightly lower than in SE (6.35×10^{-14} S/cm).
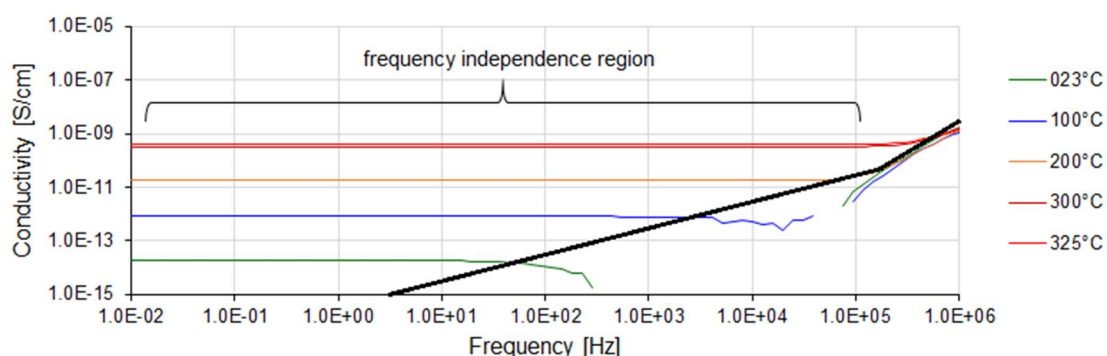
Fig 2.24 - Conductivity of DBT at various temperature

Fig 2.25 shows conductivity of DBT versus temperature at 1 Hz, and comparison with the inverse of viscosity $1/\eta$. As in SE, the variation of conductivity is larger than that of $1/\eta$. Within the range from -23°C to 325 °C, conductivity increases by nearly 4 decades, while $1/\eta$ is increased by only 3. The increase in ion mobility cannot explain alone the recorded increase in conductivity. At high temperature, an increase in ion density also contributes to enhance conductivity.
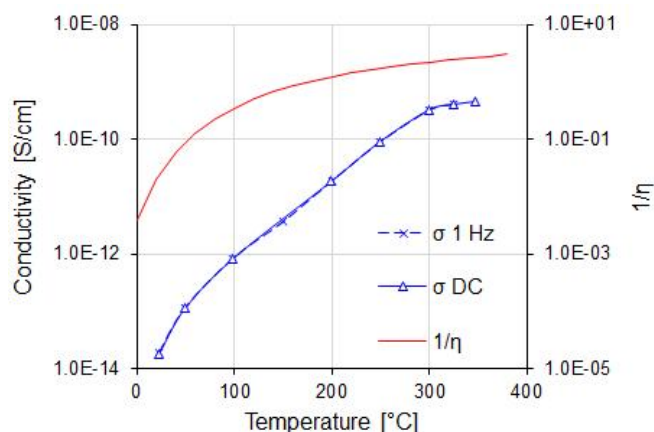
Fig 2.25 - Conductivity of DBT versus temperature at various frequency

Fig 2.26 shows the Arrhenius plot for the product $\sigma \times \eta$, versus temperature from RT to 350°C. This plot shows that the ion density with temperature increases with an activation energy of 0.273 eV, comparable that of SE (0.217 eV).
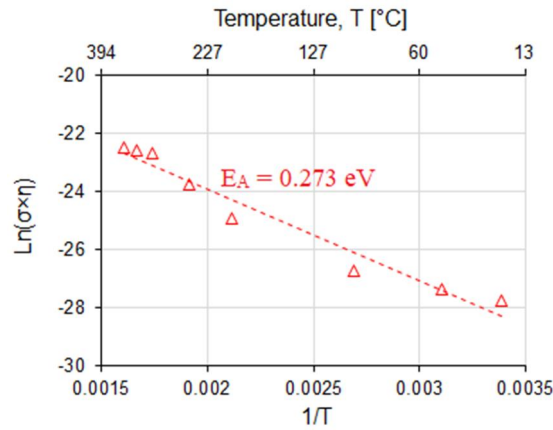
Fig 2.26 - Arrhenius plot for product of conductivity and viscosity of DBT versus temperature

2.2.6   Thermal stability of DBT

As mentioned in the technical datasheet, the operating temperature of Jarytherm® DBT ranges from 0°C up to 350°C under atmospheric pressure. During several temperature cycles up to 350°C where the pressure of N_2 inside the testcell was kept constant at 100 kPa, the conductivity remained rather stable.
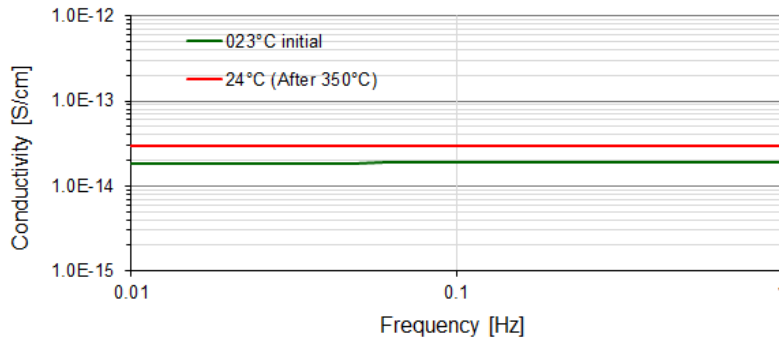
Fig 2.27 - Conductivity of DBT initial and final conditions after exposed to 350°C

Fig 2.27 shows the conductivity comparison at room temperature in the initial measurement (new liquid), and after several experimental cycles up to 350°C. The conductivity shows a slight increase from 1.89×10^{-14} S/cm up to 2.98×10^{-14} S/cm. Other properties such as relative permittivity, tan (delta) and capacitance also exhibit similar behaviour as shown in TABLE 2.2. Of course, extensive complementary measurements should be done to fully assess the long term ageing properties of DBT, including tests carried out in contact with various metals and polymers, such as in standard ageing tests for power transformers. It is also clear that the use of DBT at high temperature in air should be avoided, to supress the risk of fire (fire point: 230°C, self-ignition point: 500°C), and also to limit oxidation that would lead to rapid ageing.

TABLE 2.2 - Dielectric properties of DBT at initial and final condition at 1 Hz

Condition	Permittivity	Tan (Delta)	Conductivity [S/cm]	Capacitance [nF]
Initial	2.67	2.08×10^{-4}	1.89×10^{-14}	63.2
Final	2.66	3.97×10^{-4}	2.98×10^{-14}	63.1

2.2.7   Comparison among dielectric liquids and silicone gel

Similar measurements of conductivity and dielectric spectroscopy were carried out in the other liquids investigated, and are presented in Fig 2.28. The comparison was also carried out among liquid candidates and silicone gel, which is widely used as encapsulant. Silicone gel in this comparison was SILGARD[TM] 527 [82], a product of Dow Corning.
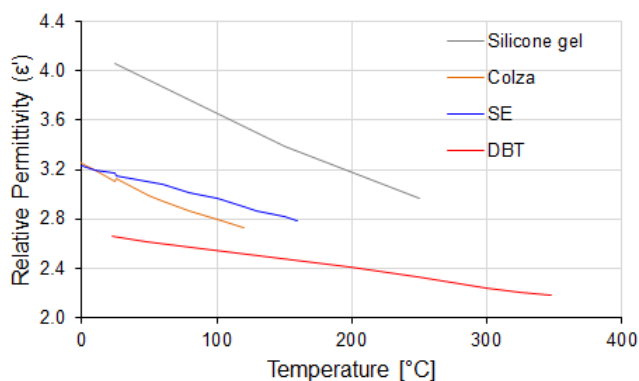
Fig 2.28 - Relative permittivity comparison at 20-60 Hz

Fig 2.28 shows dielectric constant comparison for dielectric liquids and silicone gel, averaged from 20-60 Hz. As the common knowledge, dielectric constant decreases with temperature, except with colza at low temperatures (i.e. when it becomes a gel). From RT to the highest temperatures reached in the measurements, the lowest to the highest dielectric constant are in DBT, Colza, SE and Silicone gel.

Conductivity at high temperature varies as in Fig 2.29. Silicone gel is the lowest between 100°C to 250°C. Conductivity of silicone gel appeared to be stable from RT to 150°C. Nevertheless, it cannot be used above 200°C for long time operation. DBT shows a lower conductivity compared to SE and Colza. A very low conductivity of SE occurs at temperatures < 25°C, when it transforms into a solid-like structure.
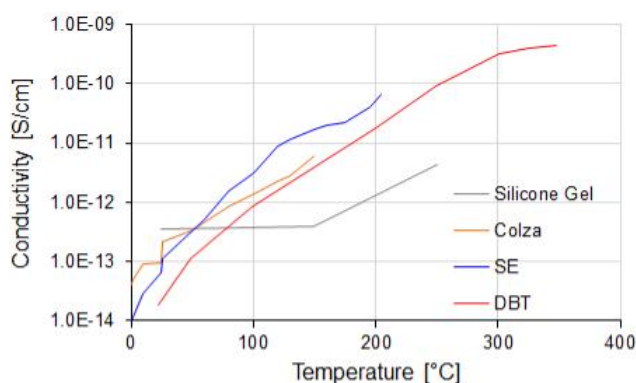
Fig 2.29 - Conductivity comparison at 20-60 Hz

Tan (delta) at 20-60 Hz exhibits similar behaviour as conductivity as shown in Fig 2.30. In this frequency range, tan (delta) of SE is the highest.
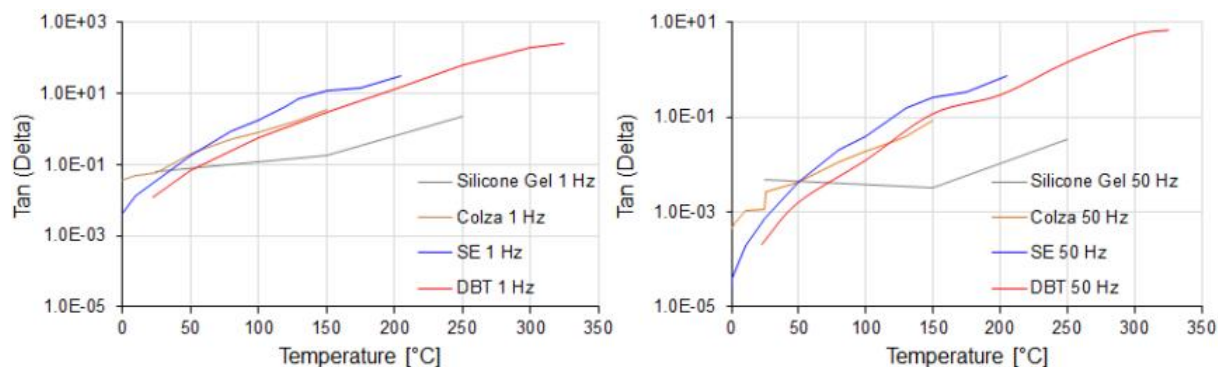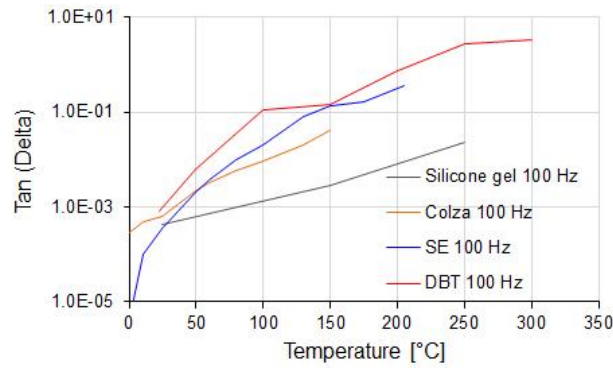
Fig 2.30 - Tan (Delta) comparison at 1 Hz, 50 Hz and 100 Hz

Fig 2.31 shows the comparison of Arrhenius plots of the product of conductivity (at low frequency i.e. 1 Hz) and kinematic viscosity of dielectric liquids. SE and DBT show comparable properties on this plot.
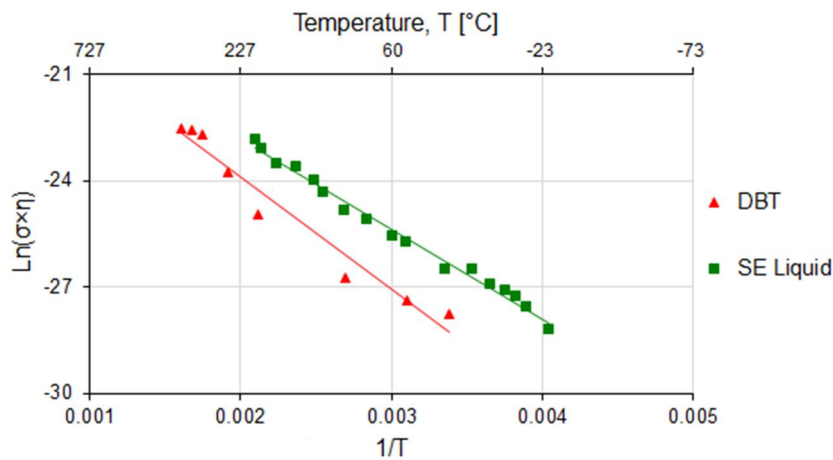
Fig 2.31 - Activation energy comparison from product of conductivity and viscosity

2.3   Ion mobility estimation at low electric fields

In addition to conductivity and spectroscopy measurements, some attempts were done in order to estimate charge mobility and its variation with temperature. The variation of mobility with temperature is a key process to better understand conductivity and spectroscopy measurements. Investigations were done using the same testcell, although it appeared later that the structure of this testcell is not optimal for such measurements, due to the presence of temperature gradients induced by the heating system. We will report here the mobility measurements carried out, and discuss their validity.

There are two basic techniques to measure ion mobility in liquids: single polarity method and reversal polarity method. Both methods consider the time of flight (TOF) (also known as "transit time") at which the current reaches the peak under step voltage, to study the ion migration in the liquid bulk. The TOF method is extremely dependent on pre-conditioning before the applied voltage, such as previous applied voltage polarity and amplitude, liquid rest time, and applied voltage time interval. Reversal polarity method to measure the ion mobility is considered to be more independent on pre-conditioning [83], and displays a clearer transient peak current after the polarity reversal. The reproducibility and repeatability of polarity reversal method is favoured when the applied periods are consistent and longer than the current stabilization time at thermal equilibrium. However, the first half cycle always show unique characteristics.

Interpreting current profiles especially at high temperature with a low uniform electric field in highly insulating liquid is a complex question. Conditions have to be set in experiments such as:

- The applied voltage should not be lower than that of electrochemical polarisation voltage at electrodes (~ 500 mV), and also must not exceed the electrohydrodynamic (EHD) enhanced conduction voltage threshold (this would enhance ion mobility to $> 10^{-7}$ m^2/V·s);
- Sufficiently low electric field (~1 kV/cm) shall be applied to minimize charge-carrier generation either in the bulk (via field-enhanced dissociation) and/or at the electrodes (via interface injection).
- For high temperature (HT) measurements, thermal equilibrium must be obtained to minimize the natural thermal convection flow that would contribute to enhance the measured ion mobility.

It is always difficult to clearly distinguish between the contribution of ions within the liquid bulk (residual conduction), and ions created at the electrodes (injection), which mostly occur simultaneously [84].

The principle of liquid ion mobility measurement requires that voltage is reversed in a short time to minimize charge elimination at recombination dominant regime, and electrodes polarisation forming double layers. Week ion injection can exist in hydrocarbons even at low applied field (e.g. 20 V/mm) in liquids with resistivity lower than 2×10^{14} Ωm.

Time of flight of ions can be derived by the shape of the current profile. At low applied voltage, the current is characterised by an initial conduction current decreasing with time. Fig 2.32a shows the transit time of ions obtained by extrapolating the transient current to zero [85]. At higher applied voltage, the current is characterised by an initial current followed by a peak. The time at which the current reaches the peak is referred to time of flight (TOF). However, these two description of transit time from the current profile may lead to discrepancies since the determination of current slope at low applied voltage may suffer from large uncertainty.
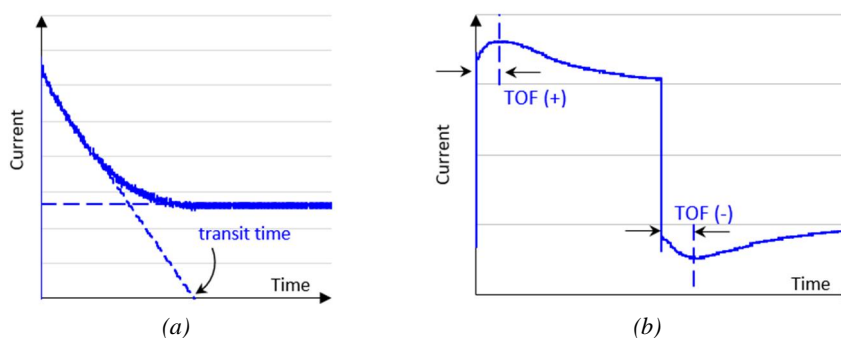
Fig 2.32 - Current profile of ion mobility measurements: (a) low applied voltage, and (b) high applied voltage

Free electrons almost do not exist in the dielectric liquids except from the impurities. When temperature is elevated, density drops allowing greater separation space between molecules, allowing swifter drift of charge-carriers. Separation of ion pairs is subjected to electric field intensity. Positive ions require less energy to escape from the pairs in the direction of the field. Measurement of transient currents under step voltage at high-field [86] on a pure hydrocarbon (cyclohexane) suggested particular current profiles to differentiate between dominant mechanisms: bulk dissociation (Fig 2.32a) and injection (Fig 2.32b).

When the applied DC voltage is sufficiently low to not create injection in nonpolar or weekly-polar liquids, the ions in the bulk migrate according to the dissociation and recombination processes. Ionic drift velocity (v_{drift}) which results from the ion mobility (μ) under electric field (E) the can expressed as:

$$v_{drift} = \mu \cdot E \qquad (2.19)$$

With a specific separation distance (d) between electrodes the time interval between field application to current peak (time of flight TOF), can be calculated as:

$$v_{drift} = \frac{d}{TOF} \tag{2.20}$$

Thus, ionic mobility is then obtained by measuring the time of flight (TOF) as:

$$\mu = \frac{v_{drift}}{E} = \frac{d}{TOF \cdot E} = \frac{d^2}{TOF \cdot V_{applied}} \tag{2.21}$$

Where the electric field strength $E = V_{applied}/d$.

2.3.1 Experimental set up

Low electric field conduction and ion mobility measurements used the same experimental set up: low electric field testcell and heating system as in Fig 2.2, programmable DC voltage generator and current measurement system (Keithley 6517B Electrometer), high resolution data logger system (temperature and current), and a data acquisition system as shown in Fig 2.33.

Keithley 6517B has an internal DC voltage source with two ranges (100V and 1000V) with settling time < 8 ms and < 50 ms each [87]. The corresponding applied DC time was set longer than the estimated TOF with 5 cycles at each ± DC voltage cycle. The data logger time resolution was set from 1 to 10 seconds according to the applied voltage and estimated TOF.

For low electric field experiments, the applied ± DC voltages were 1, 2, 5, 10, 20, 50, 100, 200, 500 V from room temperature (25°C) to 200°C. Applied voltage (> ±500 Vdc) and temperature (> 200°C) conditions were limited by the time resolution of recording system.
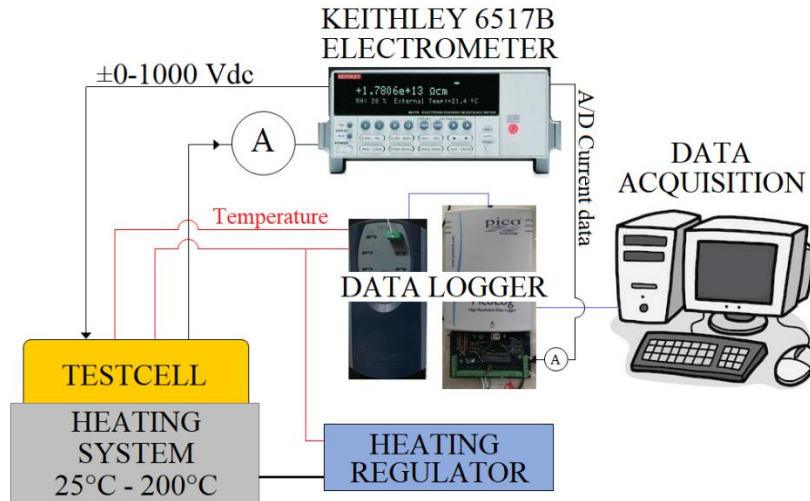
Fig 2.33 - Ion mobility experimental set up

2.3.2 Low applied voltage range: ± 10V

Current profiles include two peaks in the current profile as shown in Fig 2.34: initial transient current (charging current), and time of flight peak current (further referred as peak current).

At lower applied voltage, charging current appears before the peak current and still can be clearly observed up to ± 200 V (i.e. 57 V/mm) at 25°C, and depends on the capacitance and polarity reversal features (amplitude and rise time).
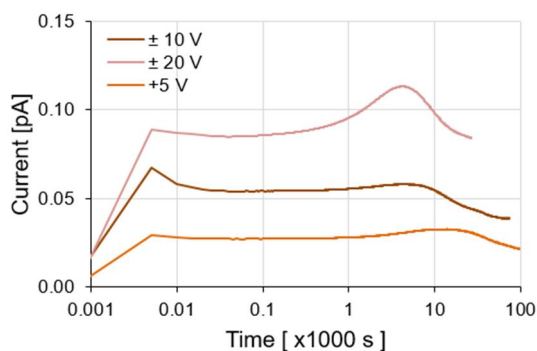
Fig 2.34 - Positive polarity current profile for lower applied voltage range measurement at 25°C

Fig 2.35 shows typical current measurements for applied voltage +1 V (0.286 V/mm) and +2 V (0.571 kV/mm) at 100°C. Current profiles show a monotonous decline up to a stationary value. Peak value occurs instantaneously after the polarity reversal. Transit time of ions is tentatively obtained by extrapolating the transient current slope to intercept the time axis as show by the dash line.
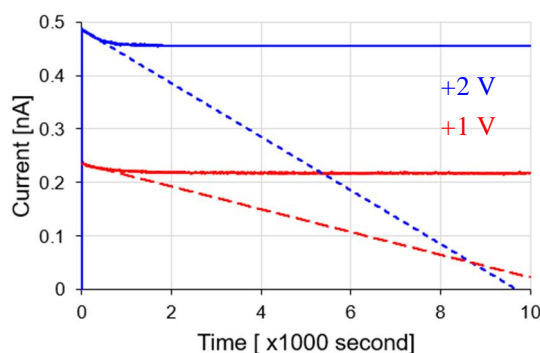
Fig 2.35 - Positive polarity current measurement at 100°C

However, this method was inapplicable for applied voltage less than ±5 V (1.43 V/mm) at 150°C. Both current profiles recorded during negative/positive transition and positive/negative transition are shown in Fig *2.36*. In a purely uniform field, both current profiles should display a similar profile. The asymmetry observed in some measurements probably result from not perfectly uniform field (coaxial cylindrical electrodes are used), and also from the presence of temperature gradients.
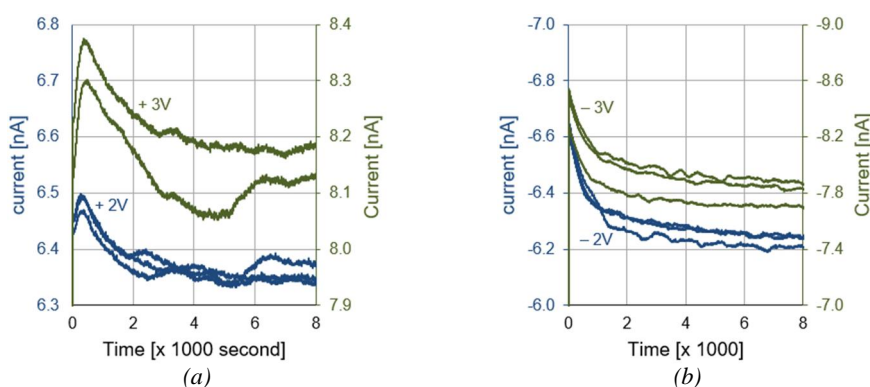
Fig 2.36 - *Current measurement at 150°C: (a) negative/positive transition, (b) positive/negative transition*

2.3.3 Higher applied voltage range (up to ± 1000 V)

The time of flight peak currents are now easily recognized as shown in Fig 2.37. Initial transient current are also observed, with amplitude lower compared to the peak current. The time of flight decreases with the applied voltage, down to about 10s minimum measurable time.
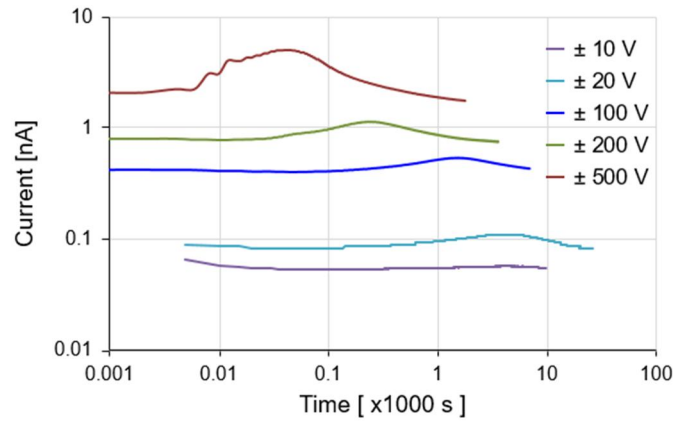
Fig 2.37 - Current profile on higher applied voltage range measurement results at 25°C

At higher applied voltage (> ±700 Vdc), the initial transient current is not any more clearly observed due to insufficient time resolution. Measurements at ± 1000 V 25°C are not any more valid due to excessive capacitive charging current and recording sampling time limitation. The measurement in Fig 2.38 shows unstable peak amplitude measurements, mainly due to insufficient time resolution.
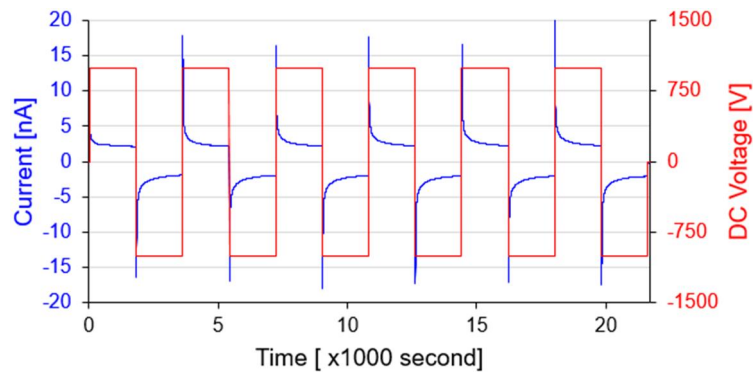
Fig 2.38 - Current and voltage measurement at ± 1000 V 25°C

2.3.3.1   Peak current

Fig 2.39 shows peak current measurements at different polarity and temperature. Red and blue symbols show the positive polarity (i.e. negative/positive voltage transition) and negative (i.e. positive/negative voltage transition) versus temperature (the absolute value of negative peak currents is displayed). Peak currents are identical in both polarities, and proportional to voltage, except with V > 200V and T < 50°C were current increases more rapidly than voltage. Currents show a large sensitivity to temperature (3.5 decades variation from 25 to 200°C).
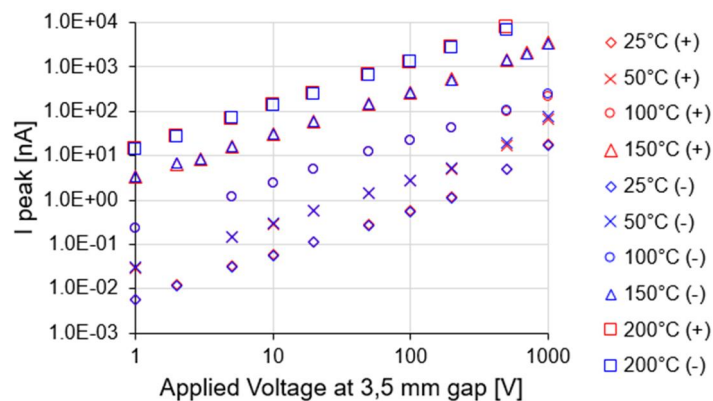
Fig 2.39 - Peak current measurement at different polarity and temperature

2.3.3.2 Stationary current

Fig 2.40 shows quasi-stationary positive and negative currents recorded immediately before voltage transition. Stationary current are also proportional to voltage, and identical in both polarities, indicating an Ohmic behaviour.
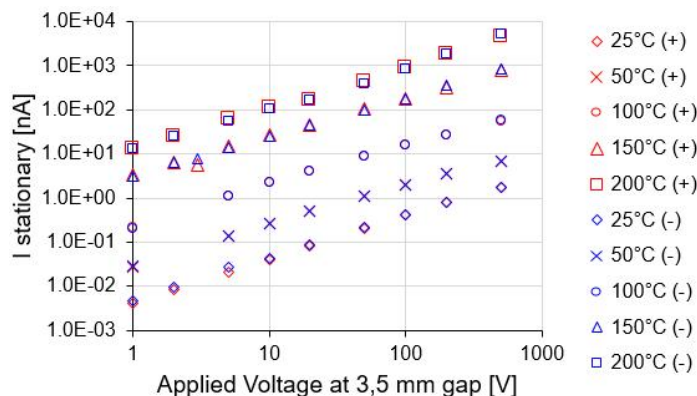
Fig 2.40 - Stationary current measurement at different polarity and temperature

The current decreases after the peak due to complete migration of ion species to the corresponding electrodes. As well as the peak current, the amplitude of positive and negative stationary current are independent from the transit time of ions.

2.3.4 Time of flight measurements and mobility estimation

Fig 2.41 show the time of flight measured at different applied voltage and temperature. At room temperature (25°C), TOF logically decreases as applied voltage increases. TOF for positive and negative polarities logically show no significant differences.

When temperature was increased, TOF measured at low voltage (< 10 V) show erratic behaviour: it either increases with voltage, or show no variation, and large differences between polarities can be seen. At higher voltage (> 20 V) a more logical decrease versus voltage is observed. The erratic behaviour at low voltage (and correspondingly long transit times) very probably comes from the presence of temperature gradients induced by the heating system. Heating is applied to the testcell body, and the outer electrode is at slightly higher temperature. As a consequence, some thermal convection should take place between electrodes, and participate to the charge transport. This effect does not exists at room temperature: no heating is applied, and temperature is uniform.
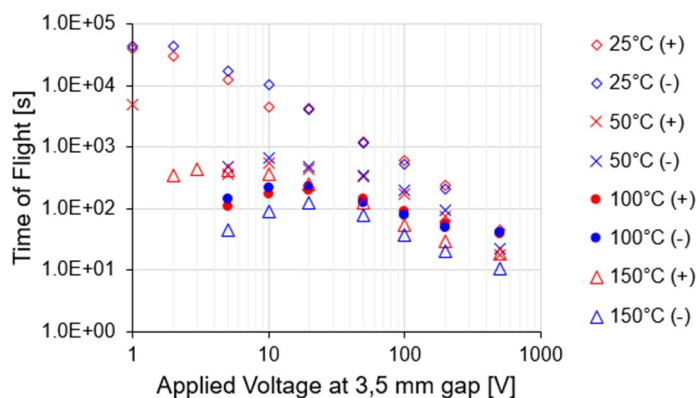
Fig 2.41 - Time of flight as function of applied voltage

At low voltage and with temperature gradients, the influence of thermal convection dominates: the measured peaks are not representative of charge transport by the electric field, which explains that TOF

becomes either independent of field, or show aberrant behaviour. Therefore, with heating only measurements carried out at high enough voltage (> 20V) can be kept for mobility calculation.

Fig 2.42 shows ion mobility as function of applied voltage at different temperatures for valid measurements. Ion mobility is nearly independent from the applied voltage, although some scatter is observed.
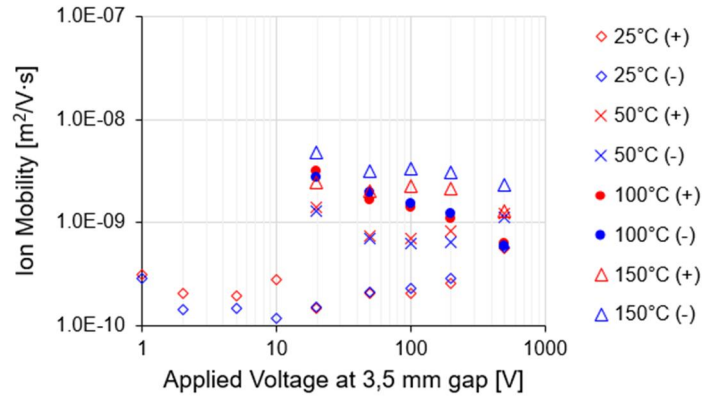
Fig 2.42 - Ion mobility as function of applied voltage

At 150°C, there are significant differences between mobility measured in positive and negative polarity, probably due to some remaining influence of temperature gradients. Ion mobility logically increases with temperature in DBT, which is usually attributed to a reduction of liquid viscosity.
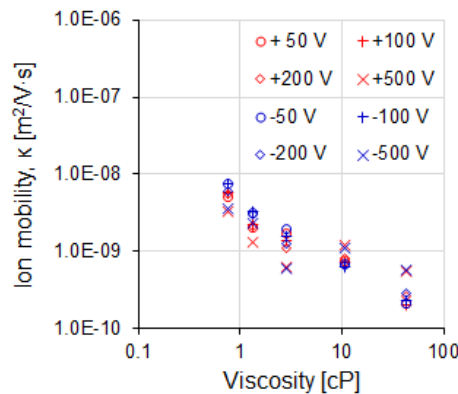
Fig 2.43 - Ion mobility as function of viscosity at different applied voltage

Fig 2.44 show the product of viscosity and ion mobility versus temperature. A better independency to temperature is observed at low voltage, whereas measurements at 500 V show a larger scatter. This could be tentatively attributed to the increasing influence of injection and EHD motion when voltage is raised.

(a)   *(b)*
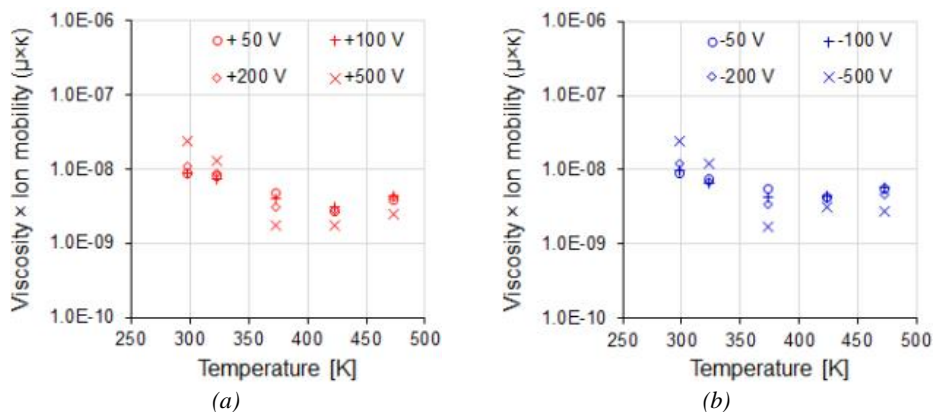
Fig 2.44 - Product of viscosity and ion mobility as function of temperature: (a) positive and (b) negative polarity

2.4 Conclusion

In this chapter, series of low electric field measurements have been carried out to the dielectric liquid candidates. Dielectric properties of DBT, SE and PFPE and silicone gel such as conductivity, relative permittivity and tan (delta) were measured and compared. Especially for DBT, which is the strongest candidate as alternative encapsulant for high temperature power electronics module to replace silicone gel, series of electrical characterisations have been intensively implemented to investigate its performances in high temperature environment. Temperature dependence have been demonstrated i.e. to the permittivity, conduction mechanism and tan (delta). Some part of dielectric properties are both temperature and frequency dependence, other parts may controvert.

Experiment results revealed and elucidated many unknown phenomena at high temperature range for dielectric liquids. Results on DBT also confirmed the high temperature electrical properties stability up to 350°C despite the long-term reliability (ageing due to long-term high temperature exposure) did not perform.

These results are necessary to establish fundamental information concerning the dielectric liquid properties under high temperature environment. Moreover, further research must be performed to fully understand the governing law such as the influence of derivative effect of high temperature and electric field such as the drop of viscosity and electrohydrodynamic, etc.

3 | Dielectric Liquids High Electric Field Characterization at High Temperature

Contents

This chapter presents the continuation of dielectric liquid characterization, with measurements at high electric field. Measurements about AC, DC and impulse breakdowns, partial discharges, and streamers in various liquids, are presented versus the influence of high temperature and different field geometry. In turn, several conclusions concerning thermal stability, PDs suppression, and self-healing properties can be also obtained.

3.1   Breakdown measurements

Breakdown strength constitutes a fundamental dielectric property of insulating material. For high voltage applications, dielectric liquid AC breakdown measurements are carried out using standard test procedures (such as IEC 60156 [88] or ASTM D1816 [89]) to obtain typical values of dielectric strength. They mainly reflect the presence of impurities (particle contaminants, dissolved water and gases), and also the intrinsic characteristics of the liquid. In such measurements carried out in quasi-uniform field (sphere-sphere electrodes), the mean breakdown field is very high (typically around 30 kV/mm), and breakdown is "controlled" by streamer initiation: every streamer initiated will propagate to breakdown, and the measured breakdown voltage represents the voltage required to initiate a streamer.

The proper interpretation of such measurements is usually not simple, because in addition to the liquid nature, many parameters (not always well known or well controlled) can have a large impact on streamer initiation under AC (or DC) voltage: pollution (particles, water), gas bubbles, space charges, electrode surface defects, etc.

This section will present the experimental results obtained on DBT and SE under variation of temperature (up to 350 °C) and pressure (4 kPa to 200 kPa) in order to better characterize breakdown properties when approaching boiling conditions. Since our high temperature testcell is limited to 30 kV, the procedure will be modified as compared to the standard method IEC 60156 [88]: lower gap distance (0.4 mm instead of 2.5 mm), smaller sphere electrodes (10 mm diameter). Measurements will be mostly performed under DC ramp, since AC is not directly relevant for power electronics applications. Since it was not possible to frequently change the liquid sample between breakdown measurements (due to the required time to heat and stabilize the testcell at high temperature, and also to problems with metallic gaskets), a special attention was paid to investigate the influence of breakdown by-products on repetitive measurements.

3.1.1 Experimental set up and procedure under DC ramp

A specific HT testcell (Fig 3.1a) was developed for high voltage characterization of liquids up to 400°C, under nitrogen atmosphere to suppress the risks of fire at elevated temperature and avoid accelerated ageing due to oxidation. Nitrogen pressure can be varied up to 500 kPa. A HV ceramic bushing up to 30 kV is installed at the bottom part of the testcell, and a pair of sphere-sphere electrodes (of diameter 10 mm at 0.40 mm gap separation) are used to measure breakdown voltage (Fig 3.1b).

(a)   (b)
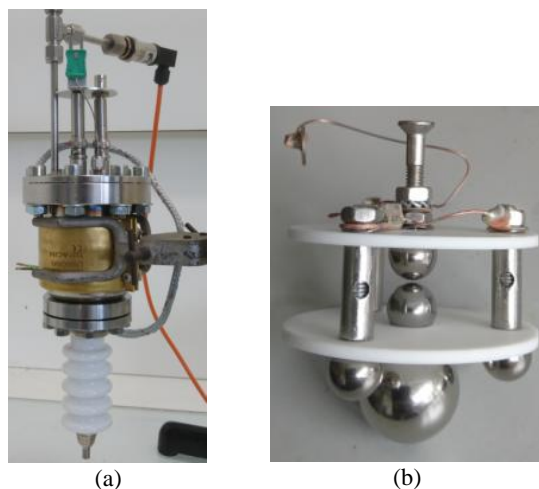
Fig 3.1 - (a) HT and HV testcell and (b) Sphere-sphere electrodes with ceramic insulator support

Ceramic insulators (made of Macor®) and metal gaskets are installed to allow high temperature operation. A metallic heating collar connected to a regulating system is used to increase the testcell temperature, and a thermocouple monitors the temperature of the liquid at a distance about 2 cm from electrodes. Since thermal gradients do exist within the testcell, the actual temperature of liquid between sphere electrodes can be slightly lower than the measured temperature, with an average difference estimated to < 10°C at 300°C.
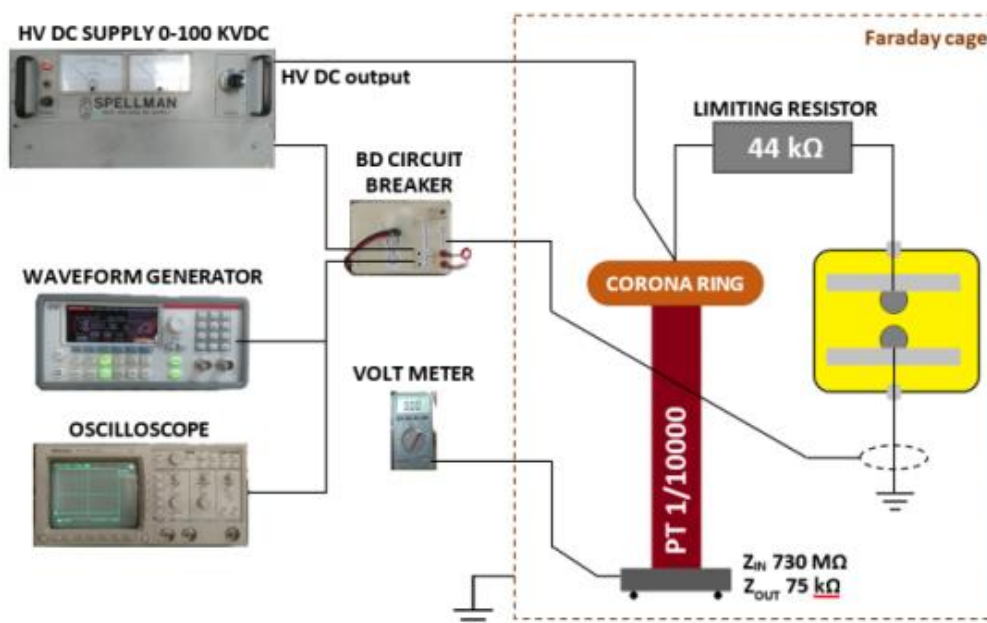
Fig 3.2 - DC breakdown experimental set up with sphere-sphere electrode system

Fig 3.2 shows the DC breakdown experimental set up. A SPELLMAN HV DC Supply 0-100 kV was used as DC generator. Breakdown voltage (BDV) was measured by applying DC voltage ramps of 1 kV/s, until the occurrence of breakdown. After breakdown, the high voltage source was rapidly

switched off (after 1 ms) in order to limit the degradation of the liquid. It took at least 1-minute rest time or the temperature recovered before the next breakdown attempt. A minimum of 20 measurements were taken in each temperature and pressure condition. Similar measurements were also done under AC with a 1 kV/s ramp.

A 44 kΩ limiting resistor was also inserted in series with the testcell to limit the breakdown energy. This breakdown energy is estimated from the testcell capacitance to about 20 mJ at 20 kV. This low energy should induce a low degradation of the liquid at each breakdown. In turn, this allows to carry out measurements series with a rather large number of breakdown measurements (some tens) without changing the liquid, i.e. with a stable liquid condition (water and particle content), provided the liquid degradation by breakdown has a negligible impact on measurements. This is especially important, considering that these factors have a large influence on breakdown voltage under uniform field. The degradation of oil during a series was monitored by measuring periodically the breakdown voltage with fixed conditions (100°C, 100 kPa).

3.1.2   Weibull statistics

Breakdown in dielectrics usually occur in a random manner, and varies even with fixed configuration and material. Therefore, the breakdown voltage (BDV) can be considered as a random variable. Breakdown data series in this work were analysed using two parameters Weibull distribution that takes into account the breakdown voltage and the breakdown frequencies. These two parameters are α (scale parameter) denoting the mean BDV tendency, and β (shape parameter) denoting the uniformity of the distribution. The probability of BDV was then linearized into the fitting of Weibull cumulative distribution function (CDF) to deduce α and β, where the CDF is defined as:

$$P(BDV) = 1 - exp\left[-\left(\frac{BDV}{\alpha}\right)^{\beta}\right] \qquad (3.1)$$

And linearized as

$$ln\left[ln\left(\frac{1}{1-P(BDV)}\right)\right] = \beta \cdot ln(BDV) - \beta \cdot ln(\alpha) \qquad (3.2)$$

Dielectric liquids were presumed not to age during breakdown test series, and this was verified experimentally. A minimum of 20 breakdown data were taken in each series with fixed conditions to obtain a sufficient accuracy of breakdown voltage estimation.

3.1.3   AC and DC breakdown in dibenzyltoluene DBT

3.1.3.1   DC Breakdown measurements at room temperature (RT)

At room temperature, a large scatter of measurements and rather poor reproducibility of measurements were observed. Fig 3.3 shows two examples of 20 consecutive BDV measurements during breakdown series DBT-1, taken with new liquid (initial), and after 35 breakdowns. First series (green line) includes two solid green dots, indicating that no breakdown occurred up to 30 kV. The second series after 35 breakdown (red line) shows a much larger scatter, with frequent low values (< 5 kV) attributable to breakdown by-products (presumably carbon particles) remaining for a long time between electrodes.

During breakdown measurements at RT, liquid was in still condition (no forced motion was applied, and no convection due to temperature gradients occurred). The electrohydrodynamic motion (EHD) due to voltage application is the only cause that may induce some fluid flow. At temperatures ≥ 100°C, the onset of EHD motion was clearly detected above some critical voltage threshold. When EHD sets on, the measured temperature of the liquid suddenly dropped by a few °C, due to the mixing of the liquid at slightly different temperatures (some temperature gradient exists within the testcell). At room temperature, this phenomenon was not detected (temperature is uniform). The large scatter observed on

breakdown measurements at 20°C is supposed to be due to decomposition by-products remaining between electrodes during repeated measurements, due to the large liquid viscosity (50 mm^2/s at 20°C). This scatter was also observed even when rest time between measurements was increased to 2 minutes.
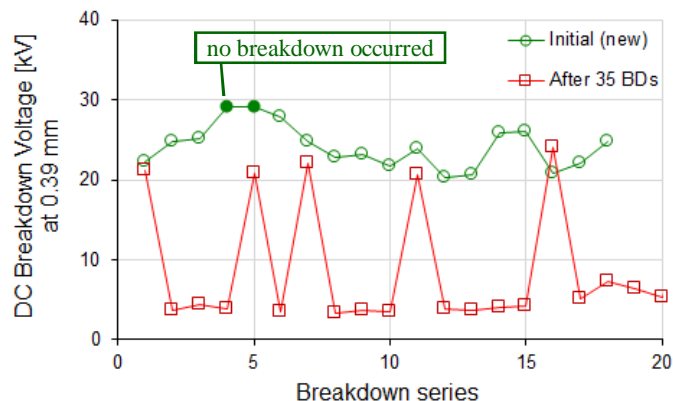
Fig 3.3 - DC BDV at RT (20°C) during initial measurement series with new DBT liquid and after 35 breakdown occurrences

Fig 3.4 shows that the distribution of the initial DC BDV measurements is regular with mean breakdown voltage of approx. 25 kV, while that recorded after 35 breakdown seems composed of two superposed distributions. The largest values measured after 35 breakdowns (above 20 kV) are consistent with those of the new liquid, while the lowest (about 5 kV) are probably due to the deleterious influence of by-products remaining in the gap.
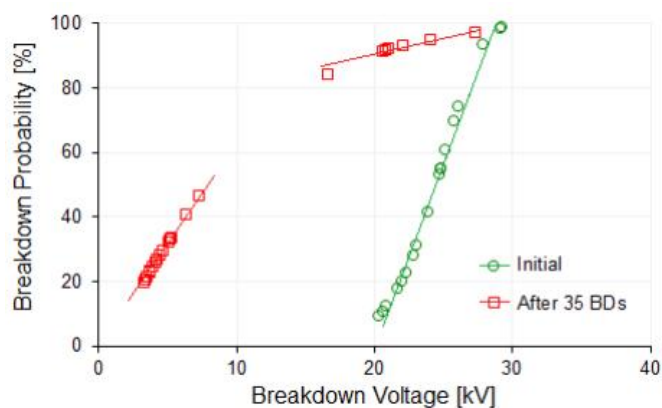
Fig 3.4 - Breakdown probability of DC BDV measurements at RT in DBT

DC breakdown field of DBT at room temperature (62 kV/mm) is rather high when compared to typical values recorded under AC in 1 mm gap (ASTM D1816 standard method) in mineral oils (58 kV/mm), or in synthetic ester (53 kV/mm) [90].

3.1.3.2 DC Breakdown measurements at 100°C

At 100°C, the kinematic viscosity decreases to 2.8 mm^2/s and thermal convection takes place, due to temperature gradients induced by the heating system. In addition, while voltage ramps are applied, the onset of EHD is clearly observed (by the corresponding slight drop of temperature) at voltage threshold about 7.2 kV, i.e. well below breakdown. The time between two successive measurements was at least 2 minutes.

Fig 3.5 shows DC BDV measurements at 100°C, taken at different moments during the long series DBT-2. This series was carried out with a single liquid sample without opening the testcell, and involved more than 355 breakdown tests at different temperatures from 20 to 350°C. At 100°C, the scatter is considerably reduced, even when measurements were done at the end of the measurement series, i.e. after up to 355 breakdown events. Due to the lower viscosity and much more intense liquid motion,

breakdown by-products are rapidly expelled by convection and EHD movements. No significant decrease of the breakdown voltage at 100°C occurred after up to 355 breakdowns, indicating a good stability of the liquid condition during measurements. This is mostly due to the low breakdown energy.

During the different measurement series carried out, measurements at 100°C were thus taken as reference tests, in order to check periodically the oil condition. One main advantage of doing numerous low-energy measurements with a single oil sample in a closed testcell is that the oil condition can be kept strictly constant, while temperature and pressure are changed. Changing the liquid during measurements would induce doubts about the results obtained, since it is very difficult to ensure a constant liquid condition in terms of pollution (particle and water content).
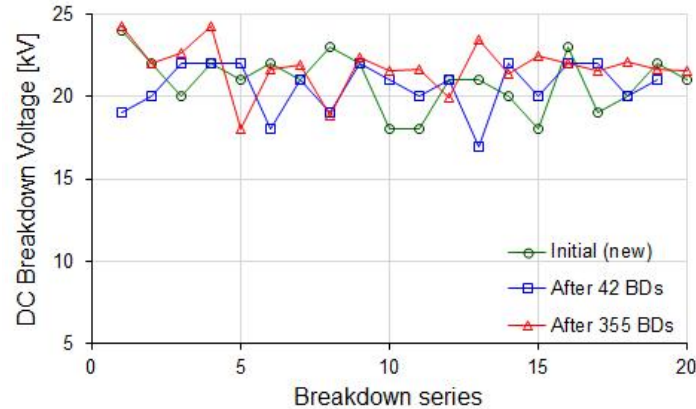
Fig 3.5 - DC BDV measurements at 100°C, 0.1 MPa

3.1.3.3   AC and DC Breakdown measurements versus temperature

Fig 3.6 shows breakdown probability in DBT at various temperature under constant pressure (100 kPa), obtained during series DBT-2, i.e. without changing the liquid. DC breakdown measurements were made in the order of 100°C, 200°C, 300°C, 20°C, 300°C, 350°C and 100°C. Sphere-sphere gap distance was 0.39 mm. Due to the electrode geometry (Fig 3.1b), a negligible influence of temperature on the gap distance can be expected (variation estimated to 0.4µm), since stainless steel spacers and electrodes had the same thermal expansion coefficient (16.10^{-6} K^{-1}).
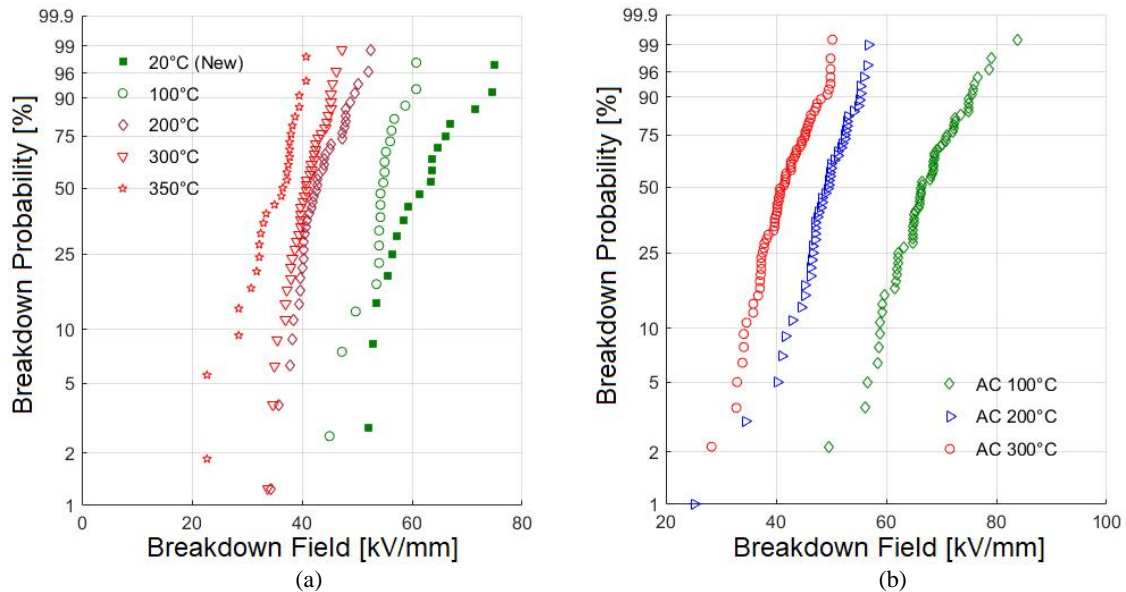
Fig 3.6 - Breakdown probability in DBT under temperature variation at 100 kPa: (a) DC and (b) AC. Initial water content was 13 ppm.

Mean DC BDVs and electric field strength in DBT under various temperature are shown in TABLE 3.1 with data distribution in Fig 3.6a. The initial water content of DBT before breakdown tests was 13 ppm.

TABLE 3.1 - DBT mean DC breakdown voltage and field at various temperature calculated by Weibull's parameter

Temp. [°C]	DC BDV [kV]	DC BDF [kV/mm]
20	23.4	65.0
100	21.5	60.3
200	18.0	51.1
300	16.9	44.7
350	14.8	37.2

Statistical analysis (see TABLE 3.2) shows that the mean DC BDV decreases with temperature, from mean breakdown value $\alpha = 23.4$ kV at 100°C, down to 14.8 kV at 350°C. The average breakdown voltage at 350°C dropped to 58.2% of the initial value at 20°C in Fig 3.4. The scatter also markedly increased: some breakdowns may occur at voltage lower than 10 kV, whereas measurements at 100°C were always higher than 16 kV.

TABLE 3.2 - Descriptive statistics and Weibull's fitting parameters of DC BDV at various temperature under 100 kPa

Temp. [°C]	Descriptive statistics				Weibull parameter	
	Mean	Median	Mode	Variance	α	β
20	24.2	24.3	24.8	7.5	23.4	10.5
100	19.5	19.8	20.4	6.1	21.5	16.5
200	16.6	16.4	15.9	1.5	18.0	16.1
300	16.3	16.3	15.9	1.8	16.9	13.9
350	14.0	14.6	15.1	2.9	14.8	9.2

Fig 3.7 shows the probability density function of DC BDV in DBT at various temperature under 100 kPa. Probability of mean breakdown (33.1%) is relatively high at 100°C with less scatter. As the temperature increased, the probability of mean breakdown dropped to 23% at 350°C as well as mean DC BDV. At elevated temperature, the breakdown voltage are more scattered.
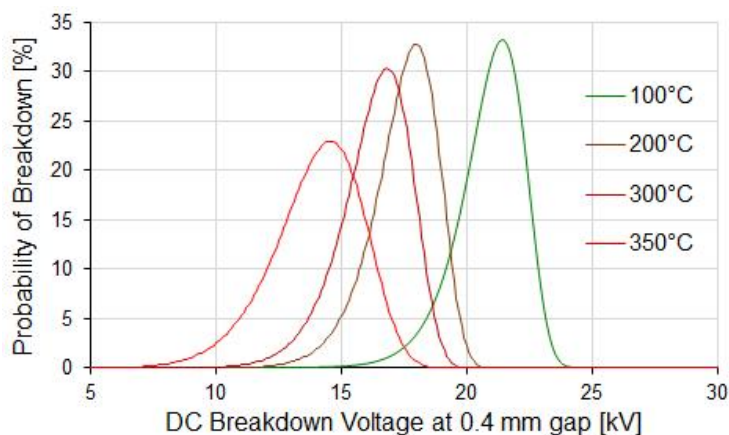
Fig 3.7 - Probability density function (PDF) of DC BDV at various temperature under 100 kPa

For AC breakdowns, measurements were made in the order of 50°C, 100°C, 150°C, 200°C, 250°C and 300°C. Sphere-sphere electrodes gap distance were 0.43 mm. Mean AC BDVs and electric field strength in DBT under various temperature are shown in TABLE 3.3 with measurement data distribution in Fig 3.6b. The initial water content of DBT before breakdown tests was 13 ppm.

TABLE 3.3 - DBT mean AC breakdown voltage and field at various temperature

Temp. [°C]	AC BDV [kV]	AC BDF [kV/mm]
100	33.0	76.7
200	22.4	52.1
300	19.9	46.3

3.1.3.4   Breakdown measurements versus pressure

Fig 3.8 shows DC breakdown probability in DBT at two fixed temperatures (200°C and 250°C) under various pressure. Vapour pressure (P_{Vap}) at 200°C and 250°C are 0.6 kPa and 3.9 kPa. For fixed temperature (200°C), a decrease of mean DC BDV was recorded when pressure P was reduced, from about 18.7 kV at 200 kPa (i.e. 333 x P_{Vap}) down to 13.6 kV at 5 kPa (i.e. 8.3 x P_{Vap}), see Fig 3.8a. The resolution of pressure measurement was about 1.0 kPa. Below 1.0 kPa, (i.e. close to boiling conditions when $P \approx P_{Vap}$), a marked change occurred, with a large drop of breakdown voltage (green star marks), and a very large scatter of measurements. The wide range of breakdown voltages (2.8 kV-14.3 kV) certainly results from the presence of permanent vapour bubbles in the liquid, explaining the lowest values recorded.
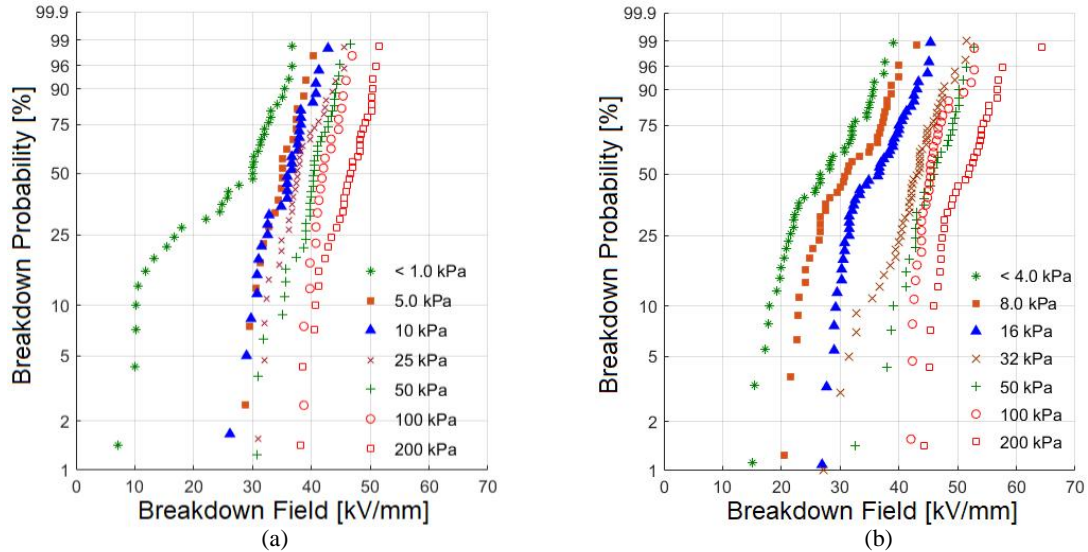
Fig 3.8 - DC breakdown probability in DBT under N₂ pressure variation at fixed temperature: (a) 200°C and (b) 250°C

The same results are obtained at fixed temperature of 250°C. Mean DC BDV dropped from 20.8 kV at 200 kPa (51 x P_{Vap}) to 11.6 kV at 4 kPa (1.0 x P_{Vap}). At 250°C when the pressure was equal to P_{Vap} (i.e. in near boiling conditions considering a 10°C uncertainty on the measured temperature), the DC BDV scattered from 5.9 kV to 15.2 kV, see Fig 3.8b.

TABLE 3.4 - Descriptive statistics and Weibull's fitting parameters of DC BDV in DBT at 200°C at various pressure

Pressure [kPa]	Descriptive statistic				Weibull Parameter	
	Mean	Median	Mode	Variance	α	β
< 1.0	10.0	11.7	11.7	13.2	11.4	2.6
5.0	13.6	13.7	13.7	1.6	14.1	12.9
10	13.9	14.2	14	2.5	14.6	10.4
25	14.8	14.7	12.5	2.4	15.5	11.6
50	15.6	15.8	15.2	2.1	16.3	12.7
100	16.5	16.4	15.1	0.9	17.0	20.8
200	18.0	18.2	18.8	2.1	18.7	15.1

TABLE 3.5 - Descriptive statistics and Weibull's fitting parameters of DC BDV in DBT at 250°C at various pressure

Pressure [kPa]	Descriptive statistic				Weibull Parameter	
	Mean	Median	Mode	Variance	α	β
<4.0	10.6	10.4	10.4	6.9	11.6	4.7
8.0	12.2	12.1	10.4	5.8	13.2	6.0
15	14.0	14.3	12.3	4.3	14.9	8.1
33	16.5	16.9	17.0	4.1	17.39	9.4
50	17.7	17.9	16.7	3.0	18.5	12.1
100	17.9	17.7	17.1	1.4	18.5	17.6
200	20.1	20.2	18.4	3.1	20.8	13.7

TABLE 3.4 and TABLE 3.5 show the corresponding statistical parameters. The large BDV scatter at 200°C under pressure much lower than P_{Vap} (<1.0 kPa) corresponds to the large statistical variance of 13.2, compared to 6.7 at 250°C. As the pressure increases above P_{Vap}, the BDV variance declines with a minimum value at atmospheric pressure.

3.1.3.5   Discussion of results

Fig 3.9 shows DC BDV in DBT at two fixed temperatures, versus pressure normalized to the value of P_{Vap} at the corresponding temperature. At 1.0 per unit of P_{Vap}, BDV at 200°C and 250°C are nearly equal. Later, as the pressure rises above P_{Vap}, BDV increases at slightly different rates.
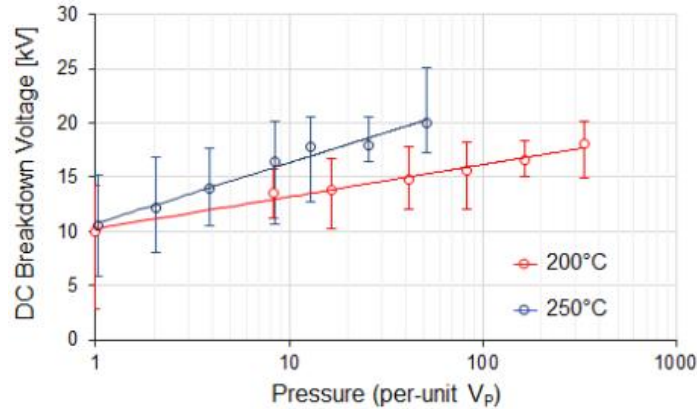
Fig 3.9 - DC BDV in DBT at fixed temperature (200°C and 250°C) versus pressure (in per unit P_{Vap})

A tentative unified explanation for the reduction of breakdown voltage versus temperature and pressure is as follows. When DBT is in the liquid state in (T, P) conditions (i.e. above the equilibrium line of Fig 2.5), a temperature increase $\Delta T = T_{boil}(P) - T$ is required to boil the liquid (with $T_{boil}(P)$: boiling temperature at pressure P). ΔT decreases when either T is increased, or P decreased. The energy required to induce the appearance of vapour bubbles ($C_p \Delta T$ + vaporisation enthalpy), which constitutes one of the basic physical processes involved in the development or pre-breakdown streamers [91], is hence facilitated.

$$\Delta T = T_{boil}(P) - T \qquad (3.3)$$
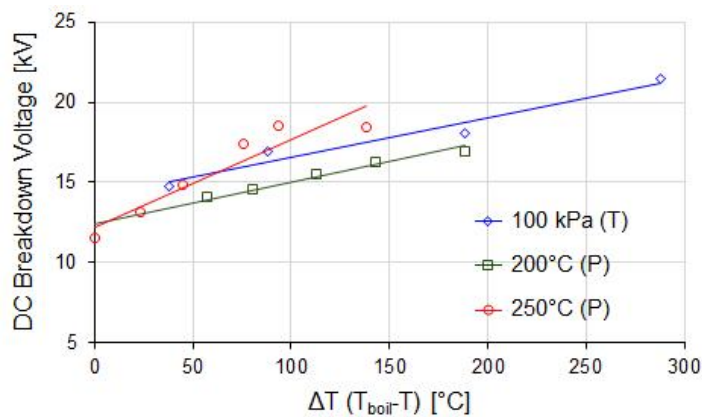
Fig 3.10 - DC BDV in DBT versus temperature difference at fixed temperature and fixed pressure condition

The plot of data obtained by changing either temperature at constant pressure, or pressure at constant temperature, **versus** ΔT is shown in Fig 3.10. The data obtained in rather different conditions tend to group together, although some discrepancy is observed. Several conclusions can be derived from these results. In addition to the effect of temperature on boiling conditions, several other parameters that may be involved in the pre-breakdown processes also change: large variation of viscosity (2 decades), and

hence of EHD motion, very large change in conductivity (3 decades), modification of density and permittivity, change of saturation level of water (not yet characterized in DBT).

In Fig 3.10 an almost equivalent effect is observed when either temperature or pressure are changed, which tends to validate the hypothesis of an influence of temperature mainly linked to the boiling process. Other parameters also affected by temperature but not by pressure (i.e. viscosity, conductivity, density, permittivity, water equilibrium) should be of secondary importance in the breakdown process:

In the next section about streamers, we will observe directly the influence of temperature on streamer initiation.

3.1.4 AC and DC breakdown measurements in synthetic ester SE

Breakdown measurements in synthetic ester Midel® (SE) were carried out at 100°C, 200°C and 250°C under 100 kPa of N_2. Fig 3.11 shown the AC and DC breakdown probability in SE. For AC breakdowns, the probabilities at 100°C and 200°C are scattered and overlap. The mean AC BDV (TABLE 3.6) indicates no significant difference between 100°C and 200°C. At 250°C, AC BDV drops to 81% at 25 kV.
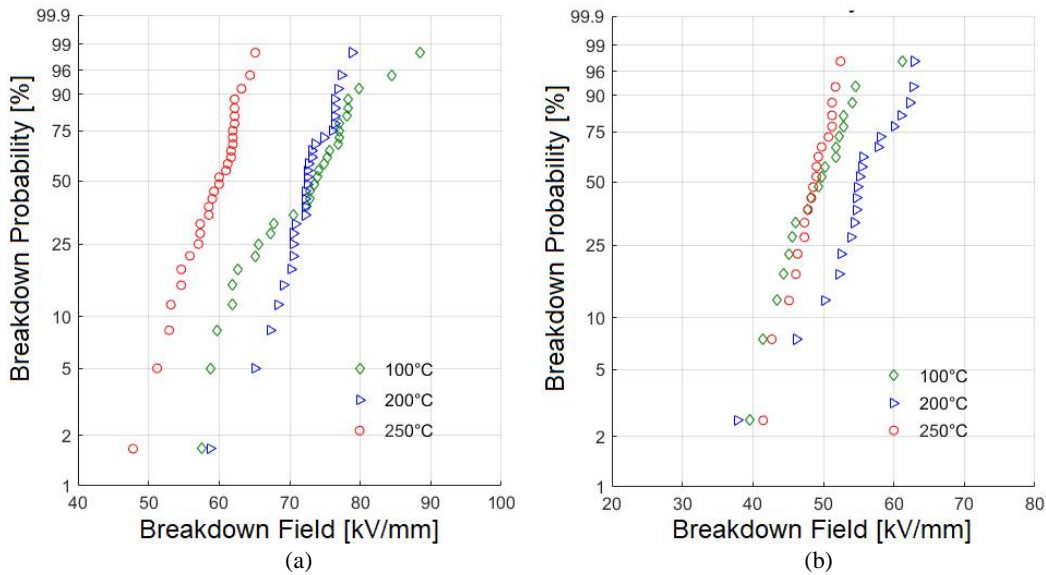
Fig 3.11 - Breakdown probability in SE under temperature variation at 100 kPa N₂: (a) AC and (b) DC breakdowns

For DC breakdowns, the probability at 100°C and 250°C are scattered and overlap. The mean DC BDV (as in TABLE 3.6) indicates no significant difference between 100°C and 250°C. AC BDV at 200°C seems higher by 15%. Before the occurrence of breakdown under DC, a strong EHD motion was observed, indicated by the unstable temperature reading. The EHD onset voltage decreases as the temperature increases.

The reason why DC BDV at 200°C is slightly higher is not clear. The general comparison between AC and DC BDV over all temperatures indicates that AC BDV is always higher than DC BDV. In contrast, values were much less different in DBT.

TABLE 3.6 - Mean AC and DC BDV in SE at gap distance 0.40 mm and 100 kPa

Temperature [°C]	Mean AC BDV [kV]	Mean DC BDV [kV]	DC EHD [kV]
100	30.9	20.8	12.5
200	30.7	23.8	8.2
250	25.0	20.4	6.5

3.1.5   Summary on breakdown measurements in Jarytherm® DBT and Midel®

Fig 3.12 shows mean breakdown strength of liquid samples at high temperatures (up to 300°C for DBT and 250°C for SE) are above 35 kV/mm, which constitutes the acceptance condition for transformers of all voltage class, either in new equipment or after filling apparatus on-site. The corresponding standards are IEEE Std. C57.106-2015 [92] for mineral oil and IEEE Std. C57.147-2018 [93] for Natural Ester. At 350°C, the breakdown strength of DBT is 37.2 kV/mm for DC and 27.1 kV/mm for AC, which is still in the range of acceptance condition for voltage class ≤ 69 kV.

(a)   (b)
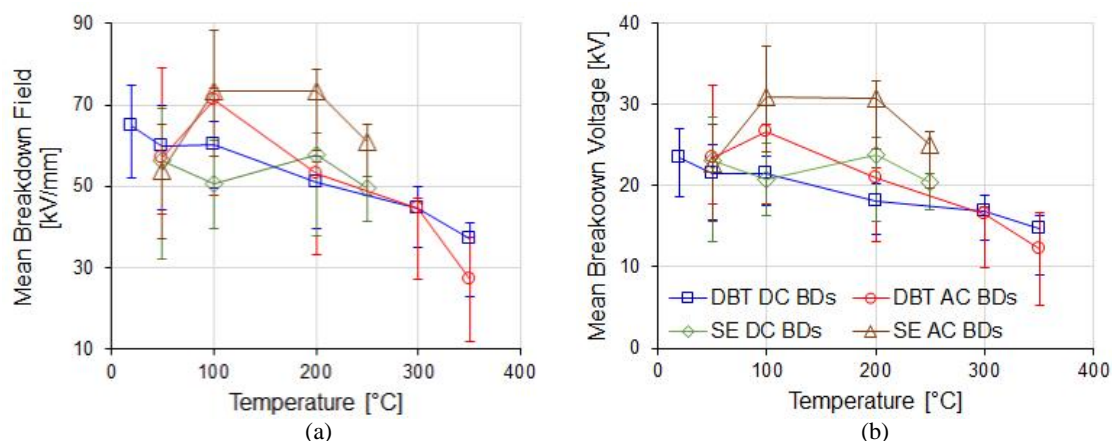
Fig 3.12 - Comparison of liquids breakdown versus temperature: (a) mean breakdown field and (b) mean breakdown voltage

The AC BDV of SE is higher than DBT while DC BDV of these two liquids are competing at certain temperature. The properties of DBT remained rather stable after the thermal cycles and series of breakdown tests carried out in this study (Fig 3.13), even though some evidence of chemical ageing existed (change of colour, turning from transparent to light yellow).

(a)   (b)

Fig 3.13 - DBT appearance: (a) new condition and (b) after measurement at 350°C

AC and DC breakdown measurements on DBT indicated a large dielectric strength above 60 kV/mm between 20°C-100°C, exceeding those usually measured in other liquids such as mineral oil or esters. When temperature is raised at atmospheric pressure, the breakdown field gradually decreases. At the highest temperature investigated (350 °C), the mean breakdown field is reduced to about 58% of its initial value at 20°C, and the scatter of measurements also increases. Breakdown at low value (down to 10 kV/mm) may sometimes occur in these conditions close to boiling conditions. At 300 °C, minimum values were around 30 kV/mm.

Altogether, these measurements with Jarytherm® DBT, previously unknown as dielectric liquid, show that this liquid has rather high dielectric strength, with a prospective usable temperature up to 300°C with reasonable safety margin, far exceeding the limits of standard liquids (mineral oils, esters). The low vapour pressure of DBT over a wide temperature range is another advantage for a simple packaging (no large pressure rises at high temperatures). Some favourable indications about its thermal stability regarding dielectric properties were also obtained, but should be confirmed by complementary ageing

investigations. For its primary use (heat transfer), a maximum temperature of 350°C in industrial applications is indicated by the manufacturer.

This liquid constitutes an excellent solution for short-term laboratory testing of high voltage and high temperature devices, such as ceramic substrates studied in the following.

3.2   Partial discharges measurements

Partial discharge characterization of materials is important for applications, since it indicates practical maximum limits in terms of electric field or voltage, and also shows how the material resists to deterioration. Most of time, partial discharge tests are done in arrangements typical for a particular application (e.g. winding samples for transformers or rotating machines). Partial discharges (PDs) addresses localized dielectric breakdown phenomena, indicating the high electric field withstand ability of dielectric. In dielectric liquids, PDs usually start in high field regions such as sharp electrode edges, boundary of dielectric materials (triple-points), etc. In the case of alternative encapsulants for high temperature and high voltage power module applications, it has been observed that PDs occur at the sharp edges of metallisation, where the electric field is very divergent, and close to the triple-point region. Therefore, liquids will be first investigated using a point-plane geometry, which also creates a highly divergent field. In the next chapter, PDs will be also checked with a real substrate geometry (triple-point).

The actual voltage present in power electronics modules is composed of DC and impulses with fast rise. It is unfortunately very difficult (or even impossible) to measure PDs with such waveform, due to the large current spike induced by impulse voltage. In the followings, we will therefore use the conventional 50 Hz AC voltage to detect and measure PDs with a high sensitivity.

3.2.1   Experimental set up and procedure

Two dielectric liquids were used for PD measurements: Jarytherm® DBT and Midel® 7131 Synthetic Ester (SE). The average water content of DBT prior to experiments at initial new condition was 13 ppm and 72 ppm in SE. Since saturation limit of SE is 2700 ppm, this corresponded to 2.7% from saturation at room temperature. Saturation level of DBT is unknown.

Fig 3.14 shows the partial discharge experimental set up. During measurements, it unfortunately appeared that the high voltage and high temperature testcell developed for breakdown measurements could not be used for PD measurements. Although its ceramic bushing can be used up to 30 kV, PDs due to this bushing were observed above 14 kV at RT when filled with DBT (Fig 3.15). This limit was acceptable for PD measurements with substrates presented in the next chapter, but not sufficient for PD measurements in the liquid alone with point-plane geometry. Therefore, these measurements were carried out with another testcell (Fig 3.16a) in open air, and limited to 100°C (Fig 3.16b). Point tip radius of curvature was 2.0 µm (Fig 3.16c), and point-plane distance 10 mm. This alternative testcell allowed carrying out PD measurements up to 25 kV.

PD measurements were carried out with a Phase Resolved Partial Discharge (PRPD) analyser (Power Diagnostix[TM] ICM system). HV supply was provided by a PD-free transformer fed by a low-noise and low-distortion power amplifier. A careful shielding of all components (including the heating circuit system, temperature sensors, etc.) allowed reducing the noise level of PD measurements to a very low value about 0.1 pC. PD measurements were calibrated using a standard 5 pC calibrator. To avoid recording noise, the rejection level of PDs was fixed to 0.2 pC. The PDs number, charge, phase position, and average current were recorded during periods of 1-minute duration under constant voltage. Series of 10 PD recordings of 1-minute duration were obtained at each applied voltage and temperature.
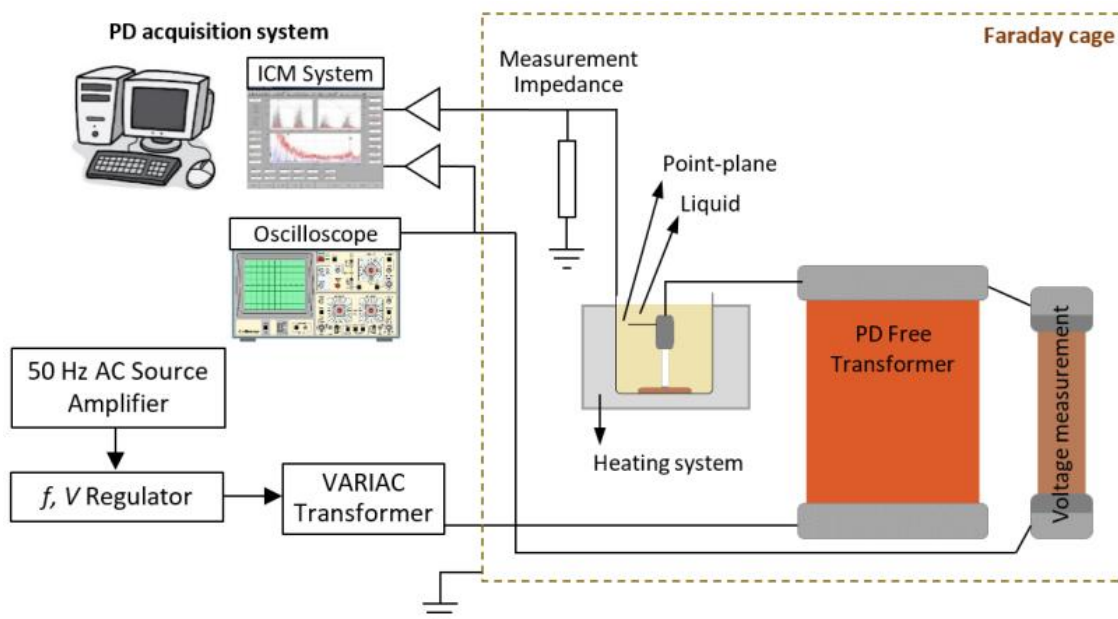
Fig 3.14 - Partial discharge experimental set up: point-plane electrodes system
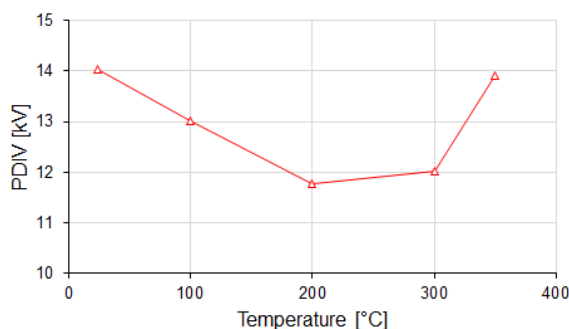
Fig 3.15 - PDIV of the high temperature testcell filled with DBT at various temperature

| (a) | (b) | (c) |
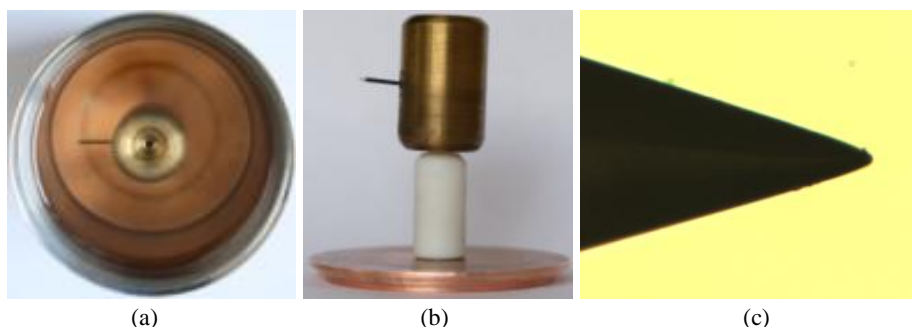
Fig 3.16 - Point-plane electrode system: (a) open testcell, (b) point electrode with support and (c) microscopic view of point with radius 2 µm

In the following, PDIV values were derived from plots of PD count versus voltage. Since no clear PD extinction threshold could be observed at low voltage, PDIV was arbitrarily defined as the voltage producing 10 PDs (of either polarity) per minute. This PD number (10) was chosen since it lead to an acceptable statistical significance of the corresponding voltage, during 1 minute duration tests. In plots, the PDIV presented corresponds to the mean values of 10 measurements.

3.2.2 Partial discharges in Jarytherm® DBT

Typical PRPD recordings in DBT under open-air (23°C) at atmospheric pressure are shown in Fig 3.17. PDIV of DBT at room temperature (RT) is 15 kV. In this liquid, most of discharges occurred at negative polarity, even when voltage was raised well above PDIV. Figures a-d correspond to applied voltage of 15, 16, 17 and 19 kV. Both the discharge number and amplitude increase as the applied voltage goes up.

Negative discharges with very low amplitude (less than 5 pC) accumulate around the voltage peak (approx. 270° phase angle). Very few small positive discharges were also detected, starting from 20 kV (< 5 discharges count/minute and < 1.1 pC). These measurements are quite similar to those already obtained in Jarylec® C101 [45], which chemical composition is close to Jarytherm® DBT (mixture of mono and di-benzyltoluene isomers). In DBT, this behaviour is observed over a large voltage range, from 15 to 25 kV in our measurements. This shows the exceptional good properties of liquids of the benzyltoluene family, producing PDs of very small amplitudes. In contrast, in many other liquids such as esters, mineral oils, or silicon oils, large positive PDs up to several nC in amplitude appear in the same conditions [45]. This explains why benzyltoluene liquids (Jarylec® C101) are used in impregnated capacitors, where PD inception is a key parameter for reliability.
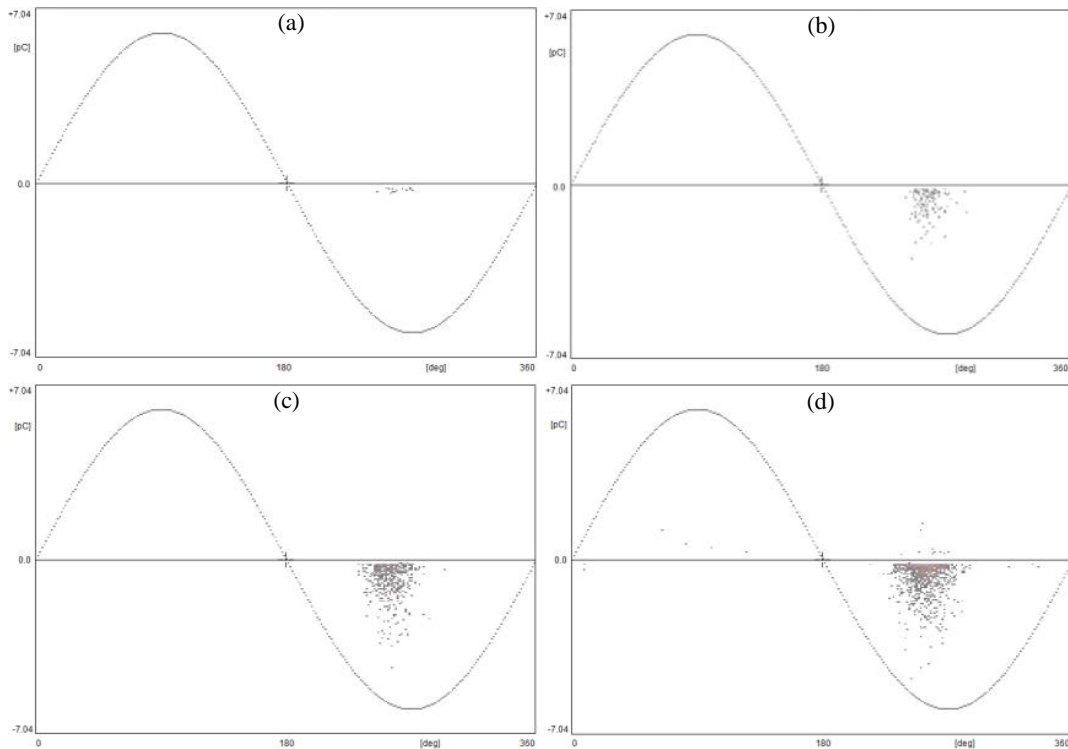
Fig 3.17 - Typical PRPD pattern in DBT at room temperature 23°C for applied voltage: (a) 15 kV, (b) 16 kV, (c) 17 kV and (d) 19 kV

From PD recordings, an "equivalent PD current" I_{PD} can be computed, by summing all recorded PD amplitudes over a period of time (1 minute in the present measurements). Each series of applied voltage with fixed temperature was taken 10 times. PDs count and PDs charge amplitude were taken from ICMsystem statistics panel as in Fig 3.18. These value and calculated PDs current were averaged from 10 records and then presented as mean PDs current, mean PDs count with maximum and minimum range.
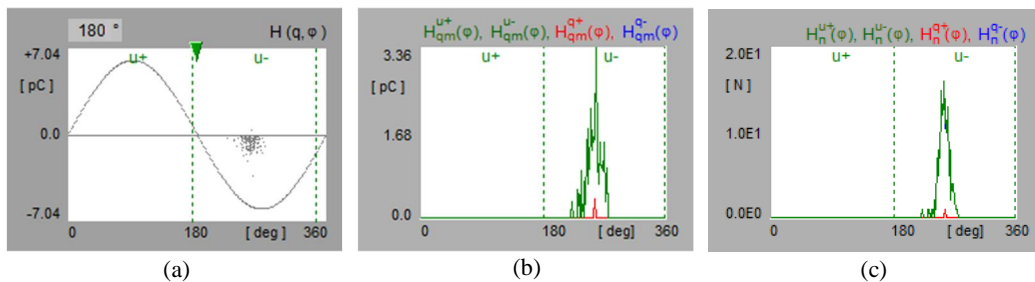
Fig 3.18 - ICMsystem statistics panel for 15 kV-rms in DBT at RT (a) PRPD pattern, (b) PD charges amplitude and (c) PD numbers count

When the temperature is raised, the discharge number decreases, and then PDIV (defined as the voltage producing 10 discharges /minute) increases with temperature. Fig 3.19 shows typical PRPD patterns at RT and 80°C for V = 20 kV, i.e. slightly above PDIV. PDIV at 80°C is 19 kV (i.e. 127% of PDIV at RT) as also shown in Fig 3.21a. The mean charge and number of PDs recorded during 1-minute in DBT at various temperatures are shown in Fig 3.20. Total negative discharges counts drops significantly from 1664 discharges/minute at RT to 17 at 80°C, with mean charge between -1.4 pC to -0.9 pC, and PD current I_{PD} = 24 pA to 0.12 pA. The same behaviour on positive discharges was also observed at high temperature. At 80°C, positive discharges were hardly detected (< 10 discharges count/ minute) throughout the applied voltage range up to 25 kV.
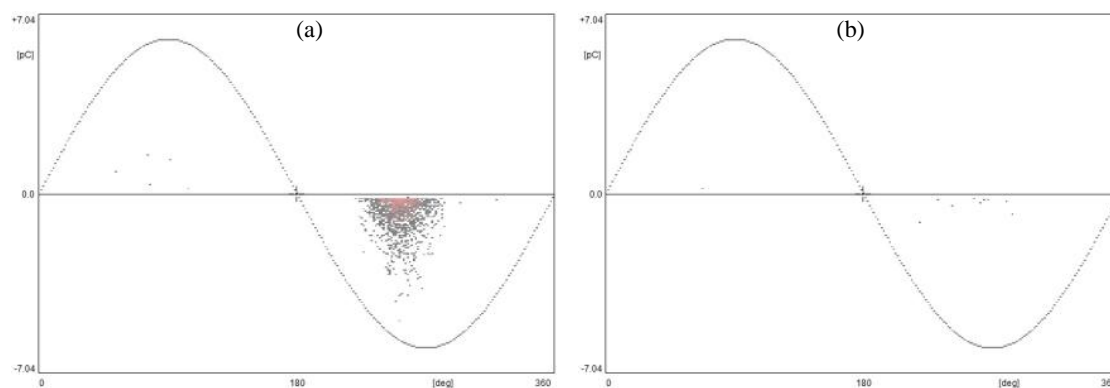
Fig 3.19 - Typical PRPD pattern in DBT for applied voltage 20 kV at: (a) room temperature 23°C and (b) 80°C

At 100°C, for applied voltage 25-28 kV, extremely few negative discharges occurred (< 5 discharges count). Hence, we concluded that at 100°C the PDIV might exceed 28 kV. Measuring PDs at higher temperatures in DBT would therefore require a quite complex high temperature testcell, PD free at voltages well in excess of 30 kV. Building such device was out of the objective of the present study.
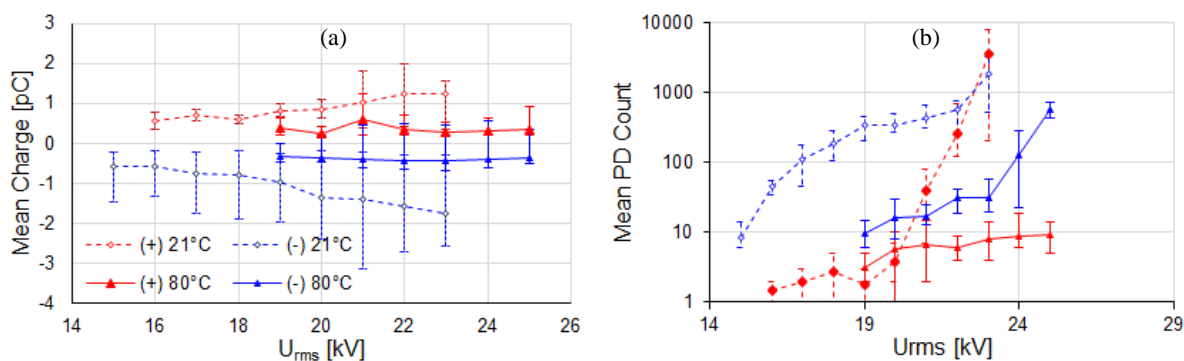
Fig 3.20 - Positive and negative discharges at 21°C and 80°C in DBT: (a) mean PDs charge and (b) PDs count per minute

Fig 3.21 also shows that no "inception threshold" for PDs can be observed at low voltage: the PD count regularly decreases down to very low values. It is therefore impossible to define an "absolute" PDIV value, that is why we used an arbitrary criterion (10 PDs/minute) to define PDIV.

As previously discussed in [45], small negative and positive PDs, a few pC in amplitude, correspond to slow "1st mode" streamers that does not propagate far in the liquid. Large positive PDs (not observed here) correspond to faster and longer "2nd mode" streamers. The fact that no large positive PDs were recorded indicates that the inception of "2nd mode" positive streamers under AC voltage in DBT occurs at higher voltage compared to other liquids.

These measurements shows that temperature has a significant impact to suppress PDs, both in discharges number and amplitude.
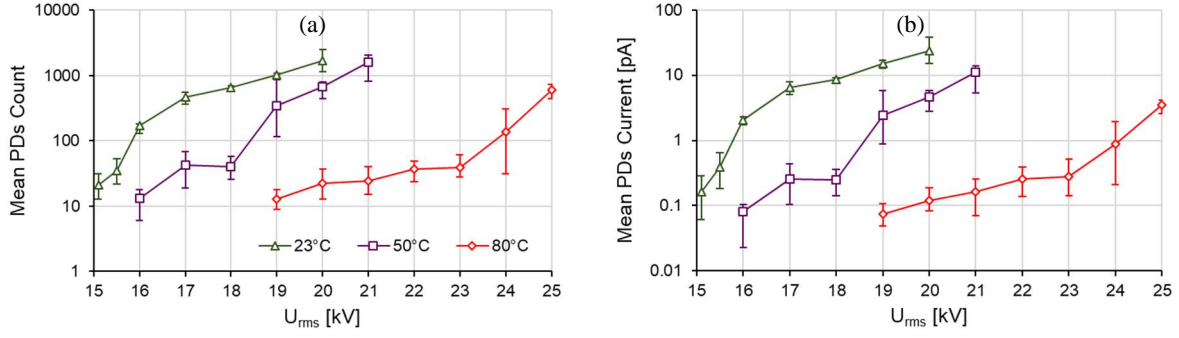
Fig 3.21 - Discharges in DBT at various temperature as function of applied voltage: (a) mean PDs count and (b) mean PDs current

3.2.3   Comparison between breakdown and PD measurement results in DBT

The fact that the breakdown voltage of DBT in uniform field decreases with temperature (Fig 3.6) seems in contradiction with the PDIV increase with temperature (Fig 3.21a). This comes from the rather different conditions existing in both experiments.
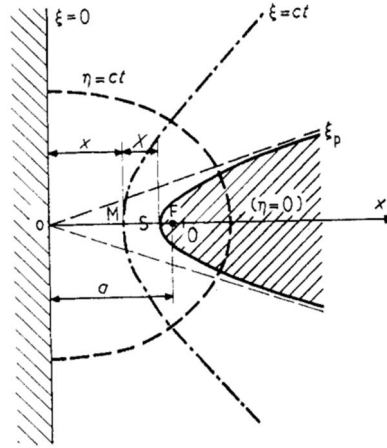
Fig 3.22 - Representation of a point-plane configuration with various quantities involved.
Note: $x + X + r/2 = a$ or $u + v + p = 1$ [94]

Under uniform field, the field at which breakdown (i.e. streamers) occur is in the range of 70 to 30 kV/mm (see Fig 3.12). In point-plane gap, the maximum tip field can be calculated from PDIV measurements with the formula proposed by Coelho and Debeau [94]. The electric field $E(X)$ at a distance from the tip as in Fig 3.22 can be calculated by the following equations:

$$E(X) = \frac{a \cdot V}{ln\left\{2\left(\frac{a}{r}\right)^{\frac{1}{2}}\right\} \cdot [X(2a-X)+(a-X)r]}$$

(3.4)

The maximum electric field (E_{max}) on the tip is then simply expressed by

$$E_{max} = \frac{V}{r \cdot ln\left\{2 \cdot \left(\frac{a}{r}\right)^{\frac{1}{2}}\right\}}$$

(3.5)

and the electric field at the plane $X = a - r/2$

$$E_{plane} = \frac{V}{a \cdot ln\left\{2 \cdot \left(\frac{a}{r}\right)^{\frac{1}{2}}\right\}}$$

(3.6)

Where V is the applied voltage, r is the point radius of curvature, and a is the distance between the middle point of needle tip and the plane electrode. Gap distance between point-plane (g) can be expressed as $a = g - r/2$.

Fig 3.23 shows field strength calculation (peak value) on the tip with 2 µm point radius of curvature at PDIV, based on eq. 3.5. The calculated field strength on the tip is very high, and varies in DBT from 2.3 MV/mm (RT) to 3.8 MV/mm (100°C), and from 2.5 MV/mm (RT) to 2.2 MV/mm (100°C) in SE.
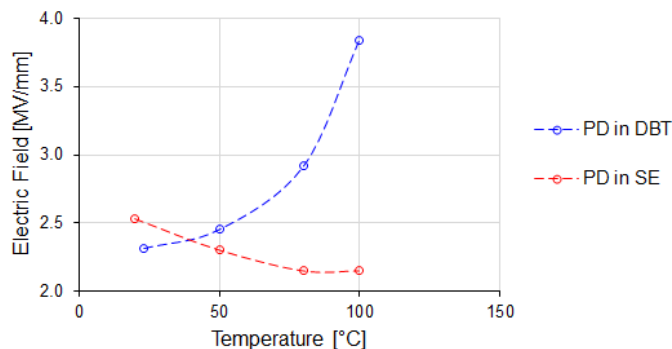
Fig 3.23 - Electric field calculation on the tip from PDIV measurements with 2 µm radius of curvature

Under uniform field, it is known that a mean field of 30 kV/mm is unable to directly induce streamers in the liquid. It is generally considered that "defects" producing local field enhancement are responsible for discharge initiation: electrode surface defect, charged solid particles with permittivity and conductivity larger than the liquid. In point-plane, the very high tip field is able to inducing directly streamers in the liquid. Under AC voltage, the influence of injected space charges (ions) prior to PD inception may also have an influence, but a much larger effect can be expected under point-plane gap, since the field is very divergent and of very high value, promoting injection and reducing the actual tip field.
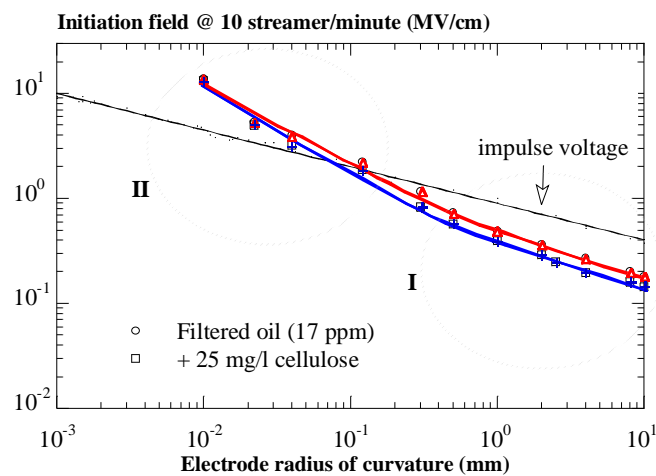
Fig 3.24 - Calculated streamer initiation tip field under AC (at 10 streamers/minute) versus electrode radius, and comparison with measurements under impulse voltage. Filtered mineral oil, and polluted with 25 mg/l cellulose (17 ppm water content) [95]

The influence of space charge on streamer inception under ac in point-plane geometry was already evidenced in mineral oil [95], by comparison with impulse voltage (Fig 3.24) where the influence of space charge is nearly absent (injected ions have no time to move away from the electrode during the impulse rise time < 1 µs). In moderately divergent field (region I in Fig 3.24), streamer inception fields under ac are logically lower than with impulse, since time duration of voltage is much longer. This is observed up to field values about 100kV/mm in mineral oil. Conversely, with sharp points (region II in Fig 3.24) calculated AC initiation fields become larger compared to impulses, and this can be only explained by the influence of injected space charge. Calculated fields without influence of space charge overestimate the field, compared to the field actually present at the point under AC.

Fig 3.25 shows a comparison of calculated maximum PD inception field (point-plane geometry, eq. 3.5), with AC and DC breakdown field (uniform geometry) versus temperature in DBT. PD inception field is calculated according to peak value of PDIV since PDs occur near the AC peak voltage. AC breakdown field in uniform geometry is calculated with reference to its peak value at 0.43 mm gap.
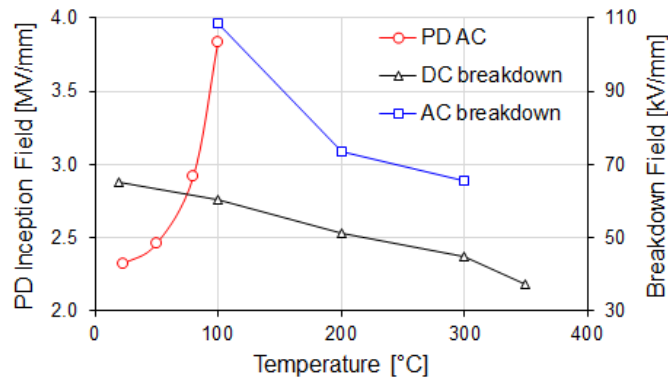
Fig 3.25 - Comparison of calculated PD inception field, AC and DC breakdowns versus temperature in DBT

Calculated AC PD fields at RT with $r_p = 2\,\mu m$ are about 40x larger than breakdown fields with $r_p = 5$ mm, i.e. a difference comparable to mineral oil in similar conditions (Fig 3.24). PD field rapidly increases with temperature whereas breakdown field slightly decreases over the same temperature range. This difference is supposed to be due to space charge injection with sharp point (tip field > 1 MV/mm), whereas space charge should have a minor influence at fields < 0.07MV/mm. The temperature can strongly promote and enhance the influence of space charges, by enhancing charge injection processes, and strongly increasing charge mobility. A study of streamer inception under impulse voltage described in next sections will confirm this hypothesis.

3.2.4   PRPD Patterns in Midel® (SE)

Fig 3.26 shows the typical PRPD pattern in SE at 21°C RT under open-air atmospheric pressure. PDs pattern in SE is totally different from that of DBT. With high detection sensitivity (±13.9 pC scale in Fig 3.26a), negative discharges with much higher amplitude as in DBT are observed. However, if sensitivity is reduced (down to ±1.39 nC in Fig 3.26c), high amplitude positive discharges are also observed in SE, and not in DBT. Negative PDs observed when voltage is positive on Fig 3.26 (black arrows) are instrumental artefacts: large positive PDs saturate the measurement system, and false recorded signals correspond to oscillating overshoots (red arrows). Observation of PDs in SE requires two widely different sensitivities to properly record positive and negative discharges, which amplitudes differ by a factor about x1000.
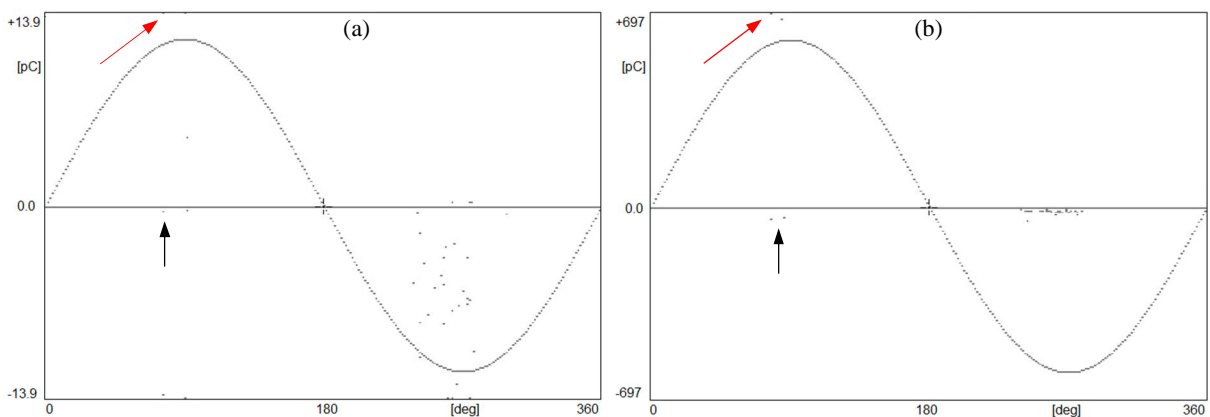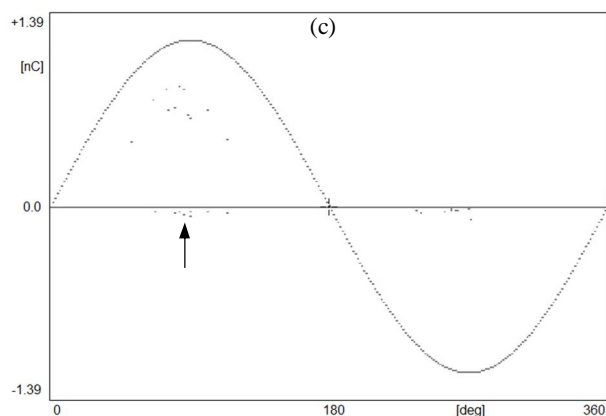
Fig 3.26 - Typical PRPD pattern in SE at room temperature 21°C for applied voltage: (a) 16.5 kV (±13.9 pC scale), (b) 18 kV (±697 pC scale) and (c) 19 kV (±1.39 nC scale)

Fig 3.27 shows typical PRPD patterns for constant applied voltage 17 kV, at RT and 80°C, recorded with high sensitivity (a) to detect negative PDs and low sensitivity (b) to properly observe large positive PDs. Their number and amplitude increases when temperature is raised (up to maximum 2.8 nC at 80°C). The corresponding PDIV of large discharges (at 10 PDs /minute) decreases with temperature. Negative discharges are not properly seen here due to low detection sensitivity.
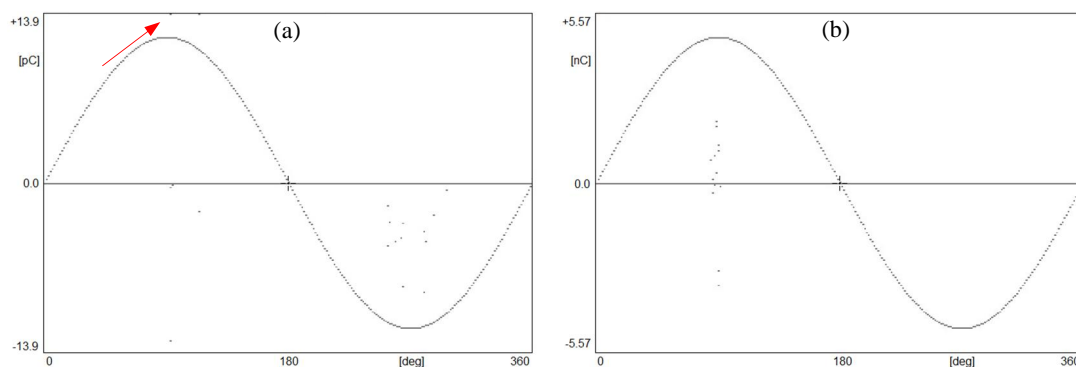
Fig 3.27 - Typical PRPD pattern in SE for applied voltage 17 kV at: (a) room temperature 21°C, max. scale ±13.9 pC; and (b) 80°C, max. scale ±5.57 nC.

PD data extracted from such measurements show the amplitude and count of large positive discharges (Fig 3.28a). Their amplitude and number are promoted by temperature (Fig 3.28b). If the PDIV of each polarity is quoted according to the same definition of 10 PDs/minute, positive PDIV is constantly higher than negative.
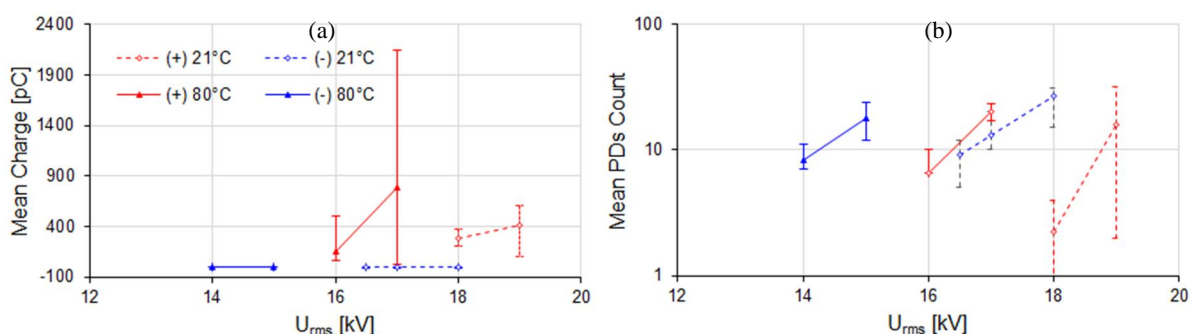
Fig 3.28 - Positive and negative discharges at 21°C (±697 pC scale for positive and ±13.9 pC scale for negative) and 80°C (±1.39 nC scale for positive and ±6.97 pC scale for negative) in SE: (a) mean PDs charge and (b) PDs count

Fig 3.29 shows the mean PDs count and current I_{PD} at various temperatures and scales. With high sensitivity (6.97-13.9 pC scale), measurements mostly refer to small negative PDs, which are more numerous, but some perturbations unfortunately exist due to false signals induced by large positives (see

Fig 3.26). Taking a value of 10 discharge per minute, the PDIV of small negative PDs can be estimated. It decreases with temperature (Fig 3.30).

With low sensitivity (±5.6 nC at 100°C) Fig 3.29b shows that few large positive PDs (10 discharges) can induce a much larger average current compared to numerous small negatives (70 discharges).
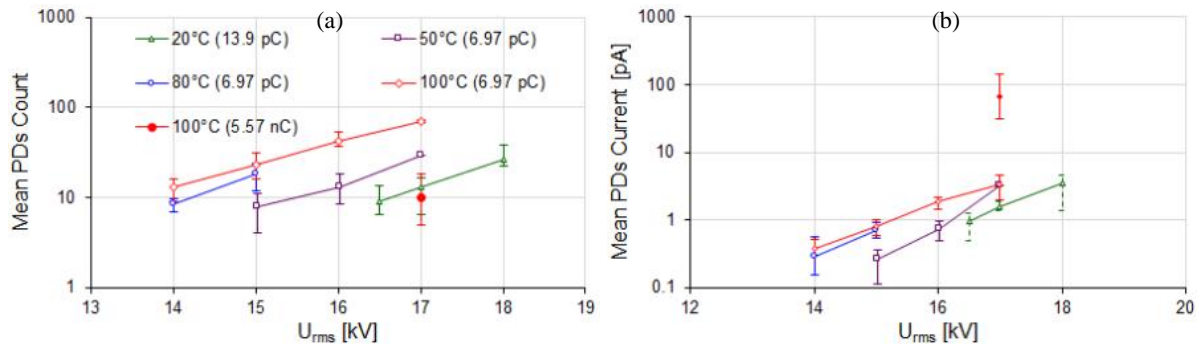
Fig 3.29 - Discharges in SE at various temperature and max scale as function of applied voltage: (a) mean PDs count and (b) mean PDs current

3.2.5   Summary of partial discharge measurements in Jarytherm® and Midel®

In SE, PDIV corresponding to small negative and large positive discharges decreases with temperature. In DBT, PDIV corresponding to small negative discharges increases with temperature and large positives are not observed. In SE, small negatives appear first. In DBT, discharges recorded over a wider voltage range (up to 25 kV) remain of very low amplitude, mostly negative with few positives. At 100°C it is suggested that the actual PDIV is above 25 kV, since at this voltage very few discharges were observed.

The comparison of PDIV in Fig 3.30 clearly shows that DBT shows very good PD suppression properties at high temperature compared to SE. Furthermore, SE is dissatisfactory due to the presence of large positive discharges. Further, positive PDIV in SE shall be defined and treated differently since it only took few large positive discharges (< 10 PDs) to induce breakdown.
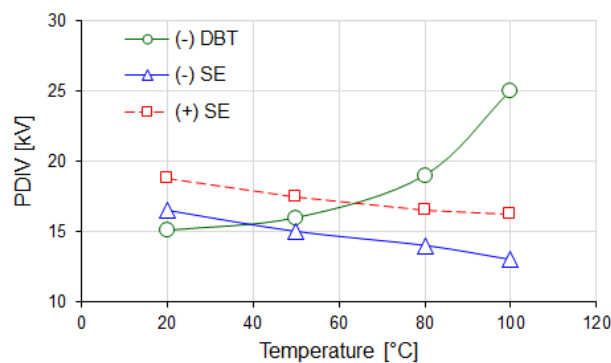
Fig 3.30 - PDIV comparison between DBT and SE at various temperature

3.3   Streamer measurements under impulse voltage

Prebreakdown phenomena in liquids (streamers) have been widely studied versus numerous parameters: type of applied voltage, polarity, electrode geometry, nature of liquids, and additives. However, very few information on the influence of high temperatures is available.

Studying streamer phenomena using point-plane geometry and impulse voltage is rather relevant for encapsulation of substrates, where discharges can occur in high divergent field regions. Another possibility would be to study streamers directly with substrates, but this solution was not considered

here due to technical difficulties (no good control of the actual electrode geometry, and optical problems to observe streamers with high magnification).

Previous studies have shown in point-plane geometry that there exists two main types of streamers in our typical conditions (few mm gap distance, and voltage < 30 kV), either with impulse voltages, ac voltage, or dc voltage,:

   a. "1st mode" streamers also known as slow 'bush-like' or "subsonic" streamers, mostly observed with the point negative and sometimes at low applied voltage in positive polarity. The velocity ranges from 0.1 to 1 km/s.
   b. "2nd mode" streamers, filamentary and faster, mainly observed with positive point and also in negative polarity in liquids containing halogens or aromatic molecules. The velocity ranges from 1 to about 10 km/s.

All measurements quoted in this study were obtained with the same point electrode, in order to get stable conditions and therefore comparative results when either the liquid nature or temperature was changed. Great care was taken to avoid the occurrence of breakdown (that would induce point electrode modification) during measurements. This was achieved by reducing the HV pulse duration t_{HV} in such a way to avoid streamer propagation up to the plane. At the end of measurements, the point showed a negligible erosion (its tip radius r_p increased from 2.5 µm to about 3 µm).

3.3.1 Experimental set up and procedure

The high temperature streamer testcell (as shown in Fig 3.31) is made of PTFE (polytetrafluoroethylene) and can contain liquid at maximum temperature of 250°C. A 30 W heating resistor was placed in the bottom part of the testcell to heat the liquid. The temperature was monitored with a thermocouple and regulated via a digital temperature controller. Preliminary temperature measurements showed that the variation of temperature of the liquid at different locations within the testcell did not exceed ±5°C. The testcell was sealed with Viton® O-ring and connected to a vacuum pump and N_2 reservoir to allow the degassing, N_2 injection, and pressure regulation.
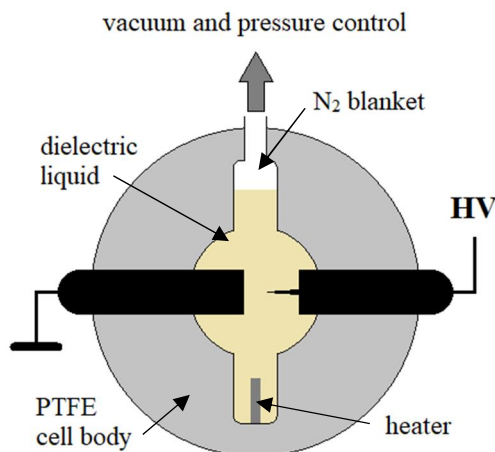
Fig 3.31 - Schematic drawing of high temperature streamer testcell

A set of point-plane electrodes was installed in the testcell, with stainless steel point (tip radius of curvature r_p = 2.5 µm), and plane electrode (diameter $\varnothing_{plane}$ = 10 mm). The gap distance (d) was set at 5 mm. After filling the testcell, liquid was degassed under vacuum for > 12 hours. Then dry nitrogen at 0.1 MPa was introduced prior to streamer measurements, in order to avoid liquid oxidation and prevent

the risk of fire. When the temperature of liquid was changed, the pressure was regulated to remain at 0.1 MPa.

Fig 3.32 shows the streamer experimental set up. A high voltage DC generator 0-60 kV/0-5 mA (Spellman® RMP60PN300) and high voltage impulse generator based on a push-pull 2x65 kV solid state switch (Behlke® HTS 651-03-GSM) with rise and fall time ≈150 ns was used. The impulse switching was controlled by a pulse generator (TGP110 10 MHz) to adjust the pulse delay and duration. To study positive streamers, the point electrode was connected to positive high voltage impulse with plane electrode to the ground, and conversely for negative streamers.
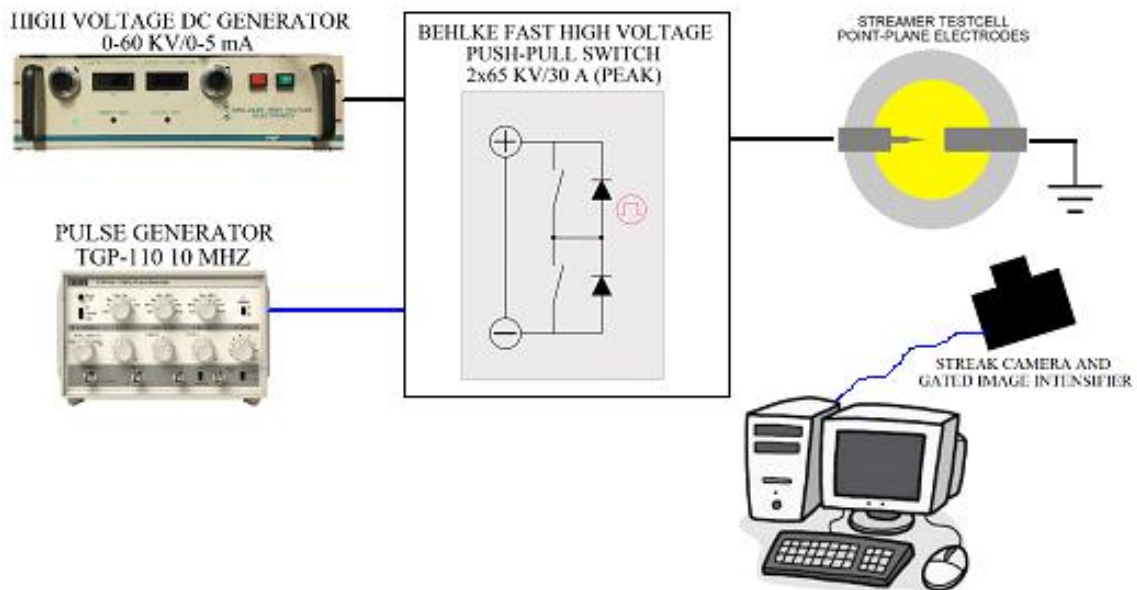
Fig 3.32 - Streamer shadow- photographic experimental set up

The time-resolved shadow-photographs of streamers were obtained from a camera with a gated image intensifier. The intensifier's gate was opened after an adjustable delay t_d after the rise of impulse voltage. Different image magnifications were applied to detect either the streamer inception with high-resolution ≈5µm, or to observe streamer propagation over longer distance.

Three dielectric liquid samples i.e. DBT, SE and PFPE, were used in streamer experiments.

3.3.2   Streamer inception voltage measurements

Streamer inception was detected from visualization using the highest magnification in order to record every streamer. In several cases, their size can be rather small, down to about 10µm in diameter. Since streamer inception usually gets a random character, a statistical method was used. Series of 20 shots were applied at fixed voltage, and the number of streamers initiated was noted. From this series, the inception frequency was calculated and plotted versus voltage. Voltage was increased in steps, ranging from 0% to 100% inception frequency.

3.3.2.1   Experimental procedures

The impulse voltage duration (t_{HV}) was adjusted between 1.0-8.0 µs depending on the dielectric liquid and polarity. Streamer images were obtained with 1.0 µs intensifier opening time, after a 1.0 µs delay (t_D) measured from 50% of impulse rise time as in Fig 3.33.
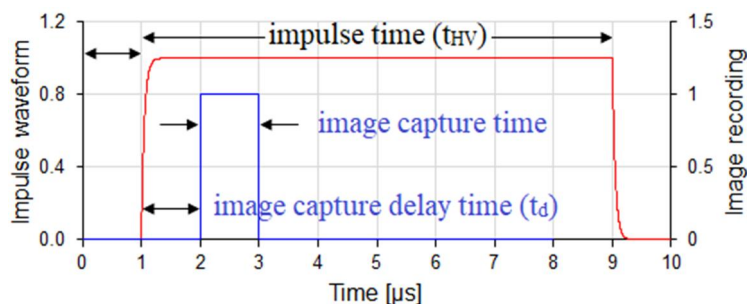
Fig 3.33 - Impulse voltage and image recording control signals

3.3.2.2 Negative streamers in Jarytherm® DBT

1st mode negative streamers in DBT at RT are characterized by a "bubble-like" shape as in Fig 3.34. The size of these negative streamers grows as the voltage is raised as in figure a to c from 17 kV to 25 kV. They develop until reaching certain size, detach from the tip, and then collapse.
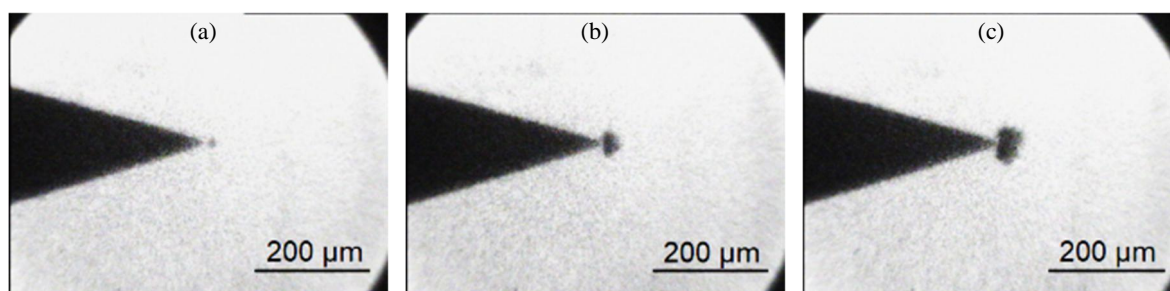
Fig 3.34 - Typical negative streamer in DBT at 24°C for V_{app}: (a) 17 kV, (b) 20 kV and (c) 25 kV. t_{HV} = 2.0 µs, t_D = 1.0 µs

Fig 3.35 shows negative streamers in DBT at 100°C versus voltage. The streamer size appears to grow slightly larger at this temperature compared to RT. The similar behaviour is also found at 200°C as in Fig 3.36.
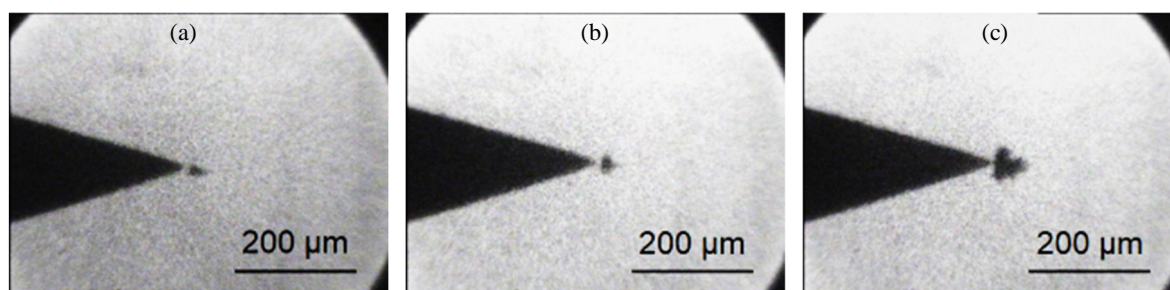
Fig 3.35 - Typical negative streamer in DBT at 100°C for V_{app}: (a) 17 kV, (b) 20 kV and (c) 25 kV. t_{HV} = 2.0 µs, t_D = 1.0 µs
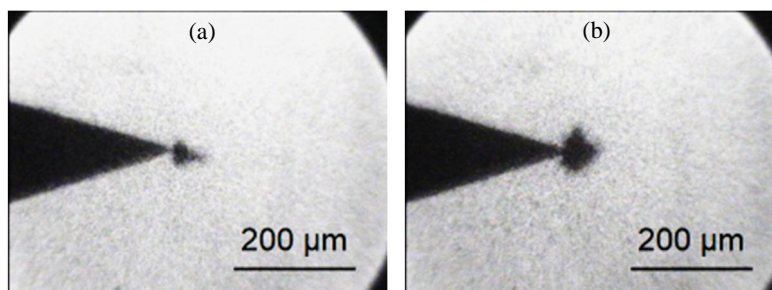
Fig 3.36 - Typical negative streamer in DBT at 200°C for V_{app}: (a) 20 kV and (b) 25 kV. t_{HV} = 2.0 µs, t_D = 1.0 µs

Meanwhile, rising temperature has a minor influence on negative streamer inception voltage V_i (corresponding to an arbitrary inception frequency of 50%) as shown in Fig 3.37. Only a small increase of V_i (about 2.5 kV) can be observed up to 200°C. Negative streamers remained with a bubble-like shape without large propagation, even when the impulse voltage was raised far above 100% inception voltage (Fig 3.36). Increasing the temperature did not induce any significant change of streamer shape.
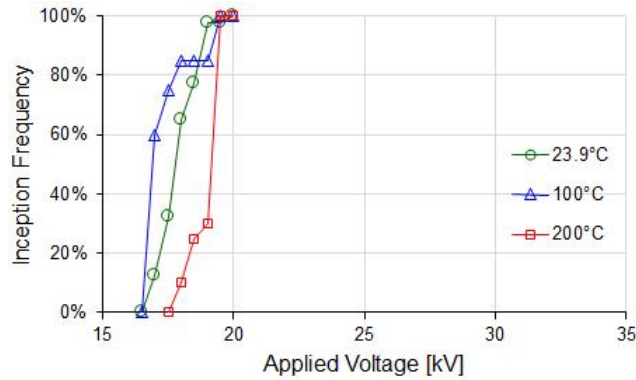
Fig 3.37 - Negative streamer inception probability in DBT at RT, 100°C and 200°C

3.3.2.3   Positive streamers in DBT

In DBT, two different positive streamer modes (1st mode and 2nd mode) were observed depending on the applied impulse voltage, as previously reported in other liquids in similar conditions [60,96]. At low voltage, the 1st mode streamers with a bubble-like shape similar to those recorded in negative polarity (Fig 3.38a) are observed. When the applied impulse voltage exceeds certain critical voltage (called V_2 in [60]), faster filamentary 2nd mode streamers are seen (Fig 3.38b). At RT, 1st mode positive streamers appear with 50% probability at $V_i = 23$ kV, and 2nd mode filamentary streamers begin to emerge at 25 kV.
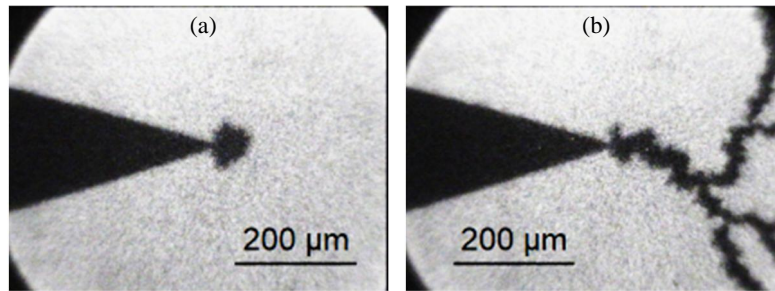
Fig 3.38 - Typical positive streamers (1st and 2nd mode) in DBT at 25°C for V_{app}= 26 kV (a) 1st mode bubble-like and (b) 2nd mode filamentary. t_{HV} = 1.0 µs, t_D = 1.1 µs

The probability of 2nd mode filamentary streamers increase while the 1st mode streamers are reduced when the applied impulse voltage is raised (Fig 3.41). Fig 3.39 shows 1st and 2nd mode positive streamers at 100°C for applied impulse voltage of 26 kV. The impulse voltage duration (t_{HV}) is 1.0 µs and streamer capture delay (t_D) and capturing time are 1.1 µs and 1.0 µs. Therefore streamer images were taken just after the end of impulse voltage.
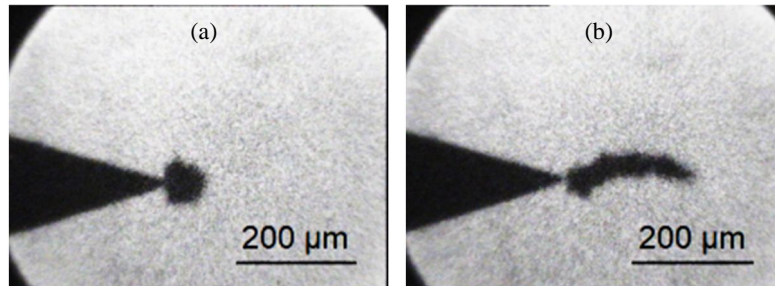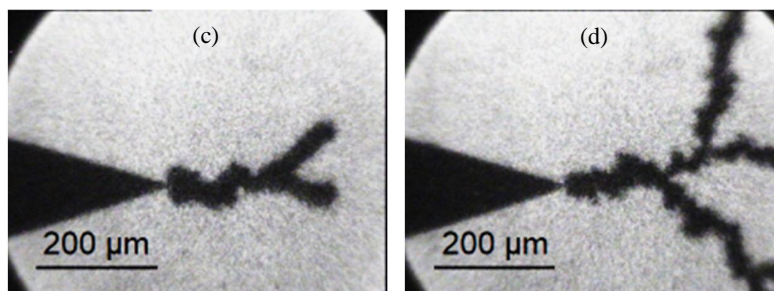
Fig 3.39 - Typical positive streamer (1st and 2nd mode) in DBT at 100°C for V_{app}= 26 kV (a) bush-like and (b, c and d) filamentary. t_{HV} = 1.0 µs, t_D = 1.1 µs

Visual comparison among positive streamers at RT, 100°C and 200°C is consistent with negative streamers. The thickness of filamentary positive streamers slightly grows as the temperature increases (see Fig 3.38, Fig 3.39 and Fig 3.40). Filamentary streamers at 200°C have a diameter about 50 µm while at 100°C and RT it is nearly 20 µm and < 20µm.
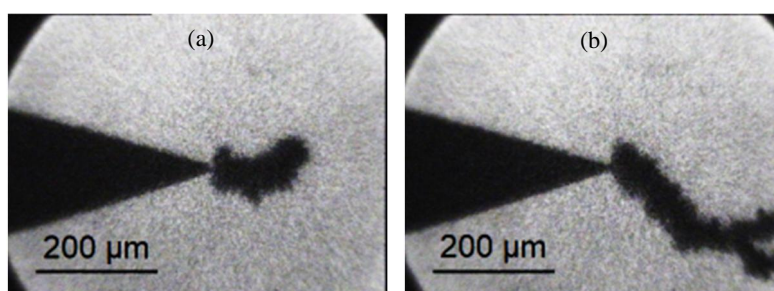
Fig 3.40 - Typical positive filamentary streamer (2nd mode) in DBT at 200°C for V_{app}= 26 kV. t_{HV} = 1.0 µs, t_D = 1.1 µs

In DBT, positive streamers start as 1st mode. The inception probability is gradually increased but never reach 100%, and drops as 2nd mode streamers appear at higher voltage. In Fig 3.41, there is no clear difference for V_i between RT and 100°C. At 200°C, 1st mode streamers no longer existed and only 2nd mode streamers remain, with very random appearance frequency. 100% probability of 2nd mode streamers at RT and 100°C occurred at nearly the same voltage (28 kV), whereas at 200°C it was approx. 33 kV.

It was previously reported that the existence of 1st and 2nd mode streamers under impulse voltage depend on the point tip radius of curvature r_p (see chapter 1, Fig 1.26). Below some "critical radius" r_c (e.g. r_c = 3 µm in pentane, see Fig 1.26), both modes are observed, and above r_c only the 2nd mode is seen. The "critical radius" r_c in DBT is not yet known. The fact that two modes were seen indicates that the critical radius in DBT should be larger than the point radius used here (2.5 µm).
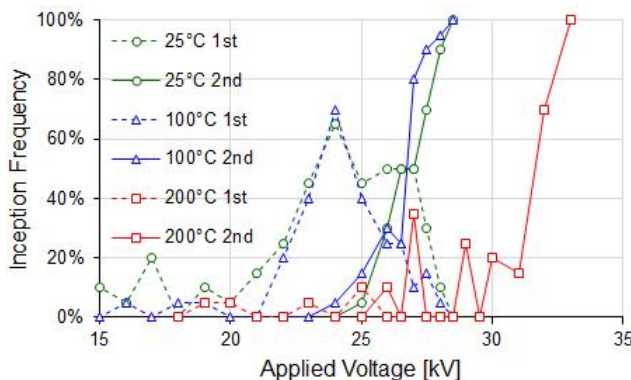
Fig 3.41 - Positive streamer inception probability in DBT at RT, 100°C and 200°C

3.3.2.4   Negative streamers in Midel® SE

Negative slow streamers in SE are characterized by a "bush-like" shape including thick branches, and propagating longer than in DBT (Fig 3.42). These streamers develop into longer and thicker filaments as the applied voltage increases.
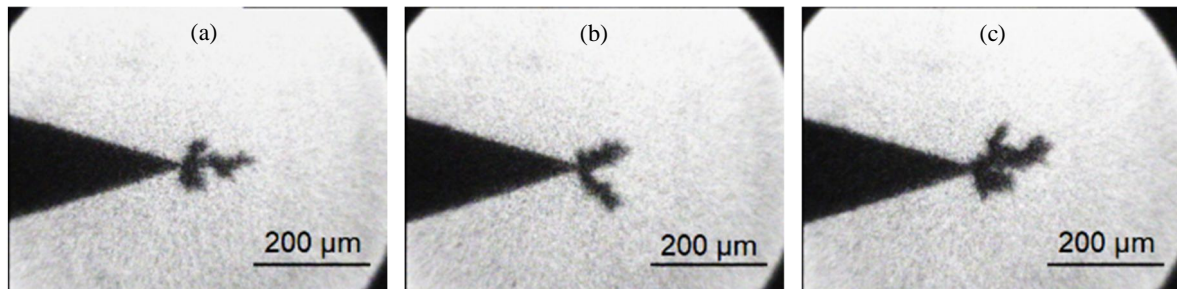
Fig 3.42 - Typical negative streamers in SE at 26°C for V_{app}: (a) 26 kV, (b) 28 kV and (c) 30 kV. t_{HV} = 2.0 µs, t_D = 1.0 µs
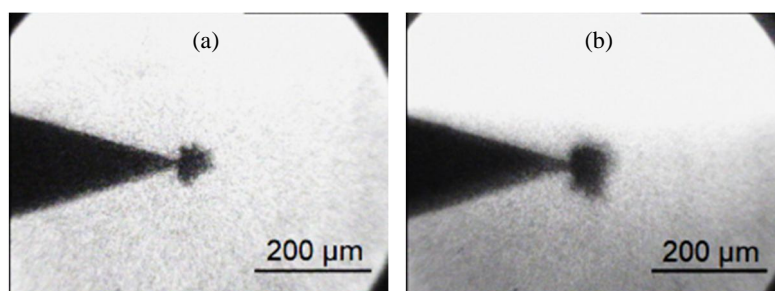
Fig 3.43 - Typical negative streamers in SE at for V_{app}= 26 kV at (a) 100°C and (b) 200°C. t_{HV} = 2.0 µs, t_D = 1.0 µs
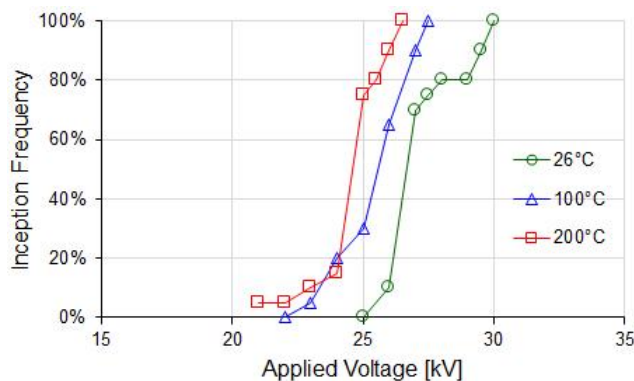
Fig 3.44 - Negative streamer inception probability in SE at RT, 100°C and 200°C

At higher temperatures (100°C and 200°C), "bush-like" negative streamers are still observed (Fig 3.43). Size of streamers slightly grows with temperature as well as in DBT.

However, when temperature was raised, inception measurements become rather unstable and more complicated in SE. When the liquid remained at 100°C in the testcell for several hours, streamer inception tend to vanish: at V = 30 kV, the streamer inception frequency dropped from 100% down to 0%. Cleaning the testcell and electrodes, and filling it again with new liquid allowed to obtain streamers again. At 200°C, this process was even faster: it became impossible to observe streamers only after some 10 minutes, making reproducible measurements very difficult. Some degradation of the ester liquid probably occurred at high temperature, which either changed the liquid properties regarding streamer inception, or changed the conditions on the point. Since the formation of gels from esters was previously reported, we may suppose that a layer of gel on the point could modify the conditions of streamer inception. Further analysis is of course required to better understand these phenomena.

When inception measurements were made rapidly to minimize these effects, a slightly reduced inception voltage V_i (50% probability) was observed, from 26.8 kV at RT to 24.5 kV at 200°C as shown in Fig 3.44.

3.3.2.5 Positive streamers in SE

Positive streamers in SE are mainly of 2nd mode filamentary streamers. Fig 3.45 shows positive streamers at RT and 100°C. These streamers are characterized by numerous and long filamentary branches. There is no significant influence of temperature on streamer inception voltage at RT and 100°C (see Fig 3.46). The inception probability of positive streamers rises sharply to 100% within a narrow voltage range (2 kV range at 100°C).

The fact that only the 2nd mode was seen indicates that the critical radius in SE (not yet known) should be smaller than the point radius used here (2.5 µm).
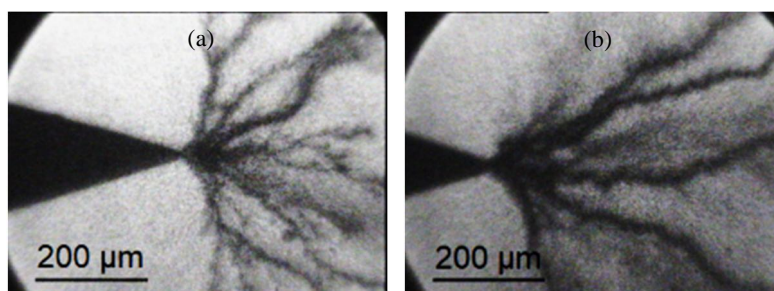
Fig 3.45 - Typical positive streamer in SE for V_{app}= 24 kV at (a) 24°C and (b) 100°C. t_{HV} = 1.0 µs, t_D = 1.0 µs
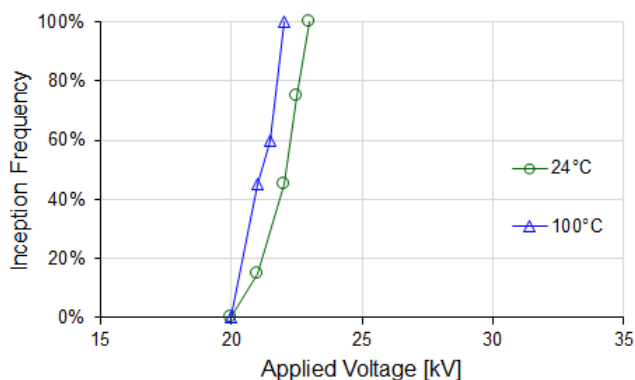
Fig 3.46 - Positive streamer (fast mode) inception probability in SE at RT and 100°C

3.3.2.6 Negative streamers in Galden® PFPE

Several complementary measurements were also done in Galden® HT 270 perfluoropolyether liquid, although this liquid was not investigated in terms of conduction and breakdown voltage. This non-polar liquid (permittivity: 1.94) shows a rather high boiling point (270°C), and is already used for cooling and electrical insulation in several power electronic systems.
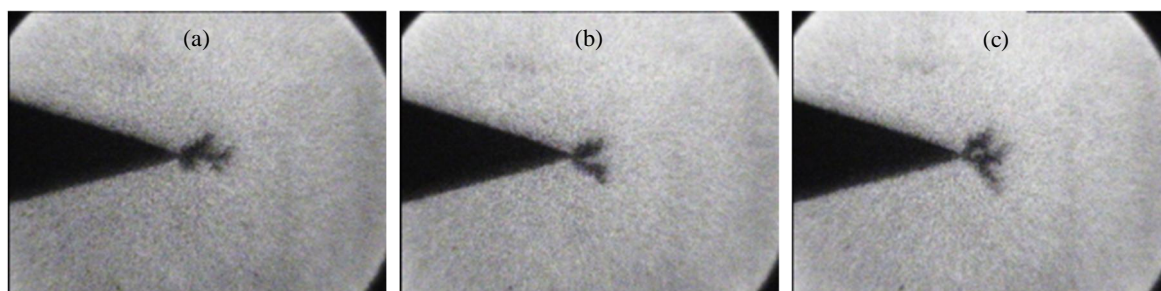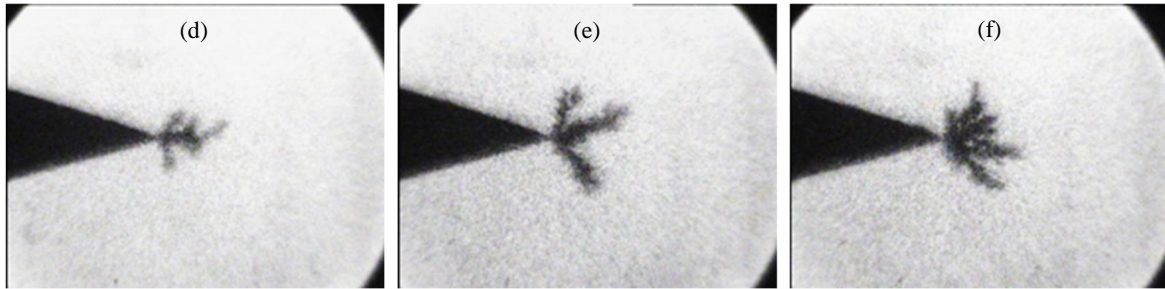
Fig 3.47 - Typical negative streamer in PFPE at RT for V_{app}: (a) 23 kV, (b) 24 kV, (c) 25 kV, (d) 27 kV, (e) 30 kV and (f) 33 kV. t_{HV} = 800 ns, t_D = 400 ns

At RT, thick bush-like negative streamers were observed in PFPE (Fig 3.47), similar to those in SE. The branches elongate as the voltage was raised from 23 kV up to 27 kV.

When liquid was heated up to 100°C, negative streamers remained of 1st mode bush-like shape (Fig 3.48). In contrast with DBT and SE, temperature seems to slightly reduce the size of bush-like streamer in PFPE (Fig 3.48 and Fig 3.49). At 150°C there are not any more branches and streamers get a "bubble-like" shape (Fig 3.49). Furthermore, 50% inception voltage of negative streamers now increases when temperature is raised (Fig 3.50), while 10% probability voltage shows almost no change.

During experiments, PFPE liquid showed strong thermal convection and unexpected boiling tendency at 150°C (appearance of vapour bubbles, although the quoted boiling temperature is 270°C), setting the maximum temperature for streamers measurements. Visual recording became also blurred with less contrast (Fig 3.49). Fig 3.49b shows a vapour bubble emerging from the bottom of the testcell. The liquid turned cloudy after cooled down to RT. No clear explanation could be provided for these phenomena.
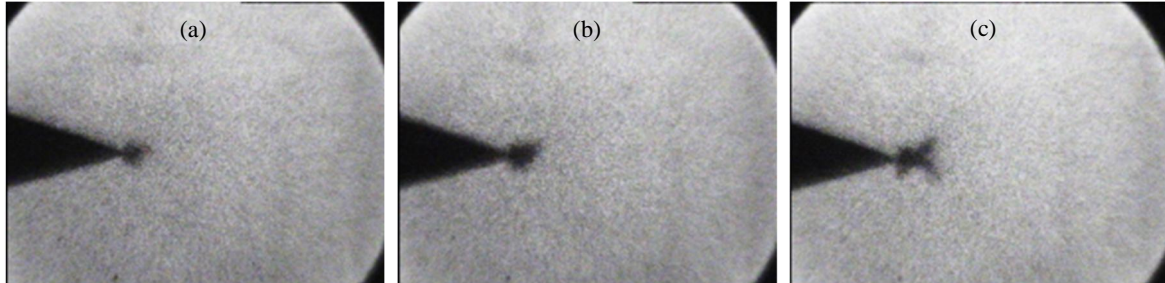
Fig 3.48 - Typical negative streamer in PFPE at 100°C for V_{app}: (a) 24 kV, (b) 25 kV and (c) 26 kV. t_{HV} = 800 ns, t_D = 400 ns
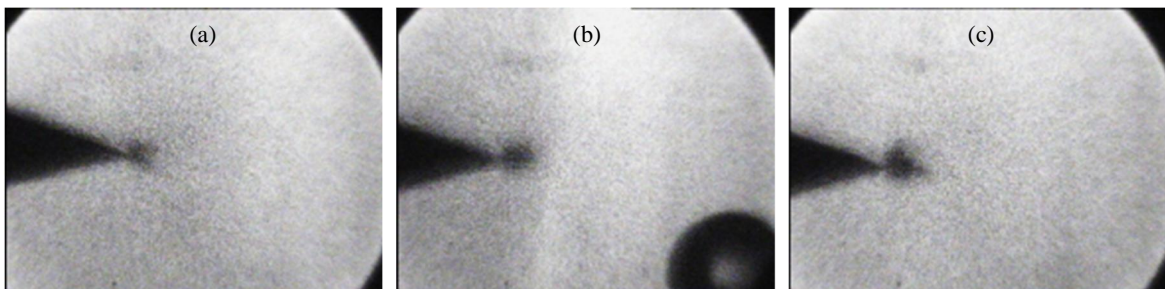
Fig 3.49 - Typical negative streamer in PFPE at 150°C for V_{app}: (a) 25 kV, (b) 27 kV and (c) 29 kV. t_{HV} = 800 ns, t_D = 400 n
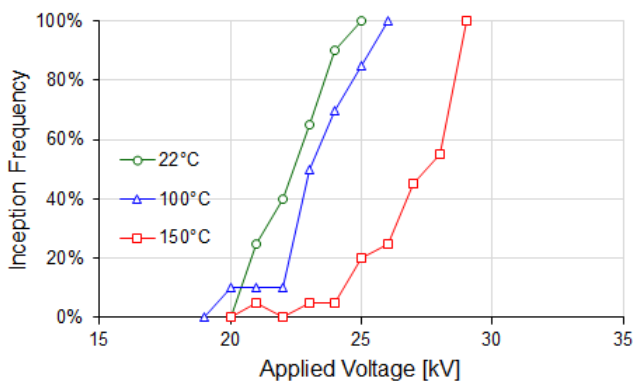
Fig 3.50 - Negative streamer inception probability in PFPE at RT, 100°C and 150°C

3.3.2.7 Positive streamers in Galden® PFPE

As well as in SE, positive streamers in PFPE are mainly of 2nd mode filamentary streamers. No slow 1st mode streamers were seen. Positive 2nd mode streamers in PFPE have a different shape compared to DBT and SE, which consists of several main thick filaments, with several thinner side branches as in Fig 3.51. The applied voltage contribute to lengthen filaments as in DBT and SE, while temperature governs the thickness of filaments. The propagation velocity of these streamers (about 4 km/s, see next sections) is faster than in DBT and SE. Inception probability (Fig 3.53) shows large fluctuations at room temperature, and increases slowly on average versus voltage. At 100°C, streamers observed between 22 to 32 kV nearly disappeared. At the maximum voltage investigated (35 kV) 50% inception probability was not reached. At higher temperature, inception probability measurements were impossible due to the lack of streamers. During measurements, one unexpected breakdown occurred at 33 kV (green solid symbol in Fig 3.53), despite the impulse duration limitation to 1 µs.

The fact that only the 2nd mode was seen indicates that the critical radius in PFPE (not yet known) should be smaller than the point radius used here (2.5 µm).
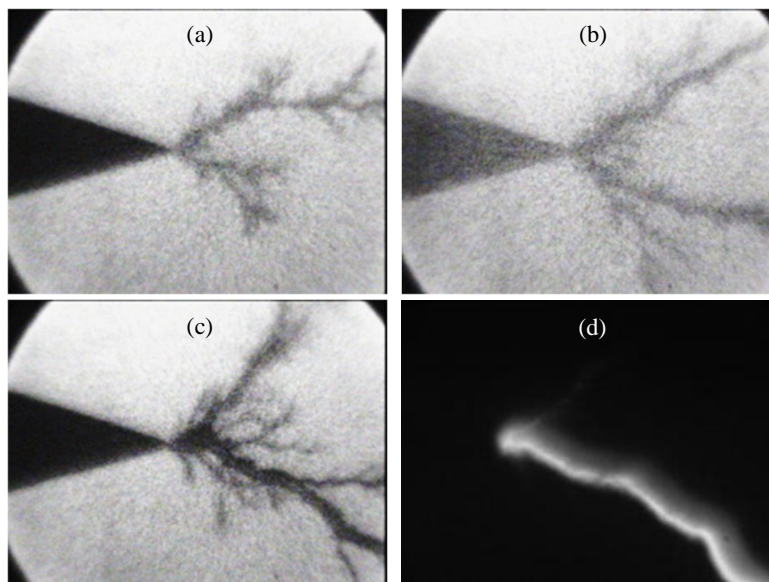
Fig 3.51 - Typical positive streamer in PFPE at 26°C for V_{app}: (a) 25 kV, (b) 29 kV, (c) 33 kV and (d) 33 kV - breakdown. $t_{HV} = 1.0$ µs, $t_D = 500$ ns
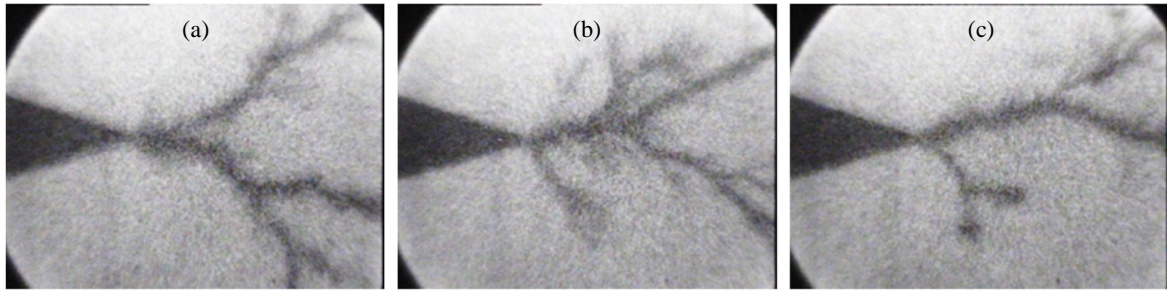
Fig 3.52 - Typical positive streamer in PFPE at 170°C for V_{app}= 30 kV, t_{HV} = 1.0 µs, t_D = 500 ns
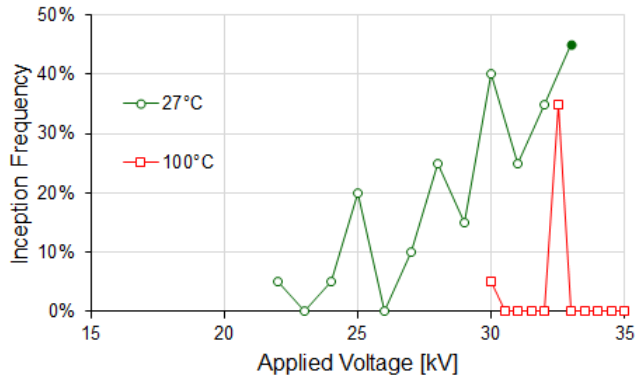
Fig 3.53 - Positive streamer inception voltage probability in PFPE at RT and 100°C

3.3.2.8   Discussion on negative and positive streamer inception, comparison with PD measurements
Fig 3.54 and Fig 3.55 show the inception frequencies of negative and positive streamers in DBT, SE and PFPE at different temperatures.
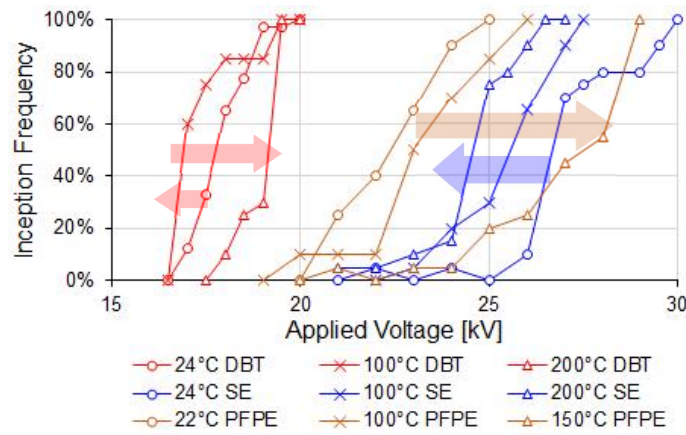
Fig 3.54 - Negative streamer inception voltage probability of DBT, SE and PFPE
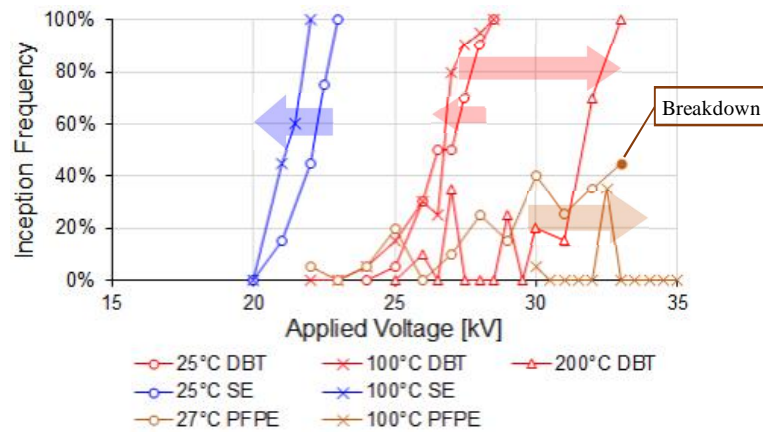
Fig 3.55 - Positive fast mode (2nd) streamer inception voltage probability of DBT, SE and PFPE

Jarytherm® DBT

In negative polarity with DBT, raising the temperature up to T = 200°C has a minor influence on streamer inception, considering the scatter of measurements. Only a small increase of inception voltage V_i (at arbitrary inception frequency of 50 %) can be observed at T = 200°C.

Two different positive streamer modes (1st mode and 2nd mode) can be observed depending on the applied voltage, as previously reported in other liquids in similar conditions [60,96]. At 25°C and 100°C, slow 1st mode streamers are gradually replaced by filamentary 2nd mode when the applied voltage exceeds 25 kV. At 200°C, the inception of 1st mode is nearly suppressed and 2nd mode is still observed at voltages above 25 kV, but it is necessary to raise applied voltage above 33 kV to obtain 100% inception frequency.

Negative inception voltage (17.5 kV @ RT) is much lower than positive (27 kV @RT), and this agrees with PD measurements (negative PDs are first detected). However, no large positive PD under AC was detected even when the voltage was raised, whereas 2nd mode streamers were observed under impulse at voltage > 15 kV. This observation can be explained by the fact that under AC, the "rise time" of voltage (some ms) is much longer than with impulse (150 ns).

It was reported in [62] that when two modes can be seen (i.e. below the critical tip radius r_c), the impulse rise time has a large influence on inception of 2nd mode. With a long rise time, a 1st mode streamer appears first during the voltage rise, later followed by a 2nd mode at higher voltage. As soon as the 1st mode appears, the tip field is reduced by the space charge contained within this 1st mode streamer, and the appearance of 2nd mode is therefore shifted to higher voltage. Therefore, 1st mode streamers produce a "stabilizing effect" under ac that prevents fast 2nd mode from occurring. This explains why large PDs due to 2nd mode positive streamers were not observed in PD measurements.

With fast voltage rise (a few ns), the 1st mode has no time to develop, the "stabilizing effect" disappears, and 2nd mode appears at the lowest possible voltage. When rise time is increased, this "stabilizing effect" appears: the longer the rise time, the larger inception voltage of 2nd mode [62]. This phenomenon does not exists when only 2nd mode are observed (i.e. above the critical tip radius).

Fig 3.56 shows comparison of PDIV and SIV (Streamer Inception Voltage) of DBT versus temperature. SIV refers to 10% inception probability of negative streamers to be more consistent with PDIV measurements. Indeed, PDIV defined at 10 PDs / minute corresponds to a low inception probability. The figure shows that PDIV is larger than SIV, and increases very rapidly with temperature, whereas SIV remains nearly unchanged. When plotted with maximum tip field instead of voltage, the conclusion are identical (Fig 3.56).

This result agrees with that already observed in mineral oil (Fig 3.24): with sharp tips, calculated inception fields are larger under AC compared to impulse. This effect can be only explained by the influence of space charge injected prior to discharge inception under AC that reduces the actual tip field compared to the calculated one without space charge. In addition, it is observed here that this effect increases rapidly with temperature. Ion injection at the tip is strongly promoted by temperature, further reducing the tip field, and shifting discharge inception at higher voltage. Under impulse, this effect is nearly absent.
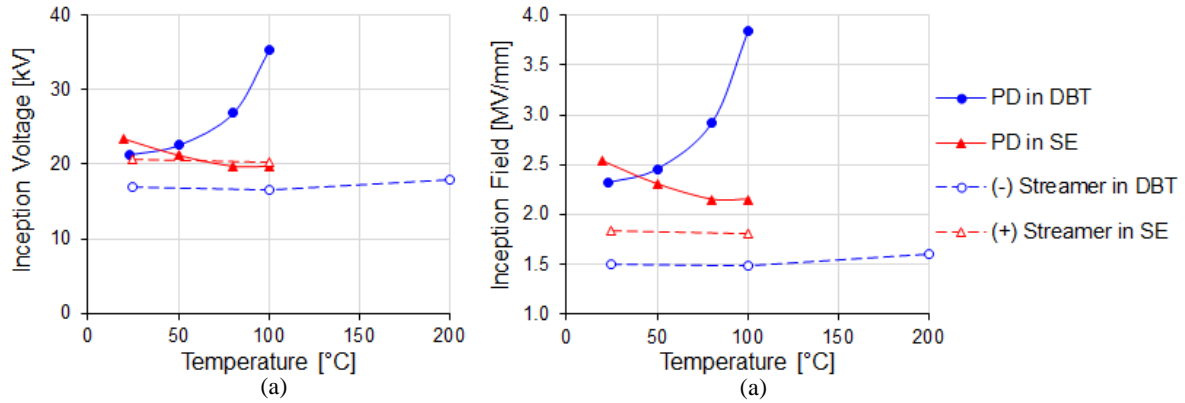
Fig 3.56 - Comparison of PDIV and SIV at 10% probability in DBT versus temperature: (a) inception voltage and (b) calculated inception field

<u>Midel® synthetic ester</u>

In ester, negative streamers under impulse voltage showed higher inception voltage as compared to DBT. Positive streamers in SE are related to the large positive PDs recorded under AC (Fig 3.56). The fact that only large positive PDs are recorded in this liquid agrees with the fact that no 1st mode positive streamers were observed in this liquid. Under AC, the first positive streamers initiated in SE are already of 2nd mode type. The "stabilizing effect" due to 1st mode positive streamers in DBT under AC does not exists in SE.

As in DBT, almost no influence of temperature on streamer inception voltage was observed, when measurements were done rapidly to avoid premature ageing. In this liquid, PD inception fields under ac are also larger than streamer inception fields. However a major difference is observed at high temperature: PDIV slightly decreases now with temperature. This would suggest that the influence of space charge enhancement under ac would be nearly absent in this liquid. This conclusion is rather unexpected since calculations also indicate a very high field (> 2 MV/mm).

3.3.3   Streamer propagation

Streamer propagation was studied from visualization at different image capture delay time (t_D), using less magnification in order to record the complete streamer extension. A statistical method was used to evaluate the propagation velocity. The impulse voltage duration (t_{HV}) was adjusted to prevent the possibility of breakdown, and enable capturing streamers propagation. Series of at least 10 shots were applied at fixed voltage and image delay time (t_D), and the length of streamers was measured. From this series, the average propagation velocity was calculated.

3.3.3.1   2nd mode positive streamers in DBT

In these measurements, the duration of HV pulse was limited to $t_{HV} = 1$ µs in order to prevent breakdown from occurring. Image capture duration was 120 ns with delay time t_D of 200, 400, 600, 800, and 1000 ns. Streamer propagation was measured at RT, 100°C and 200°C. Fig 3.57 to 2.59 shows images of streamers at RT, 100°C and 200 °C for different time delay (t_D).

Fig 3.60 shows the positive streamer propagation versus time in DBT. The average velocities at RT, 100°C and 200°C (resp. 1053 m/s, 1019 m/s and 1072 m/s) show almost no significant modification over all temperatures investigated.
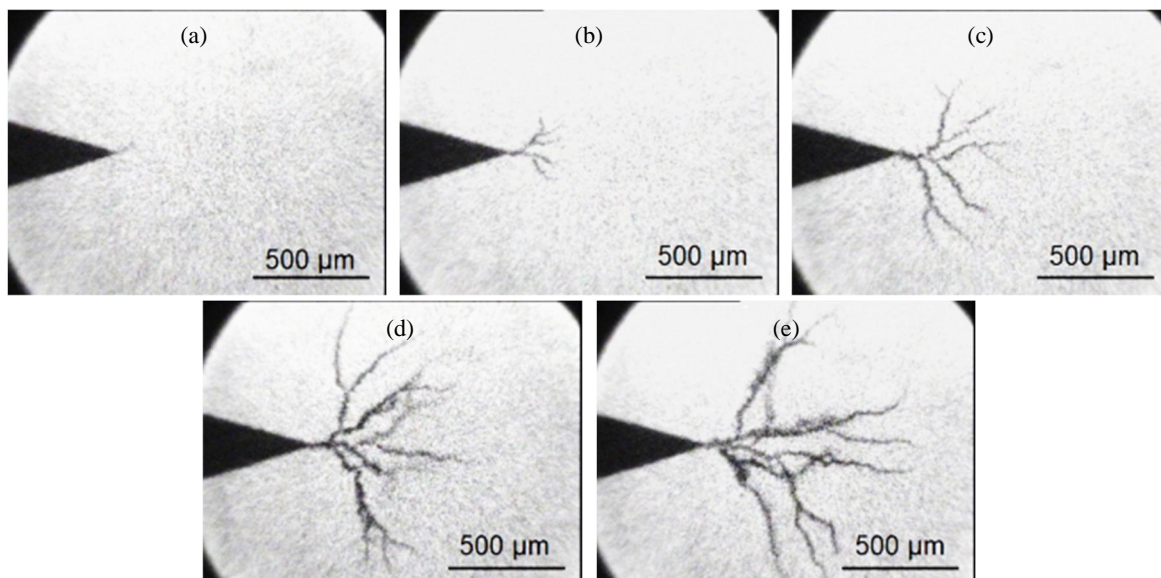
Fig 3.57 - Positive streamers in DBT at RT 29 kV after: (a) 200 ns, (b) 400 ns, (c) 600 ns, (d) 800 ns and (e) 1000 ns
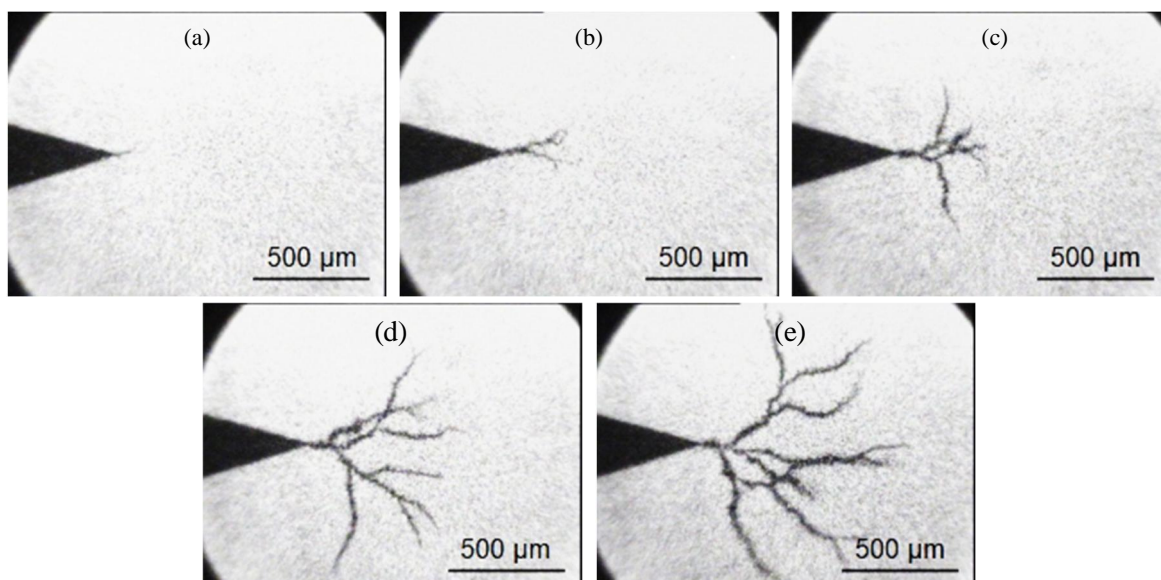
Fig 3.58 - Positive streamers in DBT at 100°C, 29 kV after: (a) 200 ns, (b) 400 ns, (c) 600 ns, (d) 800 ns and (e) 1000 ns
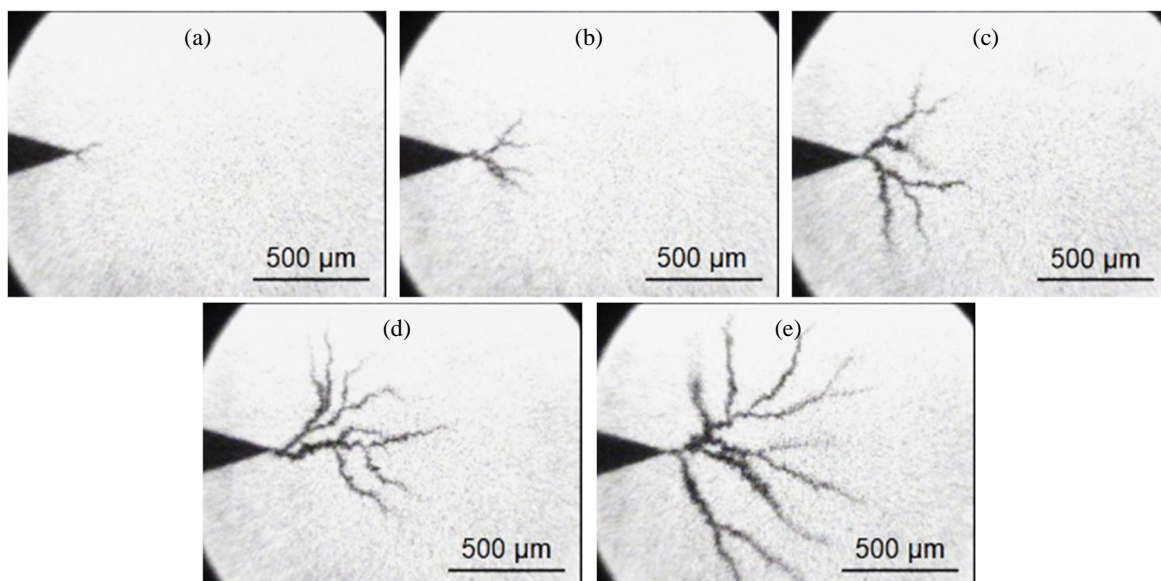
Fig 3.59 - Positive streamers in DBT at 200°C, 33 kV after: (a) 200 ns, (b) 400 ns, (c) 600 ns, (d) 800 ns and (e) 1000 ns
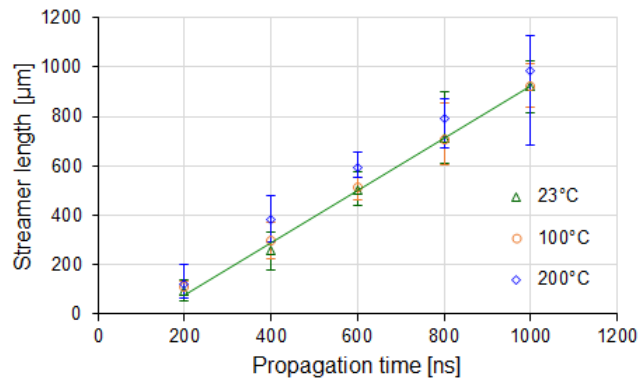
Fig 3.60 - Positive 2nd mode streamer propagation in DBT at V_{app} = 30 kV for RT and 100°C; 33 kV for 200°C,
t_{HV} = 1000 ns.

There were almost no measurable negative streamer propagation in DBT. All streamers remained of bubble-like shape with very small size, even when the voltage was raised far beyond 100% inception voltage probability (Fig 3.37).

3.3.3.2   1st mode negative streamers in SE

Unlike DBT, negative streamers have thick branches and show some limited propagation in SE. They propagated at low velocity, and the duration of HV pulse was extended to t_{HV} = 8 µs. Image capture duration was 200 ns with delay time t_D from 400 to 8000 ns. Fig 3.61 to Fig 3.63 shows the streamer propagation at RT, 100°C and 200°C, at 30 kV for different time delay (t_D).
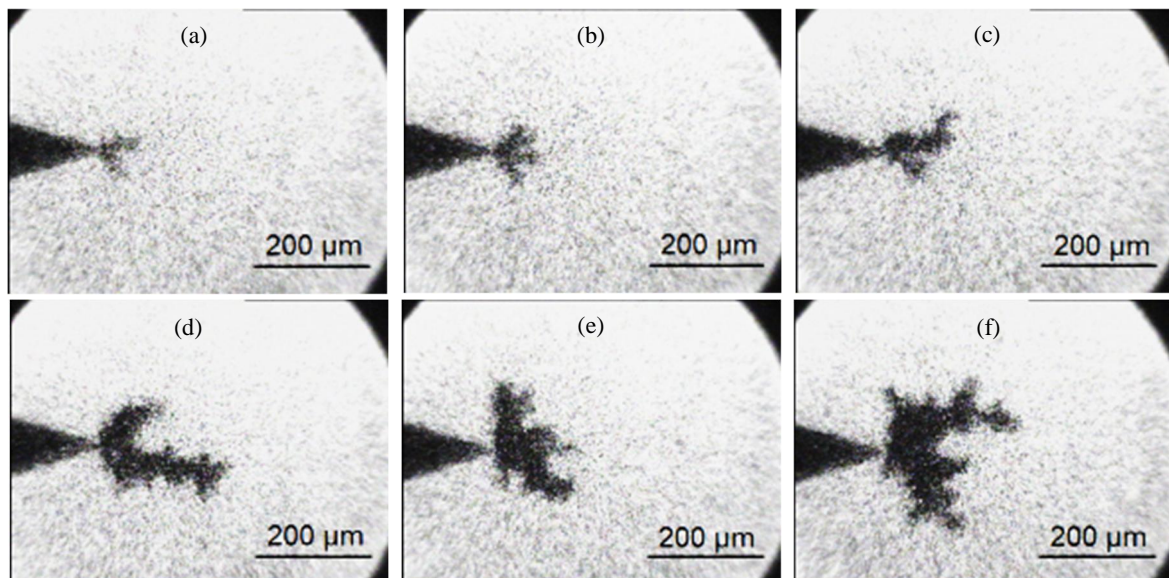
Fig 3.61 - Negative streamer in SE at 24°C 30 kV after: (a) 400 ns, (b) 600 ns, (c) 1000 ns, (d) 2000 ns, (e) 4000 ns and (f) 6000 ns
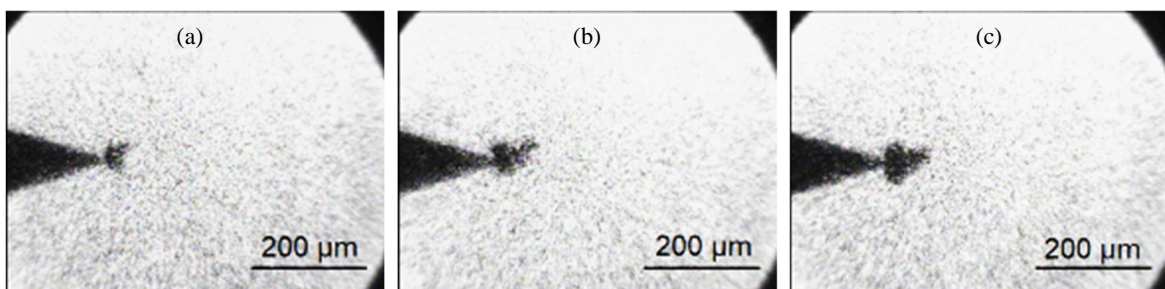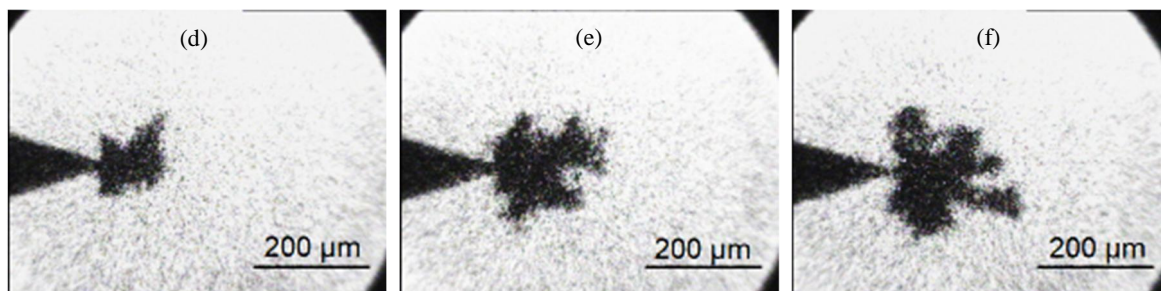
Fig 3.62 - Negative streamer in SE at 100°C 30 kV after: (a) 400 ns, (b) 800 ns, (c) 1000 ns, (d) 2000 ns, (e) 4000 ns, and (f) 6000 ns

The 1st mode streamer propagation stopped after some time (Fig 3.64). The propagation velocity (measured at the beginning of propagation) slightly decreases with temperature, from 75 m/s at RT, down to 40 m/s at 200°C. On the figure, error bars are only displayed for RT for clarity. The propagation duration increases with temperature: 2.4 µs at RT, 5 µs at 100°C, and 6 µs at 200°C. Consequently, the maximum length attained by streamers before stopping slightly increases with temperature.
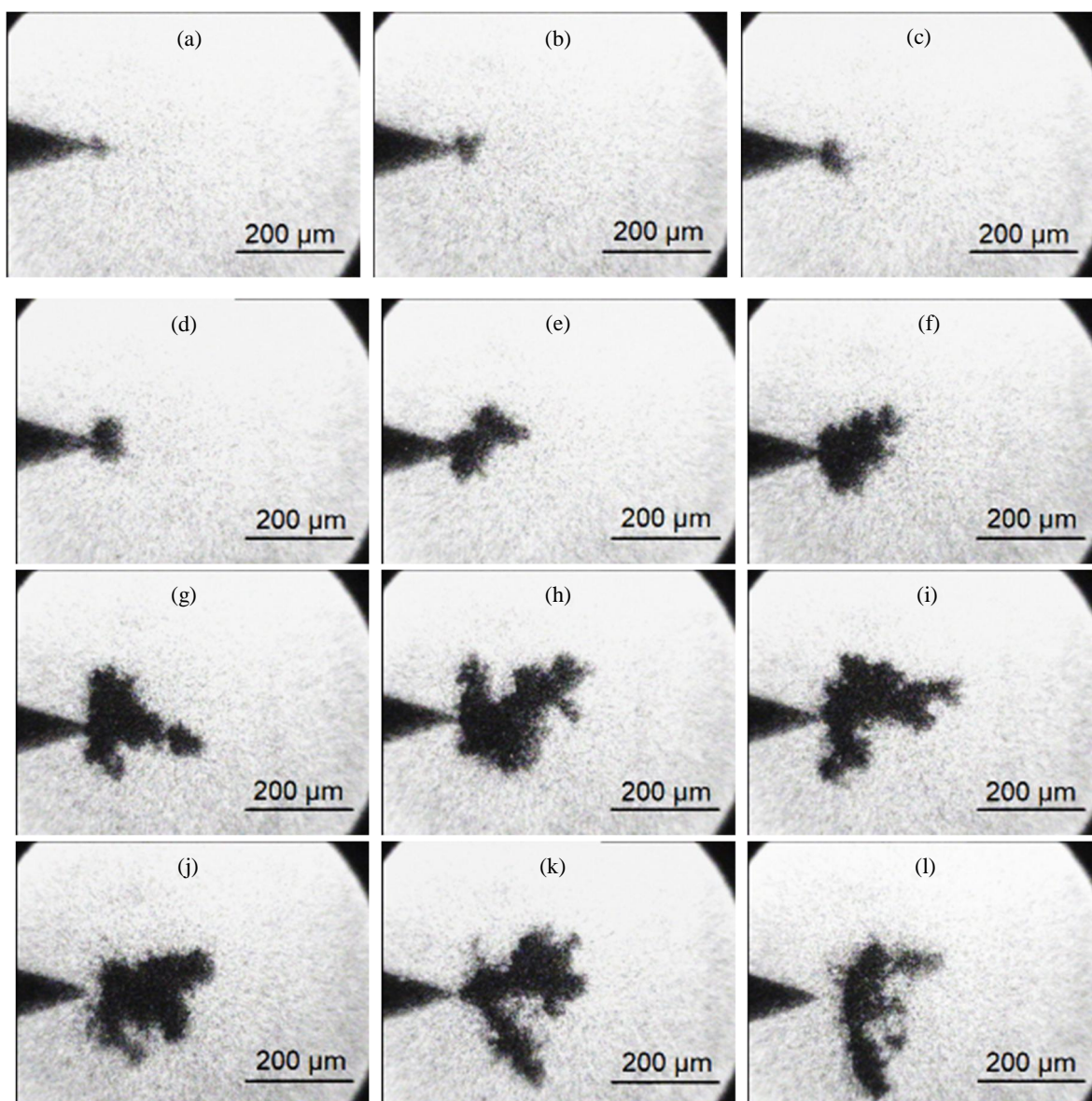
Fig 3.63 - Negative streamer in SE at 200°C 30 kV after: (a) 400 ns, (b) 600 ns, (c) 800 ns, (d) 1000 ns, (e) 2000 ns, (f) 3000 ns, (g) 5000 ns, (h) 6000 ns, (i) 7000 ns (j) 8000 ns, (k) 9000 ns and (l) 10 µs
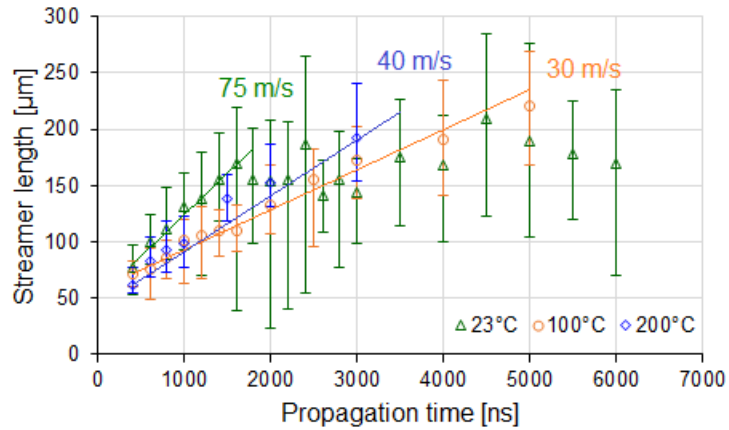
Fig 3.64 - Negative 1st mode streamer propagation in SE at V_{app} = 30 kV, t_{HV} = 8.0 µs, average velocity = 75 m/s

3.3.3.3   2nd mode positive streamer in SE

Only 2nd mode filamentary streamers were observed. In these measurements, the duration of HV pulse was limited to t_{HV} = 0.8 µs in order to prevent breakdown from occurring. Image capture duration is 120 ns with delay time t_D of 200, 400, 600, 800, and 1000 ns. Streamer propagation was measured at RT, and 100°C. Fig 3.65 and Fig 3.66 show the positive streamer propagation in SE at RT and 100°C, at 30 kV (100% inception voltage probability is 23 kV) for different time delay (t_D). In Fig 3.67, streamers propagation at 200°C continued until 1000 ns and collapsed at 2200 ns.
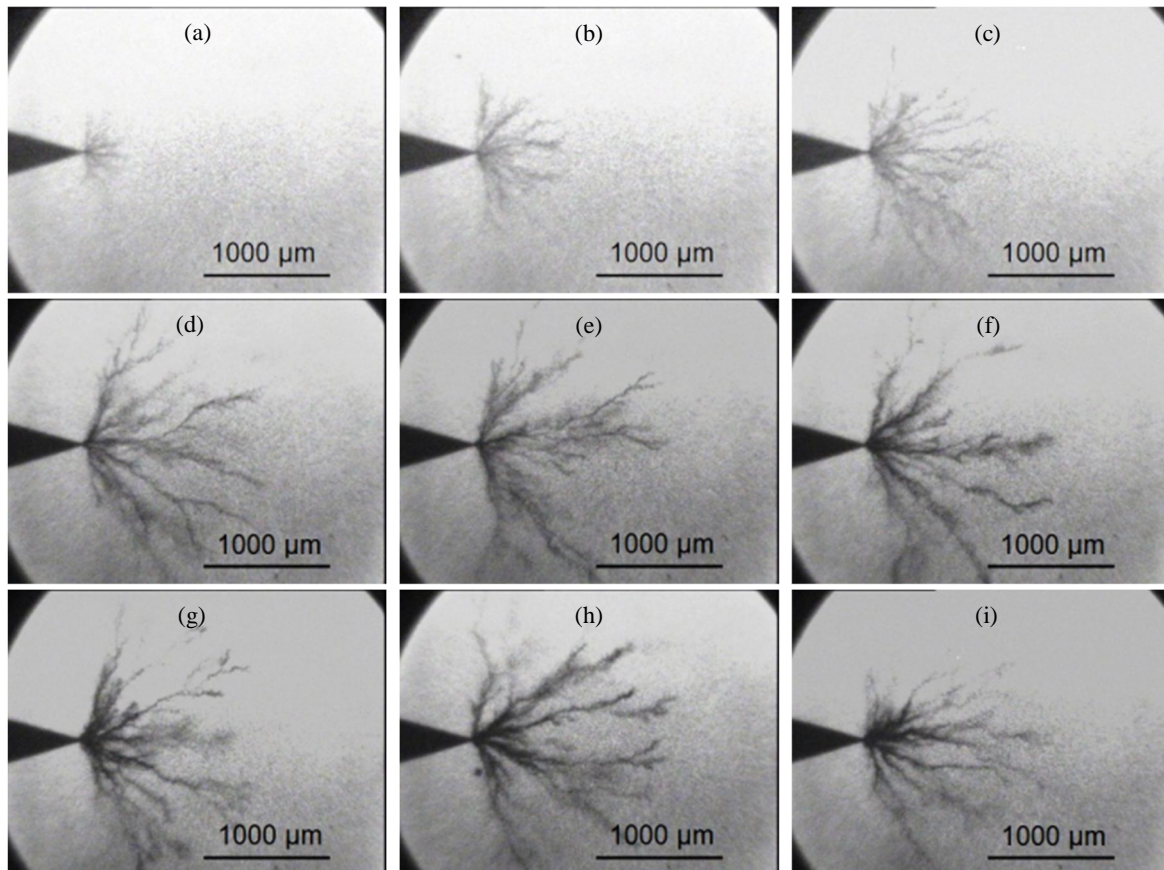
Fig 3.65 - Positive streamer in SE at 24°C 30 kV after: (a) 200 ns, (b) 400 ns, (c) 600 ns, (d) 800 ns, (e) 1000 ns, (f) 2000 ns, (g) 4000 ns, (h) 5000 ns and (i) 8000 ns
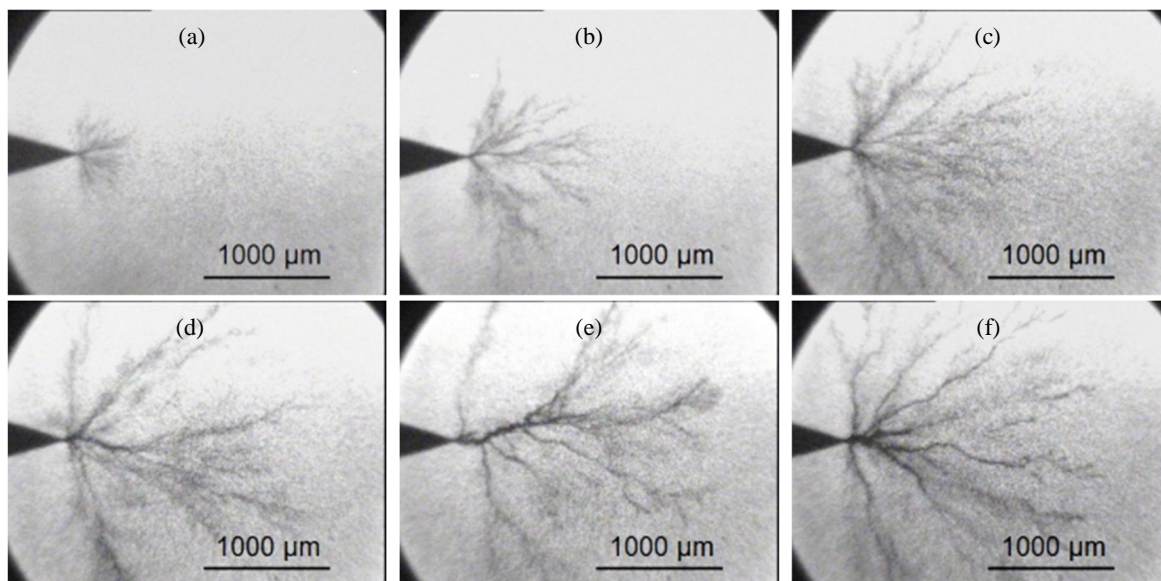
Fig 3.66 - Positive streamer in SE at 100°C 30 kV after: (a) 200 ns, (b) 400 ns, (c) 600 ns, (d) 800 ns, (e) 1000 ns, (f) 1200 ns

The propagation velocity (measured at the beginning of propagation up to 800 ns) increases slightly with temperature i.e.: at RT 2100 m/s and 100°C 2600 m/s as in Fig 3.68. Considering the applied voltage was switched off at 800 ns it seems that streamers stop immediately at RT, while still propagating for 200 ns more at 100°C.
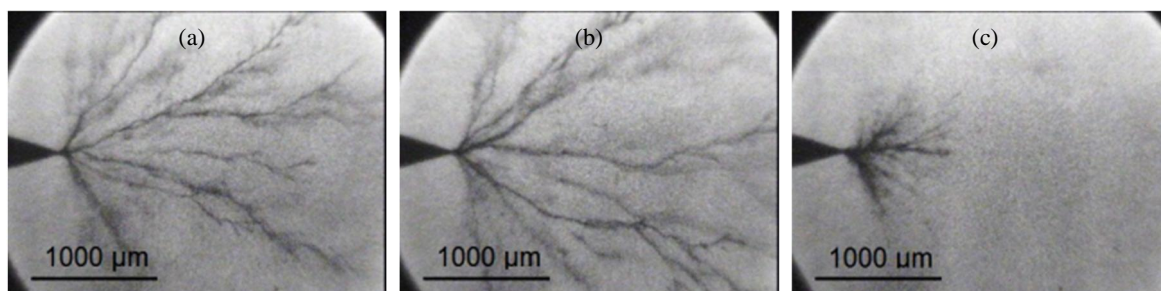
Fig 3.67 - Positive streamer in SE at 200°C 30 kV after: (a) 800 ns, (b) 1000 ns and (c) 2200 ns
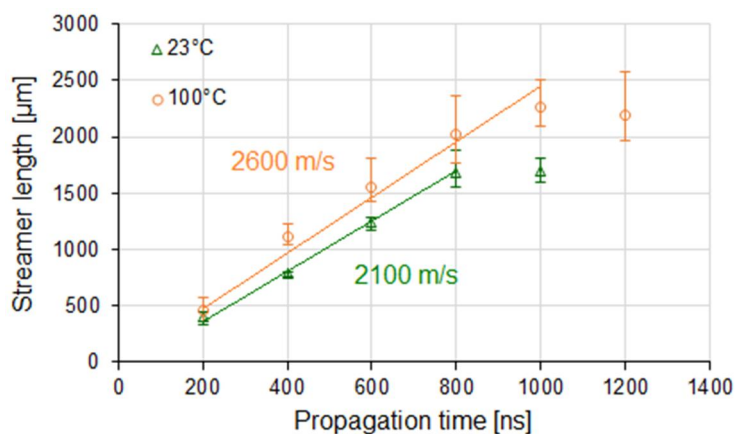
Fig 3.68 - Positive 2nd mode streamer propagation in SE at V_{app} = 30 kV, t_{HV} = 800 ns, average velocity = 2.3 km/s

3.3.3.4   1st mode negative streamer in PFPE

Similar to SE, negative streamers in PFPE show thick branches and tend to propagate at low velocity (Fig 3.69). The duration of HV pulse was set to t_{HV} = 0.8 µs. Image capture duration is 200 ns with delay time t_D from 200, 400, 600, 800 and 1000 ns. Streamer propagation was only measured at RT. Fig 3.69

shows the streamer propagation in PFPE at RT and 30 kV (100% inception voltage probability is 25 kV) for different time delay (t_D).
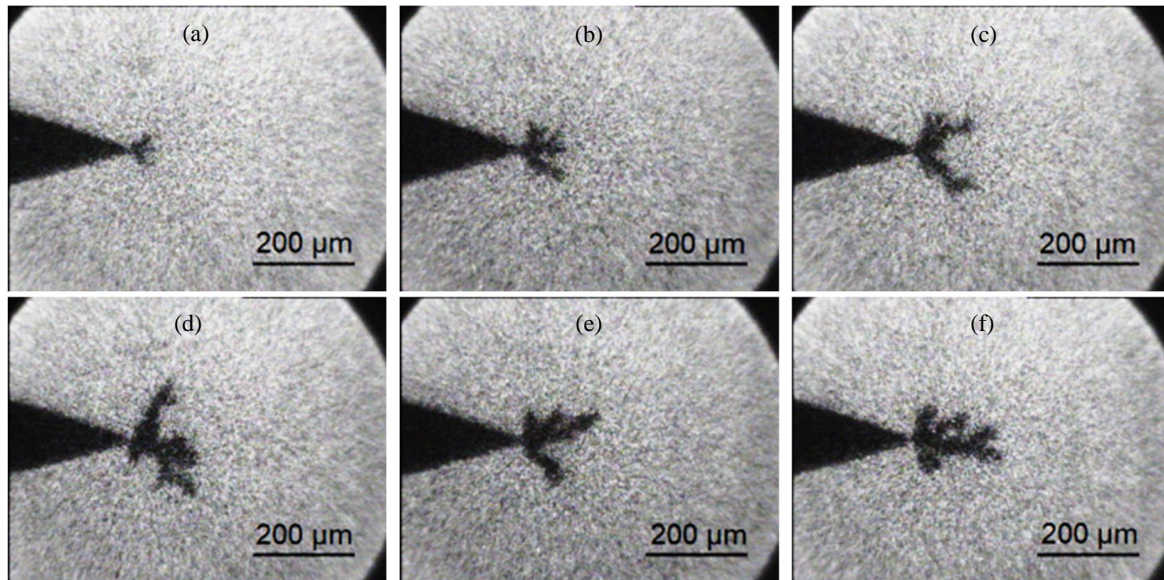
Fig 3.69 - Negative streamer in SE at 23°C 30 kV after: (a) 200 ns, (b) 400 ns, (c) 600 ns, (d) 800 ns, (e) 1000 ns and (f) 1200 ns

The 1st mode streamers grew up to 160 µm in 800 ns at RT (Fig 3.70). These streamers stopped when the applied voltage was switched off. The propagation velocity (measured at the beginning of propagation) at RT is 180 m/s, twice faster than in SE.
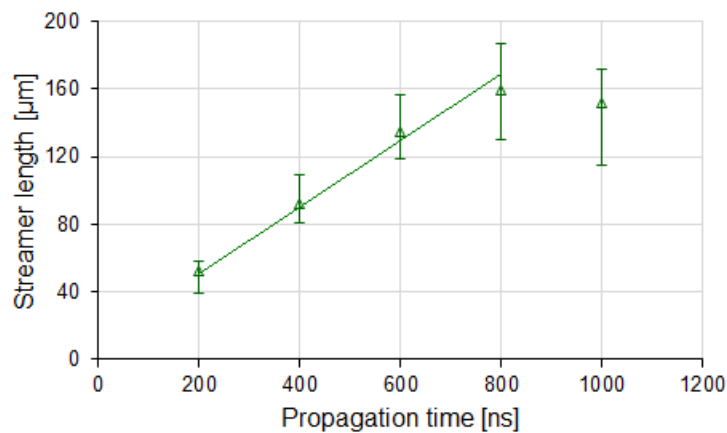
Fig 3.70 - Negative slow mode (1st) streamer propagation in PFPE at V_{app} = 30 kV, t_{HV} = 800 ns, average velocity = 180 m/s

3.3.3.5 Positive streamer in PFPE

In PFPE positive streamer observation was rather scarce since the streamer inception voltage is high and quite random, with a high risk of breakdown occurrence (even at 45% inception probability). A duration of HV pulse t_{HV} = 500 ns was set in order to prevent breakdown from occurring. Image capture duration was 120 ns with delay time (t_D) between 400 and 600 ns. Streamer propagation was measured only at RT and velocity evaluated based on these two time delays. Fig 3.71 shows the positive streamer propagation at RT and 30 kV (40% inception voltage probability) for different time delay (t_D). The 2nd mode filamentary streamers grew up to 1585 µm in 600 ns at RT (Fig 3.71).
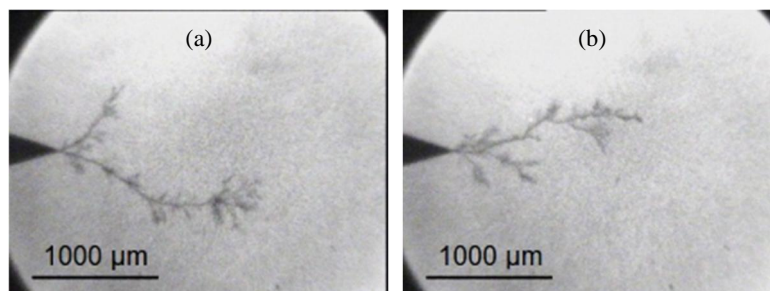
Fig 3.71 - Positive streamer in PFPE at 26°C 30 kV after: (a) 400 ns and (b) 600 ns

When temperature was raised to 100°C with applied impulse voltage 32.5 kV, the streamers propagated further (see Fig 3.72) exceeding the visualisation window. The average positive streamer propagation velocity in PFPE is 3.6 km/s at RT and at 100°C it may exceed 4.0 km/s.
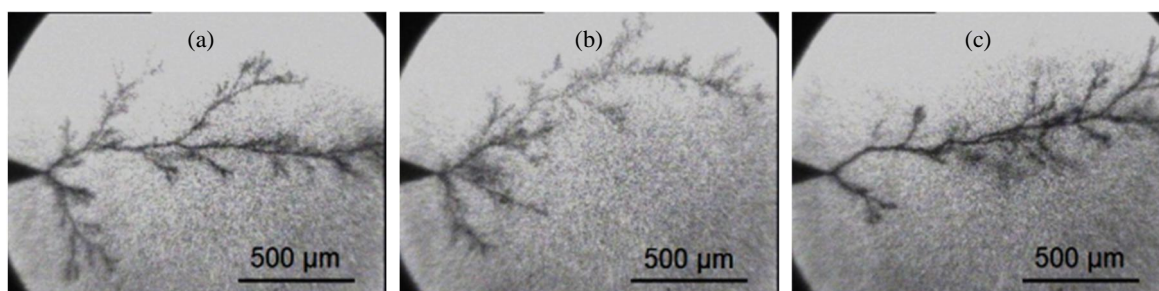
Fig 3.72 - Positive streamer in PFPE at 100°C 32.5 kV after 200 ns

Positive streamer propagation velocity in PFPE was calculated according to propagation time of 400 ns and 600 ns at RT, and 200 ns at 100°C as in Fig 3.73. Actual velocity at RT may be higher since the result was averaged from propagation length at 400 ns and 600 ns while it is probable the propagation has stopped at 500 ns as the applied voltage was switched off.
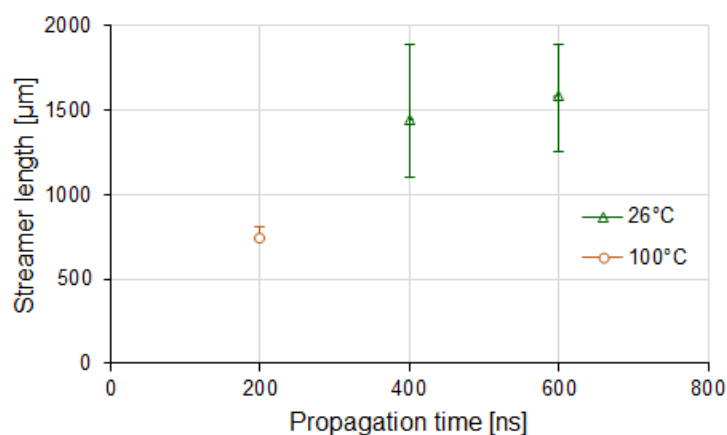
Fig 3.73 - Positive fast 2nd mode streamer propagation in PFPE at V_{app} = 33 kV, t_{HV} = 500 ns, average velocity = 3.12 km/s

3.3.4   Resume on streamers measurements in Jarytherm® DBT

In DBT, streamer characterization shows quite similar results to those previously obtained in a liquid of comparable chemical composition, the Jarylec® (mixture of mono- and di-benzyltoluene) [97]. In positive polarity, two streamer modes were observed in Jarylec®. The 1st mode showed a very limited propagation, and the 2nd mode with velocity around 1 km/s. 2nd mode streamers in Jarylec® were observed above V_2 = 12 kV (gap distance = 6 mm), i.e. a much lower value compared to DBT in the these measurements (25 kV). This large difference might be partly due to the fact that a longer voltage rise time (150 ns) was used here, instead of 20 ns in [97]. It was previously reported that the measured

threshold propagation voltage V_2 of 2nd mode streamers can be larger with longer rise time, due to the influence of injected space charge during the voltage rise [60].

However, it is obvious that in these liquids (mono and di benzyltoluene), the inception of filamentary streamers requires higher applied voltage as compared to many other liquids. In identical conditions of [97], 2nd mode streamers were observed above V_2 = 6.7 kV in mineral oil instead of 12 kV in Jarylec$^®$. In the present work, 2nd mode streamers are also observed in SE at lower voltage than in DBT (20 kV in SE instead of 25 kV in DBT), and their velocity is higher. In PFPE, despite the inception of filamentary streamers is comparable to DBT, the probability was highly scattered. When inception probability in DBT already reached 100%, it only appeared to be 45% in PFPE at 33 kV, but streamers lead to breakdown in a short time (Fig 3.51d) due to the high propagation velocity.

Increasing the temperature up to 200°C in DBT produces no large variation of streamer properties (inception voltage, propagation velocity), showing a good stability of this liquid at high temperature. A positive effect of temperature was even observed as shown in Fig 3.55 (increase of 2nd mode propagation voltage at 200°C). This is favourable for the application of this liquid in high temperature applications, such as power semiconductor encapsulation.

The observation that temperatures up to 200°C have a small influence on streamers is probably due to the fact that this temperature remains quite far from the boiling temperature (390°C in DBT). While temperature is increased, the conductivity of liquids strongly increases, starting from $5{\times}10^{-14}$ S/cm up to $1.5{\times}10^{-11}$ S/cm in DBT. In the same temperature range, viscosity decreases from 50 mm^2/s to 0.8 mm^2/s. The fact that neither streamer inception nor propagation show large variations when temperature changes confirm that liquid conductivity and viscosity are parameters of negligible influence on these processes.

The more conventional insulating liquid Midel$^®$ showed less interesting properties, with positive filamentary streamers observed at lower voltage than in DBT.

3.4   Conclusion

In this chapter, series of high electric field characterizations have been carried out with the dielectric liquid candidates. Especially for DBT, which is the most interesting candidate as alternative encapsulant for high temperature, electrical characterisations at high temperature have shown favourable dielectric properties: high breakdown strength in uniform field (higher than 30 kV/mm @ 300°C), and excellent partial discharge suppression properties. The following chapter will study the properties of dielectric liquids at high temperature, in terms of power module application for encapsulation of substrates.

4 | Characterization of Liquids at High Temperature with Power Electronics Substrates

Contents

The liquid characterization carried out in the previous chapters gives general descriptions on their properties at high temperature. Experiments were performed in liquids alone, which not truly represent the practical conditions existing in power electronics modules.

This chapter presents complementary works with the view to better assess the practical possibility of using dielectric liquid in electronics power module. Drawbacks and limitations in power module under cumulative stress of high electric field and temperature were described in chapter 1. Some critical situations involving the association of liquids and ceramic substrates were replicated and characterized in this chapter.

4.1 Ceramic substrate samples

Aluminium Oxide known as Alumina (Al_2O_3), Aluminium Nitride (AlN), and Silicon Nitride (Si_3N_4) are ceramic substrates commonly used in power electronics modules. Silicone Nitride has disadvantages at high temperature due to the presence of surface charges, which may result in discharges on the substrate or in the vicinity [98]. Alumina and AlN feature good behaviour at high temperature and at high fields. Dielectric characterization on different types of AlN substrates was carried out by Dagdag et al [99]. The insulating quality of AlN substrates mainly depends on the manufacturing processes: some exhibit good dielectric strength up to 450°C, and others not [99]. Compared to AlN, Alumina has some drawback due to its lower thermal conductivity.

TABLE 4.1 shows the main properties of ceramic materials commonly used as substrates in power electronics modules. Even though Silicon Nitride has the lowest coefficient of thermal expansion and dielectric constant with medium cost, its bulk resistivity is the lowest among commercial ceramic substrates. AlN cost is higher with superior properties, and Alumina constitutes a trade-off between several properties. Thus, we selected Alumina and AlN substrates to build application-oriented test objects in this research. In addition, we also conducted series of preliminary measurements on FR4 epoxy substrates, very cheap and easily processed, embedded in DBT and other dielectric liquids to compare their properties.

TABLE 4.1 - Properties of ceramic materials [98, 100-101]

Material	Alumina	Aluminium Nitride	Silicon Nitride	Silicon Carbide	Epoxy (FR4)
Chemical Formula	Al_3O_2	AlN	Si_3N_4	SiC	na
Melting point [°C]	2072	2397-2507	na	1478-1722	>120
Max. Temperature [°C]	1750	1027-1727	1000	297-697	na
Coefficient of Thermal Expansion [μm/°C]	7-8.4	4.3-5.6	3.3	7.9-11	11-15
Specific Heat [J/kg °C]	880	740-820	na	510-750	na
Thermal conductivity [W/m °C]	25.5-65	66-180	50-70	70-250	1.059
Dielectric Constant at 1 MHz	9.8	8.3-9.3	4.5-7.4	na	4.7
Bulk Resistivity [Ω/cm]	$> 10^{14}$	$> 10^{14}$	$> 10^{10}$	10^2-10^6	> 109
Dielectric strength [kV/mm]	16.9	17	17.7	na	20
Relative cost	1x	4x	2.5x	na	< 1x

Copper metallized Aluminium Nitride substrates are manufactured by Stellar Industries, and Alumina Curamic® Power substrates by Rogers Corporation. The thickness of ceramic substrates and copper metallization are 630 µm and 300 µm. Meanwhile, epoxy substrates are 1500 µm in thickness, with 35 µm cooper metallization. Substrate samples were etched chemically on two sides for PD measurements and only one side for breakdown measurement. Particularly for breakdown measurements, metallization on the other side was removed. For epoxy substrates, etching process was carried out until the electrodes configuration were completely shaped. For alumina substrates, etching process was initially done to remove one side of metallization, then to thin the remaining metallization from 300 µm down to 100 µm, and finalized by etching according to the electrode configuration. A thinner metallization was favourable to achieve a better resolution.
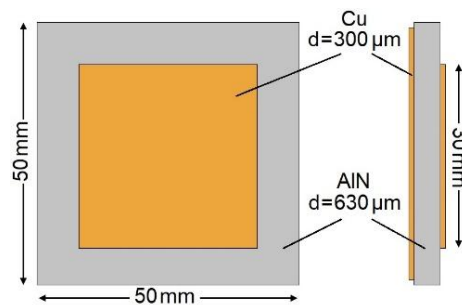
Fig 4.1 - Substrate samples geometry for PD and dielectric spectroscopy measurements

Square shaped samples as in Fig 4.1 were mainly used for dielectric spectroscopy and PDs measurements. Special samples were designed and built for surface breakdown measurements (Fig 4.2). The electrodes were set at various gap distance i.e.: 0.2 mm, 0.5 mm and 1 mm. Due to the etching process used, the actual gap distance achieved was slightly larger than the designation, particularly at shorter gap. Ceramic substrates were also cut to an octagonal shape (Fig 4.2c) with a diamond disk saw, in order to fit the cylindrical shape of the high temperature testcell.

For substrates embedded in liquids, a vacuum procedure was applied to remove dissolved gasses and water. Silicone gel (SYLGARD® 527) was prepared from the mixture of two base components in the same proportion. This mixture was stirred for 10 minutes and then degassed under vacuum for 10 minutes before pouring into aluminium cups containing substrate samples equipped with high voltage silicon cables. Cups filled with substrate samples and silicone gels were once again degassed under vacuum for 20 minutes at RT and proceed to curing procedure at 80°C under atmospheric pressure for 24 hours as recommended by the manufacturer. The use of HV silicon cables allowed heating samples up to 180 °C (Fig 4.2a).
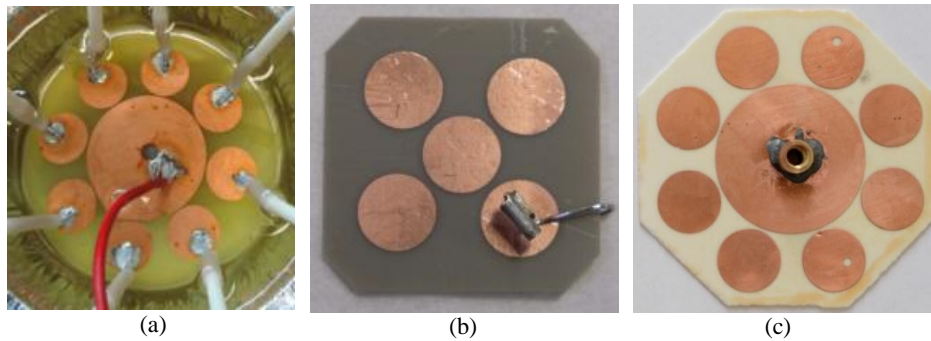
Fig 4.2 - Substrate samples for surface breakdown measurements: (a) epoxy with 8 breakdown electrodes in silicone gel, (b) AlN with 4 breakdown electrodes and (c) alumina with 8 breakdown electrodes

4.2 Dielectric Spectroscopy

4.2.1 Experimental set up and procedure

Similar procedures as in subsection 2.3.1 were applied in this experiment. Metallized substrate samples (AlN and Alumina) with electrodes as in Fig 4.1 were placed in the high temperature/high voltage testcell as shown in Fig 4.3. The larger copper metallization surface was connected to the ground-side at the top part of testcell, and smaller surface to high voltage terminal at the bottom part (Fig 4.1). In this way, a large field enhancement occurred at the edge of the smallest metallization connected to high voltage.

The testcell containing the substrate and DBT was degassed under vacuum for > 12 hours prior to dielectric spectroscopy and PD measurements. The average water content of DBT prior to experiments was 13 ppm and 72 ppm in SE. Since saturation limit of SE is 2700 ppm, this corresponded to 2.7% from saturation at room temperature. Saturation level of DBT is unknown.

After vacuum procedure was completed, nitrogen gas at 100 kPa was introduced, and a pressure sensor was used to monitor the evolution of pressure during heating cycles. A thermocouple was used to regulate and read the temperature of liquid.
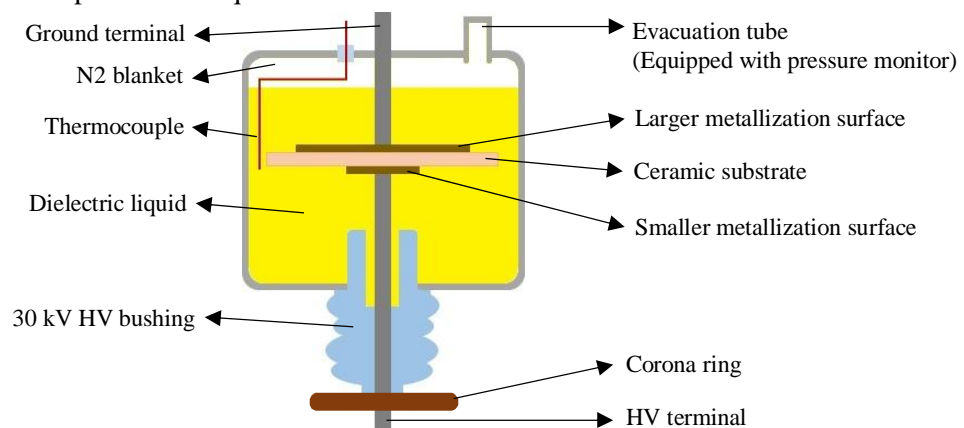
Fig 4.3 - Substrate sample in HT HV testcell for dielectric spectroscopy and PD measurements

4.2.2 Aluminium Nitride (AlN) dielectric spectroscopy up to 350°C

Fig 4.4 shows the relative permittivity of AlN substrate at various temperatures. At low frequency, the relative permittivity of AlN considerably increases with temperature, i.e.: 9.18 at RT and up to 6496 at 350°C (at 10 mHz). AlN shows a stable permittivity over the investigated frequency range only at room temperature. At 350°C the relative permittivity constantly drops as the frequency is raised up to 100 kHz, and remains stable at higher frequency range. This stable region of relative permittivity over frequency

gets narrower at high temperature. Such large variation of permittivity is not favourable for using AlN at high temperature where the field distribution will be strongly modified at high temperature.
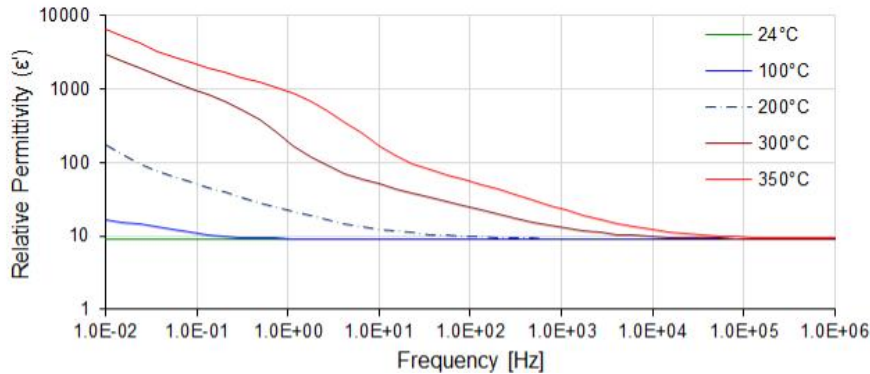
Fig 4.4 - Relative permittivity of AlN at various temperature

Fig 4.5 shows the tan (delta) of AlN substrate at various temperatures. On average, tan (delta) drops with frequency. When temperature raise, tan (delta) increases up to rather large values (about 1). AlN shows values typical of "good" insulating solids ($< 10^{-2}$) only at room temperature. Several weak rounded peaks observed on tan (delta) profiles at high temperature probably indicate relaxation processes, but no attempt was done to analyse in detail these mechanisms. At temperature above 200°C, high tan (delta) > 0.1 occupies a large frequency range from 10 mHz to 100 kHz. Although tan (delta) does not constitutes a parameter of primary importance for substrates, some thermal energy due to dielectric losses will be dissipated at these high temperature and high frequency region. However, it will probably remain much lower than that of semiconductors.
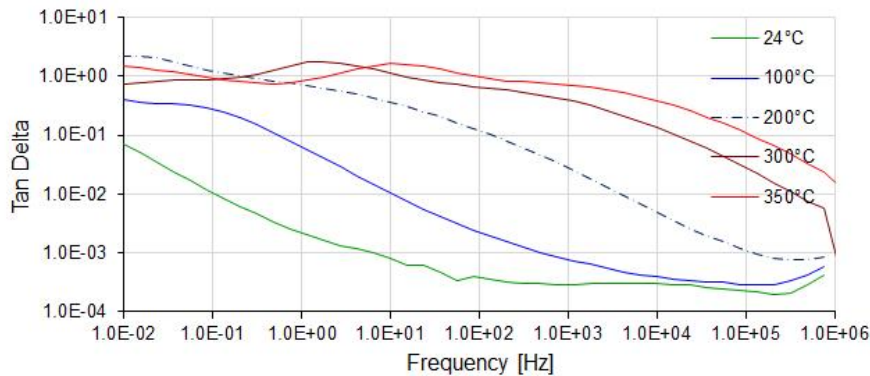
Fig 4.5 - Tan (delta) of AlN at various temperature

Fig 4.6 shows the ac conductivity of AlN substrate at various temperatures. The conductivity of AlN is frequency and temperature dependent. For frequency 10 mHz under temperature variation, it increases from 3.63×10^{-15} S/cm at RT to 5.51×10^{-11} S/cm at 350°C. The plots do not show a region where a stable DC conductivity exists.
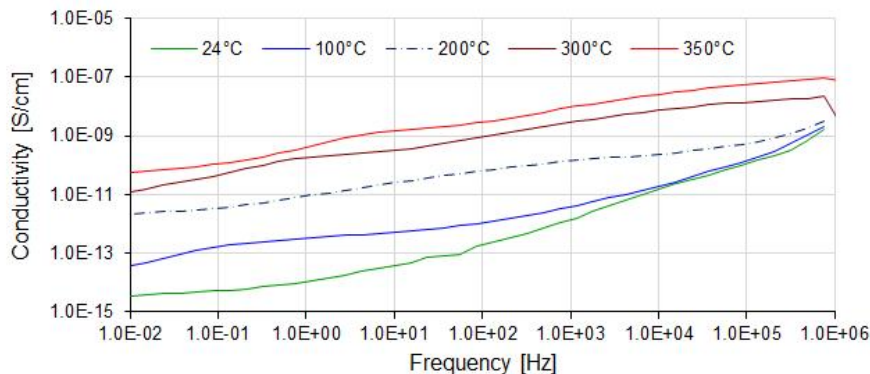
Fig 4.6 - AC conductivity of AlN at various temperature

4.2.3 Alumina (Al$_2$O$_3$) dielectric spectroscopy

Fig 4.7 shows relative permittivity of alumina substrate at various temperature. At low frequency, relative permittivity of alumina increases with temperature but maximum values are much lower compared to AlN (100 at 350°C and 10 mHz). Relative permittivity has larger stable region at corresponding temperatures, especially above 1 kHz.
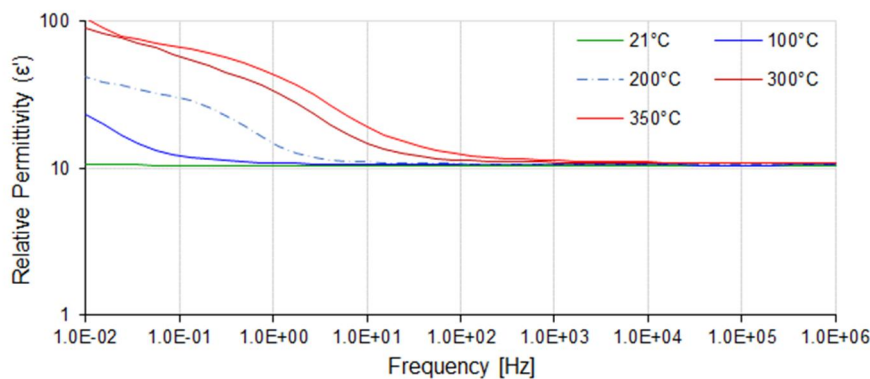
Fig 4.7- Relative permittivity of alumina at various temperature

Fig 4.8 shows the tan (delta) of alumina substrate at various temperature. Tan (delta) drops with frequency and increase with temperature.
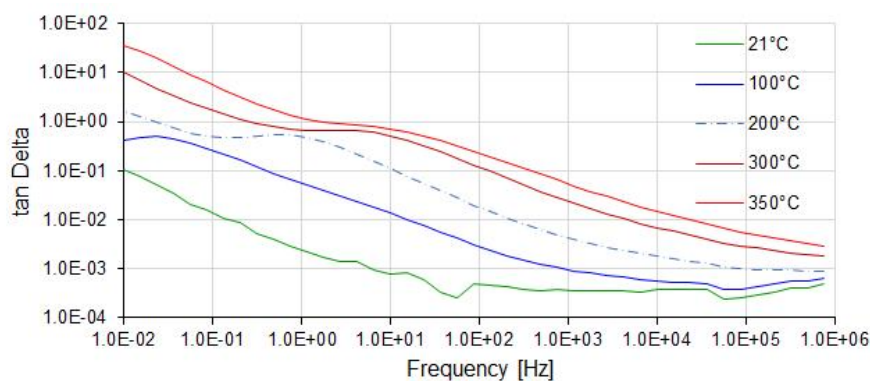
Fig 4.8 - Tan (delta) of alumina at various temperature

Fig 4.9 shows the AC conductivity of alumina substrate at various temperature. The conductivity of alumina is frequency and temperature dependent. There is a limited frequency range (10 mHz -100 mHz at 350°C) where the conductivity is nearly frequency-independent, and therefore corresponds to a true DC conductivity (about 10^{-11} S/cm).
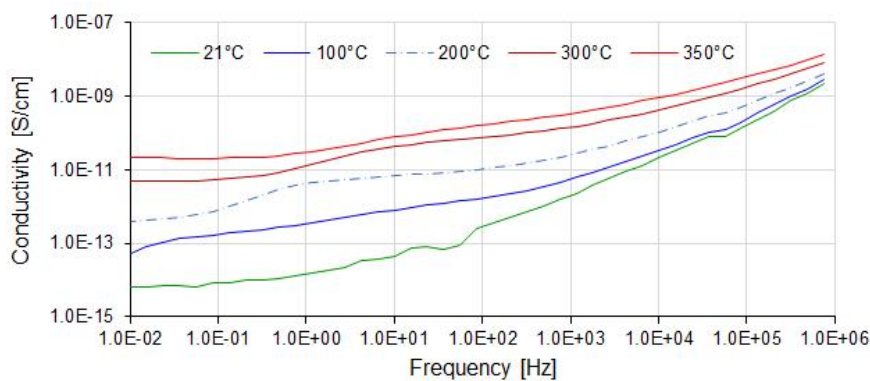
Fig 4.9 - Conductivity of alumina at various temperature

4.2.4   Comparison with liquid DBT properties

Fig 4.10 shows the dielectric spectroscopy comparison for DBT alone and ceramic substrates embedded in DBT at 50 Hz (i.e. relevant to PD measurements) and 1 MHz (relevant to impulse breakdown measurements). At high frequency (1 MHz), relative permittivity of DBT and ceramic substrates are rather stable over all temperatures. In contrast to those at 50 Hz, the relative permittivity of AlN strongly deviates above 100°C. In turn, a large modification of the field distribution can be expected at high temperature with this material. Both AlN and DBT show large losses (tan (delta) > 1) at 350°C. The influence of these properties on the field distribution will be estimated by numerical calculation.
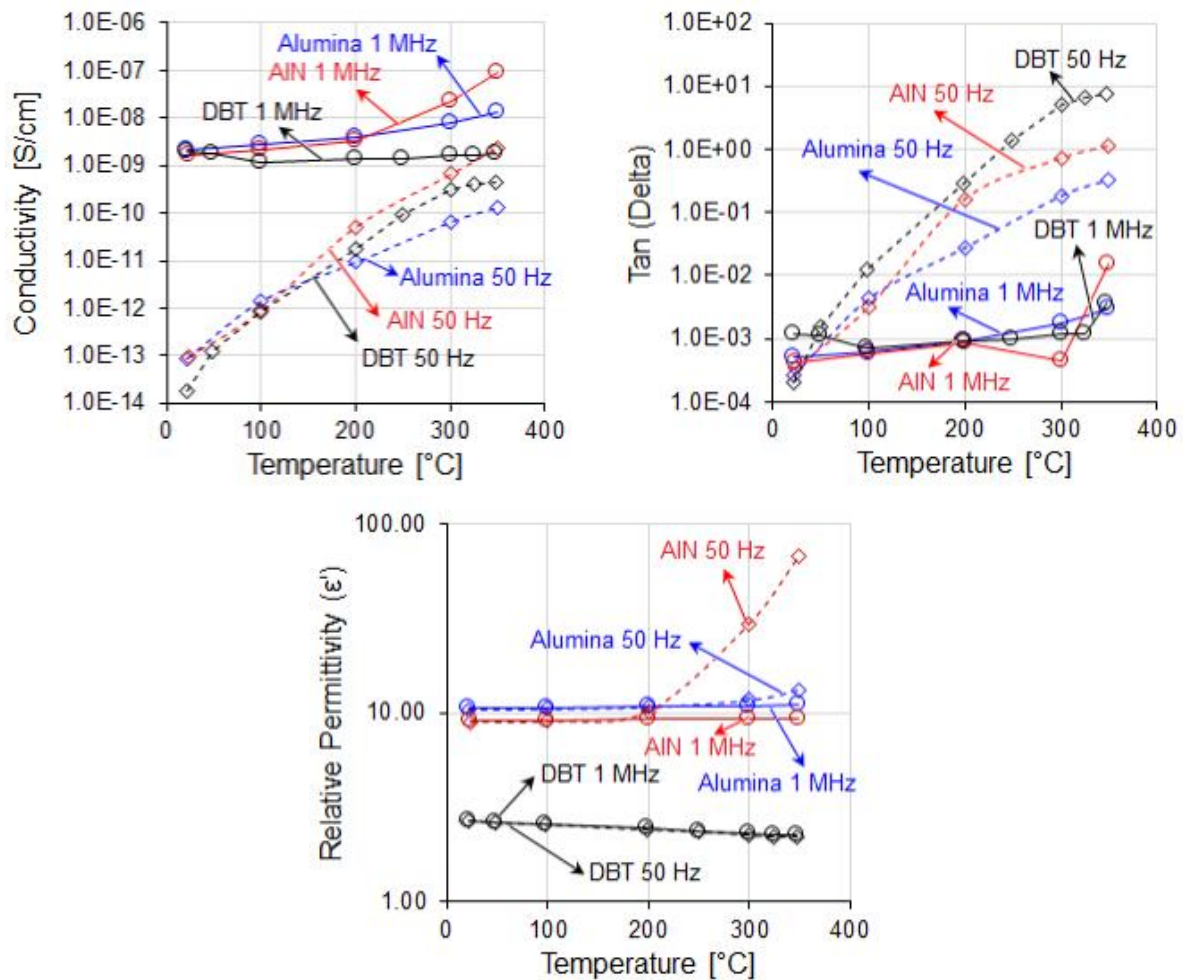
Fig 4.10 - Dielectric spectroscopy comparison for DBT only and ceramic substrates embedded in DBT: conductivity, tan (delta) and relative permittivity

4.3   Surface breakdown measurements under DC voltage

The occurrence of breakdown between adjacent metallized tracks at different potentials on a substrate constitutes a key question concerning high voltage modules. Two main types of voltage exist within a power module: DC and impulse voltages with fast rise time due to switching. Both cases will be considered here. DC breakdown measurements between tracks were carried out with 3 substrates types (epoxy, AlN, and Alumina), embedded in different liquids (DBT, SE and PFPE). In order to have a reference value with the standard silicone gel encapsulation, breakdown experiments were also done with this material. The influence of gap distance between 0.2-1.0 mm was investigated, with temperature up to 160°C for epoxy substrate. For AlN substrates embedded in DBT, some preliminary experiments were done under AC and DC at RT. Most of results were obtained with alumina, due to the availability

and cheaper cost of this material. Indeed, tests on more samples are necessary to achieve better accuracy. For alumina substrates embedded in silicone gel, breakdown measurements were done up to 160°C, and in DBT up to 200°C. For practical reasons, it was unfortunately impossible to do a large number of breakdown measurements at the maximum temperature (350°C). This would require running in parallel a large number of complex and expansive high temperature and high voltage testcells. For practical reasons, a multi-electrode breakdown testcell was developed, but its maximum temperature was limited to 200°C.

4.3.1 Experimental set up

DC breakdown measurements were carried out with the same set up as in section 3.1.1. A DC ramp (1 kV/s) was applied until breakdown occurred. The only difference is the testcell containing 8 breakdown electrodes on a single substrate sample. This allowed obtaining 8 breakdown measurements in a single series, without opening the testcell and change samples (Fig 4.2). The top closure of the testcell is made of PTFE (Teflon®), with Viton® O-rings as sealing system. Nevertheless, this is not a perfectly tight testcell as one used in liquids breakdowns measurements (chapter 3). Two types of high voltage connections were used according to the substrates under test:

1. Epoxy substrate: testing electrodes were directly connected to a HV silicon insulated cable, Fig 4.11d. The highest temperature was limited by epoxy to 160°C.
2. Alumina substrate: testing electrodes were connected via springs held by stainless steel tubes, insulated by Teflon®, Fig 4.11c. This connection system can withstand a maximum temperature of 200°C.

At each breakdown test, only one testing electrode was connected to the HV source, while others were grounded. Grounding of the testcell, heater, and thermocouples were separated from the ground return path for breakdown, in order to avoid interferences and proper detection of breakdown.

(a) (b) (c) (d)
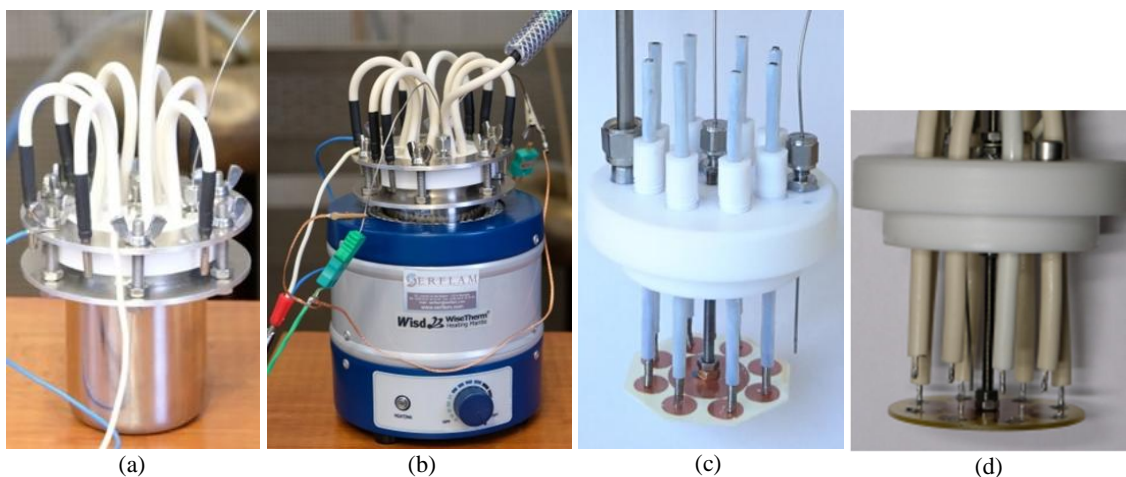
Fig 4.11 - High-temperature high-voltage breakdown testcells: (a) flexible silicone cable connection for epoxy substrates, (b) testcell with heating system and HV DC source connection, (c) spring and Teflon insulated tubes connection for alumina substrates, (d) Silicone cable connexion for epoxy substrates

This testcell is equipped with two thermocouples: close to the central grounded electrode, and near the wall of testcell to observe the uniformity of heating. Fig 4.12 shows the experimental set up for surface breakdown measurements with ceramic substrates. A 44 kΩ limiting resistor was connected in series to limit the breakdown energy. DC supply was interrupted 1 ms after the breakdown.
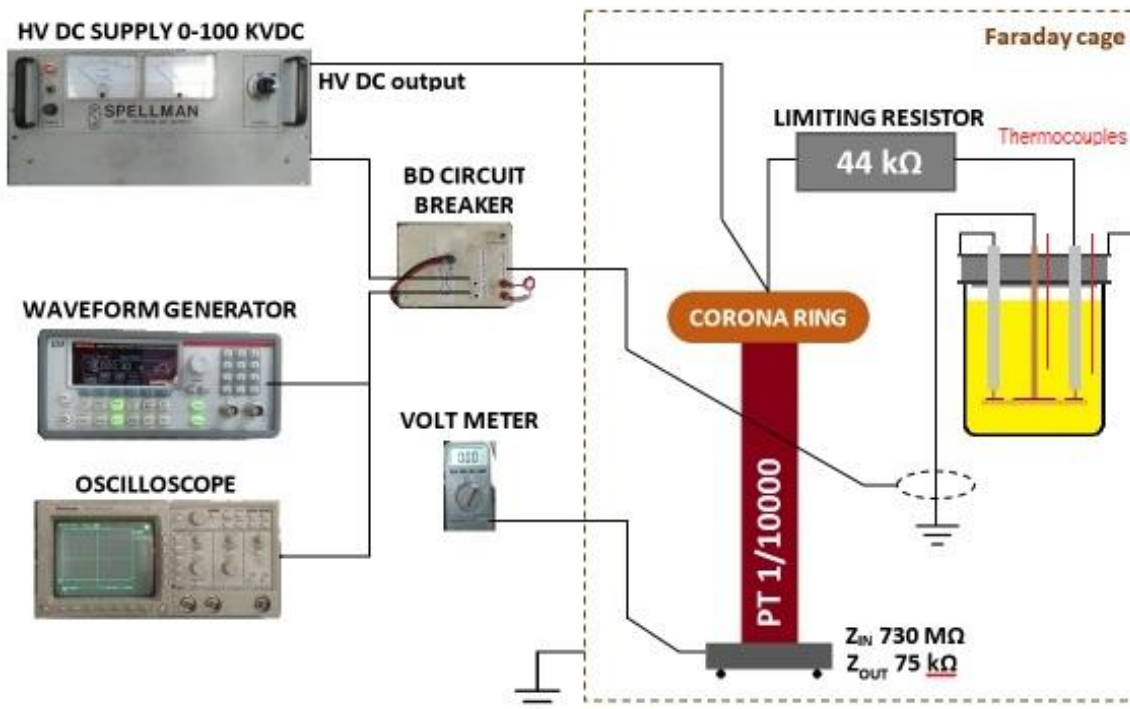
Fig 4.12 - DC breakdown experimental set up

4.3.2   Measurements with Epoxy substrates versus gap distance and liquid nature

The following series of breakdown measurements were first intended to investigate the influence of gap distance and nature of the liquid.

4.3.2.1   Epoxy substrate samples

Substrates were etched chemically with 8 high voltage electrodes (diameter 12 mm) surrounding a grounded central electrode (Fig 4.2a). Breakdown occurred in the small gap (g) between high voltage and grounded electrode. 3 gap distances were investigated: g = 0.3 mm, 0.5 mm and 1.0 mm. Due to variations during the etching process, the actual gap distance ranged from 0.2-0.4 mm (0.3 mm gap), 0.5-0.6 mm (0.5 mm gap), and 1.0-1.1 mm (1.0 mm gap). The actual gap g was measured for all investigated samples.

4.3.2.2   Epoxy substrates in DBT: repeatability tests

Series of DC breakdown tests were carried out on 6 substrate samples of with various gap distance (TABLE 4.2) at RT under atmospheric pressure. 20 consecutive shots were carried out with gap 0.2-0.5 mm, and 5 shots with largest ones. Rest time between each shot was > 3 minutes.

Fig 4.13 shows typical DC breakdown test series results correspond to different distances. At the shortest gap (g = 0.2 mm) and correspondingly lowest breakdown voltage, DC breakdown voltages (BDVs) are fluctuating while remaining rather repeatable around some mean value. In medium gap (0.5 mm) a progressive degradation was observed, and at larger gaps (1 mm) BDV immediately dropped after the first shot. The corresponding average breakdown field (DC BDV/g) decreases when g is increased, both for first and subsequent breakdown. The difference between first and subsequent average values (TABLE 4.2) show the degradation observed above 0.5 mm, when the initial breakdown voltage exceeded about 25 kV. Fig 4.14 shows images of the corresponding irreversible degradation. The breakdown arc partly propagated through epoxy. In short gaps (and correspondingly breakdown voltages below 20 kV), no similar degradation was observed.
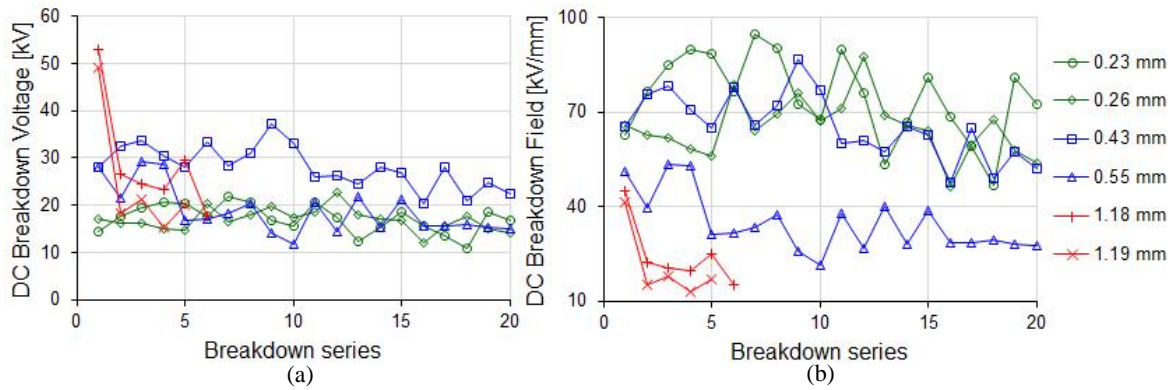
Fig 4.13 - DC breakdown voltage series of epoxy substrate embedded in DBT at RT (a) BDV and (b) average field strength

TABLE 4.2 - Breakdown voltage of epoxy substrate in DBT samples at various gaps

Sample N°	1	2	3	4	5	6
Gap [µm]	0.23	0.26	0.43	0.55	1.18	1.19
BDV [kV] 1st	14.4	17.1	28.1	27.9	53.0	49.2
BDV [kV] mean	17.2	16.9	28.2	18.4	29.1	24.8

(a)   (b)
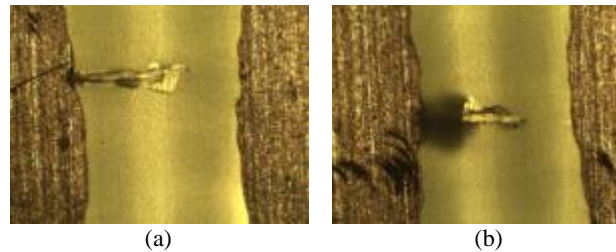
Fig 4.14 - Final samples condition after series of DC breakdown tests (a) 1.18 mm and (b) 1.19 mm

4.3.2.3   DC breakdown series with epoxy substrates in DBT

A typical series of measurements with g = 0.3 mm is presented in TABLE 4.3. Ten shots were carried out with each testing electrode. After tests, no trace of irreversible degradation could be seen on the substrate (Fig 4.15). Therefore, breakdowns likely occurred in DBT above the epoxy surface. The mean BDV of all testing electrodes (based only on the first measurement) is 15.5 kV at mean gap g = 370 µm. Mean breakdown field from these 1st shots is 42.1 kV/mm, scattering from 24.4 kV/mm to 54.1 kV/mm. Mean BDV and field of 1st shot is only 1% higher than mean of all series, showing that no modification of the substrate occurred.

TABLE 4.3 - Breakdown voltage of epoxy substrate in DBT samples group 0.3 mm

Testing electrode N°	1	2	3	4	5	6	7	8
Gap [µm]	364	362	364	375	357	347	376	410
BDV [kV] 1st shot	8.9	14.8	9.8	18.8	19.2	18.8	16.4	17.6
BDV [kV] mean of 10 shots	7.8	15.0	12.8	17.6	18.5	16.6	17.1	18.6
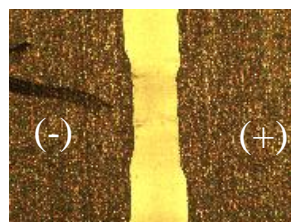
Fig 4.15 - Final condition after series of DC breakdown test of testing point n°4: 375 µm

TABLE 4.4 shows the results obtained with g = 0.5 mm. Ten shots were carried out at each testing electrode, unless the results dropped significantly (< 50% of 1st shot, then measurement was stopped). The mean BDV (based only on the first measurement) is 22.3 kV at mean gap of 574 µm. Mean

breakdown field of these 1st shots is 38.8 kV/mm scattering from 25.7 kV/mm to 48.5 kV/mm. Mean BDV and field of 1st shot is approx. 10% higher than mean of all series. Electrode no. 5 and 6 only took 5 and 6 shots since the final results reduced to 12.9 kV and 10.5 kV.

TABLE 4.4 - Breakdown voltage of epoxy substrate in DBT samples group 0.5 mm

Testing electrode N°	1	2	3	4	5	6	7	8
Gap [µm]	559	561	583	566	591	585	575	602
BDV [kV] 1st shot	17.6	14.4	22.1	24.4	28.7	22.4	24.8	24
BDV [kV] mean of 10 shots	19.6	20.9	22.2	16.9	18.0	17.5	22.7	18.3

Irreversible degradation of epoxy can be seen in testing electrodes in Fig 4.16. They always occurred close to the left electrode connected to negative polarity.

(a)   (b)   (c)   (d)   (e)
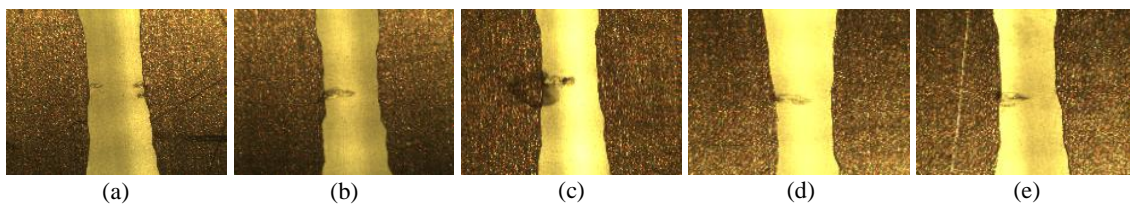
Fig 4.16 - Samples group 0.5 mm, breakdown in the substrate and traces from negative electrode for testing electrodes number: (a) 3, (b) 4, (c) 5, (d) 6 and (e) 8

TABLE 4.5 shows the results obtained with g = 1.0 mm. Five shots were carried out to each testing electrode. The mean BDV (based only on the first measurement) is 39.5 kV at mean gap of 1.1 µm. Mean breakdown field of these 1st shots is 36.3 kV/mm scattering from 26.5 kV/mm to 42.2 kV/mm. Mean BDV and field of 1st shot is approx. 20% higher than mean of all series. Large breakdown traces are evidenced, starting from both negative and positive electrodes (Fig 4.17). Further BD tests lead to BDV less than 25 kV.

TABLE 4.5 - Breakdown voltage of epoxy substrate in DBT samples group 1.0 mm

Testing electrode N°	1	2	3	4	5	6	7	8
Gap [µm]	1059	1089	1090	1097	1117	1096	1089	1067
BDV [kV] 1st shot	28.1	41	33.8	43.2	40.8	40	46	43.2
BDV [kV] mean of 10 shots	31.3	32.8	25.4	25.8	33	34	43	35.2

(a)   (b)   (c)   (d)

(e)   (f)   (g)   (h)
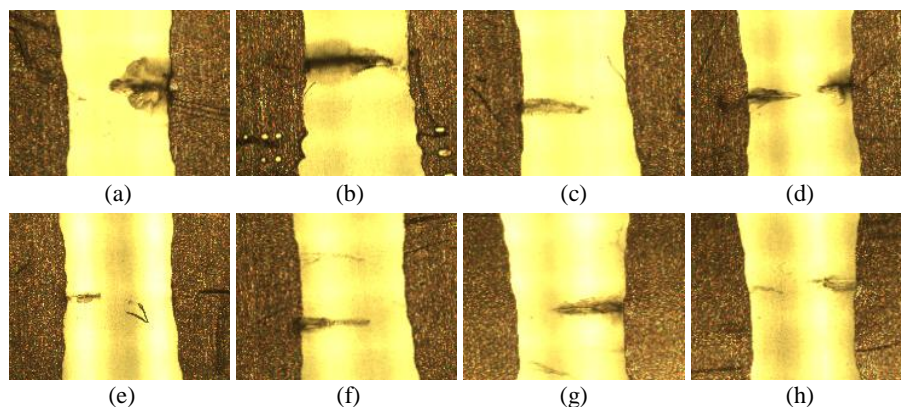
Fig 4.17 - Samples group 1.0 mm, breakdown in the substrate and traces from negative electrode for testing electrodes number: (a) 1, (b) 2, (c) 3, (d) 4, (e) 5, (f) 6, (g) 7 and (h) 8

Fig 4.18 shows the DC breakdown voltages at different gap distances. The corresponding average breakdown field (DC BDV/g) remains quite constant (close to 35 kV/mm), but the scatter increases at short gaps.
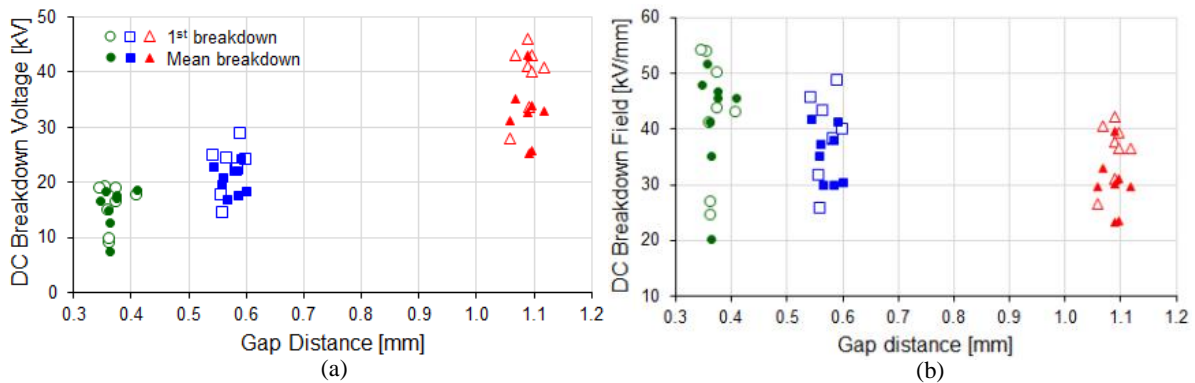
Fig 4.18 - DC breakdown on epoxy substrates embedded in DBT at various gap distance: (a) breakdown voltage and (b) breakdown electric field

4.3.2.4 DC breakdown of epoxy substrates in SE

Samples with g = 0.3 mm gap showed no trace of breakdown after five shots. The mean BDV (based only on the first measurement) is 16.9 kV at mean gap of 368 µm. Mean breakdown field of these 1st shots is 45.9 kV/mm scattering from 42.2 kV/mm to 51.4 kV/mm. Mean BDV and field of 1st shot is 8% higher than mean of all series. The 1st BDV did not differ from subsequent ones as shown in TABLE 4.6.

TABLE 4.6 - Breakdown voltage of epoxy substrate in SE samples group 0.3 mm

Testing electrode N°	1	2	3	4	5	6	7	8
Gap [µm]	367	372	348	360	421	371	350	358
BDV [kV] 1st shot	18.9	16.3	16.8	15.2	18	18.3	16	15.8
BDV [kV] mean of 5 shots	17	15	15.3	13.9	17.2	18.5	14	14.1

Samples with g = 0.5 mm gap distance also showed no trace of breakdown after five shots. The mean BDV is 20.4 kV at mean gap of 571 µm. Mean breakdown field of these 1st shots is 36 kV/mm scattering from 26.5 kV/mm to 49.7 kV/mm. The 1st BDV did not differ from subsequent ones as shown in TABLE 4.7.

TABLE 4.7 - Breakdown voltage of epoxy substrate in SE samples group 0.5 mm

Testing electrode N°	1	2	3	4	5	6	7	8
Gap [µm]	579	573	560	543	485	615	580	634
BDV [kV] 1st shot	20	21.6	20.8	14.4	24.1	19.6	22.1	20.4
BDV [kV] mean of 5 shots	21.6	18.8	16.2	17.5	19.4	21.4	21.9	19.2

Samples with g = 1 mm gap distance again showed no trace of breakdown after five shots. The mean BDV of these 1st shots is 26.7 kV at mean gap of 1144 µm. The 1st BDV did not differ from subsequent ones as shown in in TABLE 4.8.

TABLE 4.8 - Breakdown voltage of epoxy substrate in SE samples group 1.0 mm

Testing electrode N°	1	2	3	4	5	6	7	8
Gap [µm]	1163	1100	1146	1161	1200	1191	1087	1103
BDV [kV] 1st shot	28.8	26.4	23.2	25.6	29.6	28.8	27.6	23.6
BDV [kV] mean of 5 shots	29	26.1	24.1	25.2	30.2	27.7	27.8	24.7

The fact that all samples embedded in SE remained in good condition after DC breakdown series is correlated to the much lower first breakdown voltages (68%) recorded in SE (26.7 kV at 1 mm) compared to DBT (39.5 kV at 1 mm).

In contrast with DBT, the average breakdown field decreases with distance (Fig 4.19b), and are also less scattered, especially at short gaps. At g = 0.2 mm, the lowest values observed in DBT (25 kV/mm) are not observed in SE (minimum: 42 kV/mm).

<center>(a)   (b)</center>
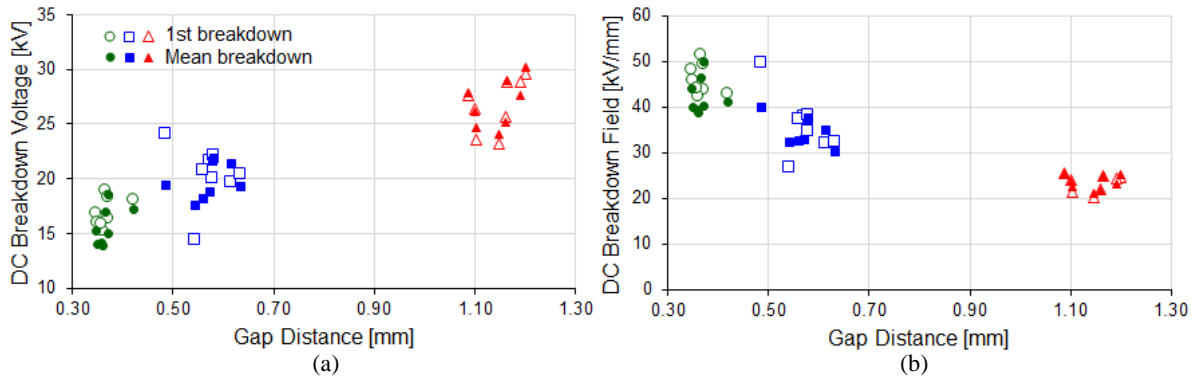
Fig 4.19 - DC breakdown on epoxy substrates embedded in SE at various gap distance: (a) breakdown voltage and (b) average breakdown electric field

4.3.2.5   DC breakdown of epoxy substrates in PFPE

As well as in SE, samples with g = 0.3 mm, 0.5 mm and 1mm showed no traces of breakdown after series of 5 shots to each sample. Breakdowns also likely occurred in the liquid, not in the substrates. The corresponding values are quoted in TABLE 4.9, TABLE 4.10, and TABLE 4.11.

TABLE 4.9 - Breakdown voltage of epoxy substrate in PFPE samples group 0.2 mm

Testing electrode N°	1	2	3	4	5	6	7	8
Gap [µm]	367	372	348	360	421	371	350	358
BDV [kV] 1st shot	21.3	19.2	16.8	15.6	22	9.6	18	16.2
BDV [kV] mean of 5 shots	20.3	18.4	16.9	15.9	17.5	11.4	15.9	15.1

TABLE 4.10 - Breakdown voltage of epoxy substrate in PFPE samples group 0.5 mm

Testing electrode N°	1	2	3	4	5	6	7	8
Gap [µm]	579	573	560	543	485	615	580	634
BDV [kV] 1st shot	26	24	22.1	24.4	25.2	20	21.8	20.4
BDV [kV] mean of 5 shots	25.8	21.8	21.6	22.3	23.4	21.1	21.9	23.2

TABLE 4.11 - Breakdown voltage of epoxy substrate in PFPE samples group 1.0 mm

Testing electrode N°	1	2	3	4	5	6	7	8
Gap [µm]	1163	1100	1146	1161	1200	1191	1087	1103
BDV [kV] 1st shot	34.4	30.4	25.6	29.6	27.6	28.4	26.4	29.6
BDV [kV] mean of 5 shots	32.4	31.2	29.2	29.5	31.4	30.5	29.6	25.9

Fig 4.20 shows comparison of DC BDV and fields at various gap distances. As in SE, the average breakdown field decreases with distance and show comparable values, but with a larger scatter.

<center>(a)   (b)</center>
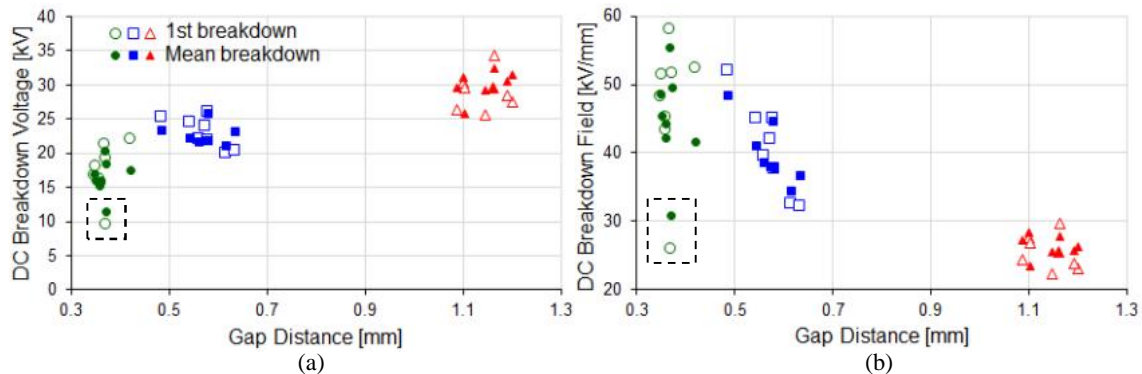
Fig 4.20 - DC breakdown on epoxy substrates embedded in PFPE at various gap distance: (a) breakdown voltage and (b) breakdown electric field

4.3.2.6 DC breakdown of epoxy substrates in silicone gel

For epoxy substrates embedded in silicone gel, only one DC breakdown measurement was carried out to each testing electrode. Breakdown occurred in the gel and produced immediate irreversible degradation, evidenced by black residues and cavities forming "tunnels" between electrodes (Fig 4.21). The subsequent tries resulted in almost zero breakdown voltage, indicating that breakdown created a short circuit. There were 4 groups of gaps in these tests i.e. g = 1.0 mm, 0.7 mm, 0.5 mm and 0.3 mm. The mean BDVs are shown in TABLE 4.12.

TABLE 4.12 - DC Breakdown voltage of epoxy substrate in silicone gel samples for various gap distance

Testing electrode N°	1	2	3	4	5	6	7	8
Gap [µm]	1150	1137	755	739	587	576	363	358
BDV [kV]	49.2	39.8	28	34	25.6	21.6	23.2	16.4

(a)　　　　　　　　　　　(b)　　　　　　　　　　　(c)
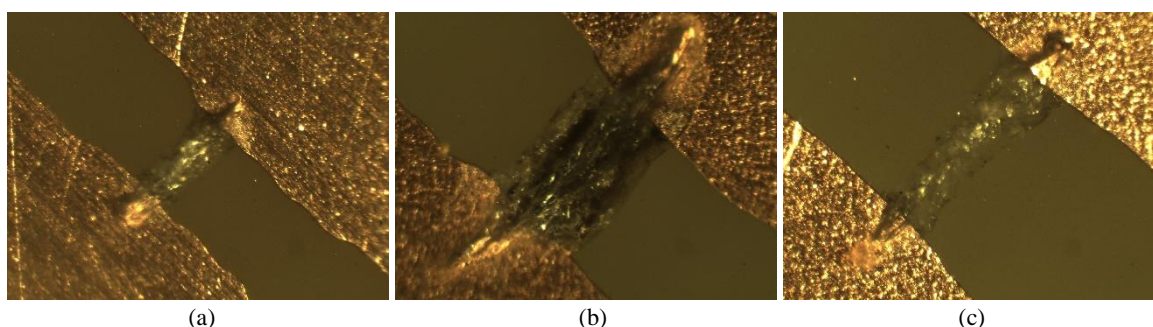
Fig 4.21 - Bridging in silicone gel after DC breakdown at gap: (a) 0.358 mm, (b) 0.587 mm and (c) 0.576 mm

Fig 4.22 shows the breakdown voltage and breakdown field at various gaps in silicone gel. On average, the breakdown field decreases with distance.

(a)　　　　　　　　　　　　　　　　　(b)
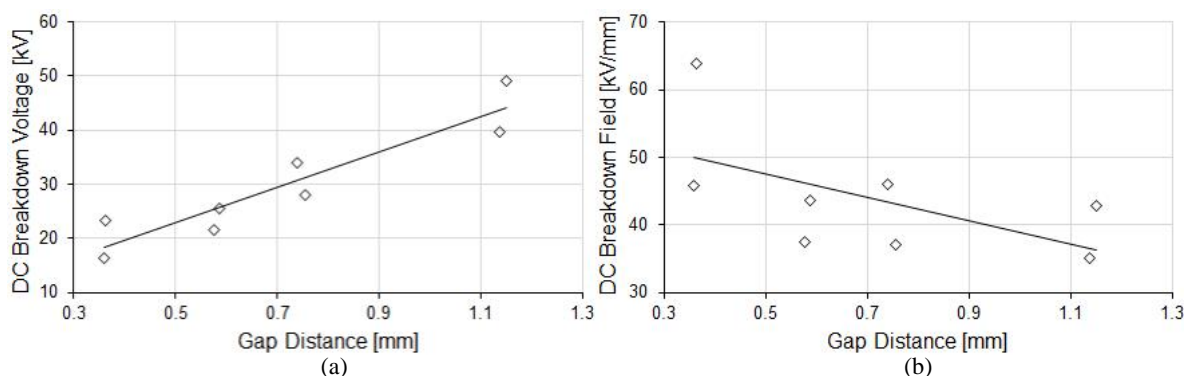
Fig 4.22 - DC breakdown on epoxy substrates embedded in silicone gel at various gap distance: (a) breakdown voltage and (b) breakdown electric field

4.3.2.7 Resume on DC breakdown of epoxy substrates

Most of substrate samples from medium and large gaps embedded in DBT showed degradation. The measured breakdown voltage can therefore be attributed to a breakdown process occurring within the substrates rather than in DBT, except with smaller gaps.

Fig 4.23 shows the comparison of 1st DC breakdown voltage and breakdown field for epoxy substrate embedded in dielectric liquids and silicone gel. Vertical and horizontal error bars indicate the range of maximum and minimum breakdown voltages, and gap. On average, the largest breakdown fields were recorded in silicone gel. The lowest are recorded either in DBT at 0.2 mm gap, or in SE and PFPE at 1 mm gaps. DBT is almost equivalent to silicone gel at 0.5 mm and 1mm gaps, but with a larger scatter.

In SE and PFPE, breakdown occurred in the liquid for all cases, indicating that liquid constituted the weakest material compared to epoxy. The larger breakdown voltage recorded in DBT at g = 1 mm

correlated to large degradations indicates that epoxy constitutes the weakest material in this situation. With silicone gel, the breakdown "tunnels" observed suggest that breakdown occurred mainly through gel, as in SE and PFPE.

(a)   (b)
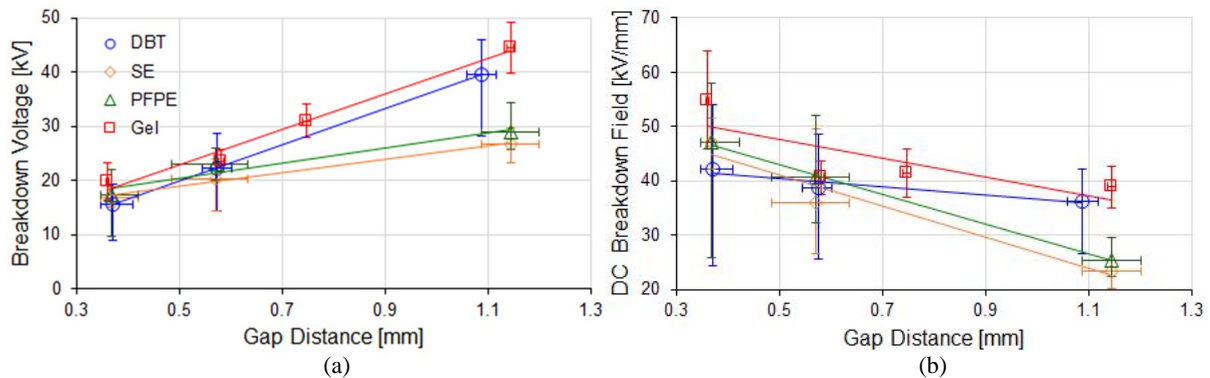
Fig 4.23 - 1ˢᵗ DC breakdown at RT on epoxy substrates embedded in dielectric liquids and silicone gel comparison

4.3.3   Breakdown with epoxy substrates under variation of temperature

4.3.3.1   DC breakdown of epoxy substrates in silicone gel

DC breakdowns of epoxy substrates in silicone gel were carried out with three samples at RT and 160°C. Only one measurement was performed to each testing electrode.

Fig 4.24 shows substrate samples embedded in silicone gel for new condition, and after measurements at 160°C. New silicone gel was transparent and clear, while epoxy substrate was light green (Fig 4.24a). After 160°C exposure for some hours, the gel turned dark and less transparent (Fig 4.24b) meanwhile epoxy became brown as well as the copper metallization (Fig 4.24c).

(a)   (b)   (c)
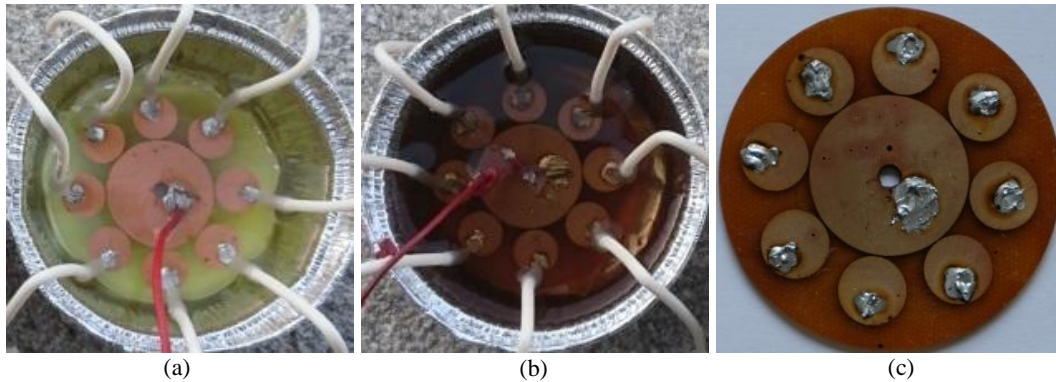
Fig 4.24 - Epoxy substrate embedded in Sylgard® 527 silicone gel: (a) new samples, (b) after 160°C and (c) epoxy substrates after 160°C

Breakdown measurements at RT on epoxy sample A4 are shown in TABLE 4.13. Mean breakdown field is 45.5 kV/mm scattering from 41.3 kV/mm to 48.2 kV/mm.

TABLE 4.13 - DC breakdown result of epoxy substrate embedded in silicone gel at RT: sample A4

Testing electrode N°	1	2	3	4	5	6	7	8
Gap [µm]	281	322	373	329	246	306	396	306
BDV [kV]	12	13.3	16.8	15.2	11.5	14.4	19.1	14.4

Breakdown creates a permanent "tunnel" containing carbon residue between electrodes (Fig 4.25) and they were not always tunnelling through the shortest distance between 2 electrodes. This corresponds to the high field enhancement at the point where the breakdown occurs.

(a)   (b)
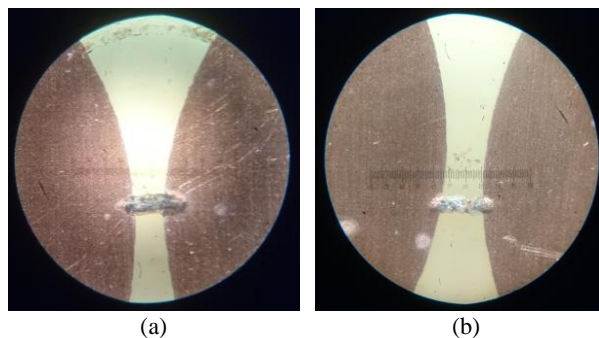
Fig 4.25 - DC breakdown in silicone gel at RT for sample A4: (a) electrode n°2 and (b) electrode n°6

TABLE 4.14 shown breakdown voltage at 160°C for sample A6, and TABLE 4.15 for sample A8.

TABLE 4.14 - DC breakdown result of epoxy substrate embedded in silicone gel at 160°C: sample A6

Testing electrode N°	1	2	3	4	5	6	7	8
Gap [µm]	301	382	292	232	283	343	301	211
BDV [kV]	7.3	10.5	8.8	9.6	6	12.1	10.5	8.5

TABLE 4.15 - DC breakdown result of epoxy substrate embedded in silicone gel at 160°C: sample A8

Testing electrode N°	1	2	3	4	5	6	7	8
Gap [µm]	366	284	231	282	315	308	216	268
BDV [kV]	14.2	10.4	4.4	8.7	13.2	10	3.6	8.7

Fig 4.26 shows the distribution at various gaps and temperatures of DC breakdown voltages of epoxy substrate in silicone gel. DC BDV increases with gap distance and drops when temperature rises. Breakdown field at RT is almost constant versus distance (about 45 kV/mm). At 160°C, it drops to about 30 kV/mm and shows a large scatter (Fig 4.27). This may be due to the irreversible thermo-chemical and physical degradation of silicone gel. Under high temperature, the long chain backbone of these soft polymers begins to be broken in a random process. The change in colour also suggests that oxidation occurred.

(a)   (b)
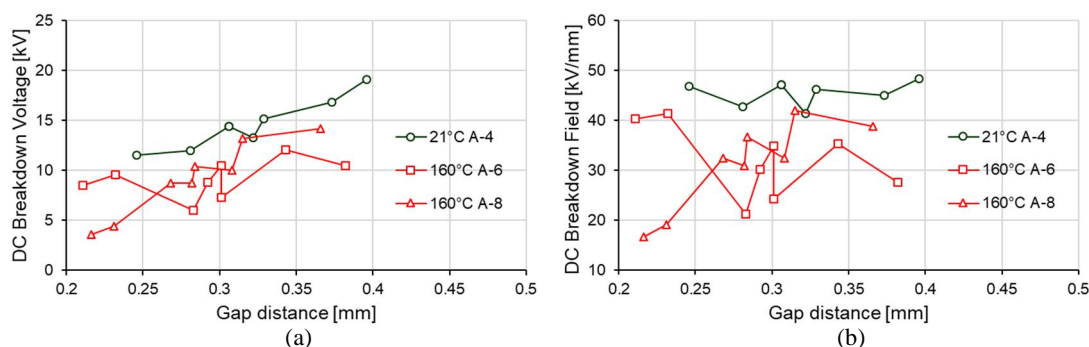
Fig 4.26 - DC breakdown on epoxy substrates embedded in silicone gel for sample A4, A6 and A8: (a) breakdown voltage and (b) breakdown field

(a)   (b)
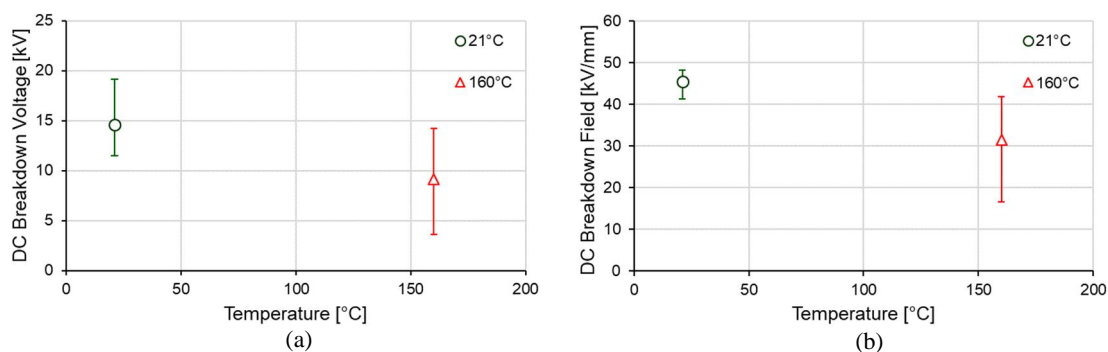
Fig 4.27 - DC breakdown on epoxy substrates embedded in silicone gel at various temperature

4.3.3.2   DC breakdown of epoxy substrates in DBT

The same sample with 0.2 mm gap was used at RT, 80°C and 160°C by applying 4 breakdown shots at each temperature. Rest time at RT and higher temperature were 3 and 10 minutes. Maximum temperature was limited to 160°C due to the thermal limit of epoxy substrate. After 160°C measurements, the sample was once again tested at RT to ensure that no significant ageing occurred.

Fig 4.28 shows sample A2 at new condition and after 160°C. No traces of breakdowns were found in the substrate sample. Only a light colour change of epoxy and copper occurred. DBT also showed some colour change, from clear transparent to slightly opaque and cloudy as in Fig 4.30.

(a)   (b)
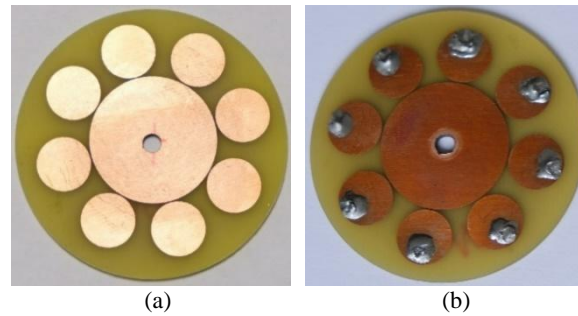
Fig 4.28 - Epoxy substrate in DBT sample A2 with average gap 295 µm: (a) new and (b) after 160°C

TABLE 4.16 shown measurements obtained at RT, 80°C, 160°C and back to RT. There was no significant modification of breakdown voltage from RT to 80°C, while at 160°C it dropped slightly.

TABLE 4.16 - DC breakdown result of epoxy substrate embedded in DBT sample A2 at various temperature

Testing electrode N°	1	2	3	4	5	6	7	8
Gap [µm]	263	299	343	292	237	287	369	268
BDV [kV] at RT 1st	14.4	10.4	20	12.8	6.5	22	18.4	13.8
BDV[1] [kV] at RT	10.1	12.7	15.2	12.4	10.1	15.5	11.2	14.1
BDV [kV] at 80°C 1st	8.8	16.8	14.8	18.4	11.2	13.2	11.8	13.8
BDV[1] [kV] at 80°C	12.2	15.6	13.5	14.2	9.2	13.9	14.9	13.6
BDV [kV] at 160°C 1st	12.6	13.8	15.2	14.7	10.9	13.1	14.7	14.8
BDV[1] [kV] at 160°C	9.5	14	11.8	9.5	8.5	12.6	10.7	11.3
BDV [kV] at RT[2]	8.5	0.5	11.2	13.6	7.2	12.6	14.4	12.7

[1] Mean breakdown voltage from 4 DC breakdown shots
[2] 1st shot the next day at RT after 160°C DC breakdown test series without opening the testcell (cooling time > 12 hours)

The final RT breakdown measurements shows no significant degradation of both epoxy substrate and DBT, except with sample n°2. Fig 4.29 shows that the average breakdown field (taken from all shots at corresponding temperature) only slightly dropped at high temperature. This may due to the accumulation of breakdown by-product from all measurement series (8×12 shots in total from RT to 160°C) and thermo-chemical reaction and oxidation of epoxy substrate and copper metallization (indicated by colour alteration in Fig 4.28b).
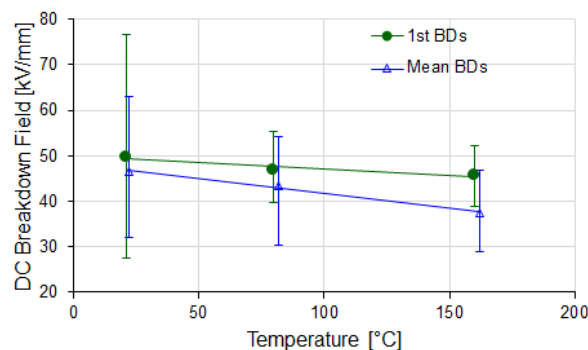
Fig 4.29 - 1st and mean DC breakdown on epoxy substrates sample A2 embedded in DBT at various temperature

The scatter was higher at room temperature in the first series measurements, unlike during breakdown measurements in the liquid alone in uniform field. This may be due to the same reason: breakdown by-products (carbon particles) remain for a long time close to the breakdown gap, due to the high viscosity at RT. As in uniform field, these by-products are probably quickly dispersed by the EHD motion at high temperature.

Breakdown fields at high temperature were higher in DBT compared to silicone gel. At 160 °C, the mean value was 45 kV/mm in DBT instead of 30 kV/mm in silicone gel. Minimum recorded values were 40kV/mm in DBT, and 17 kV/mm in gel.

(a)   (b)
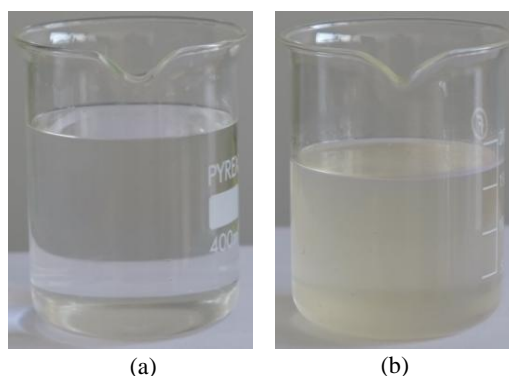
Fig 4.30 - Physical appearance of DBT: (a) new and (b) after embedded to epoxy substrate sample A2 in DC breakdown measurement series

4.3.4 Alumina (Al$_2$O$_3$) substrate embedded in silicone gel and DBT

Preliminary breakdown tests with ceramic substrates were done with AlN embedded in DBT, with large gaps up to 1.8 mm. These measurements presented in ANNEX C, evidenced a rapid degradation of the substrate after the first breakdown. Only one measurement in fixed conditions (encapsulant material, temperature, and voltage shape) can be obtained with a breakdown gap. It is thus necessary to built a large number of samples to investigate the influence of material, temperature, and voltage shape. It was then decided to make measurements with alumina substrate only (this material is cheaper than AlN), and to increase the number of breakdown electrodes (8) on a single substrate sample. The gap distance was also decreased to obtaining lower breakdown voltages, in order to allow impulse breakdown measurements.

This subsection present the DC breakdown measurements of alumina substrates embedded in DBT and silicone gel.

4.3.4.1 Alumina substrate samples

Thickness of alumina substrates and copper metallization are 630 µm and 300 µm. Fig 4.31 shows pictures of a substrate with 8 breakdown electrodes (a), and typical shapes of the breakdown gaps measured under 40x magnification (b and c).

(a)   (b)   (c)
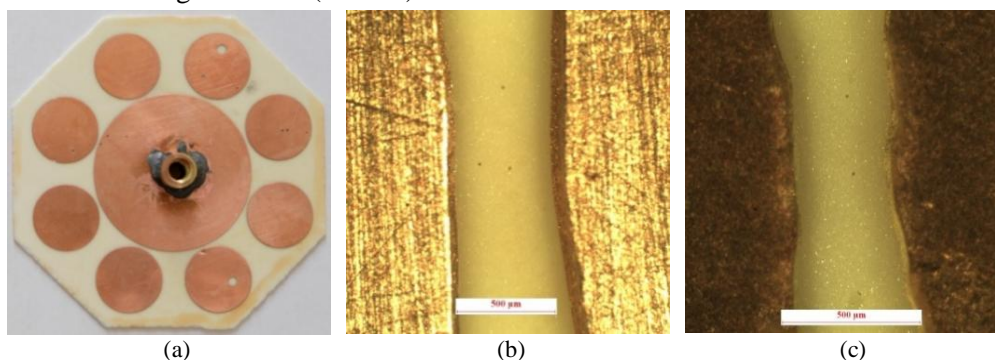
Fig 4.31 - Alumina substrate for DC breakdown measurements: (a) sample with 8 testing electrodes, (b) testing electrode Al2-05 490 µm gap and (c) Al5-03 320 µm gap

4.3.4.2   DC breakdown of alumina substrate embedded in silicone gel under influence of temperature

DC breakdown measurements were carried out with two samples (Al5 and Al7) with average gap of 366 µm. DC breakdown was applied 2 times to testing electrode at RT and 160°C (TABLE 4.17 and TABLE 4.18). Mean BDV at corresponding temperatures are 25.2 kV and 20.0 kV (Fig 4.32a), and average breakdown field 69.1 kV/mm and 54.6 kV/mm (Fig 4.32b).

TABLE 4.17 - DC breakdown voltage of alumina in silicone gel at RT

Sample Al5 testing electrode:	1	2	3	4	5	6	7	8
Gap distance [µm]	351	334	317	385	467	428	363	282
1st BDV [kV] at RT	20.3	23.6	20.4	25.1	36.3	25.8	26.2	23.8
2nd BDV [kV] at RT	1.4	1.9	0.5	2.9	3.4	1.6	1.2	1.4

TABLE 4.18 - DC breakdown voltage of alumina in silicone gel at 160°C

Sample Al7 testing electrode:	1	2	3	4	5	6	7	8
Gap distance [µm]	442	348	333	390	389	298	363	-
1st BDV [kV] at 160°C	21.8	20	9	24.8	24.1	18.6	21.8	-
2nd BDV [kV] at 160°C	8.4	8.4	4.3	1.8	2.8	3.2	5.1	-

After the first DC breakdown, BDV dropped to less than 10% at RT and less than 25% at 160°C. DC breakdowns left a channel in the silicone gel connecting electrodes (Fig 4.33b). Breakdown occurred thus mainly in silicone gel.
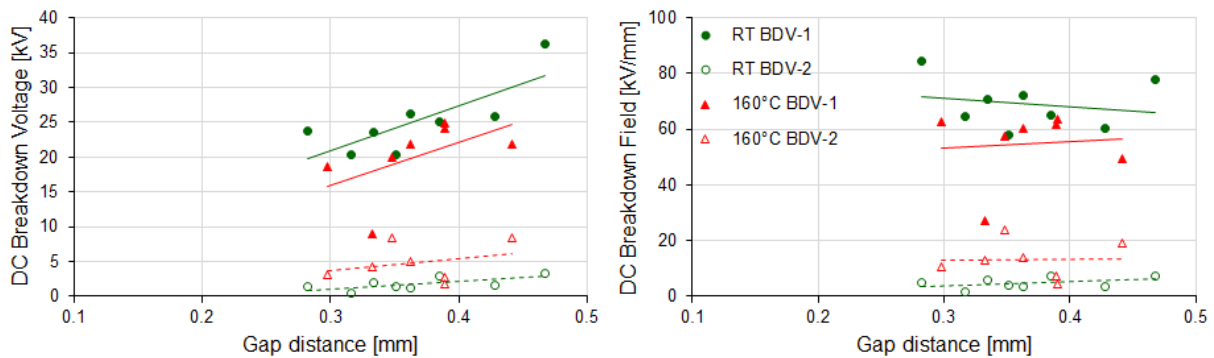
Fig 4.32 - DC breakdown of alumina substrate embedded in silicone gel at RT and 160°C: (a) breakdown voltage and (b) breakdown field
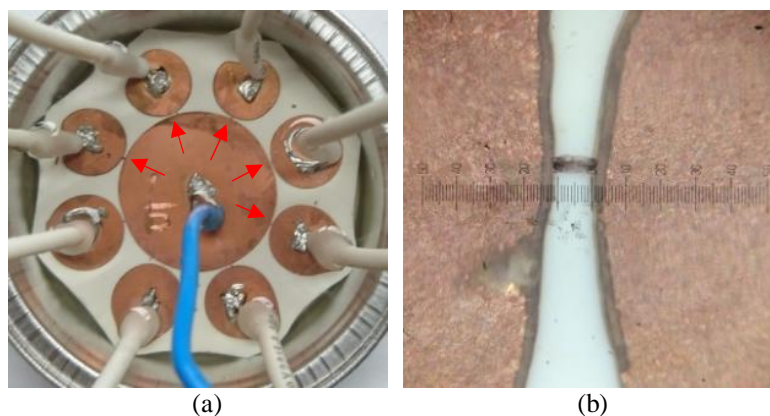
Fig 4.33 - DC breakdown of alumina embedded in silicone gel: (a) sample Al5 and (b) breakdown channel at Al5-01

4.3.4.3   DC breakdown of alumina substrate embedded in DBT under influence of temperature

DC breakdown measurements of alumina substrate embedded in DBT were carried out with two samples (Al2 and Al3) with average gap of 558 µm and 554 µm. DC breakdown was applied 1 time to each electrode at RT and 200°C.

TABLE 4.19 - DC breakdown voltage of alumina in DBT at RT

Sample Al3 testing electrode:	1	2	3	4	5	6	7	8
Gap distance [µm]	662	555	389	513	671	586	442	611
BDV [kV] at RT	29.1	26.9	21.3	23.9	31.2	25.2	17.9	24.1

TABLE 4.19 and TABLE 4.20 show DC BDV at RT and 200°C. Means BDV at corresponding temperature are 25.0 kV and 16.6 kV (Fig 4.34a) and average breakdown field 45.4 kV/mm and 29.6 kV/mm (Fig 4.34b). The mean BDV decreased to 67% as temperature increased from RT to 200°C (Fig 4.34a).

TABLE 4.20 - DC breakdown voltage of alumina in DBT at 200°C

Sample Al2 testing electrode:	1	2	3	4	5	6	7	8
Gap distance [µm]	523	627	595	451	491	598	644	533
BDV [kV] at 200°C	14.5	9.9	13.6	14.5	10.2	29	25.8	15.6

Breakdown occurred within the alumina substrate. Defects appeared in the form of permanent breakdown channels observed on the surface. Thus BDV and breakdown field obtain here represent the dielectric strength of alumina substrates, while the breakdown of DBT is supposed to be above these values. As compared to measurements with silicon gel, breakdown fields were now lower with DBT. These results are analyzed by the simulation of field distribution in the next section.

(a)   (b)
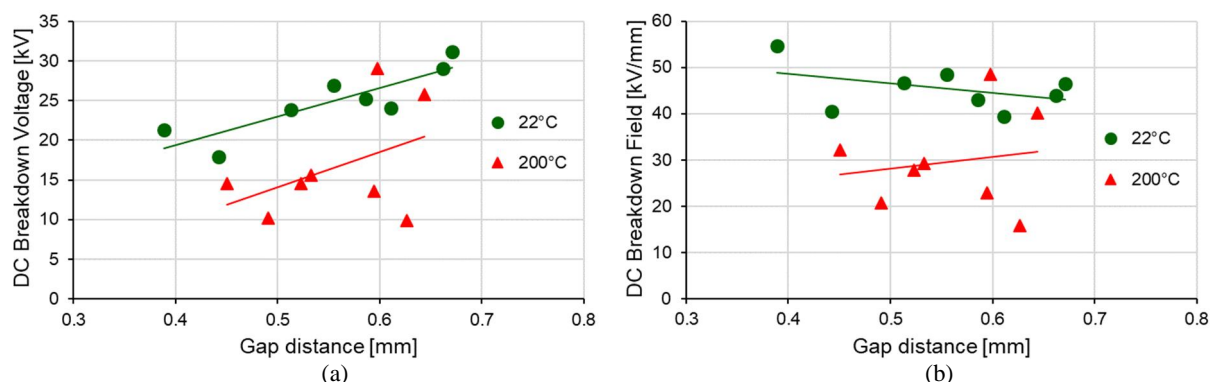
Fig 4.34 - DC breakdown of alumina substrate embedded in DBT at RT and 200°C: (a) breakdown voltage and (b) breakdown field

(a)   (b)
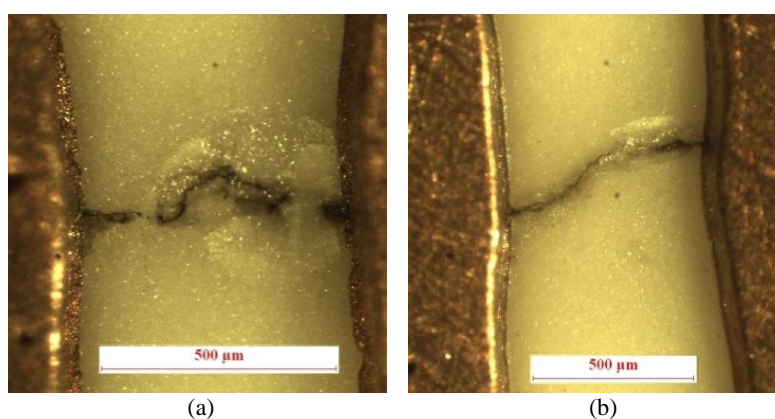
Fig 4.35 - DC breakdown of alumina embedded in DBT: (a) testing electrode no. Al3-02 26.9 kV at RT and (b) electrode no. Al2-06 29 kV at 200°C

4.3.4.4   Simulation of field distribution of alumina embedded in DBT under variation of temperature

The 2-D field simulation with substrates embedded in DBT was performed by COMSOL® Multiphysic software, to check the influence of temperature and to study the field enhancement in the triple point region. Dimensions are representative of our substrate samples. After etching of copper metallization,

its radius of curvature in the region of triple junction with DBT and ceramic is estimated to 0.5 µm. Thickness of alumina substrate and copper metallization are 630 µm and 300 µm. Electrodes were placed at 3 different gaps, i.e.: 0.2 mm, 0.5 mm and 1.0 mm. Simulation parameters such as permittivity and conductivity were taken from low voltage dielectric spectroscopy (1.5 VAC) and resistivity meter (±10 VDC) at corresponding temperature. Meshed size range from 0.01 µm to 30 µm depending on the location (the finest meshing was close to the triple point, 0.1 µm below the surface and from the tip curvature of electrode parallel to the surface). Material properties (permittivity, conductivity) at corresponding temperatures were considered linear with voltage whilst in real HV application it may differ, especially for conductivity. EHD as well as thermal convection in liquid was not accounted. All data and results presented refer to 10 mHz, i.e. close to DC properties.
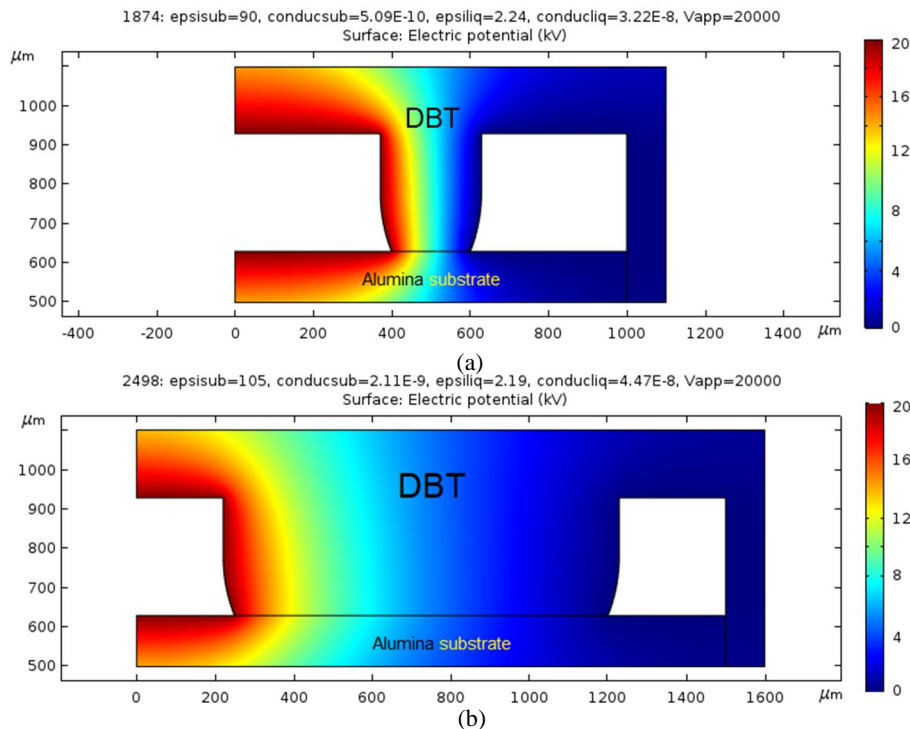
Fig 4.36 - Electric potential distribution at RT under 20 kV applied voltage for alumina substrate embedded in DBT with circular electrodes at: (a) 0.2 mm and (b)1.0 mm gaps

Fig 4.36 shows electric potential distribution for alumina substrate embedded in DBT at various gaps. Field enhancements are in the substrate and in the liquid at the tip of metallization, instead of at triple-point (Fig 4.37). It is reduced as temperature raises and at larger as in Fig 4.38. At HV electrode, high field enhancement occurs on tip curvature of metallization in DBT. In fact, electric field at triple-point precisely was not the highest and the space in DBT just after this point eventually has the lowest field (marked by blue colour) in the surrounding. Field enhancement coincide to appear in the part of surface of substrate after this region with larger volume coverage than in DBT on the tip curvature.
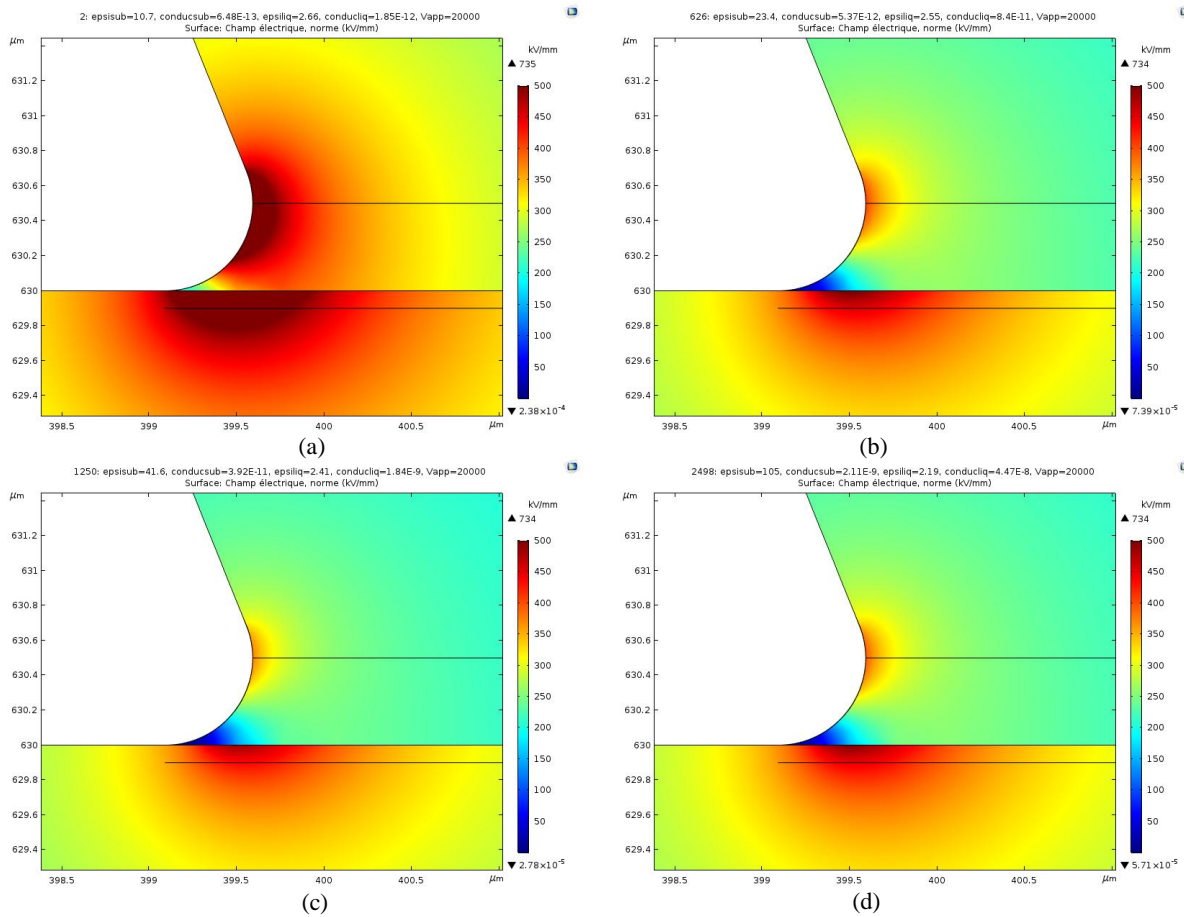
Fig 4.37 - 2D Field distribution under 20 kV DC for alumina substrate embedded in DBT with circular electrodes at g = 0.2 mm: (a) RT, (b) 100°C, (c) 200°C and (d) 350°C

Fig 4.38 shows the field calculated on the surface of alumina, versus x axis, following a line starting from the triple point. At 0.2 mm gap, the maximum field is not at the triple point (x = 0), but at about 0.5 µm from the triple point. The maximum field decreases when temperature is raised. E_{max} occurs at RT (493 kV/mm with 20 kV applied voltage), 0.459 µm from the triple-point. At 350°C, E_{max} drops to 350 kV/mm at a slightly longer distance. When the gap distance is increased, E_{max} decreases slowly. At 350°C, E_{max} decreases from 350 kV/mm to 207 kV/mm when distance is increased from 0.2 mm to 1.0 mm gap (Fig 4.38b). Fig 4.39 shows the maximum field on the surface (E_{max}) versus temperature and gap distance.
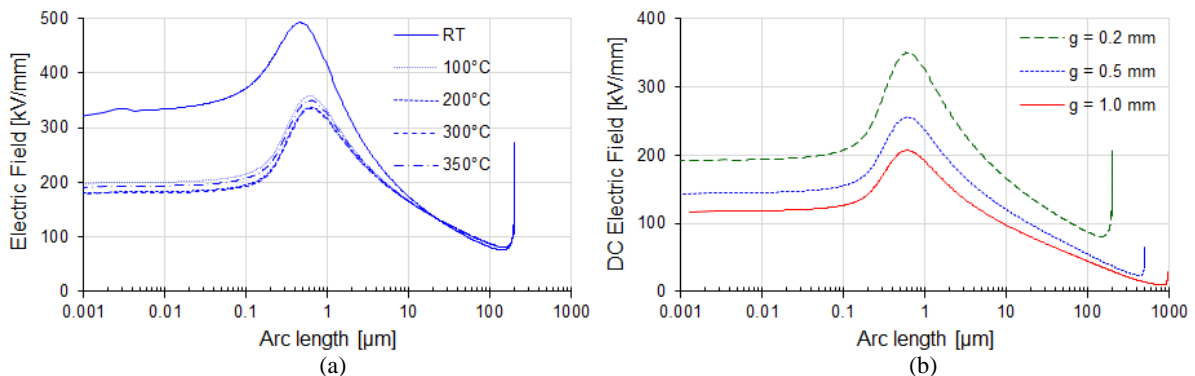
Fig 4.38 - Field distribution along the surface of alumina substrate in DBT under 20 kV at: (a) various temperature and 0.2 mm gap, (b) various gaps at 350°C
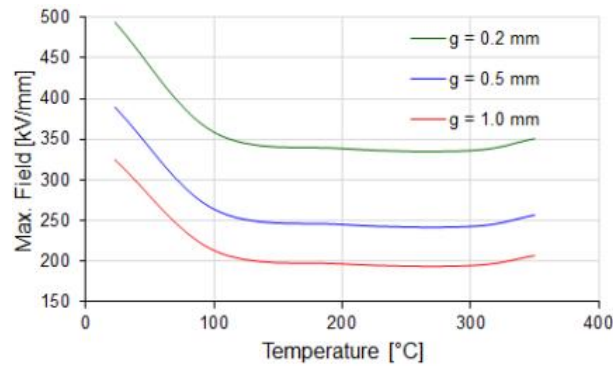
Fig 4.39 - Maximum field (E_{max}) enhancement under 20 kV DC at various gap versus temperature

In Fig 4.40, the field intensity is plotted along 3 lines:
- along the surface as above;
- in the liquid, along a line starting from the electrode tip (shown on Fig 4.37);
- in the ceramic, 0.1µm below the surface, along a line starting from the triple point position (also shown on Fig 4.37).

At room temperature, the maximum fields at the tip (600 kV/mm) and below the surface (550 kV/mm) are slightly higher than on the surface (490 kV/mm). At 350 °C, the field distribution is changed: it is maximum below the surface, followed by the tip field and the surface field.

At a distance of 10 µm from the triple point, the three fields become nearly identical, and show few variation when the temperature is changed.
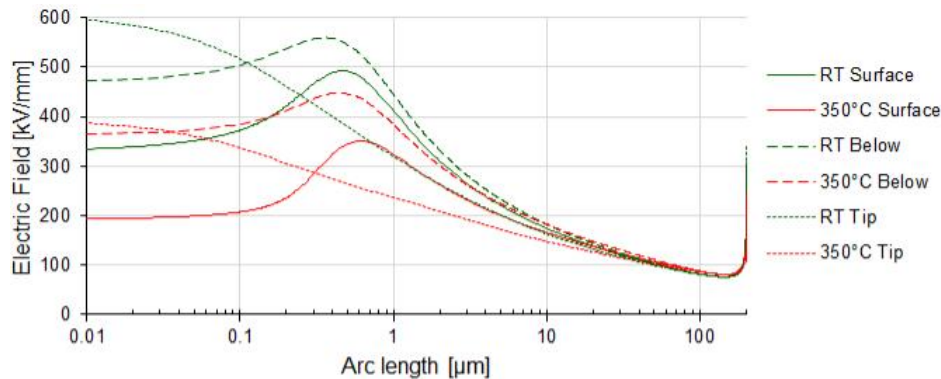
Fig 4.40 - Field distribution at RT and 350°C under 20 kV DC on the tip, surface and 0.1 µm below surface of alumina substrate at 20 kV DC.

The ratio of maximum tip field in the liquid to maximum field in the ceramic below the surface (see Fig 4.10) is > 1 at RT , and becomes < 1 at temperatures above 100°C.
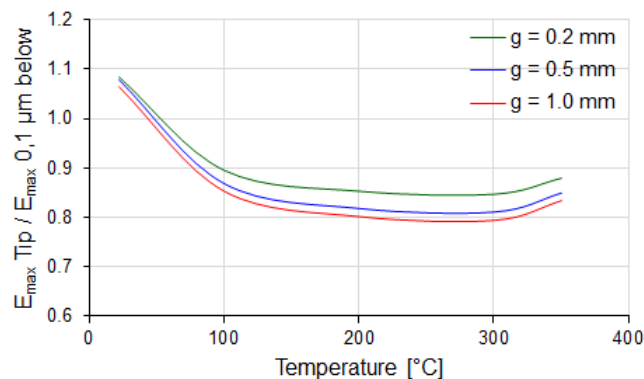
Fig 4.41 - Maximum field ratio on the tip of electrode and 0.1 µm below surface of alumina substrate at 20 kV DC

It is not easy to establish quantitative correlation between calculated fields and breakdown measurements. The fact that comparable very high fields occur in the liquid and in the ceramic agree with the observation that breakdown can occur either in the liquid alone (when no degradation of the substrate is observed), of in the ceramic itself (creating irreversible degradation). Typical values of the maximum calculated field (4 to 6 MV/cm) can be compared to typical streamer inception fields in point-plane geometry.

The slight decrease of field with temperature suggest that a moderate increase of breakdown voltage could occur at high temperature, but the opposite is usually observed in measurements.

A more realistic field calculation should take into account the influence of injected space charges, EHD motion in the liquid, and non-linear properties of materials (especially conductivity of the liquid) which should play a significant role under DC. Such calculation would be rather complex, and would require better knowledge about charge injection processes, liquid flow, and high field characterization of materials.

4.3.4.5   DC breakdown comparison

DC breakdown comparison of alumina substrate embedded in silicone gel and DBT is shown in Fig 4.42. Breakdown voltage in silicone gel and DBT indicate similar results, but slightly different gaps were used in silicone gel (avg. 366 µm) and DBT (avg. 556 µm), resulting in lower average breakdown field in DBT. The scatters of breakdown voltage in silicone gel and DBT are comparable in Fig 4.42.
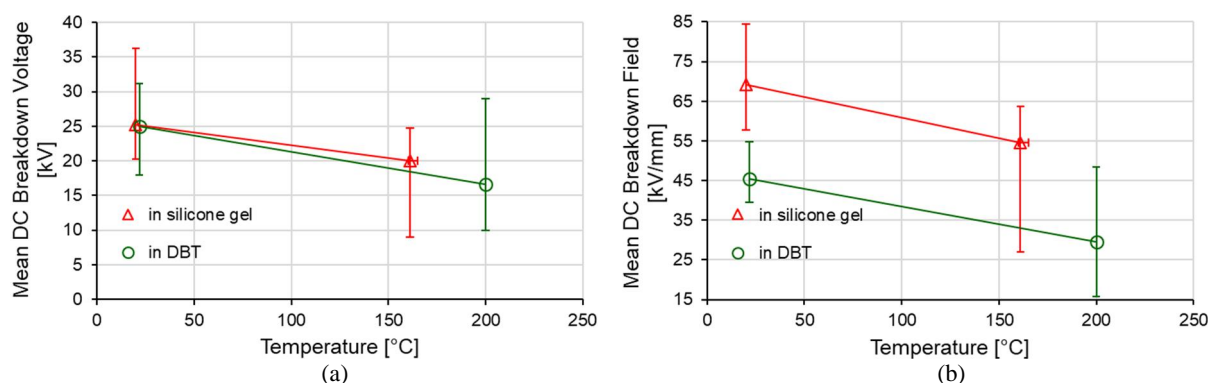
Fig 4.42 - DC breakdown comparison of alumina substrate embedded in silicone gel and DBT under various temperature (a) mean DC BDV and (b) mean DC breakdown field

4.4   Impulse breakdown measurements

Impulse breakdown measurements were carried out with epoxy and alumina substrates. Epoxy substrates were embedded in silicone gel, DBT, SE and PFPE under temperature up to 160°C. For alumina substrates embedded in silicone gel, impulse breakdown measurements were up to 160°C and in DBT up to 200°C. All impulse breakdown measurements were done under open air and atmospheric pressure.

4.4.1   Experimental set up

Impulse breakdown measurements were carried out using the experimental set up shown in Fig 4.43. A high voltage DC generator 0-60 kV/10 mA (Spellman® SL60PN600) is used to charge a capacitor (10 nF±10%). After charging, the capacitor is connected to the testcell containing samples with a 60 kV solid state switch (Behlke® HTS 600/10 HFB), via a 600 Ω series resistor. If breakdown occurs, the series resistor limits the breakdown current below 100A, in order to protect the solid-state switch.

(a)   (b)
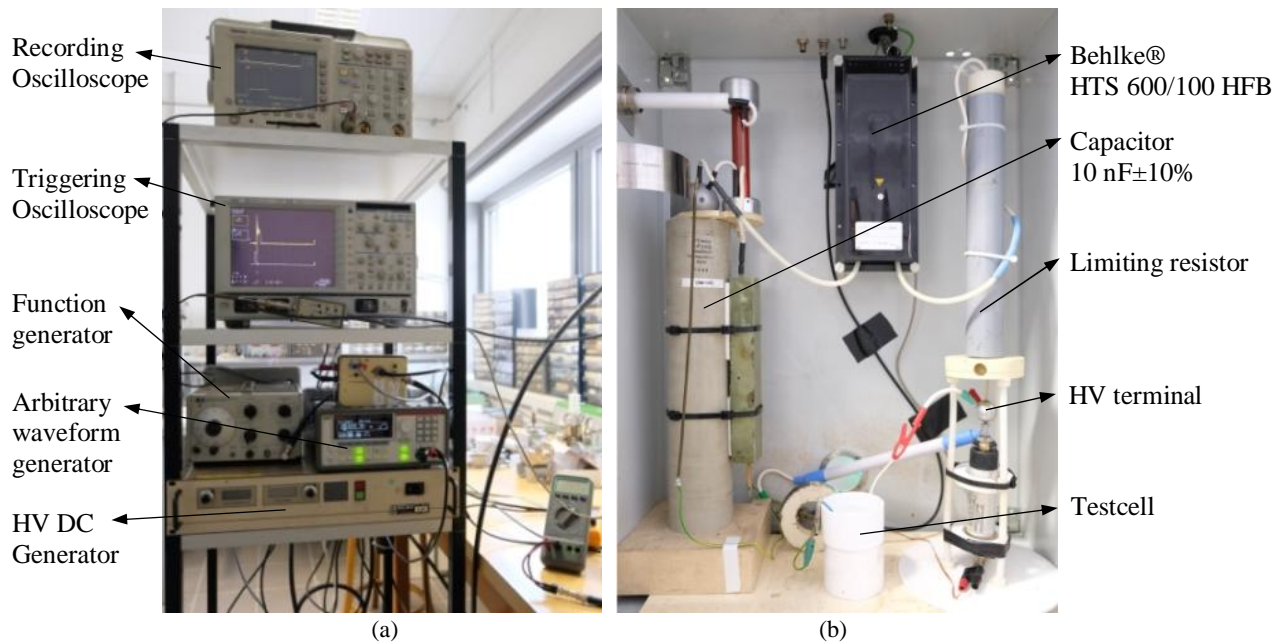
Fig 4.43 - HV impulse breakdown experimental set up: (a) control and monitoring system and (b) HV impulse switching and testing circuit

Fig 4.44 shows the typical impulse voltage waveform in these breakdown measurements. The voltage rise time is 50±5 ns, and the duration at half amplitude is 60 µs. To carry out breakdown measurements, series of repetitive impulses at frequency of 100 Hz with fixed 1 kV/s rate of rise of maximum voltage were applied until breakdown.
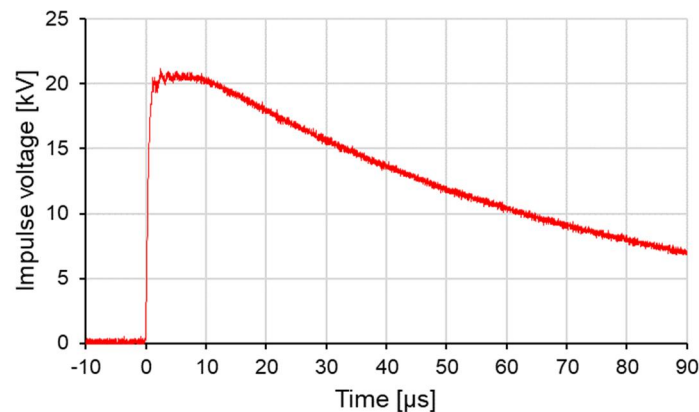
Fig 4.44 - Typical impulse voltage with rise time 50 ± 5 ns

4.4.2   Epoxy substrates embedded in silicone gel

Impulse breakdown of epoxy substrates was carried out with three samples at RT and 160°C (A1, A3 and A7). Each sample includes eight testing electrodes (Fig 4.24). Impulse breakdown measurements were performed once to each testing electrode.

TABLE 4.21, TABLE 4.22 and TABLE 4.23 show the results obtained.

TABLE 4.21 - Impulse breakdown result of epoxy substrate embedded in silicone gel at RT: sample A1

Testing electrode N°	1	2	3	4	5	6	7	8
Gap [µm]	282	321	365	314	302	321	395	324
BDV [kV]	16.4	17.1	17.2	16.9	17.1	16	19.5	15.9

TABLE 4.22 - Impulse breakdown result of epoxy substrate embedded in silicone gel at 160: sample A3

Testing electrode N°	1	2	3	4	5	6	7	8
Gap [µm]	282	302	351	292	285	309	283	322
BDV [kV]	12.3	13.1	12.9	14.1	13.4	11.6	10.6	14

TABLE 4.23 - Impulse breakdown result of epoxy substrate embedded in silicone gel at 160: sample A3

Testing electrode N°	1	2	3	4	5	6	7	8
Gap [µm]	384	311	340	384	352	301	271	292
BDV [kV]	15.9	14.8	10.5	11.4	13.7	16.8	12.9	12.3

Fig 4.45 shows the impulse breakdown voltage distribution, and the average breakdown field at various gaps. From RT to 160°C, the mean breakdown voltage drop to 77% on average.

(a)   (b)
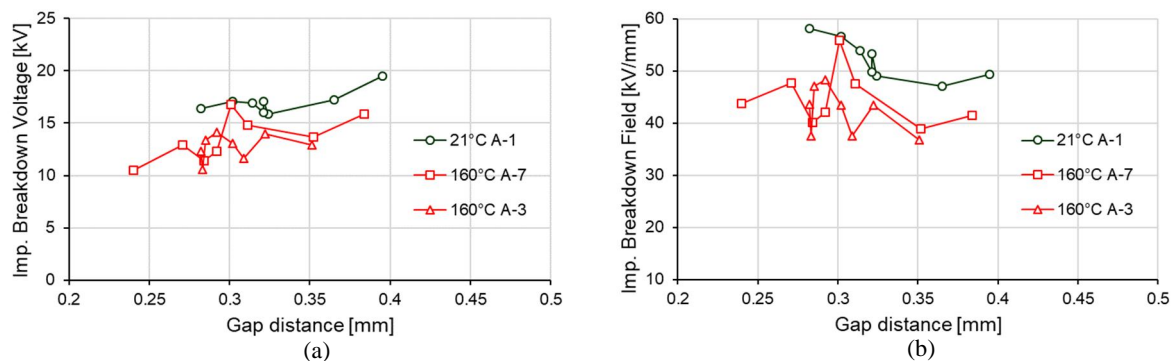
Fig 4.45 - Impulse breakdown on epoxy substrates embedded in silicone gel for sample A1, A3 and A7: (a) breakdown voltage and (b) breakdown field

4.4.3 Epoxy substrates embedded in dielectric liquids

4.4.3.1 Repeatability tests with epoxy substrate in DBT

Previous DC breakdown measurements with medium gap (0.5 mm) showed that epoxy substrates are slowly degraded after series of breakdown. Some similar experiments were done with impulses in DBT.
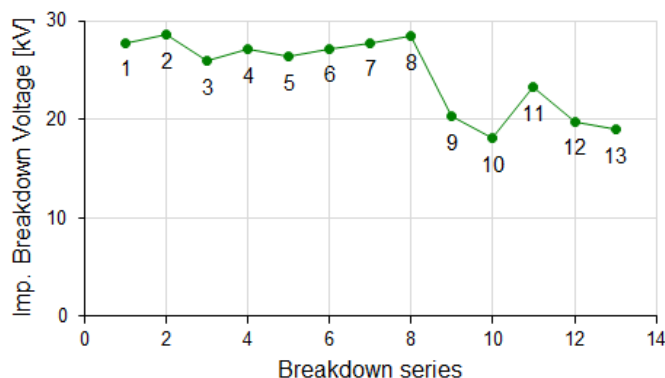
Fig 4.46 - Impulse breakdown voltage series of epoxy substrate embedded in DBT at RT with 438 µm gap

Fig 4.46 shows a series of impulse breakdown voltage measurements with epoxy substrate embedded in DBT at RT. Gap of the sample is 438 µm. The first 8 breakdown voltages were rather stable (mean BDV: 27 kV, average breakdown field: 62.5 kV/mm). Then they dropped slightly to 20.1 kV and 45.8 kV/mm.

Observation of the epoxy sample indicates there were minor defects up the 4th impulse breakdown. Afterwards, defects grew and expanded constantly until the 13th breakdown as shown in Fig 4.47. The sudden decrease after 8th breakdowns is associated to the presence of a breakdown tracks crossing from one electrode to the other. This implies that breakdown likely occurred partly in DBT and in the epoxy substrate, at least during the first breakdown experiments.

These results are comparable to those obtained under DC with comparable gaps. Impulse breakdown with short gaps (0.2 mm) were more repeatable, and some experiments (e.g. influence of temperature) could be done using the same sample with a limited number of breakdowns.
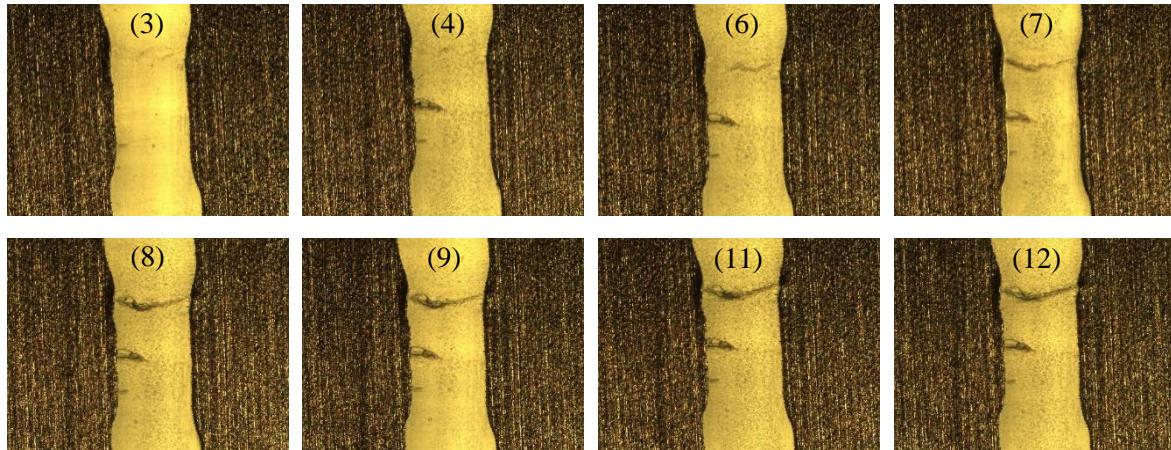
Fig 4.47 - Defect evolution in epoxy substrate embedded in DBT with 438 µm gap after series of impulse breakdown

4.4.3.2   Impulse breakdown of epoxy substrate embedded in various dielectric liquids

Impulse breakdown of epoxy substrate embedded in various dielectric liquids was studied at RT under atmospheric pressure with the same sample (A9) including 8 testing electrodes with average gap of 270 µm. Measurements were carried out consecutively in PFPE, Midel 7131 (SE), and Jarytherm® DBT, with only one breakdown performed in each dielectric liquid as shown in TABLE 4.24. In addition, the time to breakdown t_b between voltage rise and breakdown were noted in these experiments.

TABLE 4.24 - Impulse breakdowns of epoxy substrate embedded in various dielectric liquids at RT: sample A9

Testing electrode N°	1	2	3	4	5	6	7
Gap [µm]	237	271	318	255	230	270	357
BDV in PFPE [kV]	18.3	22.3	22.6	17.8	21.8	22.4	22.2
BDV in SE [kV]	15.8	19	19.4	18.9	22.2	18.6	20.1
BDV in DBT [kV]	20.7	20.8	26	22.1	25.9	21.5	25.9

The highest mean BDV was measured in DBT (23.27 kV), followed by PFPE (21.1 kV) and SE (19.14 kV). This classification was obtained despite DBT was last tested, i.e. in conditions when some small degradation of the substrate may already appeared. The fastest average breakdown time was in DBT: 1.46 µs (range: 0.39-4.14µs), followed by SE: 1.54 µs (range: 0.29-4.55 µs), and PFPE: 1.74 µs (range: 0.90-2.71 µs). There are no clear dependencies between the breakdown time and the BDV.

TABLE 4.25 shows typical epoxy substrate condition between electrodes after each series of impulse breakdown. Apparently, 6/7 testing electrodes showed a marked degradation of epoxy substrate after measurements in DBT, whereas during previous breakdown in PFPE and SE led to only 1/7 testing electrode degraded. This strongly indicates that breakdown with PFPE and SE mainly occurred in the liquid, whereas breakdown with DBT occurred also partly within epoxy. Moreover, it correlated with the higher breakdown voltage with DBT.

TABLE 4.25 - Sample A9 embedded in various dielectric liquids after series of impulse breakdowns

Testing electrode N°	New	PFPE	SE	DBT
1				
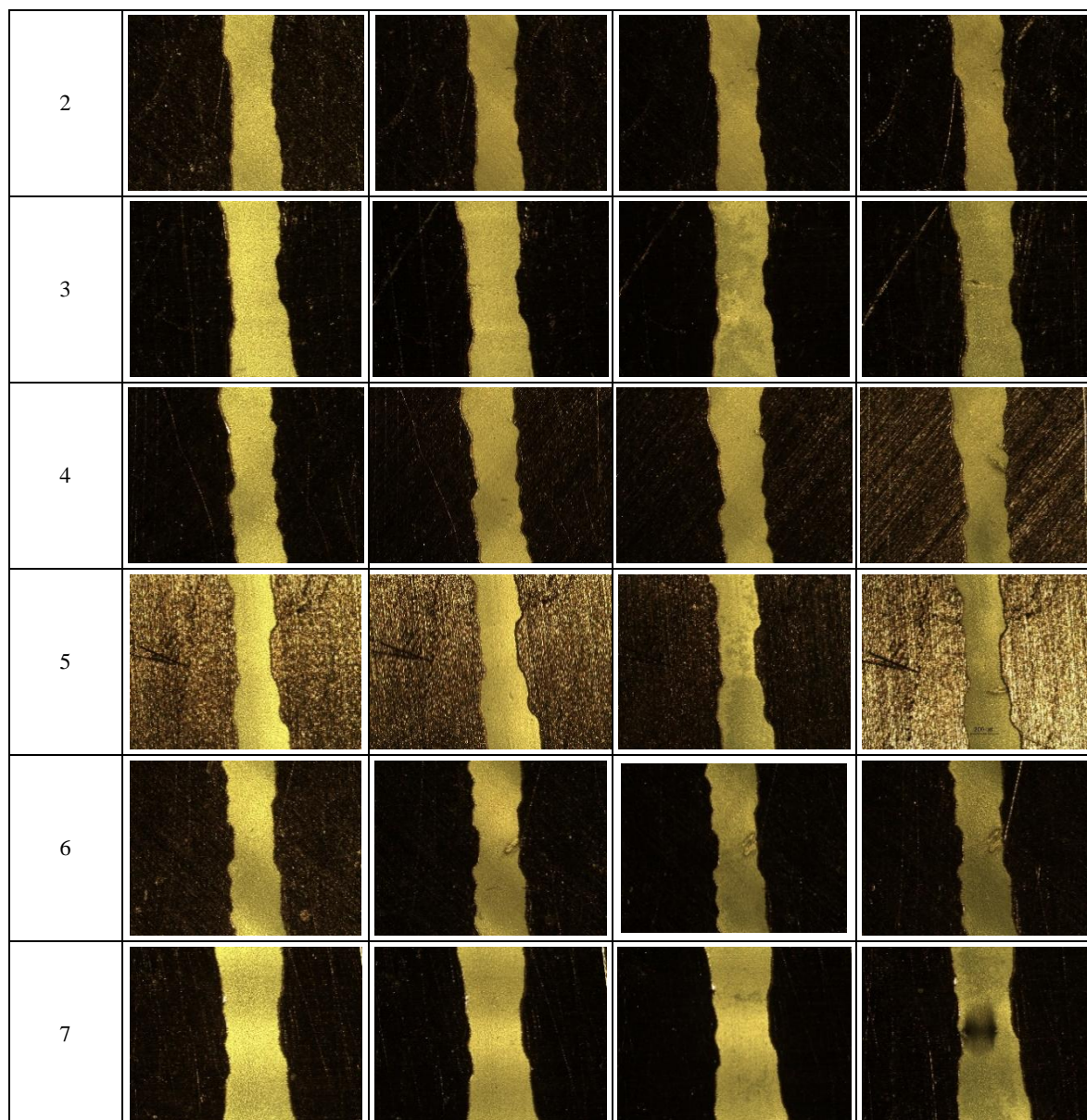
4.4.3.3 Impulse breakdown: comparison between dielectric liquids and silicone gel

In all materials, a decrease of average breakdown field versus distance is observed. Impulse breakdown of epoxy substrate in silicone gel showed the lowest BDV, and the highest in DBT (Fig 4.48). This classification is reversed as compared to results obtained under DC at the same gap distance (Fig 4.23).

(a)   (b)
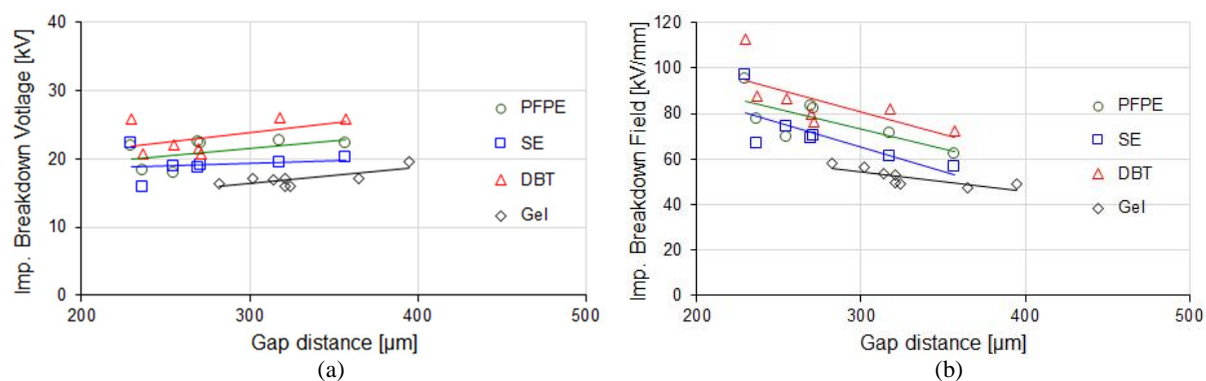
Fig 4.48 - Impulse breakdown of sample A9 at RT in dielectric liquids and silicone gel

4.4.4   Epoxy substrates embedded in dielectric liquids under variation of temperature

4.4.4.1   Impulse breakdown of epoxy substrates embedded in liquids under variation of temperature

Impulse breakdown measurements of epoxy substrate embedded in DBT were carried out at RT, 80°C and 160°C with the same sample A11 with average gap of 276 µm. Only one breakdown was performed to each testing electrode at each temperature.

Mean BDV at RT, 80°C, 160°C and final measurement back to RT are shown in TABLE 4.26.

TABLE 4.26 - Impulse breakdowns of epoxy substrate embedded in DBT at RT, 80°C and 160°C

Testing electrode N°	1	2	3	4	5	6	7	8
Gap [µm]	357	286	221	244	322	264	239	273
BDV [kV] at RT[1]	26.9	30.8	25.9	20.2	26	26.6	23.4	22.6
BDV [kV] at 80°C	20.1	25.9	21.4	17.3	19.	21.2	19.9	19.2
BDV [kV] at 160°C	20.3	22.5	21.6	18.6	18.7	16.2	14.8	17
BDV [kV] at RT[2]	16.8	23.2	22.1	15.8	21.8	22.3	16.7	18

[1] RT at new condition
[2] RT after high temperature DC breakdown test series

Impulse BDV in DBT decreases when the temperature increases, but unfortunately with this liquid some rapid degradation of the substrate occurred: going back to RT lead to lower breakdown voltage. This rapid degradation agrees with that observed in the previous section. Consequently, it is impossible to conclude whether temperature or ageing is mainly responsible for the decrease with this experiment carried out with a single substrate. Therefore, the decrease observed here at different temperatures is certainly overestimated. The actual decrease due to temperature alone, without sample degradation, should be lower.

TABLE 4.27 - Impulse breakdowns of epoxy substrate embedded in SE at RT, 80°C and 160°C

Testing electrode N°	1	2	3	4	5	6	7	8
Gap [µm]	370	294	236	275	330	285	193	273
BDV [kV] at RT	23.5	15.4	14.5	19.2	12.5	18.2	15.5	19.5
BDV [kV] at 80°C	24.7	14.9	13.9	16.6	11.6	15.9	11.3	17.7
BDV [kV] at 160°C	19.1	14.4	13.9	15.2	14.4	15.6	12.6	16.7

The results obtained with SE are quoted in TABLE 4.27. With that liquid (Fig 4.49), no clear influence of temperature is seen, considering the large scatter of measurements. Since breakdown did not produce a marked degradation with this liquid (TABLE 4.25), one may conclude that in SE temperature has a minor influence, such as in silicone gel. Similar results were obtained with the PFPE liquid.

4.4.4.2   Comparison of Impulse breakdown under influence of temperature: dielectric liquids and silicone gel

Impulse breakdown comparison of epoxy substrate embedded in various dielectric liquids and silicone gel under influence of temperature is shown in Fig 4.49. Note that in DBT, the decrease of breakdown field versus temperature is overestimated. Even though, at 160°C the mean BDV of DBT with degraded substrates remains higher than in SE and gel with new substrates. Silicone gel shows the poorest breakdown voltage under impulse, and also no self-healing properties: a large decrease is observed after the first breakdown, contrary to liquids.
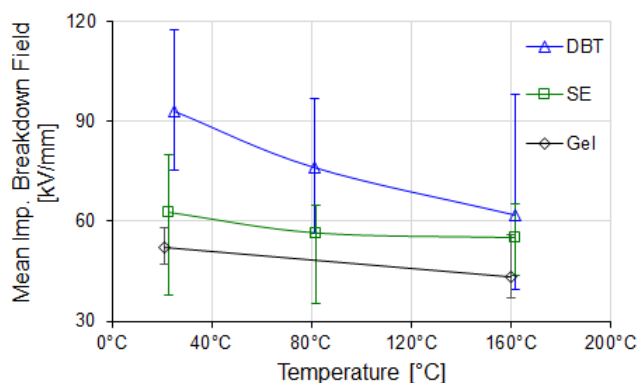
Fig 4.49 - Impulse breakdown comparison of epoxy substrate embedded in various dielectric liquids and silicone gel under influence of temperature

4.4.4.3   Comparison between impulse and DC breakdown with epoxy substrates

Fig 4.50 shown the comparison of breakdown field under DC and impulse voltage for epoxy substrate in silicone gel and DBT. Impulse breakdown in gel is slightly higher than DC breakdown at both temperatures.

In contrast, a large increase is observed in DBT under impulse voltage, where the breakdown field (up to 110 kV/mm at room temperature) is nearly doubled compared to DC.
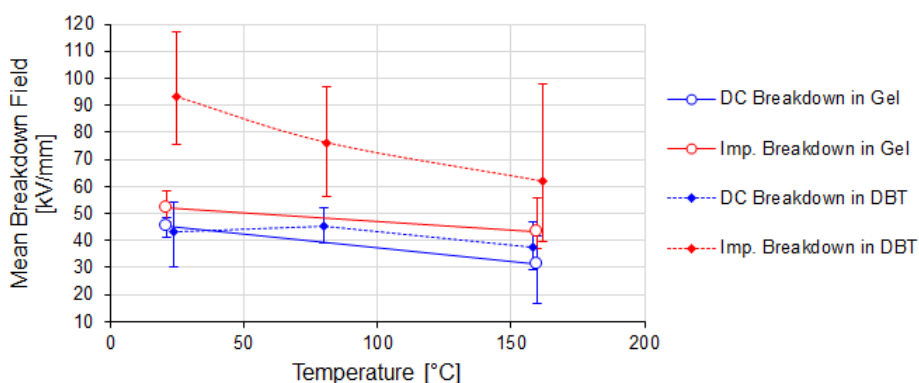
Fig 4.50 - Comparison between DC and impulse breakdown field in silicone gel and DBT at various temperature

4.4.4.4   Comparison with streamers under impulse voltage.

Since impulse breakdown is studied here with a very divergent field, possible correlations with streamer phenomena under impulse voltage can be checked. Since the breakdown gap is highly divergent and symmetrical, breakdown can be initiated either by negative discharges starting from the grounded electrode, or by positive from the electrode connected to positive impulse.

In SE, the lower initiation voltage of fast positive streamers would logically explain that they are responsible for breakdown. In addition, their high velocity (> 2 mm/µs) would agree with the lowest breakdown delay recorded (300 ns for 0.3 mm gap), equivalent to a 1 mm/s "breakdown velocity". The much lower velocity of negative streamers (< 0.08 mm/µs) is unable to explain such short breakdown delay.

In PFPE, a nearly similar conclusion can be obtained: positive and negative streamers can appear at nearly identical voltages, but the low velocity of negative streamers (< 0.2 mm/µs) cannot explain the lowest time to breakdown (down to 0.9 µs).

In DBT, negative streamers are initiated at much lower voltage than positives, but they showed almost no propagation, even when the voltage was raised. The involvement of positive streamers in breakdown would agree with the larger breakdown voltage observed with this liquid.

The fact that impulse breakdown shows minor variations with temperature in SE, PFPE, and possibly DBT, also agrees with the small variation recorded on inception voltage of streamers versus temperature.

4.4.5 Alumina (Al$_2$O$_3$) substrates embedded in silicone gel and DBT under variation of temperature

4.4.5.1 Impulse breakdown of alumina substrates embedded in silicone gel

Impulse breakdown measurements of alumina substrate embedded in silicone gel were carried out at RT and 160°C under atmospheric pressure to samples AL4 and AL6 with average gap of 397 µm and 486 µm. Breakdowns were performed three times to each testing electrode with rest time less than 10 minutes. Mean BDV at RT from each shot are shown in TABLE 4.28.

TABLE 4.28 - Impulse breakdowns of alumina substrate embedded in silicone gel at RT

AL4 Testing electrode N°	1	2	3	4	5	6	7	8
Gap [µm]	408	410	377	280	399	502	402	399
1st BDV [kV]	20.5	24.1	22.6	20.5	21.3	27.8	22.4	25.4
2nd BDV [kV]	21.3	20.6	20.1	16.2	22.3	21.4	18.9	25.5
3rd BDV [kV]	9.4	3.5	2.1	3.3	3.4	4.4	4.6	1.0

Second BDVs were slightly reduced, and the third BDV showed a large degradation. Fig 4.51 shows the corresponding impulse BDV and breakdown field. There are no large scatter of breakdown voltage at each temperature. Breakdown time ranges between 0.50-0.86 µs.

(a)   (b)
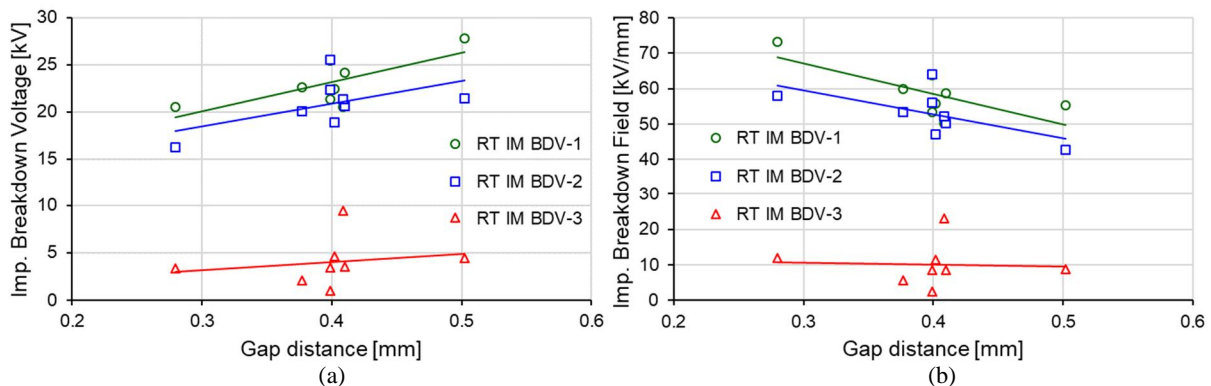
Fig 4.51 - Impulse breakdown of alumina substrate embedded in silicone gel (sample AL4) at RT

TABLE 4.29 and Fig 4.52 show impulse breakdown results obtained at 160°C. Second BDVs were slightly reduced and third BDV (not shown in the table) also showed a large degradation as those at RT in TABLE 4.28. Breakdown time ranges between 0.50-0.86 µs. Based on the first measurements only, some decrease of the breakdown field at high temperature is observed.

Comparison of the 1st impulse breakdown at RT and 160°C on different alumina substrate samples indicates no significant decrease at 160°C.

TABLE 4.29 - Impulse breakdowns of alumina substrate embedded in silicone gel at 160°C

AL6 Testing electrode N°	1	2	3	4	5	6	7	8
Gap [µm]	502	532	-	499	502	453	453	459
1st BDV [kV] at 160°C	22.5	25.8	-	25	25.7	21.8	24.5	22.3
2nd BDV [kV] at 160°C	19.3	22.6	-	19.3	17.3	22.3	20.5	18.2

| (a) | (b) |
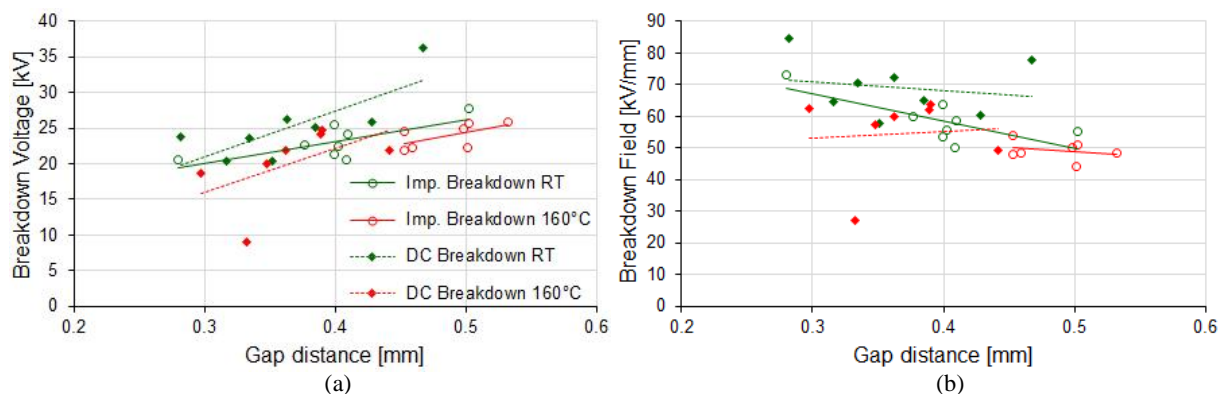
Fig 4.52 - Impulse breakdown of alumina substrate embedded in silicone gel (sample AL6) at 160°C

4.4.5.2 Impulse breakdown of alumina substrates embedded in DBT

Impulse breakdown measurements of alumina substrate embedded in DBT were carried out at RT and 200°C under atmospheric pressure using the same sample AL1 with average gap of 568 µm. Breakdowns were performed 2 times at RT and after 1 time at 200°C with rest time less than 10 minutes. Mean BDV at RT and 200°C are shown in TABLE 4.30. A large drop was recorded at the third shot such as with gel, and it was unfortunately impossible to conclude whether this drop is due to temperature alone, or to some degradation of the substrate. Due to the limited availability of ceramic substrates, it was unfortunately impossible to repeat these measurements with new substrates at each temperature.

TABLE 4.31 shows the evolution of alumina substrate after impulse breakdowns. Large degradations of the ceramics can be see after only the first breakdown at room temperature.

TABLE 4.30 - Impulse breakdowns of alumina substrate embedded in DBT at RT and 200°C

AL4 Sample N°	1	2	3	4	5	6	7	8
Gap [µm]	635	630	529	559	589	576	507	521
1st BDV at RT [kV]	29.1	26.9	24.9	24.9	26.5	26.9	25	25.1
2nd BDV at RT [kV]	27.5	25.6	24.6	23.8	27.9	22.4	25.6	23.9
3rd BDV at 200°C[kV]	11.0	17.2	15.2	14.3	18.1	13.1	14.8	15.1

TABLE 4.31 - Sample AL1 alumina substrate embedded in DBT after series of impulse breakdowns

Testing point	New	1st BDV at RT	3rd BDV at 200°C
1			
4			
5			
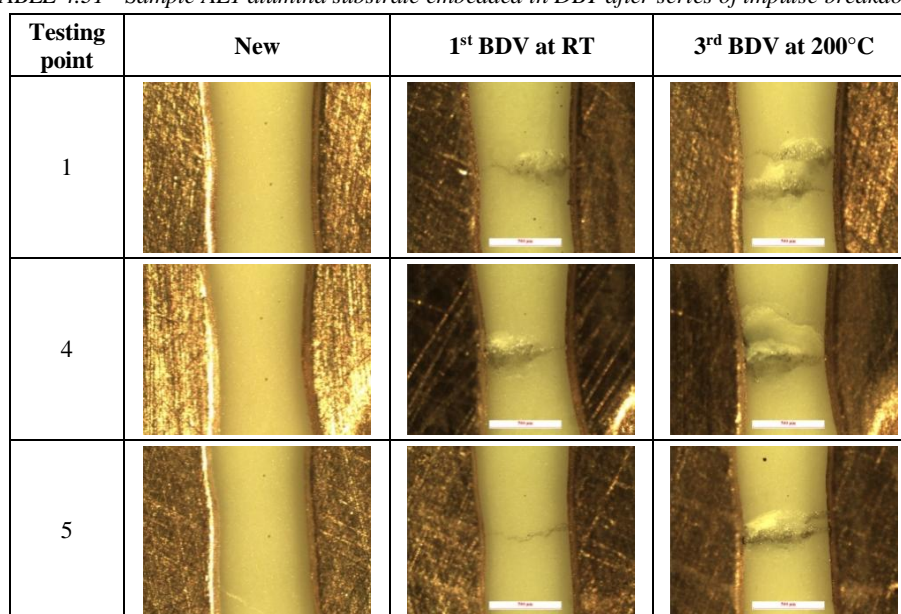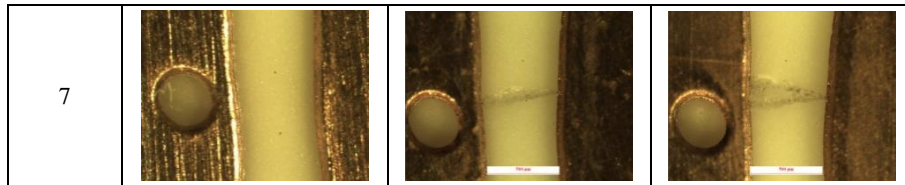
4.4.5.3   DC and impulse breakdown comparison of alumina substrates embedded in DBT

Fig 4.53 shows comparison of DC and impulse breakdowns of alumina substrates in DBT at average gap of 0.57 mm. Results of DC breakdowns were obtained from different samples (

TABLE 4.19 and TABLE 4.20) at corresponding temperature, while for impulse breakdown they came from the same sample (TABLE 4.30).
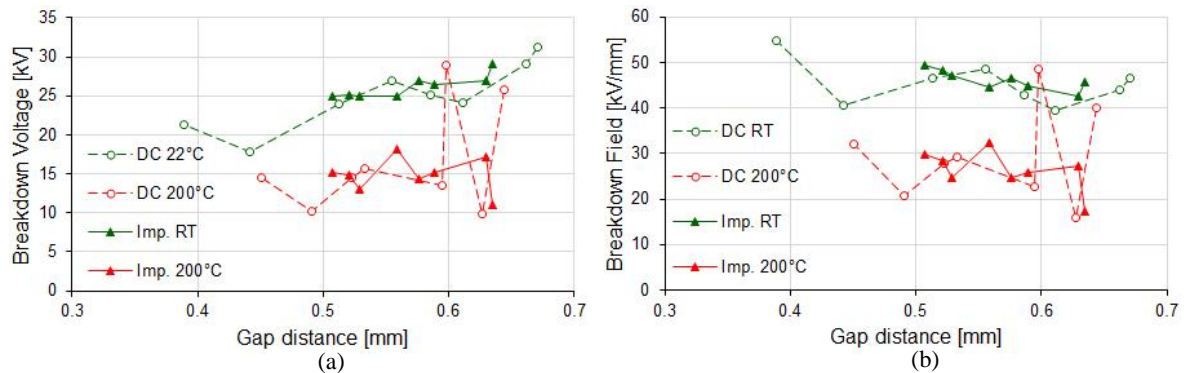
Fig 4.53 - DC and impulse breakdown of alumina substrates embedded in DBT at RT and 200°C: (a) breakdown voltage and (b) breakdown field

Results at RT show that the average breakdown fields are nearly identical under DC or impulse. This constitutes a major difference with epoxy, where breakdown under impulse was nearly doubled compared to DC. This clearly shows that the breakdown voltage is also strongly affected by the substrate nature. DC breakdown fields are comparable with epoxy (50 kV/mm) and Alumina (about 45 kV/mm), whereas impulse breakdown fields are much larger with epoxy (80 kV/mm) than with Alumina (45 kV/mm). This would suggest that breakdown with Alumina could be first triggered by breakdown of the substrate. Results at 200°C are also comparable despite impulse breakdown at high temperature was obtained with degraded substrates.

4.5 Partial discharge measurements with AlN and Alumina substrates

4.5.1 Experimental set up and procedure
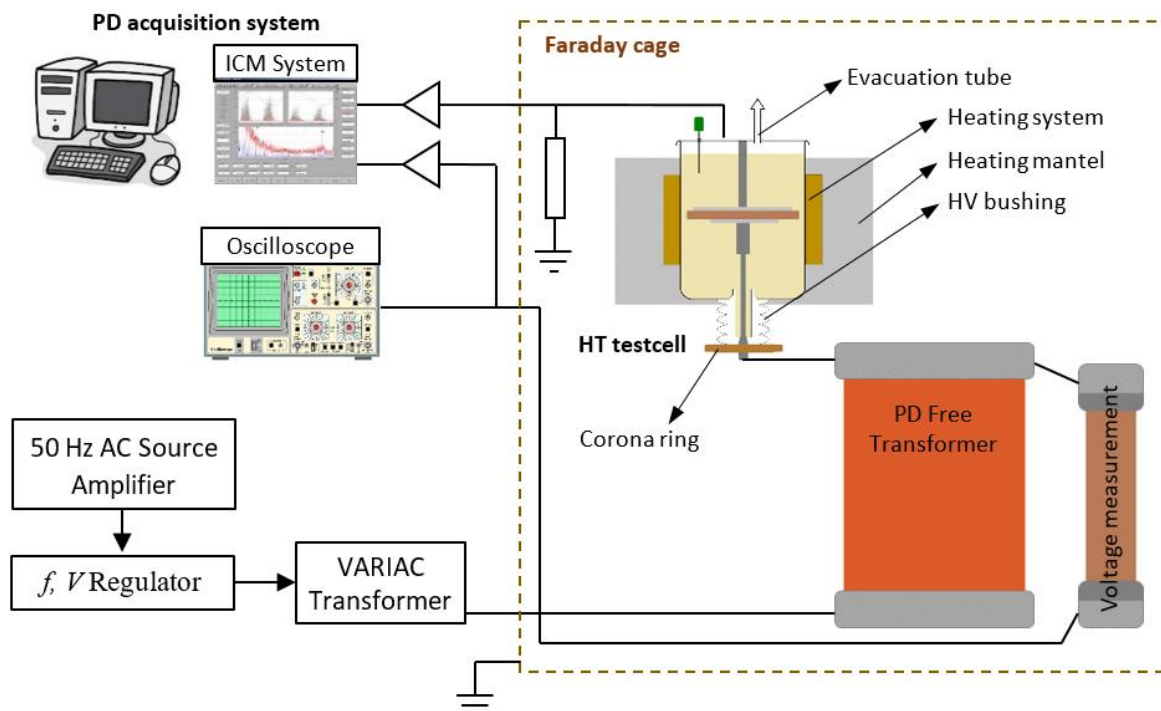
Fig 4.54 - Partial Discharge of substrates embedded in liquids experimental set up

HT testcell for partial discharge measurements is the same as one used in dielectric spectroscopy measurement in Fig 4.3. Two ceramics substrates embedded in DBT (AlN and alumina) were studied with the experimental set up as in Fig 4.54. PD measurements use the same system as described in section 3.2.1, with the same PDIV definition of 10 PDs per minute (of both polarities) with minimum discharge detection threshold of 0.2 pC. Measurements were carried out under 100 kPa of N_2 blanket from RT up to 350°C. PD measurements were calibrated at ±5 pC at maximum scale of ±7.9 pC. Minimum discharge threshold was set to 2.0% of maximum scale.

4.5.2 PDs of alumina in open air and embedded in DBT

4.5.2.1 Alumina substrate sample

Alumina substrate was etched into octagon and circle electrodes as in Fig 4.55. The circle electrode radius is 10 mm and connected to the HV while the octagon is linked to the ground side.

(a)   (b)
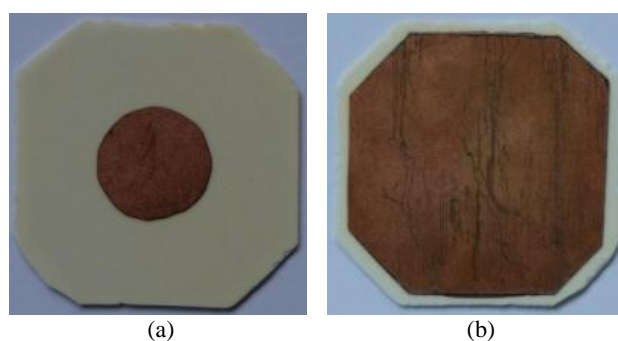
Fig 4.55 - Alumina substrate for PDs measurement up to 350°C: (a) HV side and (b) ground side

4.5.2.2   Alumina substrate in open air

A preliminary PDs measurement in open air was carried out at RT and results are shown in Fig 4.56. PDs occurred in both positive and negative polarity with mean discharge amplitude of 200-550 pC from 1.4-1.7 kV rms. Discharge numbers increase rapidly from less than 150 at 1.4 kV rms to more than 14400 at 1.7 kV rms. PDIV of alumina in open air is estimated to be below 1.4 kV and in only less than 0.3 kV rise (21%), the discharge number increased to nearly 4 order of magnitude (14400%).
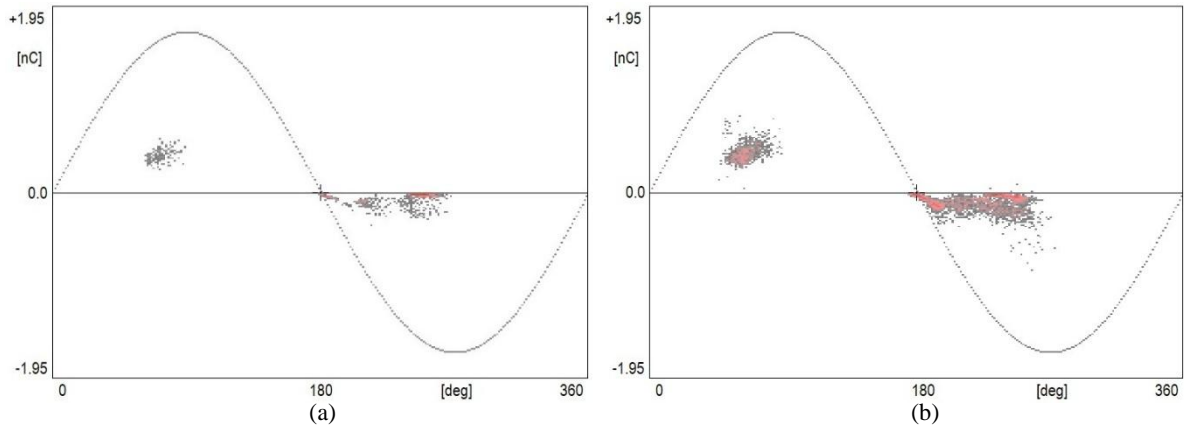
Fig 4.56 - Typical PRPD pattern of alumina in air at RT for applied voltage: (a) 1.44 kV rms and (b) 1.54 kV rms

Fig 4.58 shows PRPD pattern at 1.90 kV rms. The discharges were irregular and occurred in both polarity at both phases. Intensity of discharge is high and beyond the measurement scale. This high PDs intensity from alumina substrate in air introduces considerable interference and noise.
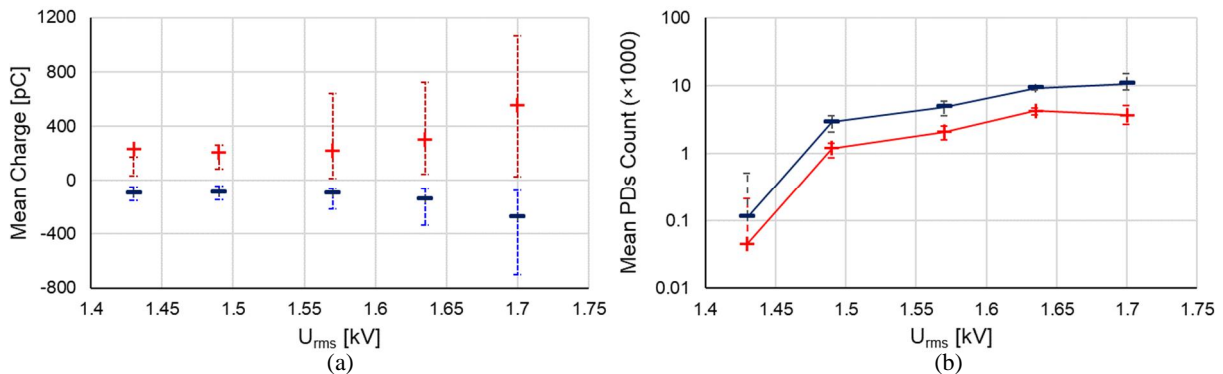
Fig 4.57 - (a) mean PDs charge and (b) mean PDs count at RT under atmospheric air
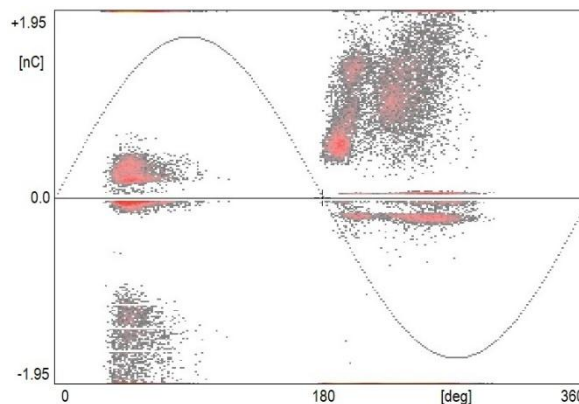
Fig 4.58 - Typical PRPD pattern of alumina in air at RT for applied voltage 1.90 kV rms

4.5.2.3   Alumina substrate embedded in DBT

Typical PRPD patterns of alumina substrate embedded in DBT from RT to 350°C are shown in Fig 4.59. It is inconvenient to present the evolution of discharge activities at fixed applied voltage. Instead,

examples in Fig 4.59 correspond to an almost constant PDs number (about 1000). As previously observed in [45], PD recordings originated from substrates are very stable, reproducible, and show almost symmetrical patterns in positive and negative polarity. PDs recordings observed here are almost similar to those previously observed with ceramic substrates embedded in silicone gel or in various liquids. As previously discussed in Chapter 1, these measurements at room temperature led to the conclusion that PDs do not occur in the encapsulant, but rather within pores of the ceramics.

Mean discharge magnitude declined and became more concentrated around the peak of applied voltage when temperature was increased, whereas PDs count first decreased up to 100°C, and increased thereafter up to 350°C (Fig 4.60). PDs magnitude reached the lowest with largest discharges number at 350°C as in Fig 4.59e.
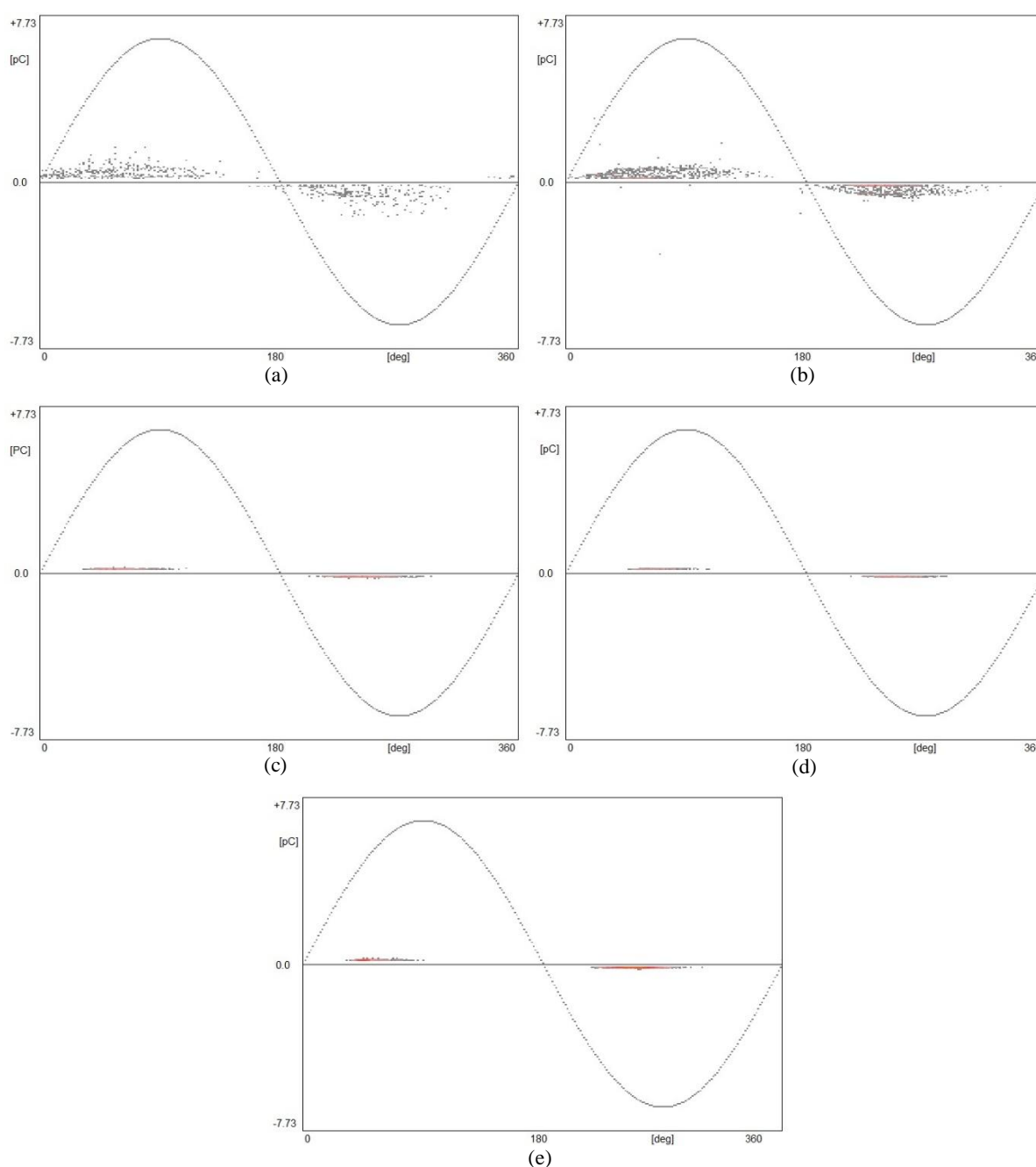
Fig 4.59 - Phase resolved PD pattern of alumina substrate embedded in DBT under AC 50 Hz for nearly 1000 PDs count at (a) 9.0 kV rms 21°C, (b) 10.5 kV rms 100°C, (c) 9.0 kV rms 200°C, (d) 5.5 kV 300°C and (e) 6.5 kV rms 350°C. Max vertical scale ±7.7 pC

PDIV increases from RT to 100°C, then repeatedly decreases at 200°C and 300°C. At 350°C, it increases again to between 300°C and 200°C. The lowest PDIV is at 300°C, at less than 5.0 kV rms, while the highest is 9.5 kV rms at 100°C.
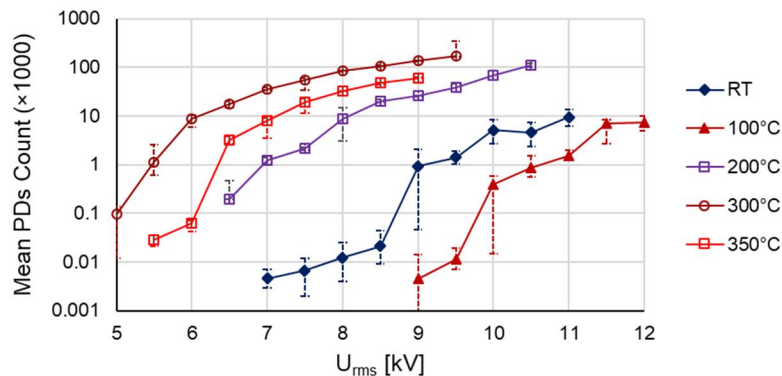
Fig 4.60 - Mean PDs number versus applied voltage for alumina substrate embedded in DBT at various temperature

Fig 4.61 shows the mean PDs charge amplitude versus temperature at various applied voltage. Temperature does not significantly influence the discharge amplitude. Only the scatter decreases significantly from RT to 100°C and above.
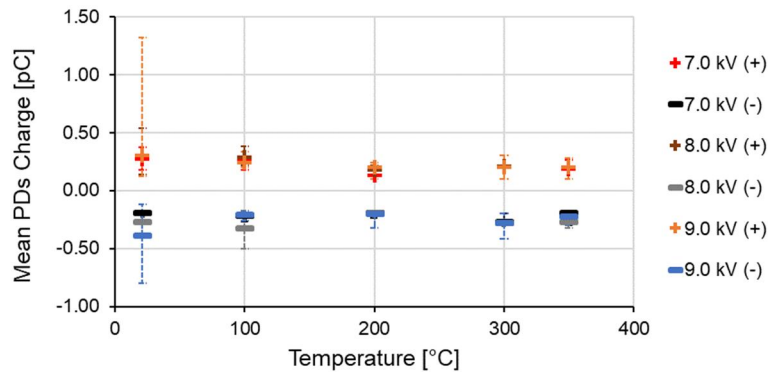
Fig 4.61 - Mean PDs charge versus temperature for alumina substrate embedded in DBT at various applied voltage in rms value

4.5.3   PDs with AlN embedded in DBT

An AlN substrate was etched into square shape as in Fig 4.1 for PDs measurement. Typical PRPD recordings in DBT at fixed voltage (7 kV rms) and under various temperatures (from 25 to 350°C) are shown in Fig 4.62.

When temperature was raised up to 300°C, both discharge amplitude and number decreased, and PDs patterns had similar shapes as in alumina (i.e. symmetrical shape in both polarity, and high stability and reproducibility). At 350°C, a sudden and large increase of PDs activity were recorded, induced by the mechanical cracking of the ceramic, probably due to thermo-mechanical stress. Such irreversible degradation at 350 °C was not observed with alumina substrate.
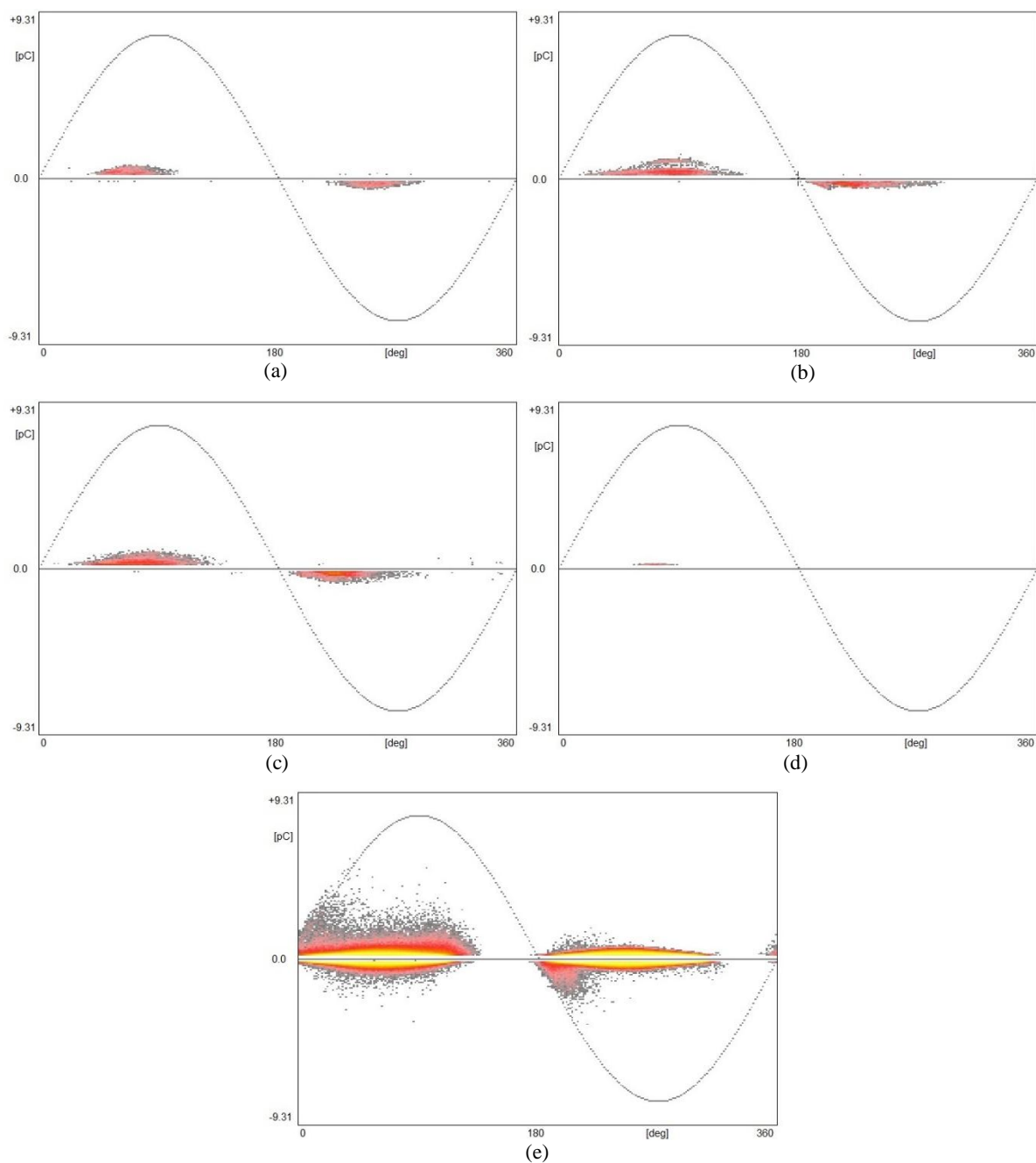
Fig 4.62 - Phase resolved PD pattern of AlN substrate embedded in DBT under 7.0 kV rms AC 50 Hz at (a) 25°C, (b) 100°C, (c) 200°C, (d) 300°C and (e) 350°C. Max vertical scale ±9.3 pC

After measurement series up to 350°C, black carbon dust was observed at the edge of copper metallization, and extended approx. 2 mm on the surface of AlN (Fig 4.63). This carbon dust was likely produced by the degradation of DBT due to partial discharges occurring at the edge of metallization. It indicates that under certain circumstances (probably at the highest voltage investigated, which may reach 2×PDIV) PDs also occurred in the liquid, in addition to those occurring within the ceramic material.

The mean PDs current versus applied voltage under variation of temperature, and mean PDs number recorded during 1 minute are shown in Fig 4.64 and Fig 4.65. Mean PDs current shows no significant changes between 20-100°C, and decreased thereafter up to 300°C.
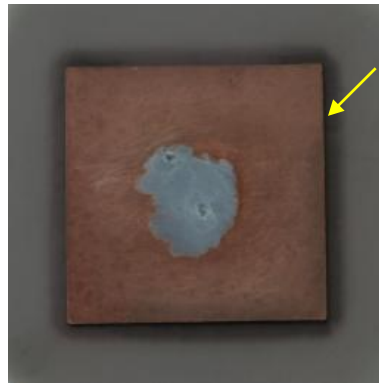
Fig 4.63 - Black carbon residue occurring along the metallization edges after PD measurement series with AlN substrate embedded in DBT
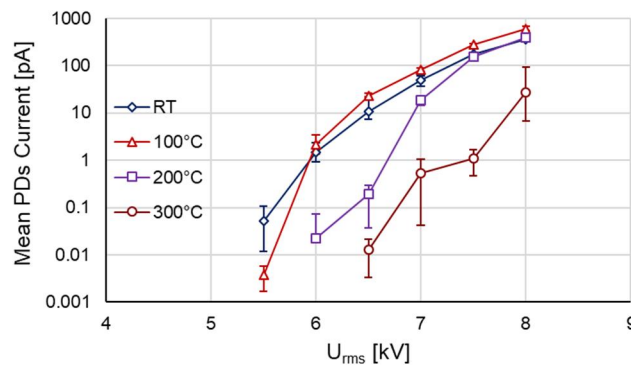
Fig 4.64 - Mean PDs current versus applied voltage for AlN substrate embedded in DBT at various temperature

A very similar tendency is observed on PDs number. This shows that the decrease of PDs current is due mainly to reduction of PDs number, which amplitudes remain almost unchanged except at 300°C.

At 350°C, following the possibility cracking in AlN, PDs occurred at much lower voltage (down to 1 kV rms), and were considerably larger. Further experiments would be however necessary to fully assess these cracking tendencies of AlN at very high temperatures.
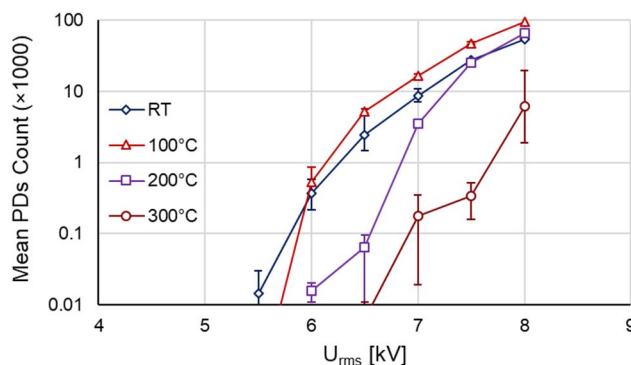
Fig 4.65 - Mean PDs number versus applied voltage for AlN substrate embedded in DBT at various temperature

4.5.4   Discussion of results

Fig 4.66 shows the comparison of PDs amplitude for alumina substrate in air and DBT. In air, these discharges can exceed 1000 pC at 1.5 kV rms, while in DBT they are tremendously reduced to less than 1 pC at voltages up to 9 kV, both at room temperature and 300°C. This measurement confirms that embedding substrates with DBT is very effective to supress PDs coming from substrates, even at high temperatures which is impossible with the standard silicone gel.

PD patterns obtained with substrates are very different from those with point-plane geometry: they are almost symmetrical in both polarities, whereas mainly negative discharges were obtained in point-plane coming from liquids. The large differences observed between PD measurements in DBT alone in point-plane geometry, and with substrates support the conclusion already obtained in [45]: PDs recorded on substrates do not occur in the encapsulant, but in the ceramic material itself. Since ceramic materials are manufactured by sintering powder at high temperature, this process includes numerous pores in which PDs may occur. However, ceramic is a highly stable mineral material, thus a negligible degradation is induced by PDs explaining these high stability of PD measurements. Therefore, most of PDs variations recorded versus voltage and temperature should be attributed to the ceramic material rather than to the liquid properties. The observation of carbon powder shows however that some PDs may also occur in the liquid, presumably at the highest voltage during tests or due to the field enhancement at edge curvature of electrode. Further tests would be necessary to confirm this hypothesis.
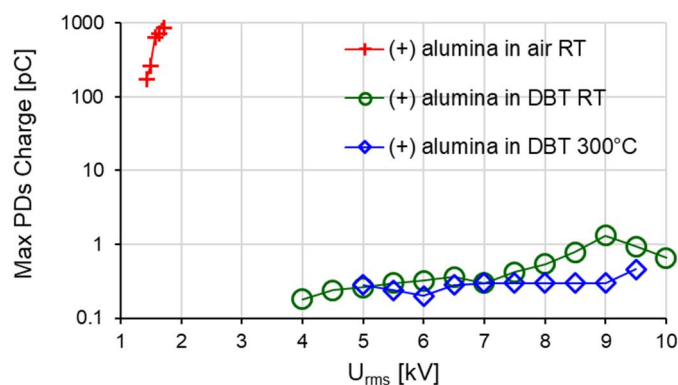
Fig 4.66 - Mean PDs charge versus applied voltage for alumina substrate embedded in air and DBT

Fig 4.67 shows the comparison of mean PDs current from AlN substrates embedded in silicone gel [102] and DBT at RT, 100°C and 300°C. Region in between two black dash-line is reference for good AlN substrate embedded in silicone oil Sil350 at RT [102].
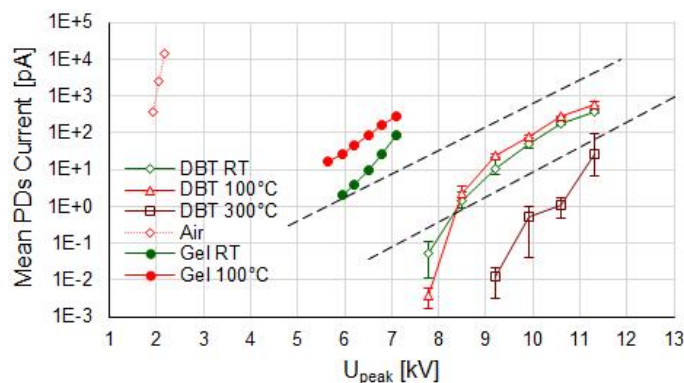
Fig 4.67 - Mean PDs current versus applied voltage for AlN substrate embedded in silicone gel [102] and DBT at RT and 100°C

At RT, it required 4.6 kV rms in silicone gel and 6.5 kV rms in DBT to have 10 pA mean PDs current. While at 100°C, it took 4.7 kV rms in gel and 7.2 kV rms in DBT resulting 100 pA mean PDs current (Fig 4.67). For AlN substrates, PDs suppressing features of DBT increases significantly from 1.4 at RT to 1.5 at 100°C compared to silicone gel. At 300°C, this PDs suppression becomes more marked. Confirming the PDs occurred in AlN substrates, DBT appears to be more effective than silicone gel and silicone oil in suppressing PDs at corresponding voltage.

The influence of temperature on PDIV in DBT alone in point-plane geometry is much larger than that observed with substrates (Fig 4.68). Furthermore, with alumina a decrease is observed while a moderate

increase is observed with AlN. This constitutes another evidence that PDs recorded with substrates are affected by properties of the substrate rather than by the encapsulant. The PDIV comparison between AlN and alumina indicates that up to 100°C AlN has slightly better properties, however for higher temperature application this material is less favourable since PDIV becomes identical to alumina, dielectric losses and permittivity considerably increase, and AlN could be more easily damaged by the thermal stress. Of course, the latter conclusion is only based on a single observation that should be confirmed by more mechanical tests, which is out of the scope of this study. Studies of mechanical damaging under thermal cycling up to 300°C [103] showed that substrates with aluminium metallization (DBA) show a much better reliability compared to those using copper (DBC) as in this study.
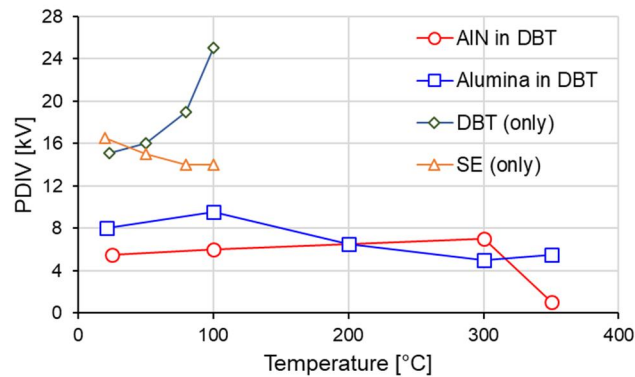
Fig 4.68 - PDIV comparison versus temperature

Since the dielectric properties of ceramic substrates and liquids, i.e.: permittivity, conductivity and tan (delta), are strongly dependent on temperature, a calculation of field distribution versus temperature has been carried out and presented in the next section.

4.6 Field simulation on substrates embedded in DBT

The field simulation with substrates embedded in DBT was performed with identical hypothesis as for breakdown measurements. The only difference was the geometry: the grounded electrode is now constituted by the metallization on the other side of substrate. All data and results presented refer to 50 Hz, which was the frequency used in PD measurements.

The objective of simulations is to give an overview of electric field distribution in the triple-point region with this different electrode geometry, and check the influence of temperature. Applied voltage was varied from 1 kV to 8 kV according to results of PD measurements.

4.6.1 AlN substrate

Fig 4.69 shows the field distribution of AlN substrate embedded in DBT around the triple-point for 6 kV applied voltage at 20°C (RT) and 300°C. Field enhancement now arises mostly in the liquid wedge located close to the triple-point. This result is rather different from that obtained with breakdown electrodes. Maximum field at boundary between AlN and DBT for 6 kV at RT and 300°C are 3.702 MV/mm and 398 kV/mm. The value at RT is very high, and shows a large decrease versus temperature. The field inside AlN below the surface is much lower than in DBT near triple-point.
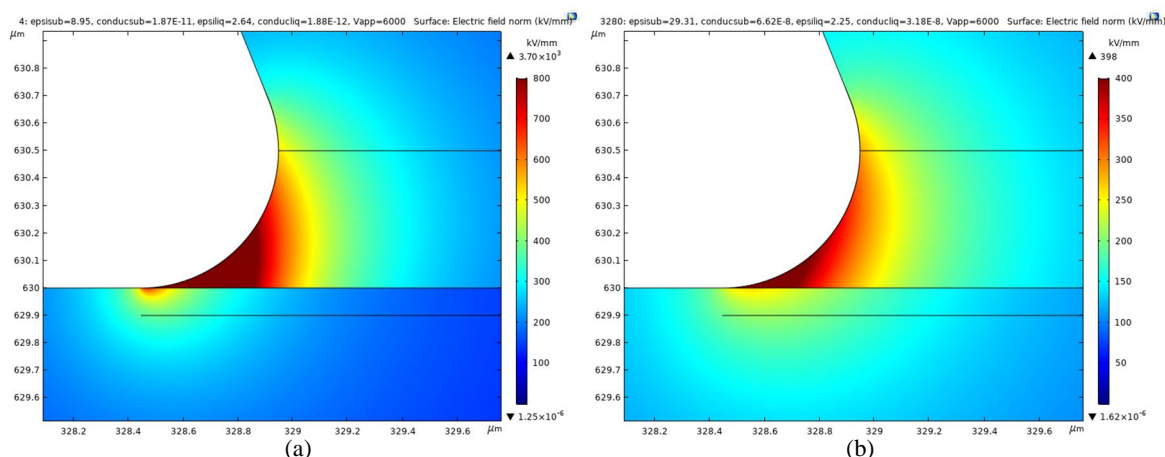
Fig 4.69 - AlN substrate embedded in DBT for 0.5 µm radius, 6 kV at: (a) 20°C and (b) 300°C

Fig 4.70 shows the field distribution along the AlN / liquid interface (starting from the triple-point along positive x-axis) at RT for 1 kV to 8 kV. With the postulated geometry, the maximum field is located in the very small liquid wedge between the metallization and the ceramic.
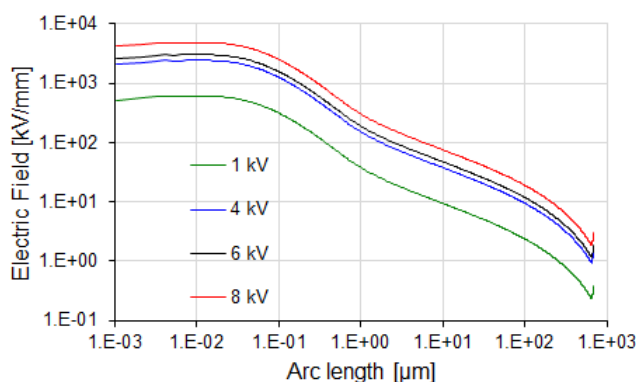
Fig 4.70 - Electric field distribution over the surface of AlN substrate in DBT at 20°C for 1 kV, 4 kV, 6 kV and 8 kV

For a typical voltage of 6 kV, the maximum field reaches 3.7 MV/mm at 0.01 µm (Fig 4.71a), i.e. a very high and somewhat unrealistic value. Since this value is highly dependent on the triple point geometry (not exactly known on real substrates), a more realistic reference value can be taken at some distance, e.g. 10 µm from the triple point. At such distance, the field reaches 56 kV/mm at 6 kV (Fig 4.71b), i.e. a value comparable to that obtained in Fig 4.40 with the breakdown geometry (also considering the 3× lower voltage used here for calculations).
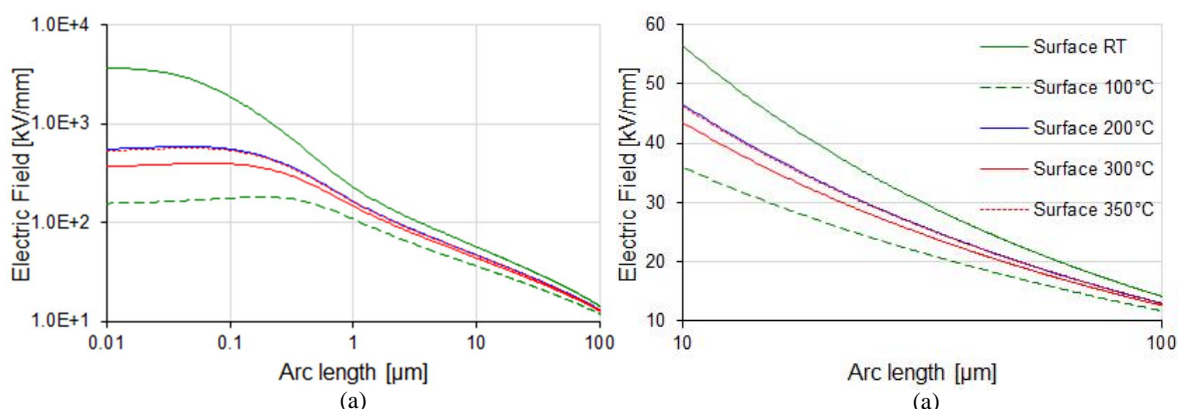
Fig 4.71 - Electric field distribution over the surface of AlN substrate in DBT under 6 kV at various temperature: (a) all arc length and (b) starting from 10 µm

The field in the liquid at the metallization tip are 438 kV/mm at RT and 276 kV/mm at 350°C as in Fig 4.72a. In the ceramic, 0.1 µm below the surface, the field is much lower (Fig 4.72b). Interestingly, a

significant field reduction also takes place from RT to 100°C. It increases thereafter at 200°C, and decreases again at 300°C. Field intensity at 350°C is close to that of 200°C.

These results are in qualitative agreement with PD measurements presented in the previous section (Fig 4.64 and Fig 4.65), showing a global decrease of PDIV activity when temperature is raised with AlN substrate.
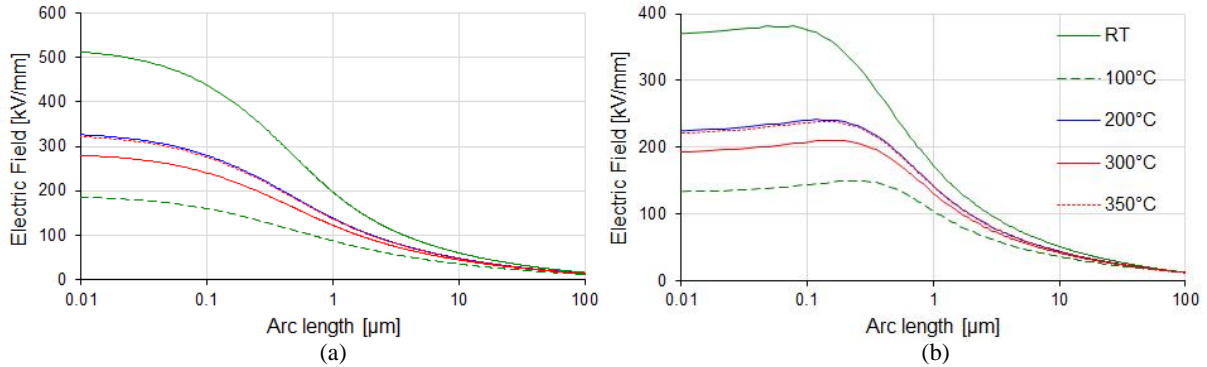
Fig 4.72 - Electric field distribution of AlN substrate in DBT for 6 kV: (a) on the tip in the liquid and (b) 0.1 µm below surface of the substrate

4.6.2   Alumina substrate

Fig 4.73 shows the field distribution of alumina substrate embedded in DBT around the triple-point for applied voltage 6 kV from RT up to 350°C. Due to the different dielectric properties of Alumina at 50Hz compared to AlN, rather different field distributions are observed. The field enhancement now shifts from the triple-point to other spots as temperature increases.

(e)
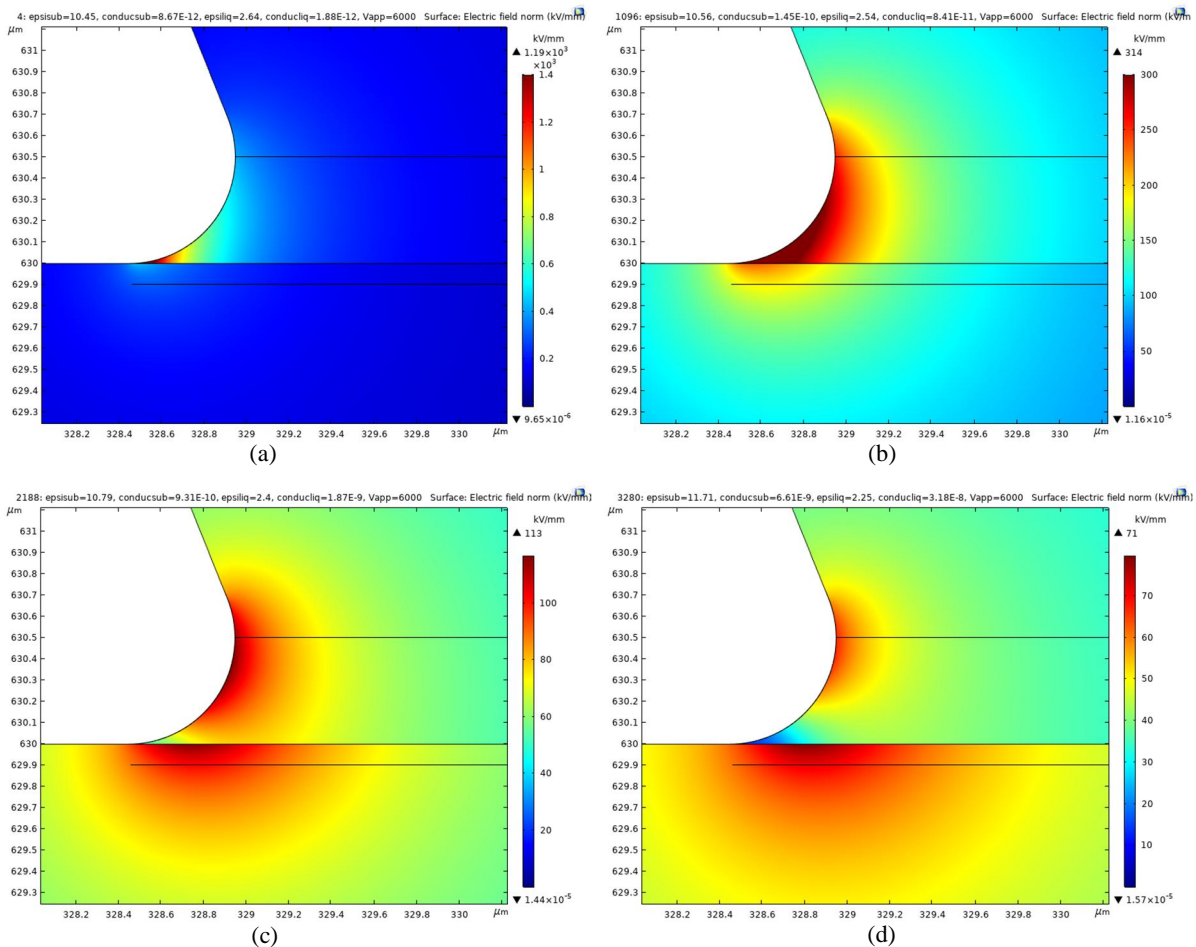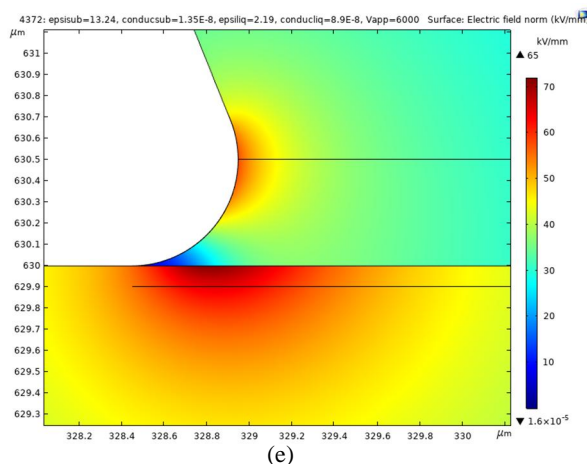
Fig 4.73 - Alumina substrate embedded in DBT for 0.5 µm radius, 6 kV at: (a) 20°C, (b) 100°C, (c) 200°C, (d) 300°C and (e) 350°C

At RT, the maximum field enhancement occurs around the triple-point in the liquid, but is then strongly reduced at high temperature, where 2 different high field spots appear: inside the alumina substrate, and around the copper metallization tip in the liquid. The maximum field on the surface around the triple-point at 6 kV (1.19 MV/mm at RT) considerably drops to 300kV/mm at 100°C, down to 51 kV/mm at 350°C.
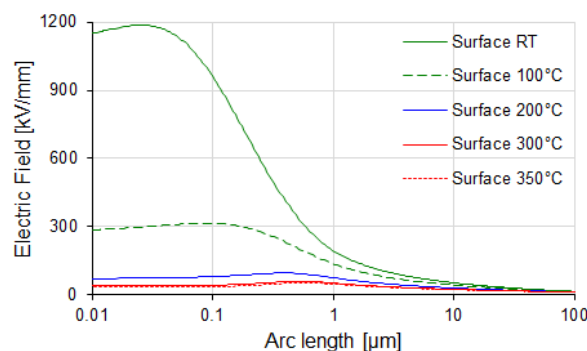
Fig 4.74 - Electric field distribution on the surface of alumina substrate in DBT for 6 kV

The decrease of fields at the tip and in the substrate below the surface is less marked. Field intensity for 6 kV at 0.1 µm from the tip curvature drops from 346 kV/mm at RT to 49 kV/mm at 350°C as presented in Fig 4.75a. Below the surface, it reduces from 298 kV/mm (at RT) down to 65 kV/mm at 350°C as in Fig 4.75b.

These results are not in qualitative agreement with PD measurements, that show a global increase of PD activity when temperature is raised. As noted above, mainly phenomena (space charges, EHD motion, non linearity of properties) should be considered to obtain a more realistic simulation.

(a)   (b)
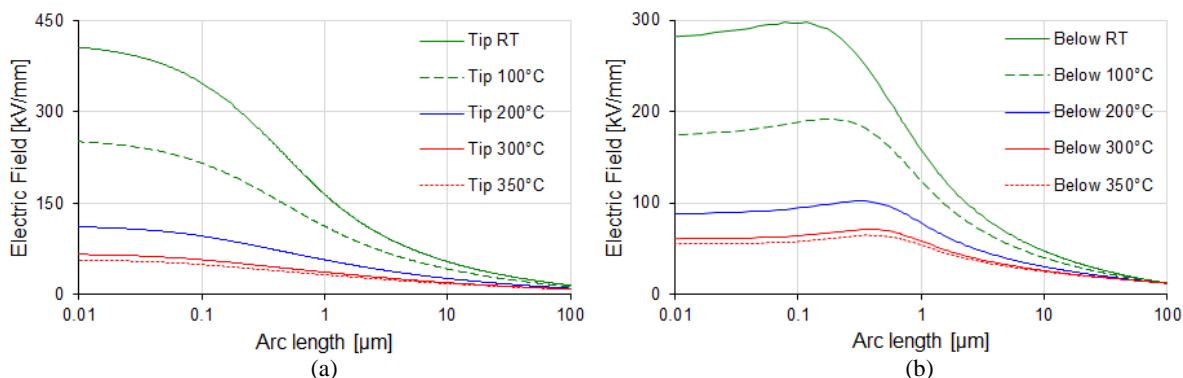
Fig 4.75 - Electric field distribution of alumina substrate in DBT for 6 kV: (a) on the tip curvature in the liquid and (b) 0.1 µm depth below surface of the substrate

4.7 Conclusion: applicability of DBT liquid to replace silicone gel for high temperature applications

4.7.1 Breakdown measurements

A summary of breakdown fields measured with a variety of conditions in silicone gel and Jarytherm® DBT is presented in TABLE 4.32. These measurements corresponds to a typical gap of 0.3 mm, and are expressed as: mean value (lowest value) in kV/mm. The lowest value is of interest for design purposes, since a very low breakdown probability should exist in real applications. Of course, more experiments would be required to get a better statistical relevance (especially at low probability).

However, from this table, several conclusions can be already obtained regarding the possibility to replacing silicone gels by the DBT high temperature liquid. Results show variations when the encapsulant material is replaced and temperature changed, but also an unexpected high sensitivity to the nature of the substrate material.

With epoxy substrate, DBT is superior to silicone gel in all conditions (DC, impulse, RT and 160°C). Only one exception is found at DBT/RT/DC where the lowest value is lower than in silicone gel.

With Alumina substrate, the opposite result is obtained: silicone gel is superior to DBT in all conditions.

Since epoxy cannot be used in high temperature applications, we may conclude that using DBT in high voltage and high temperature applications with ceramic substrates would require adapting the design, to account for a lower breakdown mean field. This can be done easily by increasing the insulation distances, since breakdown voltages increases with gap (e.g. in Fig 4.23). On should however consider that both materials show very good breakdown properties: with the minimum gap distance investigated (down to 0.3 mm with alumina) breakdown voltages were always larger than 10 kV in all conditions.

TABLE 4.32 - Breakdown field summary for substrates embedded in silicone gel and DBT

	Sil. Gel - RT	Sil. Gel - 160°C	DBT - RT	DBT - 160°C
Epoxy DC	45 (40)	30 (16)	50 (28)	45 (40)
Alumina DC	68 (58)	55 (25)	45 (40)	28 (15)
Epoxy Impulse	55 (45)	43 (37)	90 (75)	60 (40)
Alumina Impulse	65	50	45 (40)	25 (18)

In all measurements obtained with alumina, the intrinsic self-healing properties of liquids were unfortunately not helpful: in all measurements, an immediate irreversible degradation of the substrate occurred.

Of course, several conclusions obtained here should be further documented and verified by complementary measurements. The number of experiments was here limited by the availability of ceramic breakdown substrates. It turned out that breakdown measurements require a large number of substrates, since only one measurement could be obtained with a breakdown gap. These measurements could be also extended to higher temperatures, which would require building a special multi-electrode High Voltage and High Temperature testcell, with maximum voltage in excess of the 30 kV cell built in this study.

4.7.2 Partial Discharge measurements.

The PD measurements carried out here confirm the conclusion already obtained with various liquids and gels: PDs primarily originate from the porous ceramic material, and show a limited sensitivity to the encapsulant nature. Since ceramic materials of mineral nature show an excellent resistance to PDs, no significant degradations were observed during experiments lasting several days.

The PD measurements carried out here for the first time at high temperature showed different results according to the substrate nature: a decrease of PD activities were recorded with AlN, and conversely with alumina. Based on a limited number of results, it appear that alumina could be more favourable for very high temperature applications (around 300°C).

It would be however necessary to confirm this result by complementary measurements. A study of aluminium-metallized substrates (DBA) also would be of great interest, since these structures show a much better mechanical resistance to high temperatures.

4.7.3 Possible applications of DBT as high temperature insulating liquid.

The practical use of high temperature insulating liquids such as DBT in industrial systems such as power modules would require many additional investigations, dealing with technical issues such as tightness, compatibility with materials, reliability, risk of fire, long term stability, influence of pollution, etc. At the laboratory level, DBT can be already of great help when high voltage and high temperature insulation is required for testing devices (e.g. new high voltage semiconductors with SiC, Diamond), or for other specific applications (e.g. high temperature machines).

General Conclusions and Perspectives

Encapsulant plays key roles in electronics power module packaging system. In addition to basic features of providing electrical and mechanical protection for active parts, its ability to conform to high temperature conditions will be another challenge to address with wide bandgap semiconductor materials. Drawbacks and limitations of the silicone gel encapsulants due to thermal limitation below 200°C have been identified.

The objective of this thesis was to present an initial introduction of dielectric liquids as potential replacement materials. A blend of dibenzyltoluene isomers liquid, providing a high boiling point (390°C) has been identified as interesting material, and thoroughly characterized at high temperature. Studies on the conduction, losses, pre-breakdown, and breakdown process and mechanisms have been made, both by means of low and high electric field, under influence of temperature up to 350°C. Experiments were done either with liquids alone, and with substrates embedded in liquids or gels for comparison. Numerical simulations with different types of ceramic substrates embedded in dielectric liquid also were carried out to identify the high field regions, and try to better understand variations of dielectric properties at high temperature and applied voltage.

When ceramic substrates are embedded in dielectric liquid, temperature significantly governs and modify the field enhancement at triple-point region, and pre-breakdown and breakdown mechanism. Different type of electric fields such as AC, DC or impulse, uniform or divergent, also influence these mechanisms. Combining the substrates with silicone gel or dielectric liquids result in distinct and complex behaviours, either when the encapsulant is replaced, but also when the nature of substrate is modified.

To obtain these results, we have developed specific experimental set-up for dielectric liquid characterization under high temperature up to 350°C and high voltage up to 30 kV. Two specific high temperature testcells were constructed for low electric field measurements (i.e.: dielectric spectroscopy and conduction studies), and for high electric field measurements up to 30 kV applied voltage. A specific impulse generator was also developed and constructed for breakdown studies under repetitive fast impulses to 60 kV/100A. Specific substrate samples were also realized for PD and breakdown measurements.

A. Main conclusions obtained

1. Conduction and dielectric spectroscopy measurements

Bulk conduction is mainly due to the ionic dissociation and recombination processes in non-polar liquids, while other mechanisms (i.e. interface polarization, injection, etc.), may also be involved. This process is strongly enhanced by temperature rise, yielding to lower viscosity and hence higher ion mobility, and also to enhanced dissociation of impurities. In DBT and Synthetic Ester, the relation between viscosity and conductivity has been established, as well as the activation energy relevant of enhanced dissociation. Both parameters allow describing variations of DC conductivity up to high temperatures. At high temperatures, DBT show a larger conductivity compared to gel (by about one decade), but lower than in SE.

Under AC voltage, the dielectric spectroscopy allows establishing the stable DC conductivity region, that expands larger as temperature is higher. In DBT, over the investigated range (10 mHz to 1 MHz, room temperature to 350°C), dielectric losses are mainly related to conduction losses, while the influence of electrode polarization is only observed at very low frequency and high temperature. Tan (delta) shows high values at high temperatures, up to about 10^3 in DBT at low frequency and temperature above 300°C.

Under a large temperature range, permittivity shows a significant variation (up to -20% at 350°C in DBT), mainly related to the decrease of density. Comparison among silicone gel and several dielectric liquids candidates reveal that DBT has the lowest dielectric constant over wide temperature range.

Following high temperature exposure for several hours, the dielectric properties of DBT are satisfactory stable with negligible modification. This point should be however further documented with longer exposure.

2. PD and pre-breakdown streamers

In pre-breakdown measurements (i.e.: partial discharges and streamers), high field enhancement and space charge are the key factors governing the inception of discharges. For PDs in DBT, temperature rise is significantly reducing both the amplitude and number of PDs. Under space-charge free conditions (i.e. streamer initiation under impulse voltage), temperature has a minor influence on discharge inception. PD inception field calculations on the tip under 50 Hz AC voltage are larger than with impulse voltage. This difference can be attributed to the space charge limitation of the field occurring under AC. At high temperature in DBT, the difference increases rapidly, indicating that space charge limitation under highly divergent field is strongly enhanced by temperature.

PDs in DBT are mostly dominated by negative discharges, related to 1st mode negative streamers that show nearly no propagation. Larger positive discharges, related to 2nd mode filamentary streamers, are not observed in PD measurements, since 1st mode positive streamers initiated at lower voltage produce a space charge limitation of the field. This favourable effect is not observed in other liquids, when only 2nd mode positive streamers occur. DBT thus shows very good PD properties, with very small PDs even when voltage is raised.

3. Breakdown measurements under uniform field

In breakdown measurements with short gaps (< 0.5 mm) under quasi-uniform field, temperature and pressure are key factors determining the breakdown properties in DBT. Close to boiling conditions, the vapour bubble generation induces a large drop of breakdown voltage. The influence of temperature and pressure can be described by using a single parameter: the difference between ambient temperature and the boiling temperature at the considered pressure. DBT shows a high breakdown strength at room temperature, which decreases when temperature is raised.

4. PD and breakdown measurements with substrates

In terms of application of liquids to power modules, measurements of PDs and breakdown voltage (under DC and impulse) under high temperature with substrates show the advantages and disadvantages of DBT compared to the standard silicone gel. Partial discharges from ceramic substrates are evidenced with DBT, such as with other liquids. With ceramic substrates, measurements at high temperature show either a decrease of PD activity (with AlN ceramic) or conversely an increase (with alumina). DBT shows efficient PD suppression properties up to high temperatures. Dielectric spectroscopy on ceramic

substrates reveal that alumina shows more stable properties at high temperatures. At high temperatures, AlN shows a very large increase of dielectric losses and permittivity.

DC and impulse breakdown measurements with alumina embedded in silicone gel demonstrated a better behaviour as compared to DBT, with temperatures up to 160 °C. Conversely, with epoxy substrate DBT becomes unexpectedly superior to silicone gel. Using DBT for encapsulation at high temperature with ceramic substrates would require increasing gap distances between conductive tracks at high voltage.

Self-healing properties of DBT are not operative with ceramic substrates, since breakdown induces an immediate irreversible degradation of the substrates.

B. Perspectives

Even though this work does not cover all practical aspects for high-temperature and high-voltage power electronics applications, some basic experimental results are established. From both the scientific and application points of view, many complementary investigations could be done to achieve better understanding of dielectric liquids behaviour under high temperature, and better assessment of practical issues.

- ✓ complementary experiments on influence of thermal ageing, impact of oxidation and durability of liquids when exposed to high temperature for long durations;
- ✓ Better understanding of space charge effects which seems to be of primary importance at high temperature;
- ✓ Complementary PD and breakdown measurements with larger ceramic sample number, and at higher temperatures (up to 300 °C)
- ✓ Breakdown measurements at long term;
- ✓ More accurate field modelling by considering influence of space charge and EHD motion;
- ✓ Thermal measurements in order to investigate the actual efficiency of cooling induced by EHD motion.

Reference

1. A. Dutta and Simon S. Ang, "A Module-Level Spring-Interconnected Stack Power Module", IEEE Trans. on Components, Packaging and Manufacturing Technology, vol. 9, no. 1, pp. 88-95, Apr. 2019.
2. R. Wang, Z. Chen, D. Boroyevich, L. Jiang, Y.Y. Yao and R. Kaushik, "A novel hybrid packaging structure for high-temperature SiC power module", IEEE Energy Conversion Congress and Exposition, Phoenix, AZ, Sept. 2011.
3. Y.G. Wang, Y. Li, X.P. Dai, S.W. Zhu, S. Jones and G.Y. Liu, "Thermal design of a dual sided cooled power semiconductor module for hybrid and electric vehicles", IEEE Applied Power Electronics Conference and Exposition (APEC), Tampa, FL, Mar. 2017.
4. M. Horio, Y. Iizuka, Y. Ikeda, E. Mochizuki and Y. Takahashi, "Ultra compact and high reliable SiC MOSFET power module with 200°C operating capability", 24th International Symposium on Power Semiconductor Devices and ICs, Bruges, Jun. 2012.
5. S. Inokuchi, S. Saito, A. Izuka, Y. Hata, S. Hatae, T. Nakano and E.R. Motto, "A new high capacity compact power modules for high power EV/HEV inverters", IEEE Applied Power Electronics Confrence and Exposition (APEC), Long Beach, CA, Mar. 2016.
6. A. Imakiire, K. Nakamura, H. Tanabe, H. Kaisyakuji, T. Kubo, M. Kozako and M. Hikita, "Investigation of prototype SiC power module structure for low inductance and high heat operation", IEEE International Workshop on Integrated Power Packaging (IWIPP), Delft, Apr. 2017.
7. Deepak Tiku, "DC power transmission Mercury-Arc to thyristor HVDC Valves", IEEE Power and Energy Magazine, vol. 12, no. 2, pp. 76-96, Mar-Apr. 2014.
8. M.C. Duffy, "The mercury-arc rectifier and supply to electric railways", Engineering Science and Education Journal, vol. 4, no. 4, pp. 183-192, Aug. 1995.
9. T.F. Shi, J. Chang, L. Leverich and C. Leader, "500W Long-Pulse High Efficiency UHF BJT Transistor for Radar Applications", Asia-Pacific Microwave Conference, Bangkok, Dec. 2007.
10. Y. Gao, A.Q. Huang, S. Krishnaswami, J. Richmond and A.K. Agarwal, "Comparison of Static and Switching Characteristics of 1200 V 4H-SiC BJT and 1200 V Si-IGBT", IEEE Transactions on Industry Applications, vol. 44, no. 3, pp. 887-893, May 2008.
11. X. Li, Y. Luo, L. Fursin, J.H. Zhao, M. Pan, P. Alexandrov and M. Weiner, "4H-SiC BJT and Darlington switch for power inverter applications", International Semiconductor Device Research Symposium. Symposium Proceedings, Washington DC, Dec. 2001.
12. S. Rewari, R.S. Gupta, SS. Deswal and V. Nath, "Silicone carbide based DSG MOSFET for high power, high speed and high frequency applications", IEEE 6th India International Conference on Power Electronics (IICPE), Kurukhsetra, Dec. 2014.
13. N. Surana, R. Kaur and J. Mekie, "Short and deep drain MOSFET for space applications: Device and circuit level analysis", 16th European Conference on Radiation and Its Effects on Components and Systems (RADECS), Bremen, Sep. 2016.
14. Q.L. Zhu, L. Wang, L.Q. Zhang, W.S. Yu and A.Q. Huang, "Improved medium voltage AC-DC rectifier based on 10kV SiC MOSFET for Solid State Transformer (SST) application", IEEE Applied Power Electronics Conference and Exposition (APEC), Long Beach, Mar. 2016.

15. D.Y. Xiang, M. Kakefu, S. Matsumi and M. Otsuki, "T-type IGBT module with new voltage class authentic RB-IGBT for DC-1000V solar inverter application", International Power Electronics and Application Conference and Exposition, Shanghai, Nov. 2014.

16. C.L. Zhu, I. Deviny, X.P. Dai, L. Ngwendson, H.H. Luo, Q. Xiao, X.B. Ning, H.B. Xiao and G.Y. Liu, "A floating dummy trench gate IGBT (FDT-IGBT) for hybrid and electric vehicle (HEV/EV) applications", 19th European Conference on Power Electronics and Applications (EPE'17 ECCE Europe), Warsaw, Sep. 2017.

17. T. Stockmeier, R. Bayerer, E. Herr, D. sinerius and U. Thiemann, "Reliable 1200 amp 2500 V IGBT modules for traction applications", IEE Colloquium on IGBT Propulsion Drives, London, Apr. 1995.

18. H. Gibson and M.E. Bradley, "The development of high power thyristors for power system applications", IEE Colloquium on Very High Power Converter Devices and Applications, London, Dec. 1988.

19. J. Zyborski, "Thyristor circuit breaker devices for energy recovery applications", IEE Colloquium on Electronic-Aided Current-Limiting Circuit Breaker Developments and Applications, London, Nov. 1989.

20. Arunachalam, R.R. Babu, B. Bose and D. Dutta, "Evaluation of losses in thyristor valve for SVC application", International Conference on Power Electronics, Drives and Energy Systems for Industrial Growth, New Delhi, Jan. 1996.

21. T. Kimoto, "Material science and device physics in SiC technology for high voltage power devices", Japanese Journal of Applied Physics, vol. 54, no. 040103, 2015.

22. C. Raynaud, D. Tournier, H. Morel and D. Planson, "Comparison of high voltage and high temperature performances of wide bandgap semiconductors for vertical power devices", Diamond and related materials, pp. 1-6, vol. 19, no. 1, Jan. 2010.

23. R. Hanna et. al., "Reliability of elastomer encapsulation for high temperature power semiconductor devices", 11ème Conférence de la Société Française d'Electrostatique (SFE), Grenoble, Aug. 2018.

24. J. Rabkowski "Power converters with silicon carbide devices", 14th Biennial Baltic Electronic Conference (BEC), Tallinn, Oct. 2014.

25. F.H. Kreuger, E. Gulski and A. Krivda, "Classification of Partial Discharges", IEEE Transactions on Electrical Insulation, vol. 28, no. 6, pp. 917-931, Dec. 1993.

26. T.A.T. Vu, J.-L. Augé, O. Lesaint and M.T. Do, "Partial discharges in Aluminium Nitrite Ceramic Substrates", 10th IEEE International Conference on Solid Dielectrics, Postdam, Jul. 2010.

27. C.F. Bayer, U. Waltrich, A. Soueidan, E. Baer and A. Schletz, "Partial Discharges in Ceramic Substrates - Correlation of Electric Field Strength Simulations with Phase Resolved Partial Discharge Measurements", Transactions of The Japan Institute of Electronics Packaging, vol. 9, pp. E16-003-1-9, Dec. 2016.

28. M.T. Do, O. Lesaint and J.-L. Augé, "Partial Discharges and Streamers in Silicone Gel Used to Encapsulate Power Electronic Components", Conference on Electrical Insulation and Dielectric Phenomena (CEIDP), Annual Report, Oct. 2007.

29. T. Ebke, A. Khaddour and D. Peier, "Degradation of Silicone Gel by Partial Discharges due to Different Defects", 8th International Conference on Dielectric Materials, Measurements and Applications, Edinburgh, Sep. 2000.

30. T. Ebke, D. Peier and K. Temmen nee Engel, "Influence of Manufacturing Parameters on the PD-Behaviour of AlN-Substrates", 11th International Symposium on High Voltage Engineering, IET, London, Aug. 1999.

31. M.T. Do "Propriétés diélectriques des gels isolants: application aux composants d'électronique de puissance", Engineering Sciences [physics], pp. 31, Université Joseph Fourier - Grenoble I, France, 2008.

32. H. Reynes, C. Buttay and H. Morel, "Protruding ceramic substrates for high voltage packaging of wide bandgap semiconductors", IEEE 5th workshop on Wide Bandgap Power Devices and Application (WiPDA), Albuquerque, NM, Nov. 2017.

33. M.T. Do, J.-L. Augé and O. Lesaint, "Partial Discharges in Silicone Gel in the Temperature Range 20-150°C", IEEE Conference on Electrical Insulation and Dielectric Phenomena (CEIDP), Kansas City, MO, Oct. 2006.

34. M.T. Do, O. Lesaint and J.-L. Auge, "Streamers and partial discharge mechanisms in silicone gel under impulse and AC voltages", IEEE Transactions on Dielectrics and Electrical Insulation, vol. 15, no. 6, pp. 1526-1534, Dec. 2008.

35. M. Musallam, C.M. Johnson, C. Yin, H. Lu and C. Bailey, "Real-Time Comparison of Power Module Failure Modes under In-Service Conditions", 13th European Conference on Power Electronics and Applications, Barcelona, Sep. 2009.

36. Y.Y. Yao, Z. Chen, G.-Q. Lu, D. Boroyevich and K.D.T. Ngo, "Characterization of Encapsulants for High-Voltage High-Temperature Power Electronic Packaging", IEEE Transactions on Components, Packaging and Manufacturing Technology, vol. 2, no. 4, pp. 539-547, Apr. 2012.

37. R. Khazaka, L. Mendizabal, D. Henry and R. Hanna, "Survey of High-Temperature Reliability of Power Electronics Packaging Components", IEEE Transactions on Power Electronics, vol. 30, no. 5, pp. 2456-2464, May 2015.

38. T. Lebey, I. Omura, M. Kozako, H. Kawano and M. Hikita, "High Temperature High Voltage Packaging of Wideband Gap Semiconductors Using Gas Insulating Medium", International Power Electronics Conference - ECCE ASIA, Sapporo, Jun. 2010.

39. I. Fofana, "50 Years in the Development of Insulating Liquids", IEEE Electrical Insulation Magazine, vol. 29, no. 5, Oct. 2013.

40. IEEE Std C57.106TM-2015, "IEEE Guide for Acceptance and Maintenance of Insulating Mineral Oil in Electrical Equipment", IEEE Power and Energy Society, 2015.

41. ASTM D3487, "Standard Specification for Mineral Oil Used in Electrical Apparatus", ASTM, 2016.

42. O. Lesaint, "Streamer in Liquids: Relation with Practical High Voltage Insulation and Testing of Liquids", International Conference on Dielectric Liquids (ICDL), Futuroscope-Chasseneuil, Jul. 2008.

43. C.M. Barnes and P.E. Tuma, "Practical Considerations Relating to Immersion Cooling of Power Electronics in Traction Systems" IEEE Vehicle Power and Propulsion Conference (VPPC), Sep. 2009.

44. A.A. Abdelmalik, A. Nysveen and L.E. Lundgaard, "Partial discharges in liquid embedded power electronics: Effects of pressure and liquid nature under negative pulse voltage stress", IEEE Transactions on Dielectrics and Electrical Insulation, vol. 23, no. 2, pp. 1119-1125, Apr. 2016.

45. J.-L. Auge, O. Lesaint and A.T. Vu Thi, "Partial Discharges in Ceramic Substrates Embedded in Liquids and Gels", IEEE Transactions on Dielectrics and Electrical Insulation, vol. 20, no. 1, pp. 262-274, Feb. 2013.

46. P. Norgard, R.D. Curry, R. Burdt, R. Cravey, G. Anderson and S. Heidger, "A High Pressure Flowing Oil Switch for Gigawatt, Repetitive Applications", IEEE Pulsed Power Conference (PPC), Monterey, Jun. 2005.

47. R. Kattan, A. Denat and O. Lesaint, "Generation, growth, and collapse of vapor bubbles in hydrocarbon liquids under a high divergent electric field", Journal of Applied Physics, vol. 66, no. 9, pp. 4062, Jul. 1989.

48. V.T.A. Tho, J.-L. Augé and O. Lesaint, "Partial discharges and light emission from ceramic substrates embedded in liquids and gels", IEEE International Conference on Dielectric Liquids (ICDL), Trondheim, Jun. 2011.

49. K.B. Liland, C. Lesaint, L. Lundgaard, M. Hernes and W.R. Glomm, "Liquid insulation of IGBT modules: Long term chemical compatibility and high voltage endurance testing", IEEE International Conference on Dielectrics (ICD), Montpellier, Jul. 2016.

50. C. Yeckel, R. Curry and P. Norgard, "Voltage Breakdown Characterization of Oil Dielectrics for High-Power Switching Applications", IEEE International Power Modulators and High-Voltage Conference (IPMC), Las Vegas, May 2008.

51. Ramsay and S. Young, "Influence of change of condition from liquid to the solid state on vapour-pressure", Philosophical Transaction of the Royal Society of London, vol. 175, pp. 461-478, Jan. 1884.

52. E.O. Forster, "A Comparison of the AC and DC Conductivities of Liquid Hydrocarbons II", Conference on Electrical Insulation & Dielectric Phenomena (CEIDP), Buck Hill Falls, Oct. 1972.

53. B. Abedian and K.N. Baker, "Temperature Effects on the Electrical Conductivity of Dielectric Liquids", IEEE Transactions on Dielectrics and Electrical Insulation, vol. 15, no. 3, pp. 888-892, Jun. 2008.

54. T.G. Aakre, T.A. Ve and Ø.L. Hestad, "Conductivity and permittivity of midel 7131: effect of temperature, moisture content, hydrostatic pressure and electric field", IEEE Transactions on Dielectrics and Electrical Insulation, vol. 23, no. 5, pp. 2957-2964, Oct. 2016.

55. I. Fontana, A. Bouaicha, M. Farzaneh and J. Sabau, "Ageing behaviour of mineral oil and ester liquids: a comparative study", Conference on Electrical Insulation and Dielectric Phenomena (CEIDP), Quebec, Oct. 2008.

56. S. Abdi, A. Boubakeur, A. Haddad and N. Harid, "Influence of artificial thermal aging on transformer oil properties", Journal of Electric Power Components and Systems, vol. 39, no. 15, pp. 1701-1711, Oct. 2011.

57. J. Walker, A. Valot, Z.D. Wang, X. Yi and Q. Liu, "M/DBT, new alternative dielectric liquids for transformers", CIGRE D1-107, 2012.

58. C. Mazzetti, M. Pompili and R. Cecere, "The effect of molecular of dielectric fluids on their conduction and breakdown", 10th International Conference on Conduction and Breakdown in Dielectric Liquids, Grenoble, Sep. 1990.

59. Arkema, "Jarytherm: Heat transfer fluids", Technical Specifications, 2009.

60. O. Lesaint, "Prebreakdown phenomena in liquids: propagation 'modes' and basic physical properties", Journal of Physics D: Applied Physics, vol. 49, no. 14, Mar. 2016.

61. O. Lesaint, "Streamer in Liquids: Relation with Practical High Voltage Insulation and Testing of Liquids", International Conference on Dielectric Liquids (ICDL), Futuroscope-Chasseneuil, Jul. 2008.

62. P. Gournay and O. Lesaint, "A Study of the Inception of Positive Streamers in Cyclohexane and Pentane", Journal of Physics D: Applied Physics, vol. 26, no. 11, pp. 1966-1974, 1993.

63. E.O. Forster, H. Yamashita, C. Mazzetti, M. Pompili, L. Caroli and S. Patrissi, "The effect of the electrode gap on the breakdown process in liquid dielectrics", IEEE 11th International Conference on Conduction and Breakdown in Dielectric Liquids (ICDL), Baden-Dattwil, Jul. 1993.

64. Q. Liu, Z.D. Wang and O. Lesaint, "Comparison of streamer propagation in mineral oils under lightning and step impulse voltages", IEEE 18th International Conference on Dielectric Liquids (ICDL), Bled, Jul. 2014.

65. R. Tobazéon, "Streamers in Liquids", The Liquid State and Its Electrical Properties, Springer, vol. 193, pp. 465-501, 1988.

66. P. Gournay and O. Lesaint, "Evidence of the gaseous nature of positive filamentary streamers in various liquids", IEEE Conference on Electrical Insulation and Dielectric Phenomena (CEIDP), Arlington, Oct. 1994.

67. Y. Katayama, T. Nakayashiki and H. Yamashita, "The effect of viscosity on the negative streamer inception in PFPE", IEEE Conference on Electrical Insulation and Dielectric Phenomena (CEIDP), Austin, Oct. 1999.

68. K. Miyano, K. Yamazawa, M. Pompili, C. Mazzetti and H. Yamashita, "The characteristics of streamers in perfluoro liquids", IEEE Conference on Electrical Insulation and Dielectric Phenomena (CEIDP), Minneapolis, Oct. 1997.

69. Ø.L. Hestad, L.E. Lundgaard and D. Linhjell, "New experimental system for the study of the effect of temperature and liquid to solid transition on streamers in dielectric liquids: application to cyclohexane", IEEE Transactions on Dielectrics and Electrical Insulation, vol. 17, no. 3, pp. 764-774, Jun. 2010.

70. J.-S. Chang, P.A. Lawless and T. Yamamoto, "Corona Discharge Processes", IEEE Transactions on Plasma Science, vol. 19, no. 6, pp. 1152-1166, Dec. 1991.

71. MIDEL® 7131, "Technical Information Pack", M&I MATERIALS, Jun. 2016.

72. Galden® HT PFPE, "Heat Transfer Fluids", SOLVAY, ver. 2.2, 2014.

73. IRLAB LDTRP-2 Model, "Irlab analyser for electrical measurements in highly insulating liquids", Instruction manual.

74. Novocontrol Alpha-A Analyzer, "Technical Specification", Novocontrol Technologies, Mar. 2010.

75. X.P. Chen, J. Li and Y. Lv, "Electrical aging characteristics of natural ester oil-paper insulation respectively considering temperature and moisture", IEEE International Conference on High Voltage Engineering and Application (ICHVE), 2016.

76. W. Lu, Q. Liu and Z.D. Wang, "AC breakdown strength of a natural ester transformer liquid under accelerated thermal ageing", IEEE Conference on Electrical Insulation and Dielectric Phenomena (CEIDP), 2016.

77. Dhruvesh M. Mehta, P. Kundu and A. Chowdhury, "A review of critical evaluation of natural ester vis-a-vis mineral oil insulating liquid for use in transformers: Part II", IEEE Transactions on Dielectrics and Electrical Insulation, vol. 23, no. 3, June 2016.

78. Frederick I. Mopsik, "Dielectric Constant of N-Hexane as a function of Temperature, Pressure and Density," Journal of National Bureau of Standards – A. Physics and Chemistry, vol. 71A, no. 4, July-August 1967.

79. W.G.S. Scaife, "Relative Permittivity of Organic Liquids as a Function of Pressure and Temperature," Journal of Physics A: General Physics, vol. 4, 1971.

80. J. Muslim, R. Hanna, O. Lesaint, J.L. Reboud and N.I. Sinisuka, "Electrical Characterization of Synthetic Ester Liquid Over Wide Temperature Range (-60°C/200°C)", 19th IEEE International Conference on Dielectric Liquids (ICDL), Manchester, UK, Jun. 2017.

81. A.R.V. Hippel, "*Dielectric and Waves*," John Wiley & Sons, New York, 1954.

82. SILGARD® 527, "Silicone dielectric gel", Product information, Dow Corning, Ref. no. 61-0390J-01, Jun. 1998.

83. L. Yang et. al., "Measurement of Ion Mobility in Transformer Oils for HVDC Applications", International Conference on High Voltage Engineering and Application (ICHVE), Shanghai, China, Sep. 2012.

84. A. Denat, B. Gosse and J.P. Gosse, "Ion Injection in Hydrocarbons", Journal of Electrostatics, vol. 7, pp. 205-225, Aug. 1979.

85. R. Tobazéon, J.C. Filippini and C. Marteau, "On the Measurement of the Conductivity of Highly Insulating Liquids", IEEE Transactions on Dielectrics and Electrical Insulation, vol. 1, no. 6, pp. 1000-1004, Dec. 1994.

86. A. Denat, B. Gosse and J.P. Gosse, "Electrical conduction of solutions of an ionic surfactant in hydrocarbons", Journal of Electrostatics, vol. 12, pp. 197-205, Apr. 1982.

87. KEITHLEY 6517B, "Electrometer / High Resistance Meter Specifications", rev. A, Jun. 2008.

88. CEI/IEC 156:1995, "Insulating liquids - Determination of the breakdown voltage at power frequency – Test method", Second edition, 1995.

89. ASTM D1816-12, "Standard test method for dielectric breakdown voltage of insulating liquids using VDE electrodes", ASTM, 2012.

90. X. Wang and Z.D. Wang, "Particle Effects on Breakdown Voltage of Mineral and Ester Based Transformer Oils," Conference on Electrical Insulation and Dielectric Phenomena (CEIDP), Quebec, QC, Canada, Feb. 2008.

91. W. Pfeiffer, R. Plessow, N. Kolev, P. Darjanov and D. Darjanova, "About the Dimensioning of a Needle Plane Electrode Arrangement for Comparative Investigations of Partial Discharges in Air", Electrical Insulation Conference and Electrical Manufacturing and Coil Winding Conference, Rosemont, IL, Sep. 1997.

92. IEEE Std. C57.106[TM]-2015, "IEEE Guide for Acceptance and Maintenance of Insulating Mineral Oil in Electrical Equipment", IEEE Power and Energy Society, rev of IEEE Std C57.106-2006, 2015.

93. IEEE Std. C57.147[TM]-2018, "IEEE Guide for Acceptance and Maintenance of Natural Ester Insulating Liquid in Transformers", IEEE Power and Energy Society, rev of IEEE Std C57.147-2008, 2018.

94. R. Coelho and J. Debeau, "Properties of the tip-plane configuration", Journal of Physics D: Applied Physics, vol. 4, pp. 1266-1280, 1971.

95. O. Lesaint and T.V. Top, "Streamer inception in mineral oil under ac voltage", IEEE 17th International conference on Dielectric Liquids (ICDL), Trondheim, Jun. 2011.

96. O. Lesaint and P.Gournay, "Initiation and propagation thresholds of positive prebreakdown phenomena in hydrocarbon liquids", IEEE Trans. on Diel. and Elec. Insul., vol.1, n°4, pp.702-708, 1994.

97. O. Lesaint and F. Roldan, "On the correlation between positive streamer shape and propagation in benzyltoluene", 13th Int. Conf. on Diel. Liq. (ICDL), IEEE, pp. 167-170, Nara (Japan) July20-25, 1999.

98. L. Roske, TH. Lebey and Z. Valdez-Nava, "High temperature behavior of ceramic substrates for power electronics applications", Annual Report Conference on Electrical Insulation and Dielectric Phenomena (CEIDP), Shenzhen, Oct. 2013.

99. S. Dagdag, T. Lebey, S. Dinculescu, J. Saiz and E. Dutarde, "High Temperature Behaviours of Aluminium Nitride", European Conference on Power Electronics and Applications, Aalborg, Sep. 2007.

100. Tech Brief, "Selecting the Right Substrate Materials for high Power Electronics", Accumet.

101. L. Coppola, D. Huff, F. Wang, R. Burgos and D. Boroyevich, "Survey on High-Temperature Packaging Materials for SiC-Based Power Electronics Modules", Power Electronics Specialists Conference, Orlando, Jun. 2007.

102. M.T. Do, "Propriétés diélectriques des gels isolants: application aux composants d'électronique de puissance", Engineering Sciences [physics], Université Joseph-Fourier – Grenoble I, 2008. French.

103. A. Schletz, M. Nomann, M. Rauch, S. Kraft and S. Egelkraut, "Reliability of Insulating Substrates - High Temperature Power Electronics for More Electric Aircraft", 14th European Conference on Power Electronics and Applications, Birmingham, Sep. 2011.

ANNEX A - Dielectric spectroscopy measurements versus temperature

This annex presents variations of permittivity, tan delta, and conductivity, plotted versus temperature in DBT, SE, and silicone gel.

A. 1. Relative permittivity

Fig. A. 1 to Fig. A. 3 show the variation of relative permittivity of DBT, SE and silicone gel versus temperature, according to their maximum thermal applicable limits..
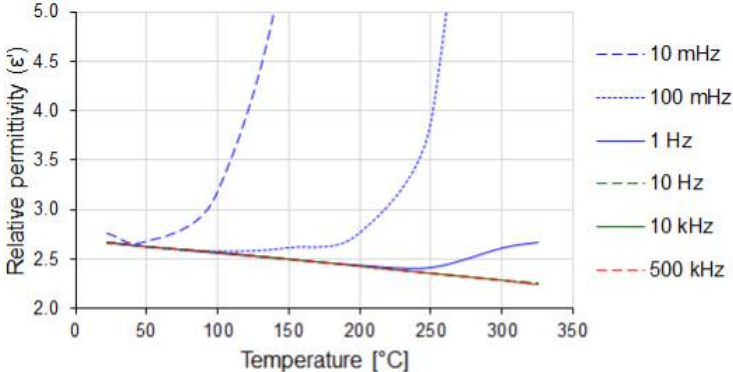

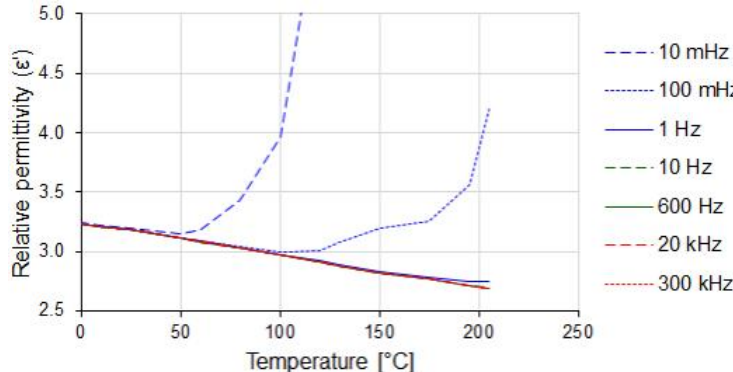*Fig. A. 1 - Relative permittivity (ε') versus temperature of DBT*

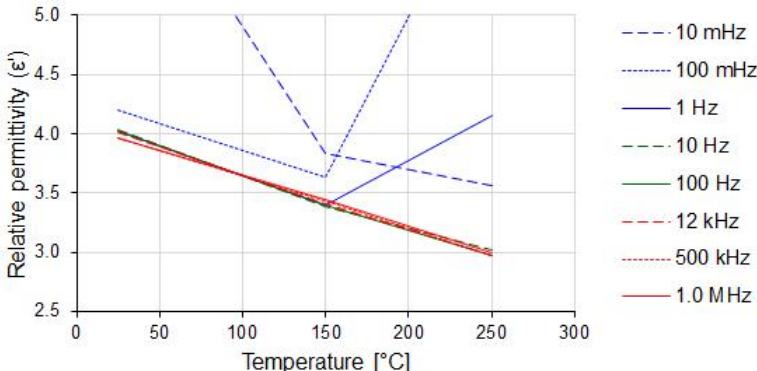*Fig. A. 2 - Relative permittivity (ε') versus temperature of SE*

Fig. A. 3 - Relative permittivity (ε') versus temperature of silicone gel

For silicone gel, dielectric spectroscopy measurements were done only at 3 temperatures: 25°C, 150°C and 250°C.

A. 2. Dielectric spectroscopy results: Tan (delta)

Tan (delta) measurements on dielectric liquids and silicone gel versus temperature indicate distinct behaviour. Measurements in DBT are shown in Fig. A. 4.
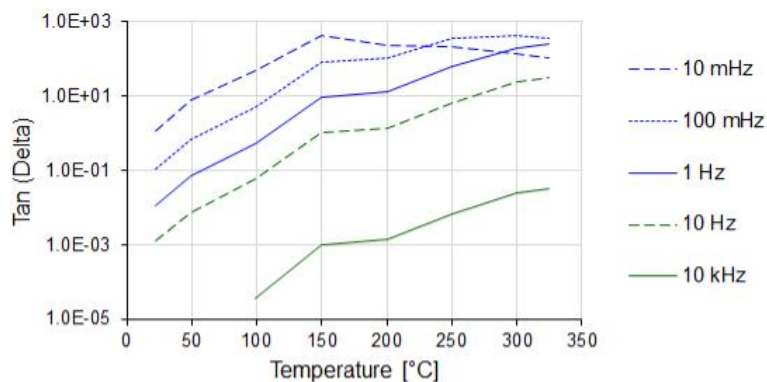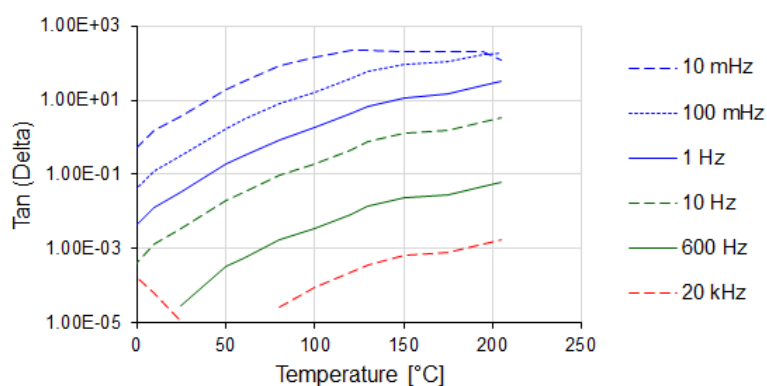

Fig. A. 4 - Tan (delta) versus temperature of DBT

Fig. A. 5 - Tan (delta) versus temperature of SE

In silicone gel, tan (delta) is nearly temperature independence at 12 kHz. Below this frequency, tan (delta) increases with temperature and exhibits opposite behaviour at higher frequency.
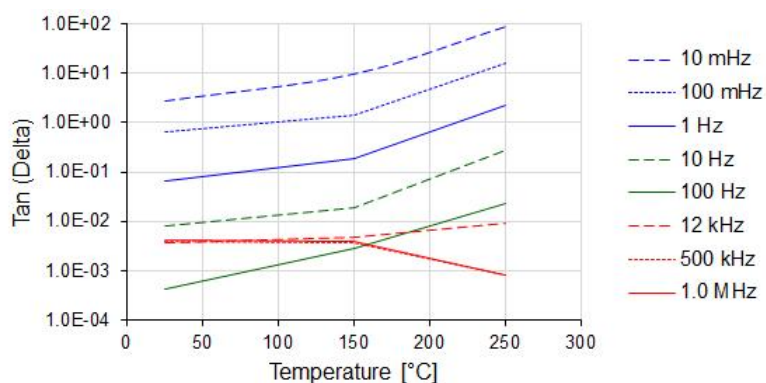

Fig. A. 6 - Tan (delta) versus temperature of silicone gel

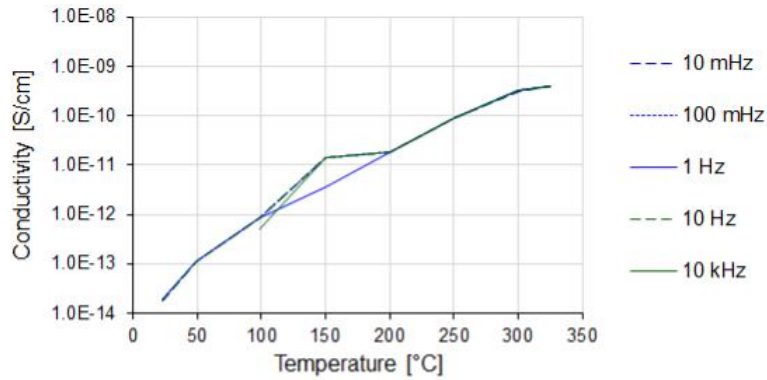## A. 3. Dielectric spectroscopy results: Conductivity

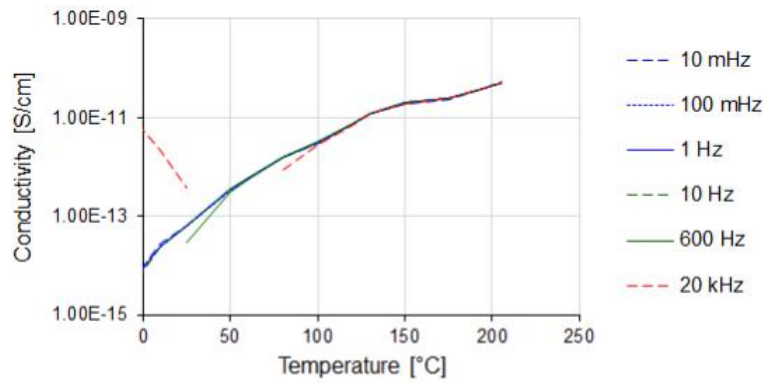*Fig. A. 7 - Conductivity versus temperature of DBT*

Fig. A. 8 - Conductivity versus temperature of SE

Conductivity of silicone gel is nearly temperature independence below 150°C and temperature dependence at temperature above 150°C in all frequency range.
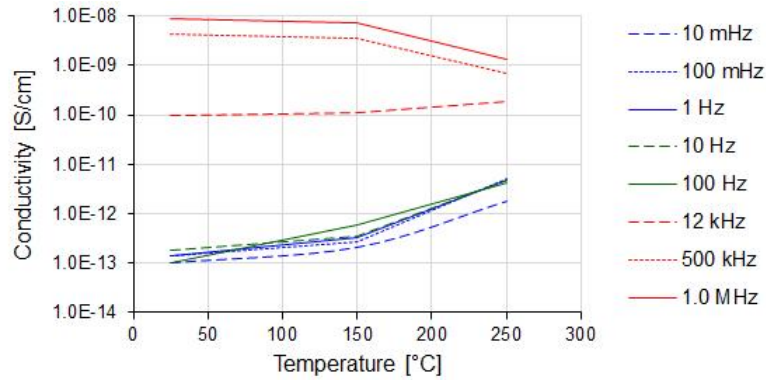

Fig. A. 9 - Conductivity versus temperature of silicone gel

ANNEX B - DC and AC breakdown of aluminium nitride (AlN) embedded in DBT

Aluminium nitride (AlN) substrate is another widely used substrate in electronics power module. This annex present the AC and DC breakdown of AlN substrate embedded in DBT

B.1. AlN substrate sample

Thickness of AlN substrates and copper metallization are 630 µm and 300 µm. Substrates samples were etched with four testing electrodes at average gap of 1.75 mm (Fig. B. 1): two testing electrodes for AC measurements and other two for DC breakdown measurements. Middle circle electrode acted as ground electrode while during a breakdown measurement the rest unused of testing electrodes were shorted to the ground electrode.

Fig. B. 1 - AlN substrate for AC and DC breakdown measurements

B. 2. DC breakdown of AlN substrate in DBT at room temperature

Four consecutive breakdowns were applied to each testing electrode (TABLE B. 1). Breakdowns were likely to occur in AlN substrate, evidenced by the large drop of BDV to less than 50% after the first breakdown. This inflicted permanent damage into the substrate. The average breakdown fields at the first BDVs are 26.5 kV/mm and 28.4 kV/mm.

TABLE B. 1 - DC Breakdown voltage of AlN in DBT at RT

DC Breakdown number	1	2	3	4
BDV [kV] at 1.73 mm	45.9	12.3	17.9	8.8
BDV [kV] at 1.72 mm	48.9	21.8	17.8	8.9

Prior to DC breakdown, strong EHD motions were observed. Black carbon residue appeared after breakdown, leaving scratches on the surface of AlN substrate as in Fig. B. 2. There is also the possibility of cracks and burning traces in the substrate beneath the surface (marked by red box). Due to the opaque properties of AlN, internal defects cannot be clearly observed.
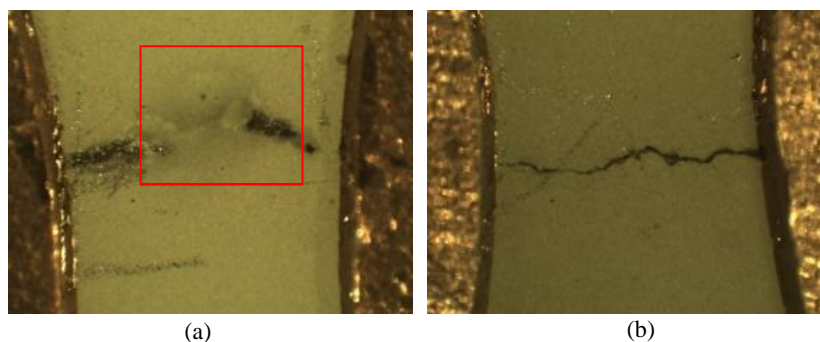

(a) (b)

Fig. B. 2 - AlN substrate embedded in DBT after last DC breakdown test for: (a) 1.73 mm and (b) 1.72 mm gap

147

B. 3. AC breakdown of AlN substrate in DBT at room temperature

Two other testing electrodes of the same gap of 1.78 mm were used for AC breakdown. Four breakdowns were also applied at each testing electrode (TABLE B. 2). AC BDVs rapidly dropped. The highest breakdown fields for both electrodes are 18.8 kV/mm and 16.3 kV/mm.

TABLE B. 2 - AC Breakdown voltage of AlN in DBT at RT

DC Breakdown series	1	2	3	4
BDV [kV] at 1.79 mm	31.7	33.4	19.6	22.8
BDV [kV] at 1.78 mm	29.0	28.0	25.7	25.1

No EHD motion in the liquid were observed during AC breakdown measurements. Similar to those in DC breakdown, permanent defects were observed after (Fig. B. 3).
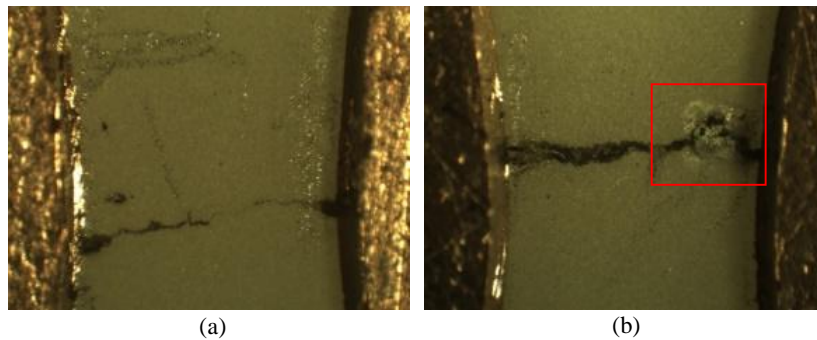

(a)   (b)

Fig. B. 3 - AlN substrate embedded in DBT after last AC breakdown test for 1.78 mm gap

DC breakdown voltage eventually is higher than in AC for the same gap (Fig. B. 4) while the physical appearances of defects are found alike. However, the impact of DC breakdown is suggested to be more severe since the subsequent breakdown voltage were reduced significantly compared to those in AC. Considering both AC and DC breakdown occurred under highly divergent field at larger gap, the breakdown voltage disparity is mainly due to the presence of space charge.
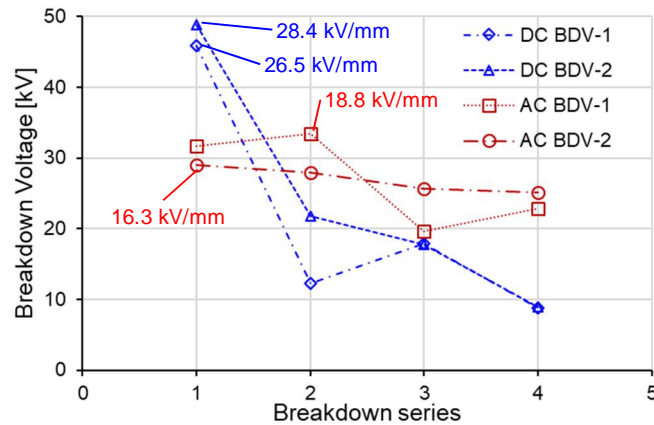

Fig. B. 4 - AC and DC breakdowns of AlN substrate embedded in DBT

Abstract

Applications of wide-bandgap semiconductor devices allow power electronics to operate at higher temperature, voltage and switching frequency. These devices such as SiC can operate up to 500°C, while the recent encapsulant material i.e. silicone gel is limited to 200°C. This is a major obstacle since encapsulant has important roles to provide mechanical and electrical protection inside a power module.

In this work, we propose dielectric liquids as alternative encapsulant that may have better thermal performance than silicone gel. We did series of electrical characterizations on several liquid candidates under high temperature environment included testing with substrates embedded in liquid. Influence of temperature, pressure, type of field i.e.: quasi-uniform and divergent field, and other relevant conditions in the applications were studied. Models were developed to observe field distribution at triple-point region. Results indicate a potential liquid comply with this application.

Résumé

Les applications des dispositifs semi-conducteurs à large bande interdite permettent à l'électronique de puissance de fonctionner à des températures, des tensions et une fréquence de commutation plus élevées. Ces dispositifs tels que le SiC peuvent fonctionner jusqu'à 500 ° C, alors que le matériau d'encapsulation récent, à savoir le gel de silicone, est limité à 200 ° C. Il s'agit d'un obstacle majeur dans la mesure où l'agent d'encapsulation joue un rôle important dans la protection mécanique et électrique d'un module de puissance.

Dans ce travail, nous proposons des liquides diélectriques comme agent d'encapsulation alternatif pouvant avoir de meilleures performances thermiques que le gel de silicone. Nous avons effectué des séries de caractérisations électriques sur plusieurs liquides candidats dans un environnement à haute température, notamment des tests avec des substrats incorporés dans un liquide. Influence de la température, de la pression, du type de champ, c'est-à-dire: un champ quasi uniforme et divergent, et d'autres conditions pertinentes dans les applications ont été étudiés. Des modèles ont été développés pour observer la distribution de champ dans la région à trois points. Les résultats indiquent qu'un liquide potentiel serait conforme à cette application.